LATTICE EFFECTS AND PHASE TRANSITIONS IN TOPOLOGICAL MATERIALS

Thesis by
MARTÍN GUTIÉRREZ AMIGO

for the degree of
DOCTOR OF PHILOSOPHY IN PHYSICS

Supervised by
JUAN LUIS MAÑES PALACIOS
and
ION ERREA

University of the Basque Country (UPV/EHU)
Donostia, Spain, June 2024

Martín Gutiérrez Amigo: *Lattice effects and phase transitions in topological materials,* June 2024

CONTENTS

RESUMEN

El estudio de la materia en su forma "condensada", se refiere a sistemas donde la densidad es suficientemente alta para que las interacciones entre las partículas constituyentes sean críticas para comprender sus propiedades. Las excitaciones disponibles en estos sistemas suelen tener una energía muy baja, especialmente en comparación con las escalas térmicas o químicas. Estas propiedades de baja energía son emergentes, lo que significa que no existen en los constituyentes individuales, sino que surgen de interacciones sutiles entre un número practicamente infinito de partículas. Este comportamiento emergente, donde "el todo es mayor que la suma de sus partes", es uno de los aspectos más cautivadores de la física de la materia condensada.

Una de las tareas principales en la física de la materia condensada es clasificar la materia basada en estas propiedades emergentes. Históricamente, la forma más básica de clasificar estos sistemas ha sido en términos de sus estructuras espaciales. Las categorías más familiares son los sólidos, donde los átomos forman estructuras ordenadas periódicamente, y los líquidos, donde dicho orden está ausente. Sin embargo, una clasificación más moderna y útil de los sistemas de materia condensada se basa en el comportamiento de los electrones dentro del sistema, ya que la mayoría de las propiedades de interés para aplicaciones dependen de este comportamiento. La idea original de distinguir entre conductores y aislantes data de 1729, pero desde entonces se ha ampliado para incluir muchas otras clasificaciones como aislantes, semiconductores, metales, superconductores, paramagnetos, ferromagnetos, etc.

Una clasificación aún más útil y precisa en muchos casos es la basada en las simetrías de los sistemas. Esta aproximación ganó especial relevancia después de que Landau, en la década de 1930, explicara exitosamente la teoría de las transiciones de fase utilizando el concepto de ruptura espontánea de simetría. Este concepto surge del hecho de que las fases de la materia a menudo exhiben menos simetría que el Hamiltoniano que las rige. Por ejemplo, los sólidos cristalinos rompen espontáneamente las simetrías continuas espaciales de traslación o rotación. El "origen" del cristal es en cierto sentido un "accidente" de la historia. Este fenómeno se conoce como ruptura espontánea de simetría, que es en sí mismo una propiedad emergente del sistema. Otro ejemplo se encuentra en los ferromagnetos o antiferromagnetos, donde se rompe la simetría de inversión temporal, inherente al Hamiltoniano subyacente.

El esquema de Landau basado en simetrías ha sido extremadamente exitoso para clasificar fases y transiciones de fase. Sin embargo, el descubrimiento del efecto Hall cuántico entero por Von Klitzing en 1980 reveló las limitaciones de este esquema. En este experimento, un sistema bidimensional de electrones es sometido a un campo magnético perpendicular mostrando una resistividad perpendicular (resistividad Hall) que, contrariamente a lo esperado, no es pro-

porcional al campo magnético. En su lugar, la resistividad muestra mesetas cuantizadas, es decir, la resistividad está cuantizada por un número entero. Aunque estas fases pueden clasificarse por diferentes números enteros, las simetrías no cambian, por lo que no encajan en el esquema de simetría de Landau.

Dos años después, en 1982, Thouless y colaboradores demostraron que este número entero estaba vinculado a un invariante topológico específico conocido como el número de Chern. Este descubrimiento abrió el camino a un nuevo esquema de clasificación basado en invariantes topológicos, donde las transiciones entre fases (cambios en los invariantes topológicos) se denominan transiciones de fase topológicas. Este concepto de fases topológicas de la materia se ha convertido desde entonces en un concepto fundamental de la física de la materia condensada contemporánea.

En la década siguiente, se dio un avance significativo cuando en 1988 Haldane propuso un modelo para el efecto Hall cuántico, en el que demostranba que un sistema podría exhibir dicho efecto Hall (que implica número de Chern no nulo) incluso en ausencia de un campo magnético externo, de manera intrinseca. Sin embargo, no fue hasta mucho después que se descubrieron materiales inherentemente topológicos. Kane y Mele en 2005 mostratron que los sistemas que preservan la simetría de inversión temporal también podían exhibir propiedades topológicas intrínsecas, caracterizadas por un nuevo invariante topológico conocido como el número de Chern de espín. Estas nuevas fases de la materia fueron denominadas aislantes topológicos, requiriendo el acoplamiento espín-órbita y la simetría de inversión temporal como elementos cruciales para una topología no trivial. La realización experimental de tales sistemas se logró tan solo dos años después por König y colaboradores, coincidiendo con la demostración de Fu y Kane de que el concepto de aislantes topológicos podía extenderse a tres dimensiones.

Aunque podría parecer que el nuevo esquema de fases topológicas no tiene ningún vínculo con las simetrías, esenciales en el esquema de Landau, esto está lejos de ser cierto. La exploración de la relación entre las simetrías internas y la topología para sistemas sin interación llevó a una clasificación conocida como la "ten-fold way". Más tarde, en 2011, Fu y colaboradores introdujeron el concepto de los aislantes topológicos cristalinos, demostrando que las simetrías cristalinas, al igual que la simetría de inversión temporal en los aislantes topológicos, también pueden dar lugar a fases topológicas. Además, Fu y Kane ilustraron que, en presencia de la simetría de inversión, se puede establecer una correspondencia entre el número de Chern de espín y la simetría de los autoestados en puntos específicos de la zona de Brillouin. Este concepto, conocido como el criterio de paridad de Fu-Kane, representa el primer ejemplo de un indicador de simetría para la topología.

Esta conexión entre la topología y la simetría fue formalizada posteriormente en 2017 por la química cuántica topológica y la teoría de los indicadores de simetría, proporcionando una clasificación de la materia en términos de invariantes topológicos que pueden relacionarse con las simetrías de los autoestados. La existencia de esta relación reduce significativamente el costo

computacional de calcular invariantes topológicos utilizando métodos *ab initio* y abre la posibilidad de filtrar bases de datos de materiales para buscar nuevos materiales topológicos. El éxito de estos métodos se ejemplifica con los resultados del primer estudio de este tipo, que encontró que aproximadamente el 12% de los 26.938 compuestos estudiados eran aislantes topológicos. Esto sugiere que las fases topológicas, previamente consideradas rareza o excepción en la naturaleza, son en realidad comunes. Por lo tanto, parece que las simetrías cristalinas no solo pueden dar lugar a la topología, sino que también servir para diagnosticarla. Sin embargo, en cierto sentido, hemos pasado de centrarnos únicamente en las simetrías del sistema (como en el esquema de Landau) a estudiar las simetrías de los autoestados.

Por lo tanto, podriamos decir que aunque la teoría de Landau ha sido notablemente exitosa en elucidar la relación entre los efectos de red y las fases tradicionales de la materia, la intrusión de la materia topológica, ha revelado un hecho ineludible: las simetrías del sistema por sí solas son insuficientes para clasificar las fases de la materia. Este cambio de paradigma, introduce un gran abanico de posibles vias de investigación, con amplias implicaciones para el futuro de las tecnologías cuánticas. Inspirados en esto, el objetivo principal de esta tesis, como se refleja en su título, ha sido explorar la interacción entre tres áreas específicas: los efectos de red, las transiciones de fase y fases topológicas de la materia. Cada uno de estos campos es ya extremadamente vasto, lo que implica que un gran numero de ideas y proyectos podrían adscribirse a esta tesis. De los diversos proyectos y colaboraciones realizados, hemos seleccionado tres proyectos particulares que creemos ilustran mejor tres distintas intersecciones entre estos campos.

Por ejemplo, es evidente que hasta ahora nuestra discusión se ha centrado principalmente en el estudio de la topología de los electrones, pero sin embargo, otras cuasipartículas, como los fonones o los fotones, también pueden exhibir características topológicas. Los fonones, en particular, juegan un papel crucial en muchas propiedades fundamentales de los sólidos, incluyendo el transporte, las respuestas ópticas y térmicas, o la superconductividad. Por lo tanto, materiales con bandas fonónicas topológicas podrían revolucionar la física del estado sólido. La búsqueda de topología no trivial en los fonones ha estado basada principalmente en métodos tradicionales y avanzado a un ritmo lento. Sin embargo, recientes estudios han acelerarado tremendamente esta búsqueda. Paralelamente a esta tesis doctoral, se publicó recientemente un catálogo de materiales con fonones topológicos, aplicando la química cuántica topológica a una base de datos de materiales tridimensionales. Sorprendentemente, al contrario que los sistemas electrónicos, este análisis reveló una ausencia casi completa de topología frágil acumulativa en los fonones.

Por nuestra parte, en el primer poyecto que abarca esta tesis doctoral, combinamos la teoría de grupos con la química cuántica topológica para caracterizar completamente la topología de posibles espectros fonónicos de la estructura bidimensional "buckled honeycomb", abordando así directamente el estudio de la topología de los efectos de red. Utilizando solo la estructura cristalina como input, demostramos que este sistema podría exhibir once fases distin-

tas, nueve de las cuales son topológicas. Nuestros hallazgos, en línea con los del reciente estudio que se hizo paralelamente a esta tesis, indican que los sistemas reales con esta estructura no exhiben una topología no trivial en sus espectros fonónicos. Además, a través de una combinación de cálculos de primeros principios y un modelo analítico, explicamos por qué, a pesar de la existencia de diversas fases topológicas, los materiales reales que se ordenan de acuerdo a esta structura se encuentran en una de las fases triviales.

En esta tesis, también se hace uso extensivo del esquema de clasificación de Landau, el cual, como demostraremos, puede complementar la clasificación topológica. Por ejemplo, las ondas de densidad de carga se caracterizan por ser un estado fundamental donde tanto la densidad de carga como las posiciones iónicas experimentan una modulación periódica en relación con una fase de alta simetría. Las transiciones de fase desplazativas de este tipo, están correctamente descritas por el formalismo de Landau, y las simetrías de la fase resultante pueden derivarse del análisis de simetría del parámetro de orden. Por otro lado, los cambios en las simetrías del sistema inevitablemente afectan la estructura de bandas y las simetrías de los estados electrónicos, influyendo así en la clasificación topológica. Por ejemplo, se ha propuesto que las ondas de densidad de carga pueden dar lugar a nuevas fases de la materia como aislantes de axiones, donde una onda de densidad de carga acopla dos fermiones de Weyl, induciendo un estado aislante. Por lo tanto, los efectos de red pueden influir profundamente en la clasificación topológica.

Con el objeto de estudiar la interacción entre las ondas de densidad de carga y el orden topológico, analizamos el SnP, un nuevo material bidimensional. En este estudio, exploramos el potencial de las ondas de densidad de carga para inducir una transición metal-aislante, dando lugar a una fase topológica emergente. Investigamos tres posibles transiciones de fase, que resultaron en fases aislantes metaestables, con una siendo topológicamente no trivial bajo tensión externa. Sin embargo, uno de los resultados principales del estudio, aunque no era la intención inicial, fue que la estructura del estado fundamental solo se manifiesta debido a la influencia de los grandes efectos anarmónicos. Esto subraya la importancia de examinar las transiciones de fase más allá de la aproximación armónica convencional, ya que incluso algo tan fundamental como el estado de menor energía del sistema habría pasado inadvertido bajo la aproximación armónica. Aunque no se pudo obtener la monocapa de SnP mediante exfoliación del material tridimensional, existe la posibilidad de que se pueda sintetizar por medios químicos.

La presencia de fuertes efectos anarmónicos en los sistemas con ondas de densidad de carga no es inesperado, principalmente, si consideramos que uno de los supuestos fundamentales de la aproximación armónica, el pequeño desplazamiento de los iones desde sus posiciones de equilibrio es un supuesto que no se mantiene cerca de la temperatura de transición, cuando los iones se desplazan de sus posiciones de equilibrio. Para el tercer estudio, nos centramos en la familia de metales kagome AV_3Sb_5, ya que proporciona una plataforma ideal para explorar los efectos de red más allá de la aproximación armónica, como el acoplamiento electrón-fonón o los efectos anarmónicos,

que se espera sean fuertes en los sistemas de este tipo. El mecanismo de transicion de fase y la estructura resultante del metal CsV_3Sb_5 han supuesto un gran desafío desde su descubrimiento hace cuatro años. La transición de fase tiene además una importancia crucial, ya que por debajo de T_{CDW} se han observado multitud de fenómenos físicos no observados previamente. En resumen, la verdadera naturaleza de la transición de fase y la estructura atómica resultante siguen siendo preguntas abiertas. Sin embargo, los intentos teóricos previos para explicar la transición de fase han pasado por alto el papel crucial de los efectos anharmónicos. En el estudio, realizamos un análisis exhaustivo de los mecanismos que gobiernan la formación y eventual disolución de la transición de fase, abordando en el proceso algunas de las principales preguntas abiertas en torno a este fenómeno. Contrariamente a las proposiciones previas respecto al mecanismo que media la transición de fase, determinamos que el acoplamiento electrón-fonón es el factor principal que da lugar a la transición de fase. Por el contrario, son los efectos anarmónicos los responsables de la estabilización de la fase de alta simetría a temperaturas más altas. Además, nuestra investigación reveló que el fonón que impulsa la transición de fase opera en un modo distinto al asumido anteriormente por la comunidad, así como proveímos de una explicación por el cual las medidas de espectroscopía no capturan el ablandamiento del fonón que condensa. Finalmente, empleando teoría de grupos, propusimos todos los grupos espaciales posibles compatibles con el parámetro de orden tridimensional que describe la transición de fase. Complementariamente a estos grupos espaciales, sugerimos propiedades espectrales que difieren entre los diferente grupos espaciales propuestos, siendo así una posible prueba experimental para resolver la fase de baja simetría.

En resumen, el objetivo de esta tesis era el de investigar la interrelación entre la topología, las transiciones de fase y los efectos de red. Para ello, primeramente se introducen los métodos fundamentales de primeros principios tanto para los cálculos de la estructura electrónica, como para los de fonones más allá de la aproximación armónica. Además, también se presenta una introducción a los conceptos fundamentales de la teoría de grupos y topología, esenciales para comprender el formalismo de la química cuántica topológica, también introducido. Posteriormente, se llevaron a cabo tres proyectos principales que destacan diferentes superposiciones entre estos campos de estudio. Primero, nos enfocamos en la clasificación topológica de los espectros de fonones posible en la red "buckled honeycomb", demostrando cómo los propios fonones pueden poseer características topológicas inherentes. Luego, exploramos la relación entre diferentes transiciones de fase y la topología de los espectros electrónicos en el material monocapa SnP. Finalmente, discutimos la importancia de los efectos de red más allá del nivel armónico en el estado de onda de densidad de carga presente en la familia de metales kagome AV_3Sb_5 recientemente descubierta.

En conjunto, esta tesis transmite el gran abanico de vías de investigación que residen en la intersección entre los efectos de red, las transiciones de fase y las fases topológicas de la materia. Principalmente, dado que la topología

sigue siendo un campo relativamente joven, especialmente en los sistemas no electrónicos, y que los efectos de red más allá de la aproximación armónica son habitualmente obviados, considero que son de especial interés los sistemas donde estos dos factores juegan roles cruciales. Un ejemplo de ello son las aplicaciones de las ondas de densidad de carga como desencadenantes de fases topológicas, especialmente teniendo en cuenta que los estados de onda de densidad de carga pueden ser creados y aniquilados utilizando láseres para estabilizar los fonones inestables que impulsan la transición de fase, dando esto lugar a posibles aplicaciones tecnológicas.

ACKNOWLEDGEMENTS

Despite the fact that they may never read these lines, I would like to start by acknowledging all the friends I have made in this town, Donostia. I will be forever grateful for how kindly and openly you received me. In just a few months, I already felt at home. Just as I was starting my thesis, the Covid pandemic struck, and we were all forced to stay at home. However, I regard those days, especially the ones following the lockdown (when pubs were closed and we had to gather at each other's homes), as some of the best of my life, and it was all because of you. I am also forever grateful for the greatest opportunity this town has given me, meeting my partner.

Now, I will proceed with thanking the people who might actually read these lines, which makes more sense...

First, I need to thank my supervisors Ion, Juan Luis, and Maia (even if not officially). The scientist I am today is largely due to your guidance.

Ion, I want to express my gratitude for always being there, just a few steps away in the corridor, and always available whenever I had a doubt, imparting invaluable knowledge to me. I genuinely aspire to attain a level of expertise in my field akin to yours. Your patience, especially during the writing of this thesis, has been invaluable, and I truly appreciate all the work you have put into helping me get through the manuscript. I know it must not have been easy, but it looks like, thanks to you, we are finally on time. I want to thank you for sincerely making me feel that you have always cared more about the person than the scientist, and for always being there when I needed help

Juan Luis, during my bachelor's degree, you stood out as my favorite teacher for good reason. I have always admired your ability to convey complex ideas in simple terms without compromising on rigor. I am grateful for your consistent availability whenever I needed to discuss anything, whether it was through Zoom meetings or your detailed emails and notes, thank you.

Maia, I want to thank you for pushing me to become a better scientist and for always looking for interesting projects and collaborations, taking care of my scientific career. I truly appreciate this. I remember that when we first met during my Master, and I must admit, I was a bit of a mess. I even recall you asking me if I read emails because I must not have been giving any signs of life. I know it hasn't been easy, and I appreciate all the work and effort you have put into my training. Also, thank you for always caring about securing appropriate funding during my thesis, from helping me get my first grant to finding me a last-minute contract to finish my thesis. I truly think I could not have asked for more from my supervisors.

I want to thank my office peers, especially those who were there when I started and helped me a lot with my first calculations: Unai, Joseba, and especially Francesco and Antonella. Having you nearby in the office has always

been a great pleasure, and there is no longer fresh coffee now that there are no Italians :(. Thank you, Josu and Manex, it has been truly great being able to reach out to you in the office, and I wish you the best with your theses. Thanks to the more experienced postdocs in the group who have always helped me: Raffaello, Diego, Yueven, and especially Djordje, who I have bothered the most.

I also want to thank all the members of the topological group at DIPC. When I arrived in Donosti for the Topological Matter School in the summer, Iñigo, Mikel, and Chiara were the first people I met. Thank you for your warm welcome. You have now all left, and I truly wish you all the best in your academic careers. Thanks to the rest of the group for the thoughtful discussions we have every week: Irian, Mikel II (García), Antonio, Jorge and Francesc. I am truly grateful to Iñigo, Mikel, Irian, Josu, and Antonio for the time we spent together at overseas conferences. I cherish both the incredibly fun moments we shared and the profound discussions about academia and our careers

To the people from Dresden: thank you to everyone I met there who made my stay so much better, Narayan, Wadji, Erica, and Noki, also for maintaining the cluster where I did half of my calculations. I would like to especially thank Irian for introducing me to everyone, showing me cool places, and hanging out with me during those three months. It was truly a great experience!

I thank Juan José Palacios, Aritz Leonardo Liceranzu, and Giorgia Fugallo for generously accepting my invitation to be a part of my PhD committee.

Finally, and of course, I want to thank my family, who have always been there supporting me.

LIST OF PUBLICATIONS

[1] Martin Gutierrez-Amigo, Fang Yuan, Davide Campi, Leslie M. Schoop, Maia G. Vergniory, and Ion Errea. "Purely anharmonic charge density wave in the two-dimensional Dirac semimetal SnP." In: *Physical Review B* 109.17 (May 14, 2024), p. 174112. DOI: 10.1103/PhysRevB.109.174112.

[2] Mengyu Yao, Martin Guierrez-Amigo, Subhajit Roychowdhury, Ion Errea, Alexander Fedorov, Vladimir N. Strocov, Maia G. Vergniory, and Claudia Felser. *Observation of Chiral Surface State in Superconducting $NbGe_2$*. Mar. 5, 2024. DOI: 10.48550/arXiv.2403.03324. preprint.

[3] Connor J. Pollak, Grigorii Skorupskii, Martin Gutierrez-Amigo, Ratnadwip Singha, Joseph W. Stiles, Franziska Kamm, Florian Pielnhofer, N. P. Ong, Ion Errea, Maia G. Vergniory, and Leslie M. Schoop. "Chemical Bonding Induces One-Dimensional Physics in Bulk Crystal BiIr4Se8." In: *Journal of the American Chemical Society* (Mar. 2, 2024). ISSN: 0002-7863. DOI: 10.1021/jacs.3c13535.

[4] Chunyu Guo, Maarten R. van Delft, Martin Gutierrez-Amigo, Dong Chen, Carsten Putzke, Glenn Wagner, Mark H. Fischer, Titus Neupert, Ion Errea, Maia G. Vergniory, Steffen Wiedmann, Claudia Felser, and Philip J. W. Moll. "Distinct switching of chiral transport in the kagome metals KV3Sb5 and CsV3Sb5." In: *npj Quantum Materials* 9.1 (1 Feb. 22, 2024), pp. 1–6. ISSN: 2397-4648. DOI: 10.1038/s41535-024-00629-3.

[5] Chunyu Guo, Glenn Wagner, Carsten Putzke, Dong Chen, Kaize Wang, Ling Zhang, Martin Gutierrez-Amigo, Ion Errea, Maia G. Vergniory, Claudia Felser, Mark H. Fischer, Titus Neupert, and Philip J. W. Moll. "Correlated order at the tipping point in the kagome metal CsV3Sb5." In: *Nature Physics* (Jan. 31, 2024), pp. 1–6. ISSN: 1745-2481. DOI: 10.1038/s41567-023-02374-z.

[6] Martin Gutierrez-Amigo, Đorđe Dangić, Chunyu Guo, Claudia Felser, Philip J. W. Moll, Maia G. Vergniory, and Ion Errea. *Phonon collapse and anharmonic melting of the 3D charge-density wave in kagome metals*. Nov. 23, 2023. DOI: 10.48550/arXiv.2311.14112. preprint.

[7] S. Chen, P. L. Leng, A. Konečná, E. Modin, M. Gutierrez-Amigo, E. Vicentini, B. Martín-García, M. Barra-Burillo, I. Niehues, C. Maciel Escudero, X. Y. Xie, L. E. Hueso, E. Artacho, J. Aizpurua, I. Errea, M. G. Vergniory, A. Chuvilin, F. X. Xiu, and R. Hillenbrand. "Real-space observation of ultraconfined in-plane anisotropic acoustic terahertz plasmon polaritons." In: *Nature Materials* (May 4, 2023), pp. 1–7. ISSN: 1476-4660. DOI: 10.1038/s41563-023-01547-8.

[8] Martin Gutierrez-Amigo, Maia G. Vergniory, Ion Errea, and J. L. Mañes. "Topological phonon analysis of the two-dimensional buckled honeycomb lattice: An application to real materials." In: *Physical Review B* 107.14 (Apr. 25, 2023), p. 144307. DOI: 10.1103/PhysRevB.107.144307.

[9] Chunyu Guo, Carsten Putzke, Sofia Konyzheva, Xiangwei Huang, Martin Gutierrez-Amigo, Ion Errea, Dong Chen, Maia G. Vergniory, Claudia Felser, Mark H. Fischer, Titus Neupert, and Philip J. W. Moll. "Switchable chiral transport in charge-ordered kagome metal CsV3Sb5." In: *Nature* (Oct. 12, 2022), pp. 1–6. ISSN: 1476-4687. DOI: 10.1038/s41586-022-05127-9.

[10] Xiangwei Huang, Chunyu Guo, Carsten Putzke, Martin Gutierrez-Amigo, Yan Sun, Maia G. Vergniory, Ion Errea, Dong Chen, Claudia Felser, and Philip J. W. Moll. "Three-dimensional Fermi surfaces from charge order in layered CsV_3Sb_5." In: *Physical Review B* 106.6 (Aug. 23, 2022), p. 064510. DOI: 10.1103/PhysRevB.106.064510.

[11] Juyeon Won, Soyeun Kim, Martin Gutierrez-Amigo, Simon Bettler, Bumjoo Lee, Jaeseok Son, Tae Won Noh, Ion Errea, Maia G. Vergniory, Peter Abbamonte, Fahad Mahmood, and Daniel P. Shoemaker. "Transport and optical properties of the chiral semiconductor Ag3AuSe2." In: *Zeitschrift für anorganische und allgemeine Chemie* n/a.n/a (May 24, 2022), e202200055. ISSN: 1521-3749. DOI: 10.1002/zaac.202200055.

[12] Martin Gutierrez-Amigo. "Revista Española de Fisica Vol 37, No 1 (2023)." In: 37.1 (2023). ISSN: 0213-862X.

LIST OF SYMBOLS

T_x	:	Kinetic energy operator and kinetic energy of particles x
V_{x-y}	:	Interacting energy between particles x and y
$\mathbf{r}_i$	:	Electronic position of electron i (in ocassions $\mathbf{r}_i \equiv (\mathbf{r}_i, \sigma_i)$)
$\mathbf{R}_I$	:	Ionic position of ion I
N_e, N_I	:	Number of electrons and ions in the system
e	:	Electron electric charge
Z	:	Ionic electric charge
m_e	:	Electronic mass
M_I	:	Ionic mass
σ	:	Spin degrees of freedom
Ψ	:	Eigenfunction (ionic and electronic) of the full Hamiltonian $\hat{H}$
$\mathbf{r}$	:	All electronic positions $\mathbf{r} \equiv \{\mathbf{r}_i\}$
$\mathbf{R}$	:	All ionic positions $\mathbf{R} \equiv \{\mathbf{R}_i\}$
K_B	:	Boltzman constant
$\psi(\mathbf{r})$	:	Electronic wavefunction
$\chi(\mathbf{R})$	:	Ionic wavefunction
$\hat{H}^{(e)}_{\mathbf{R}}$, $E^{(e)}_{\mathbf{R}}$	:	Electronic Hamiltonian ($\hat{T}_e + \hat{V}_{e-e} + \hat{V}_{e-I}$) and its eigenvalues
BO	:	Born-Openheimmer
$V^{BO}(\mathbf{R})$	:	Born-Openheimmer energy ($E^{(e)}_{\mathbf{R}} + V_{I-I}$)
$\phi(\mathbf{r}_i)$	:	Single particle electronic wavefunctions (also Kohn-Sham orbital)
$\hat{H}_{eff}$	:	Single particle efective electronic Hamiltonian
ε	:	Single particle electronic Hamiltonian eigenvalues
u_{ion}	:	Electron-ion interaction energy $\langle V_{I-e} \rangle_\psi$
u_H	:	Hartree energy term
u_x	:	Exchange energy term
$n(\mathbf{r})$	:	Electronic density
$n_\Psi(\mathbf{r})$	:	Electronic density associated with the Ψ function $\langle \Psi \vert \hat{n}(\mathbf{r}) \vert \Psi \rangle$
$n_0(\mathbf{r})$	:	Ground state electronic density
$n_{0,\mathbf{R}}(\mathbf{r})$	:	Ground state electronic density for a set of ionic positions $\mathbf{R}$
$\hat{V}_{ext}(\hat{\mathbf{r}})$	:	External potential (generalization of $\hat{V}_{e-I}$)
$\hat{v}_{ext}(\hat{\mathbf{r}})$	:	Single particle external potential (only depends on the spacial coordiante $\mathbf{r}$)
u_{ext}	:	Energy from the external potential $\langle \hat{V}_{ext} \rangle$ (generalization of u_{ion})
$E_{ext}[n]$	:	Same as u_{ext}, but in functional form

$\Phi(\mathbf{r})$	:	Slater determinant of Kohn-Sham orbitals
$F[n]$	:	Universal energy functional ($F[n] = T_s[n] + E_{Hxc}[n]$)
$T_s[n]$	:	Non-interacting kinetik energy functional
$E_H[n]$	:	Hartree energy functional
$E_x[n]$	:	Exchange energy functional
$E_c[n]$	:	Correlation energy functional ($E_c[n] = T_c[n] + U[n]$)
$T_c[n]$	:	Correlation kinetic energy functional
$U_c[n]$	:	Correlation potential energy functional
$E_{KS}[n]$	:	Kohn-Sham energy ($E_{KS}[n] = F[n] + E_{ext}[n]$)
$E_{KS}(\mathbf{R})$	:	Kohn-Sham energy corresponding to an ionic configuration $\mathbf{R}$
$v_H(\mathbf{r})$	:	Hartree potential $v_H(\mathbf{r}) \equiv \delta E_H[n]/\delta n(\mathbf{r})$
$v_{xc}(\mathbf{r})$	:	Exchange-correlation potential $v_{xc}(\mathbf{r}) \equiv \delta E_{xc}[n]/\delta n(\mathbf{r})$
$V_{KS}(\mathbf{r})$	:	Kohn-Sham potential $V_{KS}(\mathbf{r}) \equiv v_{ext}(\mathbf{r}) + v_H(\mathbf{r}) + v_{xc}(\mathbf{r})$
$\hat{H}_{KS}$	:	Kohn-Sham Hamiltonian $\left(\hat{H}_{KS} \equiv \hat{T}_e + \hat{V}_{KS}(\mathbf{r})\right)$
r_s	:	Average electron distance
ε_F	:	Fermi energy
k_F	:	Fermi wavevector
BZ, 1BZ	:	First Brillouin zone
$\mathbf{T}$	:	Real space lattice vector
$\mathbf{G}$	:	Reciprocal space lattice vector $\left(e^{i\mathbf{G}\cdot\mathbf{T}}\right) = 1$
$\mathbf{k}$	:	Reciprocal space vector within the first Brillouin zone
$N_k = N_{cell}$	:	Number of $\mathbf{k}$-points in the 1BZ (equal to the number of primitive cells)
$u(\mathbf{r})$	:	Bloch periodic function
Ω	:	Volume of the system in real space Energy in Green's functions formalism
Ω_{cell}	:	Volume of the primitive cell ($\Omega = \Omega_{cell} N_k$)
f_n	:	Fermi-Dirac occupation of state n
n_B	:	Bose-Einstein occupation
β	:	$1/K_B T$
μ	:	Chemical potential
$w_n(\mathbf{r} - \mathbf{T}_i)$	:	Wannier function n centered on lattice site $\mathbf{T}_i$
N_W	:	Number of Wannier orbitals per primitive cell (equal to the numberof bands)
Ω_S	:	Mean square spread of a set of Wannier functions
Ω_I	:	Gauge-invariant part of Ω_S
$\tilde{\Omega}$	:	Gauge-dependent part of Ω_S

$\hat{P}$	:	Projector over the space spanned by a particular set of bands
$\hat{Q}$	:	Complementary projector to $\hat{P}$ $\left(\hat{Q} = 1 - \hat{P}\right)$
$\mathbf{R}^{eq}$	:	A set of ionic equilibrium position
$\mathbf{R}_i^{eq}$	:	Ionic equilibrium position of ion i
$\mathbf{u}$	:	A set of ionic displacements from equilibrium
$\mathbf{u}_i$	:	Ionic displacement from equilibrium position of ion i
Φ	:	Force constant matrix (the order is given by the number of subindices)
$D(\mathbf{k})$	:	Dynamical matrix.
$\hat{H}^{harm}$	:	Harmonic Hamiltonian
V_n^{BO}	:	Coefficient n of the Taylor expansion of $V^{BO}(\mathbf{R})$ centered in $\mathbf{R}^{eq}$
ϵ^μ	:	Polarization vector corresponding to a normal mode μ
ω_μ	:	Frequency corresponding to polarization vector μ
q_μ	:	Amplitude of a particular normal mode μ
U^{harm}	:	Harmonic potential energy
u^{harm}	:	Harmonic potential energy per cell U^{harm}/N_{cell}
T^{harm}	:	Harmonic kinetic energy
$\hat{b}^\dagger$, $\hat{b}$	:	Bosonic creation and annihilation operators
$\hat{c}^\dagger$, $\hat{c}$	:	Fermionic creation and annihilation operators
$\hat{n}_\nu$	:	Number operator $\hat{b}_\nu^\dagger \hat{b}_\nu$ for state ν
$\hat{H}^{e-ph}$	:	Electron-phonon Hamiltonian
Σ	:	Electron selfenergy
$\Pi(z)$	:	Phonon selfenergy
$\overset{B}{\Pi}(z)$	:	Phonon selfenergy within the bubble approximation
HWHM	:	Half-Width-Half-Maximum
γ_ν	:	HWHM electron-phonon linewidth for mode μ
$\zeta(\mathbf{q})$	:	Nesting function for reciprocal vector $\mathbf{q}$
$\rho_H(\mathbf{R})$	:	Density matrix for Hamiltonian $\hat{H}$ and ionic positions $\mathbf{R}$
Z_H	:	Partition function for Hamiltonian $\hat{H}$
F_H	:	Free energy for Hamiltonian $\hat{H}$
$\mathcal{H}$	:	SSCHA auxiliary harmonic Hamiltonian
$\mathcal{V}$	:	Potential part of $\mathcal{H}$
$\mathcal{R}$	:	Ionic equilibrium positions defining $\mathcal{H}$
$\mathcal{R}^{eq}$	:	Ionic equilibrium positions defining the minimum of the Free energy
$\mathcal{F}_H(\mathcal{H})$	:	Free energy for Hamiltonian $\hat{H}$ computed with $\rho_{\mathcal{H}}$

N_c	:	Number of configurations in the stochastic sampling
$F(\mathcal{R})$	:	Positional free energy, $\left(F(\mathcal{R}) \equiv \min_{\Phi}\left[\mathcal{F}_H(\mathcal{H}]\right)\right)$
$\rho_{\mathcal{R}}$	:	Density minimizing $F(\mathcal{R})$ for a particular set of positions $\mathcal{R}$
$\Phi_{\mathcal{R}}$	:	Force constants corresponding to $\rho_{\mathcal{R}}$
$\overset{(n)}{\Phi}_{\mathcal{R}}$	:	n-th order force constants corresponding to $\rho_{\mathcal{R}}$
$D_{\mathcal{R}}$	:	$\Phi_{\mathcal{R}}$ divided by the square root of the masses
$\overset{(n)}{D}_{\mathcal{R}}$	:	$\overset{(n)}{\Phi}_{\mathcal{R}}$ divided by the square root of the masses
$D^{(F)}$	:	Positional free energy Hessian (also referred as free energy Hessian)
$D^{(\mathcal{H})}$	:	Dynamical matrix of $\mathcal{H}$, same as $D_{\mathcal{R}^{eq}}$
$\sigma(\Omega)$	:	Full spectral function for energy Ω
$\sigma_\mu(\Omega)$	:	Spectral function for energy Ω and mode μ
Ω_μ	:	Quasiparticle frequency for mode μ within the Lorentzian approximation
Γ_μ	:	HWHM phonon-phonon linewidth for mode μ within the Lorentzian approximation
$H(\boldsymbol{\lambda})$	:	Family of parametric Hamiltonians defined by $\boldsymbol{\lambda}$ parameters
$\mathcal{A}_s(\boldsymbol{\lambda}), A_{nm}(\boldsymbol{\lambda})$	:	Adiabatic Berry connection for $H(\boldsymbol{\lambda})$
$\mathcal{W}(\boldsymbol{\lambda}(t)), W_{nm}(\boldsymbol{\lambda}(t))$	:	Non-abelian Berry phase (Holonomy) for a path $\boldsymbol{\lambda}$
P_e	:	Electric polarization
$\mathcal{W}_{\mathcal{C}}$	:	Wilson loop, the holonomy for a closed path
$\Omega^{ij}_{nm}(\mathbf{k})$	:	Berry curvature
Ch	:	Chern number
ρ_g	:	Representation of group element g
ρ_G	:	Band representation for group G
$G_{\mathbf{k}}$	:	The little group of $\mathbf{k}$
EBR	:	Elementary band representation

INTRODUCTION

Condensed matter physics, as its name suggests, studies matter in its "condensed" forms. This means that the density in such systems is sufficiently high for the interactions between constituent particles to be critical (though not necessarily strong) for understanding their properties. The excitations available in these systems often have very low energy, especially when compared to thermal or chemical scales. These low-energy properties are emergent, meaning they do not exist in the individual constituents but arise from subtle interactions among $N \to \infty$ particles. This emergent behavior, where "the whole is greater than the sum of its parts" [1], is one of the most captivating aspects of condensed matter physics.

One of the primary tasks in condensed matter physics is to classify matter based on these emergent properties. Historically, the most basic way to classify such systems has been in terms of their spatial structures. The most familiar categories being solids, where atoms can form periodic arrays and exhibit long-range order, and liquids, where such long-range order is absent. However, a more modern and useful classification of condensed matter systems is the one based on the behavior of the electrons within the system, as most properties of interest for applications depend on this behavior. The original idea of distinguishing between conductors and insulators is first attributed to Stephen Gray in 1729, but it has since been expanded to include many other classifications as semiconductors, superconductors, paramagnets, ferromagnets, etc.

An even more precise classification in many cases is to classify the systems according to their symmetries. This approach gained prominence after Landau in the 1930s developed a theory that successfully explained many salient features of phase transitions using the concept of spontaneously broken symmetry [2]. This concept arises from the fact that phases of matter often exhibit less symmetry than the Hamiltonian that governs them. For instance, crystalline solids spontaneously break continuous spatial translational or rotational symmetries. This new set of discrete symmetries has an "origin" that, in a sense, is an "accident" of history, as there is no particular reason to choose it over all other possible energy-degenerate origins. This phenomenon is referred to as spontaneously broken symmetry, which is itself an emergent property of the system. Another example is found in ferromagnets or antiferromagnets, where the time-reversal symmetry (TRS), inherent in the underlying Hamiltonian, is broken.

The symmetry based Landau scheme for both classifying phases and phase transitions has been tremendously successful, and it was not until Von Klitzing's discovery of the integer quantum Hall effect (IQHE) [3] in 1980 that the Landau scheme was found insufficient to explain a particular "new" kind

of phase transition. In this experiment, a 2D electron gas subjected to a large perpendicular magnetic field exhibited perpendicular resistivity (Hall resistivity) that, contrary to predictions, was not proportional to the magnetic field. Instead, it showed quantized plateaus, or to be more precise, the transverse resistivity was quantized by an integer number. Although these phases could be classified by different integer numbers, the symmetries remained unchanged, thus not fitting into the Landau symmetry scheme.

It was only two years later, in 1982, when Thouless et al. [4] demonstrated that this integer number was linked to a specific topological invariant known as the Chern number. This discovery paved the way for a novel classification scheme grounded in topological invariants, wherein transitions between phases (manifested as changes of the invariants) are referred as topological phase transitions. This concept of topological phases of matter has since become a cornerstone in contemporary condensed matter physics.

In the following decade, new topological phases, such as the fractional quantum Hall effect (FQHE) [5], were observed experimentally. A significant breakthrough occurred in 1988 when Haldane proposed a model for the quantum Hall effect [6], showcasing the possible inherent topological nature of matter. He demonstrated that a system could exhibit integer quantum Hall Effect (a non-zero Chern number), even in the absence of an external magnetic field, while still breaking time-reversal symmetry (TRS). However, it was not until much later that inherently topological materials were discovered. Kane and Mele [7] illustrated that systems preserving TRS could also exhibit intrinsic topological properties, characterized by a new topological invariant known as the spin Chern number. These novel phases of matter were dubbed topological insulators (TI), requiring spin-orbit coupling and TRS symmetry as crucial elements for non-trivial topology. The experimental realization of such systems was achieved two years later by König et al. [8], coinciding with Fu and Kane's demonstration that the concept of topological insulators could be extended to three dimensions [9].

While it may seem that the new scheme of topological phases of matter has no link to symmetries, which were pivotal in Landau's scheme, this is far from accurate. The exploration of the relationship between internal symmetries and topology for non-interacting systems led to a classification known as the ten-fold way [10, 11]. Later, in 2011, Fu et al. [12] introduced the concept of topological crystalline insulators (TCIs), demonstrating that crystal symmetries, akin to the role of time-reversal symmetry (TRS) in topological insulators, can also give rise to topological phases. Furthermore, Fu and Kane illustrated that under the presence of inversion symmetry, a correspondence could be established between the spin Chern number and the symmetry of eigenvectors at specific points in the Brillouin zone. This relation, known as the Fu-Kane parity criterion, represents the first example of a symmetry indicator for topology.

This connection between topology and symmetry was later formalized by topological quantum chemistry (TQC) [13–15] and the theory of symmetry indicators [16, 17], providing a classification of matter in terms of topological

invariants that can be related to the symmetries of eigenstates. This mapping significantly reduces the computational cost of computing topological invariants using *ab initio* methods and opens up the possibility of conducting high-throughput studies to search for new topological materials. The success of these methods is exemplified by the results of the first high-throughput study [18], which found that approximately 12% of the 26,938 studied compounds were topological insulators. This suggests that topological phases, previously considered rare in nature, are actually commonplace. Overall, it appears that crystalline symmetries can not only give rise to topology but also serve to diagnose it. However, in a sense, we have now graduated from solely studying the symmetries of the system (as emphasized in the Landau scheme) to focus on the symmetries of the eigenstates.

Thus far, our discussion has primarily focused on the study of electron topology, but it is essential to recognize that other quasiparticles, such as phonons or photons, may also exhibit topological features. Phonons, in particular, play a crucial role in many fundamental properties of solids, including transport, optical and thermal responses, and superconductivity. Therefore, discovering materials with topological phonon bands could potentially revolutionize solid-state physics. The quest for non-trivial phonon topology, primarily grounded in traditional methods, has advanced at a sluggish pace; however, recent efforts have aimed to accelerate this search. In parallel with this thesis, a phonon catalogue was recently launched [19], applying a high-throughput analysis based on TQC to three-dimensional materials. Surprisingly, contrary to electronic systems, this analysis revealed an almost complete absence of fragile cumulative topology for phonons. In Chapter 4 of this thesis, building on previous research by Mañes [20], we conducted an in-depth analysis of the phonon topology of the buckled honeycomb lattice (BHL). Our findings, in line with those of the recent high-throughput study [19], indicate that real systems with the BHL structure do not exhibit significant topology in their phonon spectra. Later, through a detailed examination, we gained insights into why this is the case for this particular system.

In this thesis, we will also still make extensive use of Landau's classification scheme, which, as we will show, can complement the topological classification. For instance, charge density waves (CDWs) represent a phenomenon of significant interest in modern condensed matter physics. These are characterized by a ground state wherein both the charge density and ionic positions undergo periodic modulation relative to a high-symmetry phase [21]. Displacive phase transitions of this kind are effectively described by Landau's formalism, and even the resulting phase's symmetries can be derived from the symmetry analysis of the order parameter. Conversely, changes in the system's symmetries inevitably impact the band structure and symmetries of electronic eigenstates, thereby influencing the topological classification. For instance, CDWs have been suggested to contribute to novel phenomena such as axion insulators [22], where a CDW couples two Weyl fermions in a Weyl semimetal, driving it into an insulating state [23–25]. Hence, lattice effects can profoundly influence both classification schemes, underscoring their significance for compre-

hending displacive and topological phase transitions. In Chapter 5, we delve into the possibility of a topological phase transition mediated via a charge-density wave in the monolayer material SnP. Through *ab initio* calculations, we unveil the existence of a metastable phase exhibiting non-trivial topology under strain. However, as demonstrated, the inclusion of anharmonic effects introduces substantial corrections, revealing the true ground state only once these effects are accounted for.

The presence of strong anharmonic effects in CDW systems comes as no surprise, considering that one of the fundamental assumptions of the harmonic approximation is the small displacement of ions from their equilibrium positions; an assumption that proves flawed near the CDW temperature, when ions indeed shift from their equilibrium positions. A particularly intriguing CDW system that has garnered significant attention in recent years is the AV_3Sb_5 family of kagome metals. All compounds within this family exhibit a CDW at temperatures around 90 K [26]. The CDW phenomenon holds crucial significance, as below T_{CDW}, a multitude of novel and intriguing physical phenomena have been observed. These include switchable chiral transport [27, 28], specular optical rotation [29], and the presence of a chiral flux phase [30–32] accompanied by loop currents. However, the true nature of the CDW and its resulting atomic structure remain open questions. Moreover, the intricate relationship between the CDW order and the observed unconventional phenomena remains unclear. The absence of consensus regarding the CDW structure hinders the understanding of the emerging properties, primarily because these properties may be constrained by symmetry considerations. In Chapter 6, we focus on the CsV_3Sb_5 kagome metal, arguably the most intriguing member of the family and the one that has garnered the most attention. Through a non-perturbative treatment of anharmonicity from first principles, we uncover both the stabilizing and destabilizing forces that mediate the phase transition between the CDW and high-symmetry states. Additionally, we accurately predict the transition temperature, in good agreement with experimental evidence, and provide an explanation for the absence of phonon softening observed in inelastic x-ray experiments [33].

The aim of this thesis is to investigate the interplay between topology, phase transitions and lattice effects. We begin by introducing fundamental *ab initio* methods for electronic structure calculations in Chapter 1, laying the groundwork for much of the subsequent analysis. In Chapter 2, we delve into the methods used for first-principle calculations of lattice dynamics beyond the traditional harmonic approximation. Moving on to Chapter 3, we provide a review of group theory and topology, which are essential for grasping the formalism of topological quantum chemistry introduced in the latter part of the chapter. Chapter 4 focuses on the topological classification of phonon spectra within the buckled honeycomb lattice, demonstrating how lattice dynamics can possess inherent topological features. In Chapter 5, we explore the relationship between different phase transitions and the topology of electronic spectra in the monolayer material SnP, emphasizing the influence of anharmonic effects. Chapter 6 discusses the significance of lattice effects beyond

the harmonic level on the enigmatic charge-density wave state in the recently discovered family of kagome metals AV_3Sb_5. Finally, in Section 6.6, we summarize the main findings of the thesis and outline potential avenues for future research.

Part I

THEORETICAL FRAMEWORK

1

THE ELECTRONIC HAMILTONIAN

The aim of this chapter is to introduce the main many-body Hamiltonian that describes the interaction between ions and electrons in condensed matter. The magnitude of this problem's complexity can be appreciated through Avogadro's number, $N_A = 6.022 \times 10^{23}$, which indicates the order of magnitude of bodies (electrons and ions) in the system. Given that even the simple three-body problem lacks an analytic solution, solving such an enormous problem seems unimaginable. However, as we will show, it is remarkable that through clever and insightful approximations developed over the past century, including the application of symmetries, this daunting problem can be reduced to a manageable size.

1.1 BASIC HAMILTONIAN FOR INTERACTING ELECTRONS AND NUCLEI

A condensed matter system is essentially built from electrons and ions (nuclei plus the core electrons), which can be viewed as positive and negative charges dressed by their spin degree of freedom. Then, the usual *ab initio* approach holds upon the constructionist hypothesis that by knowing the main forces mediating the individual pairs, one can describe the full system. Thus, the Hamiltonian describing the full system can be built with just five terms, the kinetic energies of our constituents (T_e, T_I), where e stands for electron and I for ion, the interactions within each of the constituents (V_{e-e}, V_{I-I}) and the interaction between both of them V_{e-I}. Thus, the full Hamiltonian for the system of electrons and ions can be written as:

$$\hat{H} = \hat{T}_e + \hat{T}_I + \hat{V}_{e-e} + \hat{V}_{I-I} + \hat{V}_{e-I} \,, \tag{1.1}$$

where as stated before each of the terms can be easily written explicitly just by summing over all particular particles for the kinetic energies and over all the pairs for the interacting terms

$$\begin{aligned} \hat{H} = &\sum_{i=1}^{N_e} \frac{1}{2m_e} \hat{\mathbf{p}}_i^2 + \sum_{I=1}^{N_I} \frac{1}{2M_I} \hat{\mathbf{P}}_I^2 + \frac{1}{2} \sum_{i=1}^{N_e} \sum_{j \neq i}^{N_e} \frac{\frac{e^2}{4\pi\epsilon_0}}{|\hat{\mathbf{r}}_i - \hat{\mathbf{r}}_j|} \\ &+ \frac{1}{2} \sum_{I=1}^{N_I} \sum_{J \neq I}^{N_I} \frac{\frac{e^2}{4\pi\epsilon_0} Z_I Z_J}{|\hat{\mathbf{R}}_I - \hat{\mathbf{R}}_J|} - \sum_{i=1}^{N_e} \sum_{I=1}^{N_I} \frac{\frac{e^2}{4\pi\epsilon_0} Z_I}{|\hat{\mathbf{r}}_i - \hat{\mathbf{R}}_I|} \end{aligned} \,. \tag{1.2}$$

We assume our system contains N_e electrons and N_I ions and we have used lowercase/capital indices for electrons/ions. In equation (1.2), m_e and M_I are

the electronic and ionic masses, $(\hat{\mathbf{p}}_i, \hat{\mathbf{r}}_i)$ and $(\hat{\mathbf{P}}_I, \hat{\mathbf{R}}_I)$ are the respective momentum/position operators and Z_I is the charge of a particular ion in e (electronic charge) units. The factor $\frac{1}{2}$ in the V_{I-I} and V_{e-e} terms is there to avoid double counting each pair of equivalent particles.

In the following we will make use of atomic units, defined as

$$\hbar = m_e = e^2 = 4\pi\epsilon_0 = 1 \,, \tag{1.3}$$

which in turn allows as to write (1.2) in the simpler form

$$\begin{aligned} \hat{H} = &- \sum_{i=1}^{N_e} \frac{1}{2}\hat{\nabla}_i^2 - \sum_{I=1}^{N_I} \frac{1}{2M_I}\hat{\nabla}_I^2 + \frac{1}{2}\sum_{i=1}^{N_e}\sum_{j=1}^{N_e} \frac{1}{|\hat{\mathbf{r}}_i - \hat{\mathbf{r}}_j|} \\ &+ \frac{1}{2}\sum_{I=1}^{N_I}\sum_{J=1}^{N_I} \frac{Z_I Z_J}{|\hat{\mathbf{R}}_i - \hat{\mathbf{R}}_j|} - \sum_{i=1}^{N_e}\sum_{I=1}^{N_I} \frac{Z_I}{|\hat{\mathbf{r}}_i - \hat{\mathbf{R}}_I|} \end{aligned} \,. \tag{1.4}$$

In principle and in spite of the complexity of the problem, nothing stops us from being optimistic and writing the solution of the time-independent Schrodinger equation [34] for the eigenstates of the Hamiltonian. The eigenvalues and eigenvectors will depend on both the electronic degrees of freedom $(\mathbf{r}_i, \sigma_i)$, where $\mathbf{r}$ is the electron position and σ is the spin, and ionic degrees of freedom $\mathbf{R}_I$

$$\hat{H}\Psi_s(\mathbf{r}_1\sigma_1, \ldots, \mathbf{r}_N\sigma_N \,;\, \mathbf{R}_1, \ldots, \mathbf{R}_M) = E_s\Psi_s \,, \tag{1.5}$$

with Ψ_s being of course antisymmetric under the exchange of the fermionic degrees of freedom

$$\Psi_s(\mathbf{r}_1\sigma_1, \ldots, \mathbf{r}_i\sigma_i \ldots, \mathbf{r}_j\sigma_j \ldots, \mathbf{r}_n\sigma_n) = -\Psi_s(\mathbf{r}_1\sigma_1, \ldots, \mathbf{r}_j\sigma_j \ldots, \mathbf{r}_i\sigma_i \ldots, \mathbf{r}_n\sigma_n) \,. \tag{1.6}$$

In the following, in order to make the notation less convoluted we will combine both position and spin degrees of freedom in a single variable $\mathbf{r}_i \equiv (\mathbf{r}_i\sigma_i)$ and use $\mathbf{r}$ and $\mathbf{R}$ when referring to all the particles $\mathbf{r} \equiv \{\mathbf{r}_i\}$, $\mathbf{R} \equiv \{\mathbf{R}_i\}$.

1.1.1 *Born-Oppenheimer approximation*

The first major approximation one may perform over the full crystal Hamiltonian is to decouple the ionic and electronic degrees of freedom. The kinetic terms in (1.4) are linearly proportional to the mass and quadratic with respect to the velocity of each of the particles. On the other hand, according to the equipartition theorem both of this terms are proportional to $\frac{3}{2}K_BT$, and thus the ratio between the speeds over which ions are moving with respect to the ones of electrons goes as $\mathbf{v}_I/\mathbf{v}_e = \sqrt{m_e/M_I}$. Taking into account the mass of a hydrogen nucleus is $\sim 1836\ m_e$, then one may conclude that ions move at least about 40 times slower than electrons. As we will see, this separation between fast and slow degrees of freedom allows us to apply the adiabatic theorem when solving the Schrodinger equation (1.5), and write the solution as a product state of the solutions for the fast and slow degrees of freedom.

Theorem 1 ***(Adiabatic theorem):*** A physical system remains in its instantaneous eigenstate if a given perturbation is acting on it slowly enough and if there is a gap between the eigenvalue and the rest of the Hamiltonian's spectrum [35].

Thus, the Born-Oppenheimer (BO) approximation [36] assumes that electrons instantly accommodate to any variation on the position of the ions. This implies that for electrons, ions are essentially fixed and the ionic degrees of freedom may be treated as a parameter and not a variable when solving the electronic problem. This, leads to a solution of the form $\Psi(\mathbf{r},\mathbf{R}) = \psi_{\mathbf{R}}(\mathbf{r})\chi(\mathbf{R})$, being $\psi_{\mathbf{R}}(\mathbf{r})$ the electronic wavefunction and $\chi(\mathbf{R})$ the ionic one. For seeing this, it is useful to define the so called electronic Hamiltonian $\hat{H}^{(e)}_{\mathbf{R}}$ as

$$\hat{H}^{(e)}_{\mathbf{R}} |\psi_{\mathbf{R},j}\rangle = \left[\hat{T}_e(\hat{\mathbf{p}}) + \hat{V}_{e-e}(\hat{\mathbf{r}}) + \hat{V}_{e-I}(\hat{\mathbf{r}},\mathbf{R})\right] |\psi_{\mathbf{R},j}\rangle = E^{(e)}_j(\mathbf{R}) |\psi_{\mathbf{R},j}\rangle \ , \tag{1.7}$$

where the subindex $\mathbf{R}$ is kept in the electronic Hamiltonian $\hat{H}^{(e)}_{\mathbf{R}}$ and eigenfunctions $|\psi_{\mathbf{R},j}\rangle$ in order to highlight that both are labeled by a particular set of fixed ionic positions $\mathbf{R}$. On the other hand, j is the usual quantum number labeling the complete set of eigenfunctions $\{|\psi_{\mathbf{R},j}\rangle\}$ for each ionic configuration $\mathbf{R}$. Thus, we can propose a formal solution for the coupled system (1.5) of the form:

$$\Psi_s(\mathbf{R},\mathbf{r}) = \sum_j \chi_{s,j}(\mathbf{R})\psi_{\mathbf{R},j}(\mathbf{r}) \ , \tag{1.8}$$

where for each energy level s of the full Hamiltonian, a particular set of ionic functions $\chi_{s,j}(\mathbf{R})$ act as coefficients of the electronic wavefunctions. If we now plug the formal solution (1.8) into the full Hamiltonian (1.5)

$$\hat{H}\Psi_s(\mathbf{R},\mathbf{r}) = E_s\Psi_s(\mathbf{R},\mathbf{r}) \tag{1.9}$$

$$\downarrow$$

$$\left[\hat{H}^{(e)}_{\mathbf{R}} + \hat{T}_I(\hat{\mathbf{P}}) + \hat{V}_{I-I}(\hat{\mathbf{R}})\right] \sum_j |\chi_{s,j}\rangle |\psi_{\mathbf{R},j}\rangle = E_s \sum_j |\chi_{s,j}\rangle |\psi_{\mathbf{R},j}\rangle \ . \tag{1.10}$$

The ionic kinetic term $\hat{T}_I$ is proportional to $\hat{\mathbf{P}}^2$ and thus acts over the product of kets as:

$$\begin{aligned} \hat{T}_I |\chi_{s,j}\rangle |\psi_{\mathbf{R},j}\rangle = (-\sum_I \frac{1}{2M_I}\hat{\nabla}^2_I) |\chi_{s,j}\rangle |\psi_{\mathbf{R},j}\rangle = |\psi_{\mathbf{R},j}\rangle \hat{T}_I |\chi_{s,j}\rangle + \\ + |\chi_{s,j}\rangle \hat{T}_I |\psi_{\mathbf{R},j}\rangle - \sum_I \frac{1}{M_I} \left[\hat{\nabla}_I |\chi_{s,j}\rangle\right] \left[\hat{\nabla}_I |\psi_{\mathbf{R},j}\rangle\right] \ , \end{aligned} \tag{1.11}$$

where the brakets in the last term mean that the operator only acts on the kets inside the braket. Putting now all together and projecting over $\langle\psi_{\mathbf{R},i}|$:

$$\sum_j \left[E^{(e)}_j(\mathbf{R})\delta_{ij} + \hat{T}_I\delta_{ij} + \hat{V}_{I-I}\delta_{ij} + \Delta\hat{H}_{ij}\right] |\chi_{s,j}\rangle = \sum_j \delta_{ij}E_s |\chi_{s,j}\rangle \ , \tag{1.12}$$

where we have gathered all the non-diagonal terms into $\Delta\hat{H}_{ij}$ defined as:

$$\Delta\hat{H}_{ij} \equiv \langle\psi_{\mathbf{R},i}|\hat{T}_I|\psi_{\mathbf{R},j}\rangle - \sum_I \frac{1}{M_I}\langle\psi_{\mathbf{R},i}|\hat{\nabla}_I|\psi_{\mathbf{R},j}\rangle\,\hat{\nabla}_I\,. \tag{1.13}$$

The adiabatic or Born-Oppenheimer approximation assumes that as we vary the ionic positions, electrons stay fixed in the same energy level, and thus, implies ignoring all non-diagonal terms in $\Delta\hat{H}_{ij}$. Or in other words, there is no energy transfer between the ionic degrees of freedom $\mathbf{R}$ and electronic excitations, which would imply a change from state $j \to i$. Moreover, the diagonal terms in the second term are forced to be zero as the normalization constraint imposes that any derivative of $\langle\Psi|\Psi\rangle$ must vanish. Thus, using the Born-Oppenheimer approximation equation (1.12) reduces to:

$$\left[E_j^{(e)}(\mathbf{R}) + \hat{T}_I + \hat{V}_{I-I} + \langle\psi_{\mathbf{R},j}|\hat{T}_I|\psi_{\mathbf{R},j}\rangle\right]|\chi_{s,j}\rangle = E_s\,|\chi_{s,j}\rangle\ , \tag{1.14}$$

which means that we are left with an ionic equation of motion for each electronic state j (for example, the ground state of the electronic Hamiltonian (1.7)), which does not depend on the rest of electronic states $i \neq j$. On top of this approximation, the remaining diagonal terms $\Delta\hat{H}_{ii}$ are typically very small due to the large nuclear mass. Neglecting such terms we are left with

$$\left[\hat{T}_I + E_j^{(e)}(\mathbf{R}) + V_{I-I}(\hat{\mathbf{R}})\right]|\chi_{s,j}\rangle = \left[\hat{T}_I + \hat{V}_j^{BO}(\mathbf{R})\right]|\chi_{s,j}\rangle = E_s\,|\chi_{s,j}\rangle\ , \tag{1.15}$$

where we have defined the Born-Oppenheimer potential $\hat{V}_j^{BO}(\mathbf{R})$, which only depends on the ionic coordinates $\mathbf{R}$ and is entirely defined by a particular solution of the electronic Hamiltonian labeled as j. Finally, we can assume that our system evolves with the electrons always being in the ground state of the electronic Hamiltonian $\hat{H}_{\mathbf{R}}^{(e)}$ (which implies that $j = 0$), as well as the ionic function in equation (1.10) minimizing the total energy $E_{s=0}$. Under these assumptions, since both $j = s = 0$ we can drop both indices and write the ground state as

$$\Psi_{s=0}(\mathbf{R},\mathbf{r}) = \chi(\mathbf{R})\psi_{\mathbf{R}}(\mathbf{r}). \tag{1.16}$$

In order to obtain $\Psi(\mathbf{R},\mathbf{r})$, one first solves the electronic Hamiltonian (1.7) for $\psi_{\mathbf{R}}(\mathbf{r})$, which in turn fully defines the ionic Hamiltonian (1.15) in order to solve $\chi(\mathbf{R})$.

In general, since the BO approximation is just an application of the adiabatic theorem, it works well except for the cases where the electronic states are degenerate or nearly degenerate. When the gap in the electronic states is comparable to the energies of the ionic motion, a transition from electronic state i to state j may happen as ions shift their positions. Thus, special care must be taken in metals where we lack such energy gap and we can expect qualitative corrections. All and all, we have successfully separated the ionic an electronic degrees of freedom. The rest of the chapter will be devoted to the resolution of the electronic Hamiltonian $\hat{H}_{\mathbf{R}}^{(e)}$ defined in (1.7), where in the following, we will drop the $\mathbf{R}$ subindex to make the notation less cumbersome.

1.1.2 *Hartree approximation*

Now that we have successfully decouple the ionic and electronic degrees of freedom (1.15) we are posed with the still extremely challenging problem of solving the electronic Hamiltonian (1.7) for a particular set of fixed ionic positions. The electronic wavefunction $\psi_i(\mathbf{r})$ contains all the information of the N_e electrons in the system as well as taking into account all their interactions through the Coulomb electron-electron potential. Thus, we rely on further approximations in order to tackle the electronic problem and make it manageable. The first approach is to perform an independent electron approximation (see A.2), which essentially neglects correlation effects, and for any system with independent particles allows us to write the wavefunction as a product of wavefunctions for the individual particles.

This particular set of approximations, the Born-Oppenheimer (1.1.1) + non-interacting electrons (A.2), are the main building blocks of the Hartree approximation [37]. As shown in Appendix A.2, all non-interacting electron calculations involve single particle Schrodinger-like equation of the form

$$\psi(\mathbf{r}) = \prod_{i=1}^{N} \phi_i^\sigma(\mathbf{r}_i) \,, \tag{1.17}$$

$$\hat{H}_{\text{eff}}\phi_i^\sigma(\mathbf{r}_i) = \left[-\frac{1}{2}\hat{\nabla}^2 + \hat{V}_{\text{eff}}^{\sigma(i)}(\hat{\mathbf{r}}_i)\right]\phi_i^\sigma(\mathbf{r}_i) = \varepsilon_i^\sigma \phi_i^\sigma(\mathbf{r}_i) \,, \tag{1.18}$$

where we made explicit that now each $\phi_i^\sigma(\mathbf{r}_i)$ are single-particle wavefunctions with spin index σ (in the following we will drop the i subindex in the position $\mathbf{r}$). On the other hand, for each single-particle wavefunction ϕ_i, there exists an effective potential $V_{\text{eff}}^{\sigma(i)}(\hat{\mathbf{r}}_i)$ that acts on each electron of spin σ at point $\mathbf{r}_i$. How we do explicitly define such effective potential in order to account for the rest of the particles in the best possible way is what distinguishes the different non-interacting approximations. The Hartree approximation consists in assuming that each electron interacts with every other electron proportionally to the product of the densities of each pair. Then, equation (1.7) is written as

$$\langle \hat{H}^{(e)} \rangle_\psi = \sum_{i,\sigma} \langle \hat{H}_{\text{eff}} \rangle_{\phi_i^\sigma} \,, \tag{1.19}$$

$$\downarrow$$

$$\langle \hat{H}^{(e)} \rangle_\psi = \sum_{i,\sigma} \langle \phi_i^\sigma | \left[-\frac{1}{2}\hat{\nabla}_i^2 + \hat{V}_{e-I}(\hat{\mathbf{r}}_i)\right] | \phi_i^\sigma \rangle + \frac{1}{2}\sum_{i,\sigma}\sum_{j,\sigma' \neq i,\sigma} \langle \phi_i^\sigma, \phi_j^{\sigma'} | \frac{1}{|\hat{\mathbf{r}}_i - \hat{\mathbf{r}}_j|} | \phi_i^\sigma, \phi_j^{\sigma'} \rangle \,. \tag{1.20}$$

Now, by using the variational theorem (see Appendix A.1) we can search for the eigenstates of such Hamiltonian with the additional constrain that we want normalized wavefunctions:

$$\langle \psi | \psi \rangle = 1 \quad \Longrightarrow \quad \sum_\sigma \langle \phi_i^\sigma | \phi_i^\sigma \rangle = 1 \,. \tag{1.21}$$

Thus, we define a new functional F with the corresponding Lagrange multipliers ε_i:

$$F[\{\phi_i^\sigma\}, \varepsilon_i] = \langle \hat{H} \rangle_\psi - \sum_i \varepsilon_i \left(\sum_\sigma \langle \phi_i^\sigma | \phi_i^\sigma \rangle - 1 \right) . \tag{1.22}$$

Now, we look at the functional derivatives of the form $\delta F / \delta \phi_i^\sigma = 0$. Luckily, we are under a particular form for the functional F discussed in Appendix A.1.2 and the computation of the functional derivative is direct as shown in (A.15):

$$\frac{\delta F}{\delta \phi_i^{\sigma *}} = \left(-\frac{1}{2} \hat{\nabla}_i^2 + \hat{V}_{e-I}(\hat{\mathbf{r}}) \right) \phi_i^\sigma(\mathbf{r}_i) + \sum_{j, \sigma' \neq i, \sigma} \int d\mathbf{r}_j \frac{\phi_i^\sigma(\mathbf{r}_i) \, |\phi_j^{\sigma'}(\mathbf{r}_j)|^2}{|\mathbf{r}_i - \mathbf{r}_j|} - \varepsilon_i \phi_i^\sigma(\mathbf{r}_i) . \tag{1.23}$$

This only holds $\delta F / \delta \phi_i^{\sigma *} = 0$ given that:

$$\left(-\frac{1}{2} \hat{\nabla}_i^2 + \hat{V}_{e-I}(\hat{\mathbf{r}}_i) \right) \phi_i^\sigma(\mathbf{r}_i) + \left(\sum_{j, \sigma' \neq i, \sigma} \int d\mathbf{r}_j \frac{\left| \phi_j^{\sigma'}(\mathbf{r}_j) \right|^2}{\left| \mathbf{r}_i - \mathbf{r}_j \right|} \right) \phi_i^\sigma(\mathbf{r}_i) = \varepsilon_i \phi_i^\sigma(\mathbf{r}_i) . \tag{1.24}$$

We can clearly see that we obtain a single-particle set of equations of the form (1.18) that take the name of the "Hartree equations". These equations can be solved self-consistently by starting with an initial set of single-particle wavefunctions to define the initial effective potential. In each iteration, a new set of wavefunctions is obtained, which in turn defines a new potential. This process is repeated until convergence is achieved and (1.24) holds.

As expected from a non-interacting gas of electrons, if we assume that the sample is neutrally charged and that the ionic density is constant, it happens that the ion-electron interaction and the electron-electron interaction cancel out. This reduces the Hartree approximation to a Fermi gas (free electron gas), which is expected taking into account that we are under an independent electrons approximation. Thus, the Hartree approximation is essentially solving a free electron gas under a more complex ionic configuration.

1.1.3 *The Hartree-Fock approximation*

One big oversight we have committed in the Hartree approximation is not taking into account the proper statistics of electrons as fermions. This was done when assuming a particular form (1.17) for the solution of the electronic wavefunction, as this wavefunction is not antisymmetric as initially indicated in (1.5). The Hartree-Fock approximation [38] is essentially the addition of a proper treatment of the electron statistics on top of the previously explained Hartree model. This is done by requiring explicit anti-symmetry in the many-fermion wavefunction. Thus, the Hartree-Fock approximation starts with a

many-electron wave function defined as an Slater determinant [39] (the anti-symmetric solution for non-interacting systems):

$$\psi(\mathbf{r}_1,\sigma_1;\mathbf{r}_2,\sigma_2;\dots) = \frac{1}{\sqrt{N_e!}} \begin{vmatrix} \phi_1(\mathbf{r}_1,\sigma_1) & \phi_1(\mathbf{r}_2,\sigma_2) & \cdots & \phi_1(\mathbf{r}_N,\sigma_N) \\ \phi_2(\mathbf{r}_1,\sigma_1) & \phi_2(\mathbf{r}_2,\sigma_2) & \cdot\cdot & \phi_2(\mathbf{r}_N,\sigma_N) \\ \vdots & \vdots & \ddots & \phi_N(\mathbf{r}_N,\sigma_N)) \end{vmatrix} . \tag{1.25}$$

Then, finding the ground state consists in finding the single Slater determinant with the lowest (variational) energy (see Appendix A.1). The final expression for the energy $\langle\hat{H}\rangle_\psi$ takes the form

$$\begin{aligned} \langle\hat{H}\rangle_\psi = &\sum_{i,\sigma}\int d\mathbf{r}_i\ \phi_i^{\sigma*}(\mathbf{r}_i)(\frac{-1}{2}\nabla_i^2 + V_{I-e}(\mathbf{r}_i))\ \phi_i^{\sigma}(\mathbf{r}_i) + \\ &+\frac{1}{2}\sum_{i,\sigma,j,\sigma'}\int d\mathbf{r}_i\ d\mathbf{r}_j\ \frac{|\phi_i^{\sigma}(\mathbf{r}_i)|^2\ |\phi_j^{\sigma'}(\mathbf{r}_j)|^2}{|\mathbf{r}_i-\mathbf{r}_j|} \\ &-\frac{1}{2}\sum_{i,\sigma,j,\sigma'}\int d\mathbf{r}_i\ d\mathbf{r}_j\ \frac{\phi_i^{\sigma*}(\mathbf{r}_i)\ \phi_j^{\sigma'*}(\mathbf{r}_j)\ \phi_i^{\sigma'}(\mathbf{r}_j)\ \phi_j^{\sigma}(\mathbf{r}_i)}{|\mathbf{r}_i-\mathbf{r}_j|}\delta_{\sigma\sigma'} . \end{aligned} \tag{1.26}$$

When comparing to the energy in the Hartree approximation (1.20) one can notice several differences. First, now the second term (Hartree term) runs over all (i,σ,j,σ'), however, the self-interacting term $i,\sigma = j,\sigma'$ gets cancelled with an equivalent term in the third summation. Secondly, a new term (the exchange term) has appeared with respect to the Hartree approximation just as a result of the particular statistics of fermions. In the following, we will refer to the different energy terms in (1.26) as

$$T_e = \sum_{i,\sigma}\int d\mathbf{r}_i\ \phi_i^{\sigma*}(\mathbf{r}_i)(\frac{-1}{2}\nabla_i^2)\ \phi_i^{\sigma}(\mathbf{r}_i), \tag{1.27}$$

$$u_{ion} = \sum_{i,\sigma}\int d\mathbf{r}_i\ \phi_i^{\sigma*}(\mathbf{r}_i)V_{I-e}(\mathbf{r}_i)\ \phi_i^{\sigma}(\mathbf{r}_i), \tag{1.28}$$

$$u_H = \frac{1}{2}\sum_{i,\sigma,j,\sigma'}\int d\mathbf{r}_i\ d\mathbf{r}_j\ \frac{|\phi_i^{\sigma}(\mathbf{r}_i)|^2\ |\phi_j^{\sigma'}(\mathbf{r}_j)|^2}{|\mathbf{r}_i-\mathbf{r}_j|}, \tag{1.29}$$

$$u_x = -\frac{1}{2}\sum_{i,\sigma,j,\sigma'}\int d\mathbf{r}_i\ d\mathbf{r}_j\ \frac{\phi_i^{\sigma*}(\mathbf{r}_i)\ \phi_j^{\sigma'*}(\mathbf{r}_j)\ \phi_i^{\sigma'}(\mathbf{r}_j)\ \phi_j^{\sigma}(\mathbf{r}_i)}{|\mathbf{r}_i-\mathbf{r}_j|}\delta_{\sigma\sigma'} , \tag{1.30}$$

so that the total electronic energy can be easily rewritten as

$$E^{(e)} = \langle\hat{H}^{(e)}\rangle_\psi = T_e + u_{ion} + u_H + u_x \tag{1.31}$$

In order to obtain the equations that define the Slater determinant with the lowest variational energy we have to define the appropriate functional. Moreover, and equivalent to the case in the Hartree approximation, we need to introduce the proper Lagrange multipliers in order to force a normalized

wavefunction (1.21). Thus, we are left with the same functional defined in (1.22), but with the current expression for $\langle \hat{H} \rangle_\psi$. Using the same functional derivative described in (A.15) and imposing $\delta F / \delta \phi_i^{\sigma *} = 0$ we arrive to the "Hartree-Fock equations"

$$\begin{aligned} \varepsilon_i \phi_i^\sigma(\mathbf{r}_i) = & \left(-\frac{1}{2}\hat{\nabla}_i^2 + \hat{V}_{I-e}(\hat{\mathbf{r}}_i)\right) \phi_i^\sigma(\mathbf{r}_i) + \\ & + \left(\sum_{j,\sigma'} \int d\mathbf{r}_j \, \frac{|\phi_j^{\sigma'}(\mathbf{r}_j)|^2}{|\mathbf{r}_i - \mathbf{r}_j|} \right) \phi_i^\sigma(\mathbf{r}_i) \\ & - \sum_j \int d\mathbf{r}_j \, \frac{\phi_j^{\sigma *}(\mathbf{r}_j) \, \phi_i^\sigma(\mathbf{r}_j)}{|\mathbf{r}_i - \mathbf{r}_j|} \phi_j^\sigma(\mathbf{r}_i). \end{aligned} \tag{1.32}$$

As seen, the exchange term acts only between electrons with the same spin and is non-local in the sense that it relates $\phi_i^\sigma(\mathbf{r}_i)$ on the left-hand side of (1.32) with $\phi_i^\sigma(\mathbf{r}_j)$ on the right-hand side. Another interpretation of this exchange term is that while the Hartree term is due to a Coulomb potential produced by every occupied orbital $|\phi_j^{\sigma'}(\mathbf{r}_j)|^2$, the potential in the exchange term is proportional to the overlap between every orbital $\phi_j^\sigma(\mathbf{r}_j)$ and $\phi_i^\sigma(\mathbf{r}_j)$ weighted near $\mathbf{r}_i$ and with the same spin (thus, the exchange name). This terms is extremely important, since the fact that it only acts over particles with the same spin and is negative favours the spin alignment and magnetization. Finally, it is worth stressing that as for the Hartree approximation, when the ionic charge density is constant, the electronic plane waves are a solution of the Hartree-Fock equations (as if we had a free electron gas). However, the total energy (contrary to the Hartree case) is not defined as the sum of ε_i

$$E^{(e)} \equiv \langle \hat{H}^{(e)} \rangle_\psi \neq 2 \sum_i \varepsilon_i, \tag{1.33}$$

which emphasises the fact that despite having started with an independent electron approximation for our solution, the electrons in the problem are not fully independent because of the imposed statistics, neglecting us the possibility of just summing over the "energies" of the single-particle wavefunctions. In the next section we will discuss the true meaning of the Lagrange multipliers ε_i within the Hatree-Fock approximation and their true relation to the total energy of the system.

1.1.3.1 *Koopman's theorem*

The Koopman's theorem directly relates the Lagrange multipliers ε_i with the ionization energy $I_i = E^{(e)}(N_e - 1) - E^{(e)}(N_e)$.

Theorem 2 ***(Koopman's theorem):*** Within the Hartree-Fock approximation the Lagrange multipliers ε_i correspond to the shift in energy between a system with N_e electrons and a system with $(N_e - 1)$ electrons when the removed electron was in state ϕ_i, keeping all other orbitals the same.

$$\varepsilon_i = E^{(e)}(N_e) - E^{(e)}(N_e - 1) \, . \tag{1.34}$$

The key assumption in the Koopman's theorem for the interpretation of the Hartree-Fock equations eigenvalues ε_i is that the rest of the orbitals do not change. If we take that as a given fact, then the resulting Slater determinant after removing electron in ϕ_k has the form

$$\psi^{N-1}(\mathbf{r}_1\sigma_1 \dots \cancel{\mathbf{r}_k\sigma_k} \dots \mathbf{r}_n\sigma_n) = \frac{1}{\sqrt{(N_e-1)!}} |\text{Slater det.}\rangle \,. \tag{1.35}$$

And by using equation (1.31) for the difference in total energies $E^{(e)}(N_e) - E(e)(N_e-1)$ we get

$$(T_e + u_{ion}) \left[\psi^{N_e}\right] - (T_e + u_{ion}) \left[\psi^{N_e-1}\right] = \langle \phi_k^\sigma | \hat{T}_e + \hat{V}_{I-e} | \phi_k^\sigma \rangle \tag{1.36}$$

$$u_H \left[\psi^{N_e}\right] - u_H \left[\psi^{N_e-1}\right] = \sum_{i,\sigma'} \langle \phi_i^{\sigma'} \phi_k^\sigma | \frac{1}{|\hat{\mathbf{r}}_i - \hat{\mathbf{r}}_j|} | \phi_i^{\sigma'} \phi_k^\sigma \rangle \tag{1.37}$$

$$u_x \left[\psi^{N_e}\right] - u_x \left[\psi^{N_e-1}\right] = -\sum_{i} \langle \phi_i^\sigma \phi_k^\sigma | \frac{1}{|\hat{\mathbf{r}}_i - \hat{\mathbf{r}}_j|} | \phi_k^\sigma \phi_i^\sigma \rangle \ , \tag{1.38}$$

where the $\frac{1}{2}$ factors in the Hartree-Fock energy (1.26) have disappeared since we have joined both the (i,k) and k,i terms together.

On the other hand, if we recall the Hartree-Fock equation (1.32) for a particular single-particle wavefunction ϕ_k^σ, in braket notation we get

$$\begin{aligned} \varepsilon_k |\phi_k^\sigma\rangle = (-\frac{1}{2}\hat{\nabla}_k^2 + \hat{V}_{I-e}) \ |\phi_k^\sigma\rangle + \sum_{i,\sigma'} \langle \phi_i^{\sigma'} | \frac{1}{|\hat{\mathbf{r}}_i - \hat{\mathbf{r}}_j|} | \phi_i^{\sigma'} \rangle \, |\phi_k^\sigma\rangle \\ - \sum_i \langle \phi_i^\sigma | \frac{1}{|\hat{\mathbf{r}}_i - \hat{\mathbf{r}}_j|} | \phi_k^\sigma \rangle \, |\phi_i^\sigma\rangle \ , \end{aligned} \tag{1.39}$$

where if we now project over $\langle \phi_k^\sigma|$ and compare with (1.36) we can see that gives us an expression for ε_k equivalent to $\Delta E^{(e)} = \Delta(T_e + u_{ion} + u_H + u_x)$. And thus, we can conclude that

$$\varepsilon_k = E^{(e)}(N_e) - E^{(e)}(N_e - 1), \tag{1.40}$$

when the k electron is removed from the system. It is worth noting that this interpretation breaks down once we start to remove more particles. Imagine we want to remove a second particle from $\psi^{N_e-1} \to \psi^{N_e-2}$, in this case, the energy difference computed in (1.36) for ψ^{N_e-2} with respect to ψ^{N_e-1} would not be relatable to ψ^{N_e-1} as it does not satisfy (1.39) due to the removal of the first electron. Thus, as already mentioned

$$E^{(e)} \equiv \langle \psi | \hat{H}^{(e)} | \psi \rangle \neq \sum_i^{N_e} \varepsilon_i \tag{1.41}$$

pointing out that the electrons in the system are not fully independent after all because the wavefunction is anti-symmetric.

1.2 DENSITY FUNCTIONAL THEORY

So far, we used the Born-Oppenheimer approximation introduced in Section 1.1.1 to decouple the ionic and electronic problems. Subsequently, we used the independent particle approximation as a pivotal tool for tackling the problem of the electronic Hamiltonian (1.7). This procedure leads to a set of computationally demanding self-consistent set of equations with as many wavefunctions as electrons in the system. Moreover, in doing so we have neglected all sort of correlation effects between electrons (except those required by Pauli exclusion principle), and since the Coulomb interaction is long-ranged we expect these effects to be relevant. The beauty of density functional theory is that it manages to reformulate the same exact original problem in terms of just the electronic density.

To get an intuition of this, one should notice that all electronic systems (despite them being molecules, atoms or complex crystals) share the same kinetic term $\hat{T}_e$ and Coulomb interaction $\hat{V}_{e-e}$ (1.7). While the only differential factor for all these systems is the external potential that we so far have labeled as $\hat{V}_{I-e}$. In the following, we will refer to it as $\hat{V}_{ext}(\hat{\mathbf{r}})$ in order to account for all the possible origins of a potential that only depends on the electronic positions $\mathbf{r}$, such as electric fields, ionic configurations, etc. Moreover, this differential external potential $\hat{V}_{ext}$ can be expressed in terms of the density operator $\hat{n}(\mathbf{r})$ as

$$\hat{n}(\mathbf{r}) = \sum_{i}^{N} \delta(\hat{\mathbf{r}} - \mathbf{r}_i) \, , \tag{1.42}$$

$$\hat{V}_{ext}(\hat{\mathbf{r}}) = \sum_{i}^{N} \hat{v}_{ext}(\mathbf{r}_i) = \int d\mathbf{r} \, v_{ext}(\mathbf{r}) \hat{n}(\mathbf{r}) \, , \tag{1.43}$$

where we have written the external potential as a sum of external potentials each of them acting over a particular electron. Thus, the expectation value of the external potential is

$$u_{ext} \equiv \langle \hat{V}_{ext} \rangle = \int d\mathbf{r} \, v_{ext}(\mathbf{r}) n(\mathbf{r}) \, , \tag{1.44}$$

where $n(\mathbf{r}) \equiv \langle \hat{n}(\mathbf{r}) \rangle$. This suggests that, since the differencing factor between all electronic systems can be defined in terms of the electronic density, we could reformulate the electronic problem in terms of $n(\mathbf{r})$ instead of wavefunctions. This is in fact true and achieved thanks to two theorems proved by Hohenberg and Kohn [40] in the 1960s.

1.2.1 *The Hohenberg-Kohn theorems*

The Hohenberg-Kohn theorems [40] hold given that the Hamiltonian can be written as

$$\hat{H}^{(e)} = -\frac{1}{2} \sum_{i} \hat{\nabla}^2 + \sum_{i} \hat{v}_{ext}(\mathbf{r}_i) + \frac{1}{2} \sum_{i,i \neq j} \frac{1}{|\hat{\mathbf{r}}_i - \hat{\mathbf{r}}_j|} \, . \tag{1.45}$$

Theorem 3 ***(Hohenberg-Kohn theorem I):*** $\hat{v}_{ext}$ is uniquely determined, except for a constant, by the ground-state density $n_0(\mathbf{r})$.

Corollary 1 ***(Corollary of Hohenberg-Kohn theorem I:)*** Since $\hat{H}$ is fully determined by $n_0(\mathbf{r})$, it follows that the many-body wavefunctions for all states (ground and excited) are also determined. Therefore, all properties of the system are completely determined given the ground state density $n_0(\mathbf{r})$.

Theorem 4 ***(Hohenberg-Kohn theorem II):*** A universal functional for the energy $E[n]$ in terms of $n(\mathbf{r})$ can be defined for any $\hat{v}_{ext}$. The exact ground state energy is the global minimum, and the density that minimizes this functional is the exact ground state density $n_0(\mathbf{r})$.

Corollary 2 ***(Corollary of Hohenberg-Kohn theorem II):*** $E[n]$ alone is sufficient to determine the exact ground state density and energy. In general, excited states of electrons must be determined by other means.

This couple of theorems can be summarized in the following set of connections:

$$\begin{array}{ccc} \hat{v}_{ext}(\mathbf{r}) & \overset{\text{HK}}{\Longleftarrow} & n_0(\mathbf{r}) \\ \Downarrow & & \Uparrow \\ \{\psi_i(\mathbf{r})\} & \Longrightarrow & \psi_0(\mathbf{r}) \end{array} \tag{1.46}$$

The usual initial point is the external potential $\hat{V}_{ext}$, from there it is clear that this completely defines the Hamiltonian $\hat{H}$. Then, nothing stops us from solving such Hamiltonian to obtain the set of many-body eigenfunctions $\{\psi_i(\mathbf{r})\}$, which in particular also define the ground state $\psi_0(\mathbf{r})$ and the ground state density $n_0(\mathbf{r})$. The Hohenberg-Kohn theorems allow us to connect back this ground-state density with the external potential that defines our Hamiltonian. Thus, any vertex in the diagram (1.46) contains the same amount of information about the system. The explicit demonstrations for both theorems can be seen in Appendix A.3.

Despite these two theorems being extraordinarily general and profound, they also should be equally counter-intuitive at first glance. They are in fact reducing all the complexity of the N-particle many-body complex wavefunction $\psi(\mathbf{r})$ (with N as large as one could possibly imagine) to a single-variable real function $n(\mathbf{r})$. While at the same time claiming that the problem remains exact and all the information is conserved. However, one cannot get something for nothing, and all the complexity has been relegated to the functionals relating the density with physical properties or even the wavefunctions $\psi_i[n]$.

1.2.1.1 *V and N representable densities*

As seen in the previous section the ground-state density $n_0(\mathbf{r})$ encodes all the information of the system (given that one knows the appropriate functionals). Being such a core feature of density functional theory, it is worth asking ourselves which kinds of systems can a density represent, being N-representable and V-representable densities the main categories.

Definition 1 ***(V-representable density):***
A density $n_0(\mathbf{r})$ is said to be V-representable when it can be related to a ground-state function $\psi_0(\mathbf{r})$ with certain $\hat{v}_{ext}$. This excludes any random functions that cannot be related to a ground-state of any specific Hamiltonian.

Definition 2 ***(N-representable density):***
A density $n_0(\mathbf{r})$ is said to be N-representable if it can be related to an N-electron anti-symmetric wavefunction $\psi(\mathbf{r})$. This includes all V-representable densities, but still excludes all densities $n(\mathbf{r})$ that cannot be related to an anti-symmetric $\psi(\mathbf{r})$ by $\langle\psi|\hat{n}(\mathbf{r})|\psi\rangle = n(\mathbf{r})$.

1.2.1.2 *Levy's constrained-search formula*

According to the Hohenberg-Kohn theorems the energy of the electronic system can be written as

$$E^{(e)}[n] = \underbrace{T_e[n] + V_{e-e}[n]}_{F_{HK}[n]} + \underbrace{\int v_{ext}(\mathbf{r})n(\mathbf{r})d\mathbf{r}}_{E_{ext}[n]}, \tag{1.47}$$

where $F_{HK}[n]$ is universal for all electronic systems, and $E_{ext}[n]$ is the equivalent to u_{ext} in equation (1.44) in functional form. However, such a functional is inherently a complex object, making it difficult to intuitively grasp its specific form.

Levy [41, 42] proposed redefining this universal functional in a manner that addresses some of the issues while still leading to the same ground state. First, it extends the definition of the functional from V-representable densities to N-representable ones (which are well defined [43]), while also applying to degenerate ground states (where the HK approach fails). But more importantly, it provides a conceptual way to determine the exact functional, as well as clarifying to certain point the definition of such functional.

The Levy functional $F_L[n]$ is defined as

$$F_L[n] = \underbrace{\min\left\{\langle\psi|\left[\hat{T}_e + \hat{V}_{e-e}\right]|\psi\rangle\right\}}_{\text{min for a fixed } \langle\psi|\hat{n}(\mathbf{r})|\psi\rangle = n(\mathbf{r})} \equiv \langle\psi[n]|\left[\hat{T} + \hat{V}_{e-e}\right]|\psi[n]\rangle\ , \tag{1.48}$$

where $\psi[n]$ is by definition the wavefunction that minimizes the last braket with the constrain of having a fixed $n(\mathbf{r})$.

The novelty is that by doing so we can divide the minimization in two steps. First, the minimization is done over normalized anti-symmetric wavefunctions $\psi(\mathbf{r})$ that yield to certain fixed $n(\mathbf{r})$ (N-representable densities). While

subsequently the minimization is done over all N-representable densities. This can be written as

$$\begin{aligned} E_0^{(e)} &= \min_{\psi} \langle\psi| \left[\hat{T}_e + \hat{V}_{e-e} + \hat{V}_{ext}\right] |\psi\rangle = \min_{n} \left\{ \min_{\psi\to n} \langle\psi| \left[\hat{T}_e + \hat{V}_{e-e} + \hat{V}_{ext}\right] |\psi\rangle \right\} = \\ &= \min_{n} \left\{ \min_{\psi\to n} \langle\psi| \left[\hat{T}_e + \hat{V}_{e-e}\right] |\psi\rangle + \int v_{ext}(\mathbf{r}) n(\mathbf{r})\ d\mathbf{r} \right\} = \\ &= \min_{n} \left\{ F_L[n] + \int v_{ext}(\mathbf{r}) n(\mathbf{r})\ d\mathbf{r} \right\}. \end{aligned} \tag{1.49}$$

This process clarifies the meaning of the universal functional, which can now be defined as the minimum of the sum of kinetic and interacting energies for all possible wavefunctions that lead to a given density $n(\mathbf{r})$.

1.2.2 *The Kohn-Sham method*

One of the most striking features of density functional theory is the fact that $F_L[n]$ is *universal* for all electronic systems, from isolated atoms to complex crystalline structures. But as many times, something as general often lacks of practical use despite exceeding in conceptual importance. As stated before, the density functional has inherited all the complexity once encoded in the wavefunctions, and therefore will be in principle infinitely complex. However, a great step in making density functional theory useful was made by Kohn and Sham [44] by essentially giving a method to approximate such functionals.

1.2.2.1 *The Kohn-Sham auxiliary system*

So far we have assumed a non-interacting solution for an interacting problem. On the other hand, the novelty of the idea proposed by Kohn and Sham is instead to replace the original many-body interacting problem by an auxiliary independent-particle problem (while still maintaining all the information about the system). In principle, there is not a unique way of defining such auxiliary system; thus the ansatz consists in assuming that the ground-state density of such auxiliary system is equal to the one of the interacting system. This is referred as *non-interacting-V-reprensability*, and although is not proven we will assume it to be true.

Since the new system is truly non-interacting, it leads to independent-particle equations that are exactly solvable through a self-consistent loop. In the process all the difficult (and unknown) many-body terms are gathered into a new functional, the exchange-correlation functional $E_{xc}[n]$. Then, the accuracy to which the real system is solved is delimited only by the approximations to the exchange-correlation functional. The Kohn-Sham method can therefore be summarized into the following diagram:

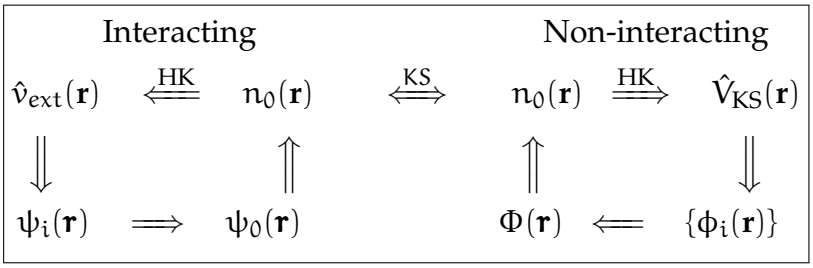

(1.50)

Where the Kohn-Sham ansatz is establishing the connection between both systems (interacting and non-interacting) by relating the ground-state density $n_0(\mathbf{r})$. Here, V_{KS} is the auxiliary non-interacting potential, $\phi_i(\mathbf{r})$ are the solutions to the single-particle equations and $\Phi(\mathbf{r})$ is the Slater determinant many-body wavefunction one builds as solution to the non-interacting problem.

1.2.2.2 *Decomposition of the universal functional*

From the Levy's constrained-search formulation (Section 1.2.1.2), we are left with the task of finding the ground state by optimizing the density $n(\mathbf{r})$ in order to minimize (1.49). However, we now face the difficulty of approximating $F_L[n]$. First it is useful to split the universal functional as

$$F[n] = T_s[n] + E_{Hxc}[n] \ , \tag{1.51}$$

where $T_s[n]$ is the non-interacting kinetic energy functional (not the actual kinetic energy); and $E_{Hxc}[n]$ is the Hartree-exchange-correlation functional.

The non-interacting kinetic part can be defined as:

$$T_s[n] = \min_{\Phi \to n} \langle \Phi | \hat{T}_e | \Phi \rangle \equiv \langle \Phi[n] | \hat{T}_e | \Phi[n] \rangle \ , \tag{1.52}$$

where Φ are single determinant wavefunctions and $\Phi[n]$ are the Kohn-Sham wavefunctions, which minimize $\hat{T}_e$ for a certain $n(\mathbf{r})$ (equivalent to the notation in Section 1.2.1.2). Thus, we can now rewrite (1.49) in terms of KS wavefunctions as

$$\begin{aligned}
E_0 &= \min_n \left\{ F[n] + \int v_{ext}\, n(\mathbf{r})\, d\mathbf{r} \right\} = \min_n \left\{ T_s[n] + E_{Hxc}[n] + \int v_{ext}\, n(\mathbf{r})\, d\mathbf{r} \right\} = \\
&= \min_n \min_{\Phi \to n} \left\{ \langle \Phi | \hat{T}_e | \Phi \rangle + E_{Hxc}[n_\Phi] + \int v_{ext} n_\Phi(\mathbf{r})\, d\mathbf{r} \right\} = \\
&= \min_n \min_{\Phi \to n} \left\{ \langle \Phi | \left[\hat{T}_e + \hat{V}_{ext} \right] | \Phi \rangle + E_{Hxc}[n_\Phi] \right\} \\
&= \min_\Phi \left\{ \langle \Phi | \left[\hat{T}_e + \hat{V}_{ext} \right] | \Phi \rangle + E_{Hxc}[n_\Phi] \right\}
\end{aligned} \tag{1.53}$$

Hence, the exact ground-state energy and density can in principle be obtained by minimizing over the single-determinant wavefunctions Φ. It may

look that we are back at the same point as we started since we have reintroduced a many-body wavefunction Φ. However, this is "only" a single-determinant wavefunction and constitutes a huge simplification over the original variational principle that considered all antisymmetric wavefunctions. Moreover, so far we have not done any approximation (besides the Kohn-Sham ansatz) and only $E_{Hxc}[n]$ has to be approximated as a functional of the density n, with a big part of the kinetic energy $\hat{T}_s$ being exact.

In practice one further decomposes the Hartree-exchange-correlation part as

$$E_{Hxc}[n] = E_H[n] + E_{xc}[n] = E_H[n] + \overbrace{E_x[n] + E_c[n]}^{E_{xc}[n]}, \tag{1.54}$$

where $E_H[n]$ is the Hartree energy functional and $E_{xc}[n]$ is the exchange-correlation energy functional that remains approximate, which can be further decomposed in to the exchange $E_x[n]$ and the correlation $E_c[n]$ parts.

The Hartree part is well defined and accounts for the classic electrostatic repulsion energy

$$E_H[n] = \frac{1}{2}\int \frac{n(\mathbf{r}_i)n(\mathbf{r}_j)}{|\mathbf{r}_i - \mathbf{r}_j|}\, d\mathbf{r}_i d\mathbf{r}_j\,, \tag{1.55}$$

while the exchange part is defined as

$$\langle \Phi[n]|\hat{V}_{e-e}|\Phi[n]\rangle \equiv E_H[n] + E_x[n], \tag{1.56}$$

$$\Downarrow$$

$$E_x[n] = \langle \Phi[n]|\hat{V}_{e-e}|\Phi[n]\rangle - E_H[n]\,. \tag{1.57}$$

So far we have that

$$F[n] = T_e[n] + V_{e-e}[n] = \overbrace{T_s[n]}^{T_e[n_\Phi]} + \overbrace{E_H[n] + E_x[n]}^{V_{e-e}[n_\Phi]} + E_c[n]\,, \tag{1.58}$$

thus, it is easy to see that the correlation part is precisely given by

$$E_c[n] = \langle \Psi[n]|\hat{T} + \hat{V}_{e-e}|\Psi[n]\rangle - \langle \Phi[n]|\hat{T} + \hat{V}_{e-e}|\Phi[n]\rangle \equiv T_c[n] + U_c[n]\,, \tag{1.59}$$

where $T_c[n]$ and $U_c[n]$ are the kinetic and potential parts of the correlation energy functional and defined as

$$T_c[n] = \langle \Psi[n]|\hat{T}|\Psi[n]\rangle - \langle \Phi[n]|\hat{T}|\Phi[n]\rangle\,, \tag{1.60}$$

$$U_c[n] = \langle \Psi[n]|\hat{V}_{e-e}|\Psi[n]\rangle - \langle \Phi[n]|\hat{V}_{e-e}|\Phi[n]\rangle\,. \tag{1.61}$$

1.2.2.3 *Summary of the decomposition*

In summary, we have divided the universal functional $F[n]$ as

$$F[n] = T_s[n] + E_H[n] + E_x[n] + E_c[n]\,, \tag{1.62}$$

where now the density corresponds to a non-interacting system. In the process, we gained intuition and properly defined the different functionals in terms of either the density $n(\mathbf{r})$ or Kohn-Sham wavefunctions $\Phi[n]$ when possible.

1. $T_s[n]$ is the non-interacting kinetic energy (exact and depending only on $\Phi[n]$).

2. The electronic part of the non-interacting system $V_{e-e}[n]$ is given by two terms:
   - $E_H[n]$, the Hartree energy containing the classic Coulomb repulsion (exact, depending directly on $n(\mathbf{r})$).
   - $E_x[n]$, the exchange energy coming from the fermionic statistics, which is also exact (defined in equation (1.30)).

3. Finally, $E_c[n]$ carries all the correlations effects, and accounts for the energy difference between the interacting and auxiliary non-interacting system. Importantly, this is the only term that is not well defined and needs to be approximated.

1.2.2.4 *The Kohn-Sham equations*

Now that we have rewritten the universal density functional in terms of a non-interacting problem we are set to get the single-particle equations (as we did for the Hartree (1.24) or Hartree-Fock approximations (1.32)). The single-determinant wavefunction of the non-interacting problem $\Phi(\mathbf{r})$, is constructed from a set of N orthonormal occupied spin-orbitals $\left\{\phi_i^\sigma(\mathbf{r})\right\}$. The density $n(\mathbf{r})$ is directly related to this single-particle orbitals as

$$n(\mathbf{r}) = \sum_{i,\sigma} |\phi_i^\sigma(\mathbf{r})|^2 \,, \tag{1.63}$$

then, the total energy of the system E_{KS} is given by

$$E_{KS}[\{\phi_i^\sigma\}] = T_s[\{\phi_i^\sigma\}] + E_{ext}[n] + E_H[n] + E_{xc}[n] \,. \tag{1.64}$$

Thus, the minimization over Φ can be recast into a minimization of $E^{(e)}\left[\left\{\phi_i^\sigma\right\}\right]$ with respect to the set of orbitals $\left\{\phi_i^\sigma\right\}$. If we add the constraint of keeping the orbitals normalized, the functional to minimize L, includes now the corresponding Lagrange multipliers:

$$L[\{\phi_i^\sigma\}] = E_{KS}[\{\phi_i^\sigma\}] - \sum_i \varepsilon_i \left(\sum_\sigma \int \phi_i^{\sigma*}(\mathbf{r})\phi_i^\sigma(\mathbf{r})\, d\mathbf{r} - 1 \right) \,. \tag{1.65}$$

If we perform the functional derivative (see Appendix A.1.2) $\delta L/\delta\phi_i^{\sigma*}(\mathbf{r})$ we obtain

$$\frac{\delta L[\left\{\phi_i^\sigma\right\}]}{\delta\phi_i^{\sigma*}(\mathbf{r})} = \frac{\delta T_s[\{\phi_i^\sigma\}]}{\phi_i^{\sigma*}(\mathbf{r})} + \left[\frac{\delta E_{ext}[n]}{\delta n(\mathbf{r})} + \frac{\delta E_H[n]}{\delta n(\mathbf{r})} + \frac{\delta E_{xc}[n]}{\delta n(\mathbf{r})}\right] \frac{\delta n(\mathbf{r})}{\phi_i^{\sigma*}(\mathbf{r})} - \varepsilon_i\phi_i^\sigma(\mathbf{r}), \tag{1.66}$$

where we have applied the chain rule and most of the terms, as we will see, are well defined. From equations (1.27), (1.44), (1.55) and (1.63) it is easy to see that

$$\frac{\delta T_s[\{\phi_i^\sigma\}]}{\phi_i^{\sigma*}(\mathbf{r})} = -\frac{1}{2}\nabla^2\phi_i^\sigma(\mathbf{r}), \tag{1.67}$$

$$\frac{\delta E_{ext}[n]}{\delta n(\mathbf{r})} = v_{ext}(\mathbf{r}), \tag{1.68}$$

$$\frac{\delta E_H[n]}{\delta n(\mathbf{r})} = \frac{1}{2}\int d\mathbf{r}' \frac{n(\mathbf{r}')}{|\mathbf{r}-\mathbf{r}'|} \equiv v_H(\mathbf{r}), \tag{1.69}$$

$$\frac{\delta n(\mathbf{r})}{\phi_i^{\sigma*}(\mathbf{r})} = \phi_i^\sigma(\mathbf{r}). \tag{1.70}$$

The remaining functional derivative, defines the exchange-correlation potential $V_{xc}(\mathbf{r})$ as

$$v_{xc}(\mathbf{r}) \equiv \frac{\delta E_{xc}[n]}{\delta n(\mathbf{r})}\ . \tag{1.71}$$

Making all the substitutions back in (1.65) and equating it to 0 we get the *Kohn-Sham equations* given by

$$\left(-\frac{1}{2}\nabla^2 + \overbrace{v_{ext}(\mathbf{r}) + v_H(\mathbf{r}) + v_{xc}(\mathbf{r})}^{V_{KS}(\mathbf{r})}\right)\phi_i^\sigma(\mathbf{r}) = \varepsilon_i\phi_i^\sigma(\mathbf{r})\ . \tag{1.72}$$

Thus, we have managed to find an expression for the "external" potential $V_{KS}(\mathbf{r})$ that defines the auxiliary non-interacting Hamiltonian $\hat{H}_{KS}$:

$$\hat{H}_{KS} = -\frac{1}{2}\nabla^2 + V_{KS}(\mathbf{r}), \tag{1.73}$$

$$\begin{aligned} V_{KS}(\mathbf{r}) &= v_{ext}(\mathbf{r}) + \frac{\delta E_H}{\delta n(\mathbf{r})} + \frac{\delta E_{xc}}{\delta n(\mathbf{r})} \\ &= v_{ext}(\mathbf{r}) + v_H(\mathbf{r}) + v_{xc}(\mathbf{r}). \end{aligned} \tag{1.74}$$

The set of equations (1.72) constitutes a set of coupled self-consistent equations as $\hat{V}_{KS}$ depends on the density $n(\mathbf{r})$, which in turn depends on the KS orbitals $\{\phi_i^\sigma\}$. Thus, the KS auxiliary system can be understood as a problem of independent particles with an "interacting density". The only unknown term in $\hat{H}_{KS}$ is the exchange-correlation potential $v_{xc}(\mathbf{r})$, which in principle is "infinitely complex" as it contains all the correlation effects and, consequently, has to be estimated through approximations. The next part of this section will be devoted to discuss some of the main approximations for the exchange-correlation potential.

1.2.3 *The local-density approximation (LDA)*

The LDA approximation consists in approximating the exchange-correlation energy per particle with the one of a uniform electron gas with density n:

$$E_{xc}^{LDA}[n] = \int \epsilon_{xc}^{unif}[n](\mathbf{r})\ n(\mathbf{r})\ d\mathbf{r}. \tag{1.75}$$

Thus, in the LDA, the exchange-correlation energy per particle of an inhomogeneous system at spatial point $\mathbf{r}$ of density $n(\mathbf{r})$ is approximated as the exchange-correlation energy per particle of a uniform electron gas with the same density.

$$\epsilon_{xc}^{unif}[n](\mathbf{r}) = \epsilon_{x}^{unif}[n](\mathbf{r}) + \epsilon_{c}^{unif}[n](\mathbf{r}), \tag{1.76}$$

where the exchange part is given by the exact analytic expression

$$\epsilon_{x}^{unif}[n] = -\frac{3}{4}\left(\frac{3}{\pi}\right)^{\frac{1}{3}} n^{\frac{1}{3}} . \tag{1.77}$$

On the other hand, $\epsilon_{c}^{unif}[n]$ cannot be calculated analytically. This quantity however, has been obtained numerically for a number of densities n using Monte Carlo calculations [45], and fitted to forms of $\epsilon_c(r_s)$, where r_s is the average electron distance defined in the usual way. Then, the corresponding correlation potential is given by

$$v_c(r_s) = \epsilon_c(r_s) - \frac{r_s}{3}\frac{d\epsilon_c(r_s)}{dr_s}. \tag{1.78}$$

Among the many implementations of the local density approximation, probably the one from Perdew and Zunger [46] is the most used one

$$\epsilon_{c}^{PZ}(r_s) = \begin{cases} -0.0480 + 0.031\ln(r_s) - 0.0116 r_s + 0.0020 r_s \ln(r_s), & r_s < 1 \\ -0.1423/\left(1 + 1.0529\sqrt{r_s} + 0.3334 r_s\right), & r_s > 1 \end{cases} \tag{1.79}$$

Due to the inherent nature of the local density approximation, it is expected to perform best for solids that resemble a homogeneous electron gas (such as metallic systems) and worst for highly inhomogeneous systems like atoms.

1.2.4 *The generalized gradient approximation (GGA)*

The next logical step beyond the local density approximation is the Gradient Expansion approximation (GEA), which includes derivatives of the density $n(\mathbf{r})$ into the functionals. One way of deriving the GEA is to start from the uniform electron gas, introduce a weak slowly varying external potential, and expand the exchange correlation energy in terms of the gradients of the density $\nabla n(\mathbf{r})$. This procedure was already originally suggested in the seminal paper from Kohn and Sham [44],and later carried out by [47]. However, it turned out that for real systems GEA performs worse than LDA.

The failure of GEA lead to define the generalized gradient approximation (GGA) methods, which modified the GEA functionals in order to preserve the sum rules. In general, GGA functionals are defined as

$$\begin{aligned} E_{xc}^{GGA}[n] &= \int n(\mathbf{r})\epsilon_{xc}(n(\mathbf{r}), \nabla n(\mathbf{r}))\, d\mathbf{r} \\ &\equiv \int n(\mathbf{r})\epsilon_{x}^{hom}(n) F_{xc}(n, \nabla n)\, d\mathbf{r} , \end{aligned} \tag{1.80}$$

where F_{xc} is the dimensionless enhancement factor and $\epsilon_x^{hom}[n]$ is the exchange energy of the homogeneous electron gas (the same used in the LDA). One of the most widely used implementations of GGA, and the one predominantly employed in the studies presented in this manuscript, is the Perdew-Burke-Ernzerhof GGA [48]. In order to provide a concise description, it is useful to define the variable s as a dimensionless fractional gradient of the density

$$s = \frac{|\nabla n(\mathbf{r})|}{2k_F(\mathbf{r})n(\mathbf{r})}\,, \tag{1.81}$$

where $k_F(\mathbf{r})$ is the Fermi wavevector corresponding given by the relation $n(\mathbf{r}) = k_F(\mathbf{r})^3/\left(3\pi^2\right)$. As a direct consequence of definition (1.80) the exchange part is then given by

$$E_x^{GGA}[n] = \int F_x(s)n(\mathbf{r})\epsilon_x^{unif}[n]\,d\mathbf{r}\,, \tag{1.82}$$

where for the particular case of PBE the enhancement factor is

$$F_x^{PBE} = 1 + \kappa - \frac{\kappa}{\left(1 + \frac{\mu s^2}{\kappa}\right)}\,, \tag{1.83}$$

with $\kappa = 0.804$ and $\mu = 0.21951$. On the other hand, the correlation part is given as a correction over the LDA correlation

$$E_c^{GGA}[n] \int d\mathbf{r}\, n(\mathbf{r}) \left[\epsilon_c^{unif}[n] + H(r_s, t)\right]\,, \tag{1.84}$$

$$t \equiv \frac{\nabla n(\mathbf{r})}{2k_s n(\mathbf{r})} \quad , \quad k_s = \left(\frac{4k_F}{\pi}\right)^2\,, \tag{1.85}$$

where the correction over LDA is encoded into $H(r_s, t)$ and for the particular case of PBE is given by

$$H^{PBE}(r_s, t) = \frac{\beta^2}{2\alpha} \ln\left[1 + \frac{2\alpha}{\beta}\frac{t^2 + At^4}{1 + At^2 + A^2t^4}\right]\,, \tag{1.86}$$

with

$$\begin{cases} A = \dfrac{2\alpha}{\beta \exp\left(\frac{-2\alpha V_c^{unif}[n]}{\beta^2}\right) - 1} \\ \alpha = 0.0716\,, \quad \beta = 0.066725 \\ t = \dfrac{\nabla n(\mathbf{r})}{2k_s n(\mathbf{r})}\,, \quad k_s = \left(\dfrac{4k_F}{\pi}\right)^{1/2}\,. \end{cases} \tag{1.87}$$

Overall, both the LDA and GGA functionals owe their success to the "smallness" of the exchange-correlation energy and are prone to failure in highly correlated systems, for which more advanced functionals exist. However, all the cases studied in this manuscript are expected to be well described using GGA functionals.

1.3 THE PSEUDOPOTENTIAL APPROXIMATION

Despite transforming the electronic problem into an independent-electron problem, the interaction persists through the self-consistent loop, as all Kohn-Sham orbitals contribute to defining the effective Kohn-Sham potential $V_{KS}(\mathbf{r})$ (1.74). Consequently, the large number of electrons still poses a computational challenge. Moreover, this approach often results in a waste of resources, as we are typically only interested in the valence electrons, which are responsible for the bonding between atoms and most observed physical properties.

The pseudopotential approximation promises to solve such issue by replacing one problem of all-electrons for another one of only valence electrons, while keeping the results equal (at least outside a sphere of radius R_c centered at the ion cores). In the process, one reframes the problem by replacing the Coulomb potential of the nucleus and core electrons by an effective ionic potential (that now only acts over valence electrons). Additionally, one should be able to generate such pseudopotential, by performing an all-electron calculation of the isolated atom, and then transfer it to molecular or crystalline systems by assuming that core electrons will not change.

As an equivalent example, when one wants to study the scattering properties of a localized spherical potential (like a nucleus), one can find a square well with the same scattering properties for a particular energy. The aim of pseudopotential theory is similar, in the sense that it aims to find an auxiliary potential (or pseudopotential) that leads to the same scattering properties across a desired energy range, while lowering the cost of the calculations.

Most pseudopotential approximations draw inspiration from the orthogonalized plane waves (OPWs) method originally formulated by Herring [49]. The general formalism attempts to provide a basis for the valence electrons that allows to write their eigenfunctions ψ^v_{lm} (where lm labels the angular momentum) as

$$\psi^v_{lm}(\mathbf{r}) = \tilde{\psi}^v_{lm}(\mathbf{r}) + \sum_j B_{lmj} u_{lmj}(\mathbf{r}), \tag{1.88}$$

where $\tilde{\psi}(\mathbf{r})$ are the smooth part of the wavefunctions, while $u_{lmj}(\mathbf{r})$ are localized functions around the nucleus. However, one can define a linear transformation $\mathcal{T}$ that relates the solution of the smooth pseudofunction with the full all-electron function as

$$|\psi^v_{lm}\rangle = \mathcal{T}\,|\tilde{\psi}^v_{lm}\rangle\,. \tag{1.89}$$

Then, the pseudopotential transformation developed by Philips and Kleinman [50] and Antoncik [51] replaces the eigenfunctions (1.88) into the Kohn-Sham equations (1.72) and the problem splits for the localized and smooth parts. The smooth part is now governed by a new external potential $\hat{V}^{PKA}$, which can be shown to be weaker than the original one, as the effect of the localized core electrons V^R is repulsive

$$\hat{V}^{PKA} = V_{KS} + \hat{V}^R. \tag{1.90}$$

In fact, the stronger the original nuclear potential happens to be, the deeper core electrons will be and the more repulsive V^R will be. This tendency results

in the "cancellation theorem" proven by Cohen and Heine [52], which justifies drastic pseudopotential approaches as the Ashcroft "empty core" pseudopotential [53] (with the pseudopotential being zero inside de radius R_c). While $\hat{V}^{PKA}$ is indeed smoother and weaker, leading to smooth pseudo-wavefunctions, it comes at the cost of the new potential also being a non-local operator and the pseudo-wavefunctions not being orthonormal. Thus, in order to benefit from the advantages of the pseudopotential formulation, the pseudopotential approximation rests on the formal properties of $\hat{V}^{PKA}$, while using the fact that different potentials can lead to the same scattering properties. Thus, the aim is to select a pseudopotential that is both weaker and smoother.

1.3.1 *Norm-conserving pseudopotentials*

Norm-conserving pseudopotentials (NCPP) appear as an evolution of the PKA approach, with the aim of rendering the application of the pseudopotential approximation simpler, as well as more accurate and transferable. In contrast to the PKA approach where the solutions have both a smooth part as well as a localized part, norm-conserving pseudofunctions $\psi^{PS}(\mathbf{r})$ are both normalized and solutions of an auxiliary potential chosen to reproduce the valence-states properties as if it was an all-electron calculation

$$\langle \psi_i^{\sigma,PS} | \psi_j^{\sigma',PS} \rangle = \delta_{i,j}\delta_{\sigma,\sigma'}. \tag{1.91}$$

Thus, the Kohn-Sham equations have the same form as in (1.72,1.74), but with $\hat{H}_{KS}^{\sigma,PS}$ given by substituting the external potential by the pseudopotential.

In order for a potential to be considered a "good" norm-conserving pseudopotential, it must fulfill five main requirements [54]:

1. All-electron and pseudo-valence *eigenvalues* agree for the chosen atomic reference configuration.
2. All-electron and pseudo-valence *wavefunctions* agree beyond a chosen core radius R_c.
3. The *logarithmic derivatives* of the all-electron and pseudo wavefunctions agree at R_c.
4. The *integrated charge inside* R_c for each wavefunction agrees (norm-conserving condition).
5. The *first energy derivative* of the logarithmic derivatives of the all-electron and pseudo-wavefunctions agree at R_c, and therefore, for all $r \geqslant R_c$.

The dimensionless logarithmic derivative D is defined as

$$D_l(\varepsilon, r) \equiv \frac{r\psi_l'(\varepsilon, r)}{\psi_l(\varepsilon, r)} = r\frac{d}{dr}\ln\left[\psi_l(\varepsilon, r)\right]. \tag{1.92}$$

From points (1,2), it follows that NCPP equals the original atomic potential outside from the *"core region"* delimited by a radial distance R_c. From point

(3), it follows that pseudo-wavefunctions and their radial derivatives are continuous at R_c. Point (4) requires that the integrated charge

$$Q_l = \int_0^{R_c} r^2 \, |\psi_l(r)|^2 \, dr \equiv \int_0^{R_c} \phi_l(r)^2 dr, \tag{1.93}$$

is the same for ψ_l^{PS} as for the all-electron wavefunction ψ_l for any valence state. The conservation of the integrated charge Q_l, implies that the amount of charge in the core region of the atom is correct as well as that the normalized pseudo-wavefunction is equal to the all-electron valence wavefunction outside R_c (this equality only holds for local functionals). This, in contrast to the smooth function in the PKA (1.88), which only equals the all-electron solution when not normalized.

Altogether, this ensures that both the normalized pseudo-wavefunctions and the external potential are accurate outside the radius R_c, as a spherically symmetric potential depends only on the charge within the sphere. This is crucial because it is in this region where the chemistry and bonding between atoms occur.

Point (5) happens to be implied by point (4) as shown by Hamann et al. [54] and is pivotal to ensure the transferability of the pseudopotential. In a molecule or solid, compared to the isolated atom, the wavefunctions and eigenvalues will change. By satisfying point (5), the pseudopotential will reproduce these changes in the eigenvalues to linear order in the change of the self-consistent potential.

In practice, one defines the non-local pseudopotential as a sum of a local and a non-local part

$$V_l(r) = V_{local}(r) + \delta V_l(r), \tag{1.94}$$

where l stands for the orbital dependence of the pseudopotential. However, the constraint of the pseudopotential matching the atomic potential for $r > R_c$, implies that $\delta V_l(r) = 0$ when $r > R_c$; and thus, all the long-range effects of the Coulomb interaction are contained in the local part $V_{local}(r)$.

Even while applying the norm-conserving condition, there is still freedom for the choice of $V_l(r)$. And sadly, there is not such thing as a "best pseudopotential" and the selection must be case specific. The main factors to take into account being:

1. *Accuracy and transferability*, which in general are better achieved by a small cutoff radius R_c. This are referred as "hard" potentials, since one attempts to extend the range over which the pseudo-wavefunctions coincide with the all-electron valence electrons.

2. *Smoothness of the resulting pseudofunctions* allows for describing the solutions with a smaller basis, which in turn drastically reduces the computational cost. This, however is obtained "softening" the potential by increasing the cutoff radius R_c (which affects the accuracy and transferability).

Thus, one must find a balance between both sets of characteristics to ensure they align well with the particular system under study.

1.3.2 *Ultrasoft pseudopotentials*

Contrary to norm-conserving pseudopotentials, which require to sacrifice accuracy in order to gain smoothness, the main goal of ultrasoft pseudopotentials is to obtain pseudo-functions that are as smooth as possible, while not loosing accuracy. The main advantage of the softness being that in turn functions can be described with a smaller basis (for example of plane-waves), which lowers the computational cost (which scales as a power of the number of Fourier components needed). They fulfill this by re-stating the original problem in terms of a smooth function and an auxiliary function around each nucleus that represents the rapidly varying part of the density.

The proposal by [55] and [56] rewrites the non-local potential involving smooth functions $\tilde{\phi} = r\tilde{\psi}$, which are *not norm-conserving*. Thus, the difference in the "norm equation" (1.93) with respect to the norm-conserving wavefunction is given by

$$\Delta Q_{s,s'} = \int_0^{R_c} \Delta Q_{s,s'}(r)\, dr, \tag{1.95}$$

with

$$\Delta Q_{s,s'}(r) = \phi_s^*(r)\phi_{s'}(r) - \tilde{\phi}_s^*(r)\tilde{\phi}_{s'}(r), \tag{1.96}$$

where $\tilde{\phi}$ and ϕ are respectively, the non-norm-conserving and norm-conserving wavefunctions. This leads to the appearance of new terms in the eigenvalue problem that are proportional to $\Delta Q_{s,s'}$.

The advantage of relaxing the norm-conserving condition $\Delta Q_{s,s'} = 0$ is that each pseudofunction $\tilde{\psi}$ can be formed independently, with the only constraint of matching the value of the all-electron functions at R_c. Thus, it becomes possible to select a much larger R_c, maintaining the accuracy while increasing the smoothness. All at the cost of adding the auxiliary function $\Delta Q_{s,s'}$

1.3.3 *Projector augmented wave method*

The projector augmented wave (PAW) method is a general approach to the solution of the electronic structure problem that reformulates the original OPW method. Similar to the ultrasoft method, it introduces projectors and auxiliary localized functions. The main difference is that the PAW keeps the full many-body wavefunction in a form similar to the general OPW method.

Since the full wavefunction varies rapidly near the nucleus, the evaluation of integrals is also divided into integrals of smooth wavefunctions plus localized contributions over the ionic cores.

Following the ides of the OPW method, the smooth part of the function $|\tilde{\psi}\rangle$ can be expanded in partial waves $|\tilde{\psi}_m\rangle$ as

$$|\tilde{\psi}\rangle = \sum_m c_m |\tilde{\psi}_m\rangle\,, \tag{1.97}$$

with the corresponding all electron-wavefunction $|\psi\rangle$ given by the linear application (1.89)

$$|\psi\rangle = \mathcal{T}|\tilde{\psi}\rangle = \sum_m c_m |\psi_m\rangle\,, \tag{1.98}$$

given that $|\psi_m\rangle = \mathcal{T}|\tilde{\psi}_m\rangle$. Hence the full wavefunction can be written as

$$|\psi\rangle = \overbrace{|\tilde{\psi}\rangle}^{(1)} + \sum_m c_m \left\{ |\psi_m\rangle - \overbrace{|\tilde{\psi}_m\rangle}^{(2)} \right\}, \tag{1.99}$$

since the terms (1) and (2) cancel each other, and has then the same form as (1.88) and (1.89). Then, given that a set of projection operators $\tilde{p}$ satisfy the biorthogonality condition of the form

$$\langle \tilde{p}_m | \tilde{\psi}_{m'} \rangle = \delta_{mm'}, \tag{1.100}$$

we can get the coefficients c_m as

$$c_m = \langle \tilde{p}_m | \tilde{\psi} \rangle\,. \tag{1.101}$$

Just as for pseudopotentials, there are many possible choices for the set of operators $\tilde{p}(\mathbf{r})$. However, the main difference from pseudopotentials is that the transformation $\mathcal{T}$ still involves the all-electron wavefunction $|\psi\rangle$ and can be written in terms of the projectors as

$$\mathcal{T} = 1 + \sum_m \left\{ |\psi_m\rangle - |\tilde{\psi}_m\rangle \right\} \langle \tilde{p}_m |\,, \tag{1.102}$$

which is direct, as when acting with $\mathcal{T}$ over $|\tilde{\psi}\rangle$ is clear that we recover (1.99).

The general equations of the PAW method can be obtained in the same form as (1.102). For a general operator $\hat{A}$ in the all-electron problem, one can introduce a transformed operator $\tilde{A}$ that operates on the smooth part of the wavefunctions by simply noting that

$$\langle \psi_i | \hat{A} | \psi_j \rangle = \langle \tilde{\psi}_i \mathcal{T}^\dagger | \hat{A} | \mathcal{T} \tilde{\psi}_j \rangle = \langle \tilde{\psi}_i | \overbrace{\mathcal{T}^\dagger \hat{A} \mathcal{T}}^{\tilde{A}} | \tilde{\psi}_j \rangle\,. \tag{1.103}$$

Thus,

$$\tilde{A} = \mathcal{T}^\dagger \hat{A} \mathcal{T} = \hat{A} + \sum_{mm'} |\tilde{p}_m\rangle \left\{ \langle \psi_m | \hat{A} | \psi_{m'} \rangle - \langle \tilde{\psi}_m | \hat{A} | \tilde{\psi}_{m'} \rangle \right\} \langle \tilde{p}_{m'} |\,. \tag{1.104}$$

1.4 TRANSLATIONAL SYMMETRY AND THE PLANE-WAVE BASIS

In the preceding sections, we have so far significantly simplified the electronic problem by first decoupling electronic and ionic degrees of freedom, then replacing the interacting problem with a non-interacting one, and subsequently removing core electrons. However, one of the most powerful tools physicist

have in hand in order to reduce complexity of problems is using symmetries and group theory to our advantage. A particular symmetry of crystals is the spontaneously broken continuous translational symmetry in favour of a discrete translational symmetry. The consequences of solving the Schrodinger's equation in a periodic effective potential that satisfies

$$v_{eff}(\mathbf{r}) = v_{eff}(\mathbf{r}+\mathbf{T}), \tag{1.105}$$

with $\mathbf{T}$ being a lattice vector, are captured by Bloch's theorem.

Theorem 5 ***(Bloch's theorem):*** Solutions to the Schrodinger's equation in a **periodic potential** can be expressed as plane waves modulated by periodic functions $u(\mathbf{r})$:

$$\psi(\mathbf{r}) = e^{i\mathbf{k}\cdot\mathbf{r}}u(\mathbf{r}). \tag{1.106}$$

For the particular case of condensed matter, this theorem applies to the Kohn-Sham equations (1.72) and allows us to write the Kohn-Sham states as $\phi_i^\sigma(\mathbf{r}) \to \phi_{n,\mathbf{k}}^\sigma(\mathbf{r})$, where we have divided the label i into two labels: $\mathbf{k}$ which refers to a particular plane wave $e^{i\mathbf{k}\cdot\mathbf{r}}$ and n which refers to a particular periodic modulation $u_{n,\mathbf{k}}(\mathbf{r})$

$$\phi_{n,\mathbf{k}}(\mathbf{r}) = e^{i\mathbf{k}\cdot\mathbf{r}}u_{n,\mathbf{k}}(\mathbf{r}). \tag{1.107}$$

As described in A.4, the $\mathbf{k}$ vector belongs to the first Brillouin zone (1BZ), and the index n is usually referred as the "band index". Since the $u_{n,\mathbf{k}}$ has the periodicity of the lattice, the only plane waves $|\mathbf{G}\rangle$ that can appear in its Fourier decompositions are the ones corresponding to reciprocal lattice vectors satisfying

$$e^{i\mathbf{G}\cdot\mathbf{T}} = 1. \tag{1.108}$$

Thus, the Kohn-Sham states can be written as

$$|\phi_{n,\mathbf{k}}\rangle = \sum_{\mathbf{G}} c_{n,\mathbf{k}+\mathbf{G}} \, |\mathbf{k}+\mathbf{G}\rangle \,, \tag{1.109}$$

$$\langle \mathbf{r}|\mathbf{q}\rangle \equiv \frac{1}{\sqrt{\Omega}} e^{i\mathbf{q}\cdot\mathbf{r}}, \tag{1.110}$$

where Ω is the volume of the system.

When inserting this form for the Kohn-Sham states in the corresponding equation (1.72), it can be easily seen that the first kinetic energy term goes as $\frac{1}{2}|\mathbf{k}+\mathbf{G}|^2$, while in principle the expansion over $\mathbf{G}$ vectors is infinite. Therefore, in order to stop the energy from diverging, the coefficients $c_{n,\mathbf{k}+\mathbf{G}}$ are expected to get smaller (and eventually zero) when $|\mathbf{G}|^2$ grows. This, justifies taking an energy cutoff E_{cut}, from which we discard all coefficients not satisfying

$$E_{cut} \leqslant \frac{1}{2}|\mathbf{k}+\mathbf{G}|^2 , \tag{1.111}$$

achieving a truncation of the basis and reducing the computational cost. Finally, the Kohn-Sham equations transform into an eigenvector problem for the $c_{n,\mathbf{k}+\mathbf{G}}$ coefficients of the form

$$\begin{cases} \sum_{\mathbf{G}'} H_{\mathbf{G},\mathbf{G}'}(\mathbf{k}) c_{i,\mathbf{k}+\mathbf{G}'} = \varepsilon_i(\mathbf{k}) c_{i,\mathbf{k}+\mathbf{G}}, \\ H_{\mathbf{G},\mathbf{G}'}(\mathbf{k}) \equiv \langle \mathbf{k}+\mathbf{G}|\hat{H}_{KS}|\mathbf{k}+\mathbf{G}'\rangle = \frac{1}{2}|\mathbf{k}+\mathbf{G}|^2 \delta_{\mathbf{G},\mathbf{G}'} + V_{KS}(\mathbf{G}-\mathbf{G}'), \end{cases} \tag{1.112}$$

as the one described in Appendix A.4. Now, the label i for the eigenvalues, has also been divided into a 1BZ reciprocal vector $\mathbf{k}$ and the band index n, from where we can obtain bandstructures. Then, the electron density can be related to the Kohn-Sham states as

$$n(\mathbf{r}) = \sum_n \sum_{\mathbf{k}} f_{n,\mathbf{k}} \left\{\phi_{n,\mathbf{k}}(\mathbf{r})\right\}^2, \tag{1.113}$$

where the sum is done over the 1BZ and $f_{n,\mathbf{k}}$ is the occupation number given by the Fermi-Dirac distribution

$$f_{n,\mathbf{k}} = \frac{2}{e^{\beta(\varepsilon_{n,\mathbf{k}}-\mu)}+1}. \tag{1.114}$$

Here, the factor 2 comes from the spin degeneracy, $\beta = 1/K_B T$, with K_B being Boltzmann's constant and T the temperature, and μ the chemical potential (state for which the occupation probability is 50%). Finally, it is worth mentioning that akin to the periodic nature of the solid, we often are mostly interested in *per unit cell* values. This, can be easily shown that correspond to sums over the N_k values on the 1BZ, so that for any function $f_n(\mathbf{k})$ (where the n denotes the band index), the average per cell value $\bar{f}_n$ is

$$\bar{f}_n = \frac{1}{N_k}\sum_{\mathbf{k}} f_n(\mathbf{k}) \to \frac{\Omega_{cell}}{(2\pi)^d}\int_{BZ} f_n(\mathbf{k})\, d\mathbf{k}, \tag{1.115}$$

where in the second expression we have used the fact that N_k is equal to the number of lattice sites in real space N, which in the limit leads to a continuum of $\mathbf{k}$ with the total volume of the 1BZ being $(2\pi)^d/\Omega_{cell}$, with d being the dimension and Ω_{cell} the volume of the unit cell. Thus, for example, the density of Kohn-Sham states per unit cell is given by

$$N(\varepsilon) = \frac{1}{N_k}\sum_n \sum_{\mathbf{k}} \delta(\varepsilon - \varepsilon_{n,\mathbf{k}}) = \frac{\Omega_{cell}}{(2\pi)^d}\int_{BZ} \delta(\varepsilon - \varepsilon_{n,\mathbf{k}})d\mathbf{k}. \tag{1.116}$$

1.5 WANNIER FUNCTIONS

Expressing the Schrodinger's equation in reciprocal space as shown in equation (1.112), results in a simplification of the electronic problem by block diagonalizing the Hamiltonian. However, also as a consequence of Bloch's theorem, the eigenfunctions are now extended objects across the whole crystal,

making the interpretation in real space more cumbersome. It is often useful to rewrite the electronic problem back to real space through a set of Wannier functions [57], which can be defined as a localized basis of orthonormal functions that span the same space as the eigenstates of a band or set of bands. Their localized nature provides them with great utility in order to analyze the chemistry or developing tight-binding models. In addition, in our pursue for simplification of the problem, one can even settle in a particular set of Wannier functions that only reproduce the bands of interest, reducing further the complexity of the electronic problem.

From Bloch's theorem, we know that the eigenstates of a Hamiltonian $\hat{H}$ that commutes with a set of translation operators $\hat{T}_n$ will be also eigenstates of $\hat{T}_n$ and thus

$$\psi_{n,\mathbf{k}} = e^{i\mathbf{k}\cdot\mathbf{r}} u_{n,\mathbf{k}}(\mathbf{r}), \tag{1.117}$$

which we take to be normalized over a unit cell.

However, eigenstates are only well-defined up to an arbitrary phase factor, which allows for a gauge transformation of the form

$$\psi_{n,\mathbf{k}}(\mathbf{r}) \to \tilde{\psi}_{n,\mathbf{k}}(\mathbf{r}) = e^{i\theta_n(\mathbf{k})}\psi_{n,\mathbf{k}}(\mathbf{r}), \tag{1.118}$$

where in general $\theta_i(\mathbf{k})$ is taken as a continuous function in $\mathbf{k}$ (differentiable gauge), so that $\psi_{n,\mathbf{k}}$ are smooth functions of $\mathbf{k}$. Then Wannier functions can be defined as nothing more than Fourier transforms of Bloch eigenstates, so that for a band n the Wannier function associated with a lattice site $\mathbf{T}_m$ is given by

$$w_n(\mathbf{r}-\mathbf{T}_m) = \frac{\Omega_{cell}}{(2\pi)^3}\int_{BZ} e^{-i\mathbf{k}\cdot\mathbf{T}_m}\psi_{n,\mathbf{k}}(\mathbf{r})\,d\mathbf{k} = \frac{\Omega_{cell}}{(2\pi)^3}\int_{BZ} e^{i\mathbf{k}\cdot(\mathbf{r}-\mathbf{T}_m)}u_{n,\mathbf{k}}(\mathbf{r})\,d\mathbf{k}, \tag{1.119}$$

which can be shown to vanish when $(\mathbf{r}-\mathbf{T}_m) \to \infty$. It is also evident that the Wannier function associated with a different cell $w_n(\mathbf{r}-\mathbf{T}_{m'})$ is the same function translated by $\mathbf{T}_{m'}-\mathbf{T}_m$; so that in the process we have transformed N Bloch functions labeled by $\mathbf{k}$ into N Wannier functions centered in each lattice site. Of course, the original wavefunction can be recovered by the inverse transform

$$\psi_{n,\mathbf{k}}(\mathbf{r}) = \sum_m e^{i\mathbf{k}\cdot\mathbf{T}_m} w_n(\mathbf{r}-\mathbf{T}_m). \tag{1.120}$$

Wannier functions can in principle also be defined for a set of bands instead of a particular band. In general, the functions $u_{n,\mathbf{k}}$ can be replaced by a linear combination of Bloch functions, such as

$$u^W_{i,\mathbf{k}} = \sum_n U_{n,i}(\mathbf{k})u_{n,\mathbf{k}}, \tag{1.121}$$

where $U_{n,i}(\mathbf{k})$ is a unitary matrix defining a $\mathbf{k}$-dependent transformation and the $u^W_{i,\mathbf{k}}$ functions are referred as Wannier rotated Bloch functions. Then, when replacing (1.121) in (1.119) we obtain the general expression for the Wannier functions for a set of bands

$$\langle \mathbf{r}|\mathbf{T}_m, i\rangle \equiv w_i(\mathbf{r}-\mathbf{T}_m) = \frac{\Omega_{cell}}{(2\pi)^3}\int_{BZ} e^{i\mathbf{k}\cdot(\mathbf{r}-\mathbf{T}_m)}\left(\sum_n U_{n,i}(\mathbf{k})u_{n,\mathbf{k}}(\mathbf{r})\right)d\mathbf{k}, \tag{1.122}$$

and thus

$$u^W_{i\mathbf{k}}(\mathbf{r}) = \sum_{\mathbf{T}_m} e^{i\mathbf{k}(\mathbf{T}_m - \mathbf{r})} w_i(\mathbf{r} - \mathbf{T}_m). \tag{1.123}$$

When defined in such way, the Wannier functions form an orthonormal basis so that

$$\langle \mathbf{T}_m, i | \mathbf{T}_n, j \rangle = \int_{\text{all space}} w_i^*(\mathbf{r} - \mathbf{T}_m) w_j(\mathbf{r} - \mathbf{T}_n)\, d\mathbf{r} = \delta_{ij}\delta_{mn}, \tag{1.124}$$

which is rather direct by using (1.119) and the fact that $\psi_{i,\mathbf{k}}$ are orthonormal.

In practice, calculations are done over a discrete mesh in reciprocal space, so that integrals over reciprocal space are discretized and Fourier transforms are written as

$$\frac{\Omega}{(2\pi)^3} \int e^{-i\mathbf{k}\cdot\mathbf{T}}\, d\mathbf{k} \to \frac{1}{N_k} \sum_{\mathbf{k}} e^{-i\mathbf{k}\cdot\mathbf{T}}. \tag{1.125}$$

However, one of the added benefits of a localized basis is the possibility of performing a Wannier interpolation, in order to obtain a finer $\mathbf{k}$-mesh in reciprocal space to perform integrals. The original Hamiltonian $\hat{H}$ is diagonal in the Bloch basis with the components given by

$$\langle n, \mathbf{k} | \hat{H} | m, \mathbf{k}' \rangle = \delta_{\mathbf{k},\mathbf{k}'} H(\mathbf{k}) = \varepsilon_n(\mathbf{k}) \delta_{nm}. \tag{1.126}$$

If we rewrite the components in the Wannier rotated basis defined in equation (1.121) we get

$$H^W_{nm}(\mathbf{k}) = \langle u^R_{n,\mathbf{k}} | \hat{H} | u^R_{m,\mathbf{k}} \rangle = \left[U^\dagger(\mathbf{k}) H(\mathbf{k}) U(\mathbf{k}) \right]_{nm}. \tag{1.127}$$

Since we only have performed a change of basis, the eigenvalues of $H^W_{nm}(\mathbf{k})$ are the same as the ones for the original $H(\mathbf{k})$. Now, we can Fourier transform $H^W_{nm}(\mathbf{k})$ to real space as

$$H^W_{nm}(\mathbf{T}) = \frac{1}{N_k} \sum_{k} e^{-i\mathbf{k}\cdot\mathbf{T}} H^W_{nm}(\mathbf{k}), \tag{1.128}$$

and then, we transform back to any $\mathbf{k}'$ point not originally in the $\mathbf{k}$-mesh

$$H^W_{nm}(\mathbf{k}') = \sum_{\mathbf{T}} e^{i\mathbf{k}\cdot\mathbf{T}'} H^W_{nm}(\mathbf{T}). \tag{1.129}$$

Finally, by diagonalizing the new interpolated $H^W_{nm}(\mathbf{k}')$, we obtain a new set of eigenvalues $\varepsilon_n(\mathbf{k}')$ and eigenstates orbitals $\psi_{n,\mathbf{k}'}(\mathbf{r})$. Since the Wannier basis only reproduces a particular set of bands, the cost of diagonalizing such $N_W \times N_W$ matrix, with N_W being the number of Wannier orbitals, is much cheaper than non-self-consistently solving the Hamiltonian at $\mathbf{k}'$.

1.5.1 *Non-uniqueness and maximally localized Wannier functions*

One of the main drawbacks of the Wannier representation is that it is not uniquely defined, which implies that there exist different sets of Wannier functions that represent the same set of bands. This can be deduced from equation (1.122), if we take into account the gauge freedom described in equations (1.117) and (1.121). The different representations can widely vary in shape, localization or range (contrary to Bloch functions that are all well defined), therefore, it is useful to stablish a criterion that removes such ill-definiteness. One of the most used criteria is the one of "maximal localization".

Maximally localized Wannier functions (MLWF) can be understood as a particular transform (linear combination) of Wannier functions that minimize the mean square spread Ω_S defined as

$$\Omega_S \equiv \sum_{i=1}^{N_W} \left[\langle r^2 \rangle_i - \langle \mathbf{r} \rangle_i^2 \right] = \sum_{i=1}^{N_W} (\Delta \mathbf{r})^2, \tag{1.130}$$

where i labels the i-th Wannier function in a particular unit cell and $\langle \ldots \rangle_i$ is the means the expectation value over the ith Wannier function.

It was shown by Marzari and Vanderbilt [58] that the spread function can be divided in two parts

$$\Omega_S = \Omega_I + \tilde{\Omega}, \tag{1.131}$$

$$\Omega_I = \sum_{i=1}^{N_W} \left\{ \langle r^2 \rangle_i - \sum_{\mathbf{T},j} |\langle \mathbf{T}, j | \hat{\mathbf{r}} | 0, i \rangle|^2 \right\}, \tag{1.132}$$

$$\tilde{\Omega} = \sum_{i}^{N_W} \sum_{\mathbf{T},j \neq 0,i} |\langle \mathbf{T}, j | \hat{\mathbf{r}} | 0, i \rangle|^2 . \tag{1.133}$$

Here Ω_I is gauge-invariant, while $\tilde{\Omega}$ is gauge-dependent and thus one can define a minimization procedure in order to find the particular form of $U_{i,j}(\mathbf{k})$ (1.121), such that it minimizes $\tilde{\Omega}$. On the other hand, the fact that Ω_I is gauge-invariant points to the physical nature of this term. In order to understand this physical meaning, first, it is useful to define a projection operator $\hat{P}$, which projects over the space spanned by a particular set of bands (or by their related Wannier functions)

$$\hat{P} = \sum_{i}^{N_{bands}} \sum_{\mathbf{k}} |\psi_{i,\mathbf{k}}\rangle \langle \psi_{i,\mathbf{k}}| = \sum_{i}^{N_{bands}} \sum_{\mathbf{T}} |\mathbf{T}, i\rangle \langle \mathbf{T}, \mathbf{i}| . \tag{1.134}$$

Then, it is trivial to define the projector over the rest of the bands as $\hat{Q} = 1 - \hat{P}$. In terms of this operator, Ω_I (1.132) can be rewritten as

$$\Omega_I = \sum_{i=1}^{N_{bands}} \sum_{\alpha=1}^{3} \langle 0, i | \hat{\mathbf{r}}_\alpha \hat{Q} \hat{\mathbf{r}}_\alpha | 0, i \rangle , \tag{1.135}$$

where α are the vector indices of the $\mathbf{r}$ vector. This, leads to the interpretation of the invariant spread as the quantum fluctuations of the position operator from the space spanned by the Wannier functions into the space of the rest of the bands.

2

LATTICE DYNAMICS OF CRYSTALS

2.1 THE HARMONIC HAMILTONIAN

After separating the ionic and electronic problems via the Born-Oppenheimer approximation discussed in 1.1.1 and solving the electronic part with the methods presented in Chapter 1 we can now rewrite the ionic Hamiltonian initially presented in equation (1.15) and give an explicit expression for the electronic energy in terms of the Kohn-Sham energy E_{KS} given in equation (1.64):

$$\left[\hat{T}_I + E_{KS}(\mathbf{R}) + \hat{V}_{I-I}(\mathbf{R})\right]\chi(\mathbf{R}) = \left[\hat{T}_I + \hat{V}^{BO}(\mathbf{R})\right]\chi(\mathbf{R}) = E\,\chi(\mathbf{R}). \tag{2.1}$$

Notice how the electronic energy E_{KS} is a functional of the ground state density n_0, which in turn is defined by a particular set of ionic positions $\mathbf{R}$ that define the external potential (which is part of the Kohn-Sham ansatz (1.50)). Hence, the Hamiltonian initially introduced in (1.1) now written as

$$\begin{cases} \hat{H} \equiv \hat{T}_I + \hat{V}^{BO}(\mathbf{R}), \\ \hat{V}^{BO}(\mathbf{R}) \equiv \hat{V}_{I-I}(\mathbf{R}) + E_{KS}[n_{0,\mathbf{R}}]), \end{cases} \tag{2.2}$$

where $n_{0,\mathbf{R}}$ is the ground state electronic density for an external potential v_{ext} defined by the ionic positions $\mathbf{R}$ and the Born-Oppenheimer potential $\hat{V}^{BO}(\mathbf{R})$ (also referred as BO energy surface) is the effective potential felt by the ions and contains all the effects from the electrons (within the BO approximation).

In a solid, ions oscillate around a set or particular equilibrium position $\mathbf{R}^{eq}$. As we will see, it is convenient to redefine the ionic positions as displacements with respect to equilibrium positions. Hence, for a particular ion i

$$\mathbf{R}_i = \mathbf{R}_i^{eq} + \mathbf{u}_i, \tag{2.3}$$

where $\mathbf{u}_i$ are the displacements from the equilibrium positions. We can then perform a Taylor expansion of the BO potential around the equilibrium positions $\mathbf{R}^{eq}$

$$\begin{aligned} V^{BO}(\mathbf{R}) =& V^{BO}(\mathbf{R}^{eq}) + \left(\partial_{i\alpha} V^{BO}\Big|_{\mathbf{R}^{eq}}\right) u_{i\alpha} + \frac{1}{2}\left(\partial_{i\alpha}\partial_{j\beta} V^{BO}\Big|_{\mathbf{R}^{eq}}\right) u_{i\alpha}u_{j\beta} \\ &+ \frac{1}{3!}\left(\partial_{i\alpha}\partial_{j\beta}\partial_{k\gamma} V^{BO}\Big|_{\mathbf{R}^{eq}}\right) u_{i\alpha}u_{j\beta}u_{k\gamma} + \dots, \end{aligned} \tag{2.4}$$

where we are using Einstein's notation (repeated indices are summed) with *roman* indices for particles, *greek* indices for Cartesian coordinates and $\partial_{i\alpha} \equiv \partial/\partial r_{i\alpha}$.

The first term in equation (2.4) is just the energy in equilibrium. The second term on the other hand, is forced to be zero, which is easy to see from Hamiltonian mechanics. The force over a particular ion is given by $F_{i\alpha} = -\partial V^{BO}/\partial r_{i\alpha}$, but at equilibrium all forces must be zero $F_{i\alpha} = 0$. Thus,

$$V^{BO}(\mathbf{R}) - V^{BO}(\mathbf{R}^{eq}) = \sum_{n=2}^{\infty} V_n^{BO}, \tag{2.5}$$

where

$$\begin{aligned} V_n^{BO} &= \frac{1}{n!} \left(\partial_{s_1\alpha_1} \dots \partial_{s_n\alpha_n} V^{BO}(\mathbf{R}) \right) \Big|_{\mathbf{R}^{eq}} u_{s_1\alpha_1} \dots u_{s_n\alpha_n} \\ &= \frac{1}{n!} \Phi^{\alpha_1\dots\alpha_n}_{s_1\dots s_n} u_{s_1\alpha_1} \dots u_{s_n\alpha_n}, \end{aligned} \tag{2.6}$$

with $\Phi^{\alpha_1\dots\alpha_n}_{s_1\dots s_n}$ being the n-th order force constants defined as

$$\Phi^{\alpha_1\dots\alpha_n}_{s_1\dots s_n} \equiv \left(\partial_{s_1\alpha_1} \dots \partial_{s_n\alpha_n}\right) V^{BO}(\mathbf{R}) \,|_{\mathbf{R}=\mathbf{R}^{eq}}\,. \tag{2.7}$$

2.1.1 *The Harmonic approximation*

If we now assume $\mathbf{u}_i$ to be small, we can truncate the expansion of the BO potential (2.4) to second order, which defines the **Harmonic approximation**. Hence, the dynamics of the ionic degrees of freedom are determined by

$$\hat{H}^{harm} = \sum_{s=1}^{N} \sum_{\alpha=1}^{3} \frac{\hat{P}^2_{s\alpha}}{2M_s} + \frac{1}{2} \Phi^{\alpha\beta}_{st} \hat{u}_{s\alpha} \hat{u}_{t\beta}, \tag{2.8}$$

where $\Phi^{\alpha\beta}_{st}$ is the (second order) force constant matrix defined in equation (2.7), which satisfies a series of relations discussed in Appendix A.5.

2.1.1.1 *Classical dynamics of lattice vibrations*

Having that $F_{s\alpha} = M_s \ddot{u}_{s\alpha}$, the classical equations of motion for the ionic degrees of freedom can be written as

$$M_i \ddot{u}_{i\gamma} = F_{i\gamma} = -\frac{\partial H^{harm}}{\partial u_{i\gamma}} = -\frac{\partial V_2^{BO}}{\partial u_{i\gamma}}, \tag{2.9}$$

$$M_i \ddot{u}_{i\gamma} = -\frac{1}{2} \left(\Phi^{\gamma\beta}_{it} u_{t\beta} + \overbrace{\Phi^{\alpha\gamma}_{si}}^{=\Phi^{\gamma\alpha}_{is}} u_{s\alpha} \right) = -\Phi^{\gamma\alpha}_{is} u_{s\alpha}, \tag{2.10}$$

where we have used the symmetric property of the force constants (Appendix A.5). It is clear from the equations of motion that within the harmonic approximation the system is defined as a set of coupled classic harmonic oscillators,

where the coupling between the different oscillators is given by the force constants matrix Φ.

Thus, the solution to the equations of motion will be the set of independent oscillators of the form

$$u_{i\gamma} = \frac{\epsilon_{i\gamma}}{\sqrt{M_i}} e^{i\omega t}, \tag{2.11}$$

each of them with their own frequency ω and polarization vector $\epsilon_{i\gamma}$.

It is easy to check that the displacement field described by (2.11) is indeed a solution. Just by plugging this ansatz in the equations of motion (2.10) leads to

$$-M_i\omega^2 \frac{\epsilon_{i\gamma}}{\sqrt{M_i}} e^{-i\omega t} = -\sum_{s\alpha} \Phi_{is}^{\gamma\alpha} u_{s\alpha} = -\sum_{s\alpha} \Phi_{is}^{\gamma\alpha} \frac{\epsilon_{s\alpha}}{\sqrt{M_s}} e^{-i\omega t}, \tag{2.12}$$

$$\Downarrow$$

$$\omega^2 \epsilon_{i\gamma} = \sum_{s\alpha} \underbrace{\frac{\Phi_{is}^{\gamma\alpha}}{\sqrt{M_i M_s}}}_{\text{Dyn matrix}} \epsilon_{s\alpha} = \sum_{s\alpha} D_{is}^{\gamma\alpha} \epsilon_{s\alpha}, \tag{2.13}$$

where we have defined the **Dynamical matrix** as

$$D_{ij}^{\alpha\beta} = \frac{\Phi_{ij}^{\alpha\beta}}{\sqrt{M_i M_j}}, \tag{2.14}$$

and implies that (2.11) will be a solution as long as the polarization vector $\epsilon_{i\gamma}$ is an eigenvector of the Dynamical matrix with eigenvalue ω^2.

In the previous description we have treated the crystal as a super-molecule, without taking into account the translational symmetry, for the sake of simplicity. This leads to the particular expression (2.14) for the Dynamical matrix. However, the same procedure can be done taking into account the translational symmetry (Appendix A.6) by writing the displacement field as a Bloch wave

$$u_{i\gamma}(\mathbf{T}) = \frac{\epsilon_{i\gamma}(\mathbf{k})}{\sqrt{M_i}} e^{-i\omega t} e^{i(\mathbf{k}\cdot\mathbf{T})}, \tag{2.15}$$

where now i denotes a particular ion in the primitive cell, and $\mathbf{T}$ denotes the cell in which the ion lies. Then, the force constant matrix is also rewritten as

$$\Phi_{i,j}^{\alpha\beta} \to \Phi_{i,j}^{\alpha\beta}(\mathbf{T}), \tag{2.16}$$

where in the left-hand side of (2.16) the atom indices i, j run over all the atoms in the crystal, while on the right-hand side they only run over the atoms of the primitive cell and $\mathbf{T} = \mathbf{T}_j - \mathbf{T}_i$ is the Bravais lattice vector relating both atoms. Then, the dynamical matrix is defined as the Fourier transform of the force constants (2.14)

$$D_{ij}^{\alpha\beta}(\mathbf{k}) = \sum_{\mathbf{T}} \frac{\Phi_{ij}^{\alpha\beta}(\mathbf{T})}{\sqrt{M_i M_j}} e^{i\mathbf{k}\cdot\mathbf{T}}, \tag{2.17}$$

and is related to the eigenvectors $\epsilon_{i\gamma}(\mathbf{k})$ in the same way as (2.13)

$$\omega(\mathbf{k})^2 \epsilon_{i\gamma}(\mathbf{k}) = \sum_{s\alpha} D_{is}^{\gamma\alpha}(\mathbf{k}) \epsilon_{s\alpha}(\mathbf{k}), \tag{2.18}$$

but with the explicit dependence on the $\mathbf{k}$ wavevector lying in the first Brillouin zone. In the spirit of Bloch's theorem, this allows us to rewrite the problem of N_I ions (with N_I being the total number of ions in the crystal), into N_{cell} problems of n particles, with N_{cell} being the number of primitive cells and n the number of atoms per cell $n \equiv N_I/N_{cell}$.

2.1.1.2 *The harmonic energy*

After solving the dynamics of the lattice vibrations (2.13), we can compute the total harmonic kinetic (T) and potential energies $U^h \equiv V - V_0$ for a particular set of displacements $\mathbf{u}_i$

$$\begin{cases} u_{i\gamma} = \sum_{\mu} q_\mu \frac{\epsilon_{i\gamma}^{\mu}}{\sqrt{M_i}} e^{-i\omega_\mu t}, \\ U^{harm} = \frac{1}{2} \Phi_{st}^{\alpha\beta} u_{s\alpha} u_{t\beta}, \\ T^{harm} = \frac{1}{2} \sum_{i\alpha} M_i |\dot{u}_{i\alpha}|^2, \end{cases} \tag{2.19}$$

where the displacements have been written as a sum of the independent oscillators (2.11), μ labels the different modes and q_μ is the amplitude of a particular normal mode. Thus, the kinetic part is given by

$$\begin{aligned} T^{harm} &= \frac{1}{2} M_i \sum_{i\alpha} \left(\sum_{\mu} q_\mu \frac{\epsilon_{i\alpha}^{\mu}}{\sqrt{M_i}} (-i\omega_\mu) e^{-i\omega_\mu t} \right) \left(\sum_{\nu} q_\nu^* \frac{\epsilon_{i\alpha}^{\nu *}}{\sqrt{M_i}} (i\omega_\nu) e^{i\omega_\nu t} \right) \\ &= \frac{1}{2} \sum_{i\alpha\mu\nu} q_\mu q_\nu^* \omega_\mu \omega_\nu \overbrace{\epsilon_{i\alpha}^{\mu} \epsilon_{i\alpha}^{\nu *}}^{\text{sum in } i,\alpha} \exp(i(\omega_\nu - \omega_\mu)t) \\ &= \frac{1}{2} \sum_{\mu\nu} q_\mu q_\nu^* \omega_\mu \omega_\nu \delta_{\mu\nu} \exp(i(\omega_\nu - \omega_\mu)t) = \frac{1}{2} \sum_{\mu} |q_\mu|^2 \omega_\mu^2, \end{aligned} \tag{2.20}$$

while the harmonic part is given by

$$\begin{aligned} U^{\text{harm}} &= \frac{1}{2}\sum_{\mu\mu',s\alpha,t\beta}\underbrace{\Phi_{st}^{\alpha\beta}\frac{1}{\sqrt{M_s M_t}}}_{D_{st}^{\alpha\beta}} q_\mu^* q_{\mu'} \epsilon_{s\alpha}^{\dagger\mu}\epsilon_{t\beta}^{\mu'} e^{-i(\omega_{\mu'}-\omega_\mu)t} \\ &= \frac{1}{2}\sum_{\mu\mu',s\alpha} q_\mu^* q_{\mu'} \underbrace{\left(\sum_{t\beta} D_{st}^{\alpha\beta}\epsilon_{t\beta}^{\mu'}\right)}_{\omega_{\mu'}^2\epsilon_{s\alpha}^{\mu'}} \epsilon_{s\alpha}^{\dagger\mu} e^{-i(\omega_{\mu'}-\omega_\mu)t} \\ &= \frac{1}{2}\sum_{\mu\mu'} q_\mu^* q_{\mu'}\omega_{\mu'}^2 \underbrace{\left(\sum_{s\alpha}\epsilon_{s\alpha}^{\mu}\epsilon_{s\alpha}^{\dagger\mu'}\right)}_{\delta_{\mu\mu'}} e^{-i(\omega_{\mu'}-\omega_\mu)t} = \frac{1}{2}\sum_{\mu}|q_\mu|^2\,\omega_\mu^2. \end{aligned} \tag{2.21}$$

Equivalent to the dynamics of the lattice, the energies can also be derived in terms of displacements written as sum of Bloch-like independent oscillators (2.15), this is done in Appendix A.6 and leads to a total potential energy per cell given by

$$u^{\text{harm}} = \frac{U^{\text{harm}}}{N_{\text{cell}}} = \frac{1}{2}\sum_{\mu\mathbf{k}}\left|q_{\mu\mathbf{k}}\right|^2\omega_{\mu\mathbf{k}}^2, \tag{2.22}$$

that reduces to the same expression as (2.21) if we take $N_{\text{cell}} = N_k = 1$.

2.1.1.3 *Canonical quantization of harmonic lattice vibrations*

The expression for the total energy given in (2.22) is useful for computing phonons within a direct method as the frozen phonon method or finite differences, which compute derivatives of the total energy per cell u^{harm}. However, this expression for the total harmonic energy is still classical and thus we should go beyond in order to get a proper quantum treatment of the lattice vibrations.

It can be shown (see Appendix A.7) that by choosing the appropriate ladder operators $\hat{b}^\dagger, \hat{b}$ (satisfying the usual algebra for bosons), the Fourier transforms of the ionic momenta and displacements can be rewritten as

$$\hat{u}_{s\alpha}(\mathbf{k}) = \sum_\nu \frac{1}{\sqrt{2M_s\omega_\nu(\mathbf{k})}}\epsilon_{s\alpha}^\nu(\mathbf{k})\left(\hat{b}_\nu(\mathbf{k}) + \hat{b}_\nu^\dagger(-\mathbf{k})\right), \tag{2.23}$$

$$\hat{P}_{s\alpha}(\mathbf{k}) = -\sum_\nu \sqrt{\frac{M_s\omega_\nu(\mathbf{k})}{2}}\epsilon_{s\alpha}^\nu(\mathbf{k})\left(\hat{b}_\nu(\mathbf{k}) - \hat{b}_\nu^\dagger(-\mathbf{k})\right). \tag{2.24}$$

Given that the polarization vectors $\epsilon_{s\alpha}^\nu(\mathbf{k})$ hold the relation (2.18), the Hamiltonian (2.8) can be now written as

$$\hat{H}^{\text{harm}} = \sum_{\nu\mathbf{k}}\omega_\nu(\mathbf{k})\left(\frac{1}{2} + \hat{b}_{\nu\mathbf{k}}^\dagger\hat{b}_{\nu\mathbf{k}}\right) = \sum_{\nu\mathbf{k}}\omega_\nu(\mathbf{k})\left(\frac{1}{2} + \hat{n}_{\nu\mathbf{k}}\right), \tag{2.25}$$

where $\hat{n}_{\nu\mathbf{k}} \equiv \hat{b}_{\nu\mathbf{k}}^\dagger\hat{b}_{\nu\mathbf{k}}$ is the number operator.

If we now compute the total energy for a particular quantum state defined by the occupation numbers $|n_1, n_2, \ldots\rangle$, which is direct from (2.25), it is clear the quantum nature of this Hamiltonian. Contrary to the expression for the classical total energy (2.22) resembling a sum of classic oscillators, now we get a sum of quantum harmonic oscillators with the characteristic zero point energy coming from the $\frac{1}{2}$ term in (2.25).

2.2 DENSITY FUNCTIONAL PERTURBATION THEORY

From a theoretical point of view there is no problem in defining the dynamical matrix of a crystal and diagonalizing it to compute the phonon spectrum. However, this procedure can get very expensive. For example, one needs to perform the calculations in a commensurate supercell with respect to the $\mathbf{k}$ point in which we want to compute the phonon spectra, which turns impossible when $\mathbf{k}$ differs from any fractional number. Density functional perturbation theory (DFPT) provides a solution in which essentially, the lattice displacements are studied through their effects in $n_{\mathbf{R}^{eq}}(\mathbf{r})$

For computing the dynamical matrix one should compute the static energy of the system at equilibrium (neglecting $\hat{T}_I$) given by

$$V^{BO}(\mathbf{R}^{eq}) = V_{I-I}(\mathbf{R}^{eq}) + \langle \psi^e_{\mathbf{R}^{eq}} | \hat{H}^e | \psi^e_{\mathbf{R}^{eq}} \rangle = V_{I-I}(\mathbf{R}^{eq}) + E_{KS}(\mathbf{R}), \tag{2.26}$$

and then, compute derivatives with respect to the ionic displacements $\mathbf{u}$. The first derivative can be obtained using the Hellman-Feynman theorem

$$\frac{\partial V^{BO}(\mathbf{R})}{\partial u_{i\alpha}} = \frac{\partial V_{I-I}(\mathbf{R})}{\partial u_{i\alpha}} + \int n_{\mathbf{R}}(\mathbf{r}) \frac{\partial v_{ext}(\mathbf{r})}{\partial u_{i\alpha}} \, d\mathbf{r}. \tag{2.27}$$

Then, the second derivative can be done on top of the previous one and gives

$$\begin{aligned} \frac{\partial^2 V^{BO}(\mathbf{R})}{\partial u_{i\alpha} \partial u_{j\beta}} = & \int \frac{\partial n_{\mathbf{R}}(\mathbf{r})}{\partial u_{i\alpha}} \frac{\partial v_{ext}(\mathbf{r})}{\partial u_{j\beta}} \, d\mathbf{r} \\ & + \int n_{\mathbf{R}}(\mathbf{r}) \frac{\partial^2 v_{ext}(\mathbf{r})}{\partial u_{i\alpha} \partial u_{j\beta}} \, d\mathbf{r} + \frac{\partial^2 V_{I-I}(\mathbf{R})}{\partial u_{i\alpha} \partial u_{j\beta}}. \end{aligned} \tag{2.28}$$

Hence, the second derivatives require the knowledge not only of the electron density $n_{\mathbf{R}}(\mathbf{r})$, but also from its derivatives with respect to variation of the ionic positions. This derivatives of the density can be calculated using linear response theory, but it is very computationally demanding. The DFPT methods provide an alternative way of performing this computation, by providing an alternative self-consistent set of equations derived from perturbation theory. The core idea is to study the change of the Kohn-Sham levels and wavefunctions when the density is perturbed in a particular way. Thus, if we make

a first order expansion in the Hamiltonian, the eigenstates and eigenfunctions are redefined as

$$\hat{H}_{KS} \to \hat{H}_{KS} + \Delta\hat{H}_{KS}, \tag{2.29}$$

$$\varepsilon_{n\mathbf{k}} \to \varepsilon_{n\mathbf{k}} + \Delta\varepsilon_{n\mathbf{k}}, \tag{2.30}$$

$$|\phi_{n\mathbf{k}}\rangle \to |\phi\rangle + |\Delta\phi_{n\mathbf{k}}\rangle\,, \tag{2.31}$$

$$n_{\mathbf{R}}(\mathbf{r}) \to n_{\mathbf{R}}(\mathbf{r}) + \Delta n_{\mathbf{R}}(\mathbf{r}). \tag{2.32}$$

Then, the eigenvalue problem at linear order is given by Sternheimer's equation and reads as

$$(\hat{H}_{KS} - \varepsilon_{n\mathbf{k}})\,|\Delta\phi_{n\mathbf{k}}\rangle = -(\Delta\hat{H}_{KS} - \Delta\varepsilon_{n\mathbf{k}})\,|\phi_{n\mathbf{k}}\rangle\,, \tag{2.33}$$

with the density change being

$$\Delta n_{\mathbf{R}}(\mathbf{r}) = 2\mathrm{Re}\left[\sum_{n\mathbf{k}} f_{n\mathbf{k}}\phi^{*}_{n\mathbf{k}}(\mathbf{r},\mathbf{R})\Delta\phi_{n\mathbf{k}}(\mathbf{r},\mathbf{R})\right], \tag{2.34}$$

where $f_{n\mathbf{k}}$ are the Fermi-Dirac occupations.

Finally, the change in the Hamiltonian is given by

$$\Delta\hat{H}_{KS}(\mathbf{r}) = \Delta v_{ext}(\mathbf{r}) + \int\left[\frac{1}{|\mathbf{r}-\mathbf{r}'|} + f^{xc}(\mathbf{r},\mathbf{r}')\right]\Delta n_{\mathbf{R}}(\mathbf{r}')\,d\mathbf{r}', \tag{2.35}$$

where the factor f^{xc} is defined in terms of the exchange-correlation potential as

$$f^{xc}(\mathbf{r},\mathbf{r}') = \frac{\delta v_{xc}(\mathbf{r})}{\delta n_{\mathbf{R}}(\mathbf{r}')}. \tag{2.36}$$

Equations (2.33), (2.34) and (2.35), form a set of self-consistent equations for the perturbed system, equivalent to the one for the equilibrium Kohn-Sham problem. Therefore, the change in the density $n_{\mathbf{R}}(\mathbf{r})$ can be obtained through a self-consistent loop. Computationally, the main advantage of DFPT is that only the occupied states matter and one can discard the unoccupied valence bands. On the other hand, compared to the direct methods as frozen phonon or finite differences, it allows to compute the dynamical matrix at any $\mathbf{k}$ point, without needing a commensurate supercell.

2.3 THE ELECTRON-PHONON INTERACTION

So far, we have made extensive use of the Born-Oppenheimer approximation introduced in Section 1.1.1. However, since this approximation is nothing more than the adiabatic theorem, there is no energy transfer between ionic and electronic degrees of freedom, which negates any kind of electron-phonon interaction. This, is explicitly done when discarding the non-diagonal terms in equation (1.12) contained in the $\Delta\hat{H}$ term (1.13). Thus, in order to study any kind of interaction between the lattice and the electronic degrees of freedom we must conserve at least some of the non-diagonal terms of $\Delta\hat{H}$. As a consequence, the electron-phonon interaction can be considered as the next step

beyond the Born-Oppenheimer approximation, which will be more relevant in metals where electronic excitations can be as small as one may want.

Considering that the first term in $\Delta\hat{H}$, given by (1.13), includes second derivatives of the electronic wavefunction with respect to the ionic displacements, while the second term only first derivatives; we approximate the interaction at linear order as

$$\hat{H}^{e-ph}_{ij} = \sum_I \frac{1}{M_I} \langle \psi_{\mathbf{R},i} | \hat{\mathbf{P}}_I | \psi_{\mathbf{R},j} \rangle \, \hat{\mathbf{P}}_I, \tag{2.37}$$

and thus, the electron-phonon Hamiltonian can be written as

$$\hat{H}^{e-ph} = \sum_I \frac{1}{M_I} [\hat{\mathbf{P}}_I]_e \, \hat{\mathbf{P}}_I, \tag{2.38}$$

where $[\hat{\mathbf{P}}_I]_e$ implies acting with the ionic momentum operator over the electronic states. We can write this term in second quantization as

$$[\hat{\mathbf{P}}_I]_e = \sum_{nn'} \sum_{\mathbf{k}\mathbf{k}'} \hat{c}^\dagger_{n'\mathbf{k}'} \hat{c}_{n\mathbf{k}} \langle \phi_{n'\mathbf{k}'} | \hat{\mathbf{P}}_I | \phi_{n\mathbf{k}} \rangle , \tag{2.39}$$

where $\hat{c}^\dagger_{n\mathbf{k}}$ and $\hat{c}_{n\mathbf{k}}$ create and annihilate Kohn-Sham states and is now clear that (2.37) is the same operator as (2.38), but in matrix form.

Then, using regular first order perturbation theory, we can study the effect of the perturbation (the change of ionic positions) over Kohn-Sham states as

$$|\phi_{n\mathbf{k}}\rangle \to |\phi_{n\mathbf{k}}\rangle + |\Delta\phi_{n\mathbf{k}}\rangle , \tag{2.40}$$

with $|\Delta\phi_{n\mathbf{k}}\rangle$ given by

$$|\Delta\phi_{n\mathbf{k}}\rangle = \sum_{m\neq n} \sum_{\mathbf{q}\neq\mathbf{k}} \frac{\langle \phi_{m\mathbf{q}} | \Delta\hat{H}_{KS} | \phi_{n\mathbf{k}} \rangle}{\varepsilon_{n\mathbf{k}} - \varepsilon_{m\mathbf{q}}} |\phi_{m\mathbf{q}}\rangle , \tag{2.41}$$

which taking into account that $\hat{\mathbf{P}}_I = -i\hat{\nabla}_I$, allows us to rewrite the braket in (2.39) as

$$\langle \phi_{n'\mathbf{k}'} | \hat{\mathbf{P}}_I | \phi_{n\mathbf{k}} \rangle = -i \langle \phi_{n',\mathbf{k}'} | \Delta\phi_{n\mathbf{k}} \rangle = -i \frac{\langle \phi_{n'\mathbf{k}'} | \Delta\hat{H}_{KS} | \phi_{n\mathbf{k}} \rangle}{\varepsilon_{n\mathbf{k}} - \varepsilon_{n'\mathbf{k}'}}. \tag{2.42}$$

If we now consider that $\Delta\hat{H}_{KS} = \frac{\partial\hat{V}_{KS}}{\partial u_{i\alpha}(\mathbf{T})}$, we need to sum over i, α, and $\mathbf{T}$. Then, we substitute (2.39) and (2.42) into (2.38). Finally, rewriting the remaining ionic momentum operator $\hat{\mathbf{P}}_I$ in terms of ladder operators as in (2.24) (but transformed to real space (A.56) leads to

$$\begin{aligned} \hat{H}^{e-ph} = -\sum_{i\alpha\mathbf{T}} \left(\sum_{nn'} \sum_{\mathbf{k}\mathbf{k}'} \hat{c}^\dagger_{n'\mathbf{k}'} \hat{c}_{n\mathbf{k}} \frac{\langle \phi_{n'\mathbf{k}'} | \frac{\partial\hat{V}_{KS}}{\partial u_{i\alpha}(\mathbf{T})} | \phi_{n\mathbf{k}} \rangle}{\varepsilon_{n\mathbf{k}} - \varepsilon_{n'\mathbf{k}'}} \right) \\ \times \left(\frac{1}{\sqrt{N}} \sum_{\mathbf{k}\nu} e^{-i\mathbf{k}\cdot\mathbf{T}} \sqrt{\frac{M_s \omega_\nu(\mathbf{k})}{2}} \epsilon^\nu_{i\alpha}(\mathbf{k}) \left(\hat{b}_\nu(\mathbf{k}) - \hat{b}^\dagger_\nu(-\mathbf{k}) \right) \right). \end{aligned} \tag{2.43}$$

From the ladder operator combinations in the electron-phonon Hamiltonian $\hat{H}^{e-ph}$, $(\hat{c}^{\dagger}_{n'\mathbf{k}'}\hat{c}_{n\mathbf{k}}\hat{b}_{\nu\mathbf{k}})$ and $(\hat{c}^{\dagger}_{n'\mathbf{k}'}\hat{c}_{n\mathbf{k}}\hat{b}^{\dagger}_{\nu-\mathbf{k}})$, it is direct to interpret these terms as the emission or absorption of a phonon by an electron that changes electronic state. In such processes, the energy and momentum is conserved, which can be derived from $\sum_{\mathbf{T}} e^{i\mathbf{k}\cdot\mathbf{T}} \langle n'\mathbf{k}'|\frac{\partial \hat{V}_{KS}}{\partial u_{i\alpha}(\mathbf{T})}|n\mathbf{k}\rangle$ and noting that the derivatives are periodic in real space.

With that being said, $\hat{H}^{e-ph}$ can then be written in the more usual Fröhlich form

$$\hat{H}^{e-ph} = \frac{1}{\sqrt{N}} \sum_{\nu\ n\ m} \sum_{\mathbf{kq}}^{1BZ} g^{\nu}_{m\mathbf{k}+\mathbf{q},n\mathbf{k}} \hat{c}^{\dagger}_{m\mathbf{k}+\mathbf{q}} \hat{c}_{n\mathbf{k}} \left(\hat{b}_{\nu\mathbf{q}} + \hat{b}^{\dagger}_{\nu-\mathbf{q}}\right), \tag{2.44}$$

$$g^{\nu}_{m\mathbf{k}+\mathbf{q},n\mathbf{k}} = \sum_{\mathbf{T}i\alpha} e^{i\mathbf{q}\cdot\mathbf{T}} \frac{1}{\sqrt{2M_s\omega_{\nu}(\mathbf{q})}} \langle \phi_{m\mathbf{k}+\mathbf{q}}|\frac{\partial \hat{V}_{KS}}{\partial u_{i\alpha}(\mathbf{T})} \epsilon^{\nu}_{i\alpha}(\mathbf{q})|\phi_{n\mathbf{k}}\rangle, \tag{2.45}$$

where all the ingredients to construct the Fröhlich Hamiltonian can be obtained with the Density Functional Perturbation theory methods discussed in Section 2.2.

In order to analyze the effects of the electron-phonon coupling over both electrons and phonons is useful to work in the Green's function formalism. In order to obtain the corresponding Green functions, the starting Dyson's equations [59] take the form

$$\mathcal{G}_n(\mathbf{k}, i\omega_m) = \mathcal{G}^0_n(\mathbf{k}, i\omega_m) + \mathcal{G}^0_n(\mathbf{k}, i\omega_m) + \Sigma_n(\mathbf{k}, i\omega_m)\mathcal{G}_n(\mathbf{k}, i\omega_m) \tag{2.46}$$

for the electron Green function $\mathcal{G}_n(\mathbf{k}, i\omega_m)$, and

$$\mathcal{D}_n(\mathbf{k}, i\Omega_m) = \mathcal{D}^0_n(\mathbf{k}, i\Omega_m) + \mathcal{D}^0_n(\mathbf{k}, i\Omega_m) + \Pi_n(\mathbf{k}, i\Omega_m)\mathcal{D}_n(\mathbf{k}, i\Omega_m) \tag{2.47}$$

for the phonon Green function $\mathcal{D}_n(\mathbf{k}, i\Omega_m)$. Here $\mathcal{G}^0_n(\mathbf{k}, \omega_m)$ and $\mathcal{D}^0_n(\mathbf{k}, i\Omega_m)$ are the non-interacting Green functions, and $\Sigma_n(\mathbf{k}, i\omega_m)$ and $\Pi_n(\mathbf{k}, i\Omega_m)$ are the electron and phonon selfenergies. In principle, one should sum for infinite diagrams, but according to *Migdal's theorem* all vertex corrections are of order $\sqrt{m_e/M_I}$, and therefore, the lowest order diagram is expected to be the most important. Thus, the selfenergies to lowest order diagram can be approximated as

$$\begin{aligned}\Sigma_n(\mathbf{k}, \omega_m) = -\frac{1}{N_q} \sum_{\nu,\mathbf{q},n'} \left|g^{\nu}_{n'\mathbf{k}+\mathbf{q},n\mathbf{k}}\right|^2 \Bigg[&\frac{n_B(\omega_{\nu}(\mathbf{q})) + \frac{1}{2}f_{n'\mathbf{k}+\mathbf{q}}}{\omega + i\delta + \omega_{\nu}(\mathbf{q}) - \varepsilon_{n'\mathbf{k}+\mathbf{q}}} \\ &+ \frac{n_B(\omega_{\nu}(\mathbf{q})) + 1 - \frac{1}{2}f_{n'\mathbf{k}+\mathbf{q}}}{\omega + i\delta - \omega_{\nu}(\mathbf{q}) - \varepsilon_{n'\mathbf{k}+\mathbf{q}}} \Bigg]\end{aligned} \tag{2.48}$$

for electrons and

$$\Pi_{\nu}(\mathbf{q}, \omega) = \frac{1}{N_k} \sum_{n,n',\mathbf{k}} \left|g^{\nu}_{n'\mathbf{k}+\mathbf{q},n\mathbf{k}}\right|^2 \frac{f_{n\mathbf{k}} - f_{n'\mathbf{k}+\mathbf{q}}}{\varepsilon_{n\mathbf{k}} - \varepsilon_{n'\mathbf{k}+\mathbf{q}} + \omega + i\delta} \tag{2.49}$$

for phonons, where f are Fermi-Dirac occupations and n_B are boson occupations. The shift in phonon frequencies due to the electron-phonon interaction

is proportional to the real part of the self-energy. Furthermore, the electron-phonon self-energy $\Pi_\nu(\mathbf{q}, \omega)$, apart from the square of the electron-phonon matrix elements, closely resembles the Lindhard function [60], whose real part is negatively defined. As a result, the electron-phonon interaction will always soften phonon frequencies, potentially leading to instabilities.

In principle, one can derive all the relevant properties form the electron-phonon interaction from equations (2.48) and (2.49). For example, the electron-phonon contribution to the phonon linewidth $\gamma_\nu(\mathbf{q})$, given as half with half maximum (HWHM), is given by the imaginary part of the selfenergy

$$\gamma_\nu(\mathbf{q}) = -\text{Im}\ \Pi_\nu(\mathbf{q}, \omega(\mathbf{q})), \tag{2.50}$$

which after some assumptions, as focusing in excitations happening only in the Fermi surface due to the smallness of phonon energies, we get

$$\gamma_\nu(\mathbf{q}) = \frac{2\pi\omega_\mu(\mathbf{q})}{N_k} \sum_{\mathbf{k}nm} \left| g^\mu_{n\mathbf{k},m\mathbf{k}+\mathbf{q}} \right|^2 \delta(\varepsilon_{n\mathbf{k}} - \varepsilon_F)\delta(\varepsilon_{m\mathbf{k}+\mathbf{q}} - \varepsilon_F), \tag{2.51}$$

which is the usual formula to compute the electron-phonon linewidth. A very closely related quantity is the nesting function $\zeta(\mathbf{q})$, which can be defined as

$$\zeta(\mathbf{q}, \varepsilon_F) = \frac{1}{N_k} \sum_{\mathbf{k}nm} \delta(\varepsilon_{n\mathbf{k}} - \varepsilon_F)\delta(\varepsilon_{m\mathbf{k}+\mathbf{q}} - \varepsilon_F), \tag{2.52}$$

which tells us how much of the Fermi surface is connected by the $\mathbf{q}$ vector. As can be seen from equations (2.51) and (2.52), the electron-phonon linewidth is both proportional to the electron-phonon coupling elements and to the nesting function.

2.4 BEYOND THE HARMONIC APPROXIMATION

So far we have limited ourselves to the study of the lattice vibrations within the harmonic approximation, with the extension of the electron-phonon coupling as a perturbation of the harmonic system. However, we have assumed that the Born-Oppenheimer energy surface is well described, despite the truncation of the Taylor expansion in equation (2.4) at second order.

A clear limitation of any expansion of this kind is that it only holds as long as the displacements $\mathbf{u}$ from the center of the expansion $\mathbf{R}^{\text{eq}}$ are small. However, there are many circumstances in which this is not true. For instance, when we are dealing with very light atoms, or when there exists a displacive phase transition.

Moreover, within the harmonic approximation, phonons are well defined quasi-particles with infinite lifetimes and without accounting for finite thermal conductivity or thermal expansions. Sometimes, even the real equilibrium positions of the nuclei are missed within the harmonic approximation.

Therefore, in order to depict such phenomena, one must go beyond the usual harmonic approximation and introduce anharmonic terms in the de-

scription. While the most straightforward method involves incorporating additional terms in the Taylor expansion of the Born-Oppenheimer energy surface (2.4) as perturbations, the assumption of displacements being small remains essential.

From inspecting the expression for the displacements given in equation (2.23), it can be seen that it is inversely proportional to both the mass, but more importantly the frequency ω. This implies, than when a phonon softens up to the point of triggering a phase transition when $\omega = 0$, the displacements diverge, which is obviously not true, but signals that perturbative approaches are bound to fail.

Among the possible non-perturbative methods for addressing strong anharmonic effects, as we attempt in this thesis, are molecular dynamics simulations and path integral molecular dynamics. The former, while practical, do not capture quantum effects. The latter, considered the gold standard, come with a significant computational cost. In our case, we will use a stochastic implementation of the Self-Consistent Harmonic Approximation (SCHA) [61]. Although this method remains computationally demanding, it is far more affordable than path-integral molecular dynamics while still capturing quantum effects.

2.4.1 *The self-consistent harmonic approximation (SCHA)*

The Self-Consistent Harmonic Approximation (SCHA) was originally proposed by Hooton in 1955 [61] as a non-perturbative treatment that fully accounts for both thermal and anharmonic (also referred as quantum) effects. The non-perturbative nature implies that one does not at any point approximate the Born-Oppenheimer energy surface in equation (2.1), and in turn one opts for a variational approach. The approximation comes when assuming that the solution to the ionic Hamiltonian $\hat{H}$ (2.1) is given by a Gaussian density matrix $\rho(\mathbf{R})$. Then by a variational method one finds the Gaussian density matrix that minimizes the free energy of the full Hamiltonian $\hat{H}$ without approximating the BO energy surface. Since the solution of a harmonic Hamiltonian is always given by a Gaussian, there is a mapping between any Gaussian and the harmonic Hamiltonian from which it is solution. This particular Hamiltonian will be referred as the auxiliary Hamiltonian $\mathcal{H}$. In essence, the SCHA method is equivalent to the Hartree-Fock approximation discussed in Section 1.1.3, in which one assumes a non-interacting solution for the interacting problem.

2.4.1.1 *The variational principle*

The free energy we aim to minimize for the full ionic Hamiltonian (2.1) is given by the sum of the total energy and the entropic contribution

$$F_H = \mathrm{tr}(\rho_H H) + \frac{1}{\beta}\mathrm{tr}(\rho_H \ln \rho_H) = -\frac{1}{\beta}\ln Z_H, \tag{2.53}$$

where $Z_H = \mathrm{tr}(e^{-\beta H})$ is the partition function, and $\rho_H = e^{-\beta H}/Z_H$ is the density matrix.

Since explicitly computing F_H is computationally challenging, instead, a quantum variational principle in the free energy is defined. By substituting the density matrix by any other $\rho_{\mathcal{H}}$ defined by a trial Hamiltonian $\mathcal{H} = T + \mathcal{V}$, one has that if

$$\mathcal{F}_H(\mathcal{H}) = \mathrm{tr}(\rho_{\mathcal{H}} H) + \frac{1}{\beta}\mathrm{tr}(\rho_{\mathcal{H}} \ln \rho_{\mathcal{H}}), \tag{2.54}$$

then, by the Gibbs-Bogoliubov inequality we have that

$$F_H \leqslant \mathcal{F}_H(\mathcal{H}). \tag{2.55}$$

Finally, by adding and subtracting $\mathrm{tr}(\rho_{\mathcal{H}}\mathcal{H})$ in (2.54) is direct to arrive to

$$\mathcal{F}_H(\mathcal{H}) = F_{\mathcal{H}} + \mathrm{tr}[\rho_{\mathcal{H}}(V^{BO} - \mathcal{V})]. \tag{2.56}$$

Hence, $\mathcal{F}_H(\mathcal{H})$ is minimized with respect to the trial Hamiltonian $\mathcal{H}$ and a variational principle is established. The SCHA restricts the trial potential $\mathcal{V}$ to a harmonic one. One of the benefits of this is that the free energy and the probability density of finding certain $\mathbf{R}$ ionic configuration $\rho_{\mathcal{H}}(\mathbf{R}) = \rho_{\mathcal{R},\Phi}(\mathbf{R}) = \langle \mathbf{R}|\rho_{\mathcal{H}}|\mathbf{R}\rangle$, can be expressed in terms of phonon frequencies, eigenvectors (contained in the force constants Φ) and equilibrium positions ($\mathcal{R}$) of the auxiliary Hamiltonian $\mathcal{H}$.

2.4.1.2 *Expectation values and the free energy gradient*

The trial density function $\rho_{\mathcal{H}}$ used in the SSCHA minimization is totally defined by the auxiliary trial Hamiltonian $\mathcal{H}$, which in turn is defined by a set of centroid positions $\mathcal{R}$ and force constants Φ

$$\rho_{\mathcal{H}}(\mathbf{R}) \quad \leftrightarrow \quad \mathcal{H} \quad \leftrightarrow \quad (\mathcal{R}, \Phi), \tag{2.57}$$

where in this case, Φ are the force constants associated with auxiliary BO potential $\mathcal{V}_2$. Diagonalizing the dynamical matrix of the auxiliary Hamiltonian $\mathcal{H}$ we obtain auxiliary polarization vectors $\epsilon^{i\alpha}_{\mu\mathcal{H}}$ and frequencies $\omega_{\mu\mathcal{H}}$ satisfying the usual eigenvalue problem (2.12) for a harmonic system.

The probability of finding the system in a general ionic configuration $\mathbf{R}$, is given by

$$\rho_{\mathcal{H}}(\mathbf{R}) = A_{\mathcal{H}} \exp\left(-\sum_{st\alpha\beta\mu} \frac{\sqrt{M_s M_t}}{2a^2_{\mu\mathcal{H}}} \epsilon^{s\alpha}_{\mu\mathcal{H}} \epsilon^{t\beta}_{\mu\mathcal{H}} u^{s\alpha} u^{t\beta}\right), \tag{2.58}$$

where A_μ is a normalization constant (so that the density matrix integrates to unity) and a_μ is the normal length of the mode μ defined as

$$a_{\mu\mathcal{H}} = \sqrt{\hbar \coth(\beta\hbar\omega_{\mu\mathcal{H}}/2)/(2\omega_{\mu\mathcal{H}})}. \tag{2.59}$$

Having such explicit expression for the probability of finding the system in particular ionic configuration $\mathbf{R}$, it is direct to write the expectation value for any observable $O(\mathbf{R})$ that depends on the ionic positions

$$\langle O \rangle = \mathrm{tr}(\rho_{\mathcal{H}} O) = \int d\mathbf{R}\, O(\mathbf{R}) \rho_{\mathcal{H}}(\mathbf{R}). \tag{2.60}$$

Now, we can evaluate the expected value of the free energy given in equation (2.56), which turns to be analytic for the case of $\mathcal{H}$ being harmonic

$$\mathcal{F}_H(\mathcal{H}) = F_{\mathcal{H}} + \int dR[\, V^{BO}(\mathbf{R}) - \mathcal{V}(\mathbf{R})] \rho_{\mathcal{H}}(\mathbf{R}). \tag{2.61}$$

In order to minimize the free energy for the trial Hamiltonian (2.57), we need to compute the gradient of the free energy (2.61) with respect to the degrees of freedom of the trial Gaussian. The trial density function is defined by two sets of parameters, the equilibrium positions $\mathcal{R}$ and the force constants Φ, and thus the total gradient can be written as

$$\nabla \mathcal{F}_H(\mathcal{H}) = [\nabla_{\mathcal{R}} \mathcal{F}_H(\mathcal{H}), \nabla_{\Phi} \mathcal{F}_H(\mathcal{H})], \tag{2.62}$$

where $\nabla_{\mathcal{R}} \mathcal{F}_H(\mathcal{H})$ is the gradient with respect to the equilibrium positions and $\nabla_{\Phi} \mathcal{F}_H(\mathcal{H})$ with respect to the force-constants, which are given by

$$\nabla_{\mathcal{R}} \mathcal{F}_H(\mathcal{H}) = -\int [\mathbf{f}(\mathbf{R}) - \mathbf{f}_{\mathcal{H}}(\mathbf{R})]\, \rho_{\mathcal{H}}(\mathbf{R})\, d\mathbf{R}, \tag{2.63}$$

$$\begin{aligned} \nabla_{\Phi} \mathcal{F}_H(\mathcal{H}) = & \sum_{st\alpha\beta\mu} \sqrt{\frac{M_t}{M_s}} \left(\epsilon^{s\alpha}_{\mu\mathcal{H}} \nabla_{\Phi} \ln a_{\mu\mathcal{H}} + \nabla_{\Phi} \epsilon^{s\alpha}_{\mu\mathcal{H}} \right) \epsilon^{t\beta}_{\mu\mathcal{H}} \\ & \times \int [f^{s\alpha}(\mathbf{R}) - f^{s\alpha}_{\mathcal{H}}(\mathbf{R})]\, (R^{t\beta} - R^{t\beta}_{eq}) \rho_{\mathcal{H}}(\mathbf{R})\, d\mathbf{R}, \end{aligned} \tag{2.64}$$

where $\mathbf{f}(\mathbf{R})$ is a vector formed by all the atomic forces for the ionic configuration $\mathbf{R}$, and $\mathbf{f}_{\mathcal{H}}(\mathbf{R})$ denotes the forces derived from the auxiliary potential $\mathcal{V}$.

2.4.2 *The stochastic self-consistent harmonic approximation (SSCHA)*

The stochastic implementation of the Self-consistent Harmonic Approximation (SSCHA) was introduced by Errea et al [62] and extended in [63–65]. This implementation evaluates the integrals that define a particular observable (2.61) by performing a summation over an stochastic sampling of $\rho_{\mathcal{H}}(\mathbf{R})$ as

$$\int O(\mathbf{R}) \rho_{\mathcal{H}}(\mathbf{R}) d\mathbf{R} \to \frac{1}{N_c} \sum_{i}^{N_c} O(\mathbf{R}_I), \tag{2.65}$$

which turns into an equality when the number of configurations $N_c \to \infty$. This, allows to compute the free energy gradients in equations (2.63) and (2.64) in order to minimize the free energy. Then, by performing a gradient descent, at each step of the minimization both the equilibrium positions $\mathcal{R}$ and

force-constants Φ are updated, defining a new auxiliary Hamiltonian. Finally, the minimization is stopped when the gradients lie below certain threshold.

Technically, in each step of the minimization $\rho_{\mathcal{H}}(\mathbf{R})$ is updated and a new stochastic sampling is necessary, which would turn the method exceedingly expensive. To overcome this issue, a reweighting procedure is implemented by including the factor $\rho_{\mathcal{H}_i}(\mathbf{R})/\rho_{\mathcal{H}_0}(\mathbf{R})$, where $\rho_{\mathcal{H}_i}$ is the density corresponding to the auxiliary Hamiltonian in the i step of the minimization. Then the mean value of an observable $O(\mathbf{R})$ can be rewritten as

$$\langle O\rangle_{\mathcal{H}_i} = \int O(\mathbf{R})\rho_{\mathcal{H}_i}(\mathbf{R})\,d\mathbf{R} = \int O(\mathbf{R})\left(\frac{\rho_{\mathcal{H}_i}(\mathbf{R})}{\rho_{\mathcal{H}_0}(\mathbf{R})}\right)\rho_{\mathcal{H}_0}(\mathbf{R})\,d\mathbf{R} \approx \frac{1}{N_c}\sum_{I}^{N_c} O(\mathbf{R}_I)\frac{\rho_{\mathcal{H}_i}(\mathbf{R})}{\rho_{\mathcal{H}_0}(\mathbf{R})}, \tag{2.66}$$

which allows to use the same set of configurations for several steps in the minimization.

After the minimization, the final equilibrium positions including anharmonic effects are given by $\mathcal{R}$. The density matrix $\rho_{\mathcal{H}}$ has by definition a Gaussian shape, centered at the centroid positions $\mathcal{R}$ and with variance determined by the force constants Φ. The phonons obtained from the auxiliary Hamiltonian $\mathcal{H}$, are called the auxiliary phonons, which should not be confused with the "real" measurable phonons. Notice how, for example, these phonons will always have positive frequencies since the Gaussian trial density matrix would diverge otherwise.

2.4.3 *Anharmonic phonons as the Hessian of the free energy*

It was shown by Bianco et al [63] that the equivalent to phonons within the harmonic approximation but with anharmonic corrections, in the sense that a negative frequency indicates an instability, are given by the Hessian of the free energy. First, it is useful to define the positional free energy as the free energy obtained by keeping the centroid positions $\mathcal{R}$ fixed

$$F(\mathcal{R}) \equiv \min_{\Phi} \mathcal{F}[\mathcal{R}, \Phi], \tag{2.67}$$

where $\rho_{\mathcal{R}}$ is the density matrix that minimizes the free energy under such constraint, and being $F = F(\mathcal{R}_{eq}) = \min_{\mathcal{R}} F(\mathcal{R})$ the standard free energy. Then, the role of eigenvalues and eigenvectors of the positional free energy Hessian is equivalent to the role of the dynamical matrices and polarization vectors in the Harmonic approximation, being $D^{(F)}_{ab}$ the natural generalization of such dynamical matrices

$$D^{(F)}_{ab} = \frac{1}{\sqrt{M_a M_b}}\left.\frac{\partial^2 F(\mathcal{R})}{\partial \mathcal{R}^a \mathcal{R}^b}\right|_{\mathcal{R}_{eq}}, \tag{2.68}$$

where now we have switched to a more compact notation where $a \equiv (a, \alpha)$ is now a double index of both ion and cartesian coordinate. Luckily, there is an analytic formula for such Hessian

$$\frac{1}{\sqrt{M}}\cdot\frac{\partial^2 F(\mathcal{R})}{\partial\mathcal{R}\partial\mathcal{R}}\cdot\frac{1}{\sqrt{M}} = D_{\mathcal{R}} + \overset{(3)}{D}_{\mathcal{R}} : \Lambda_{\mathcal{R}}[0] : \left[1 - \overset{(4)}{D}_{\mathcal{R}} : \Lambda_{\mathcal{R}}[0]\right]^{-1} : \overset{(3)}{D}_{\mathcal{R}} \tag{2.69}$$

where we now switch to a more compact notation, $a \equiv (i, \alpha)$ serves as a double index, representing both the ion and the Cartesian coordinate. The dynamical matrices $D_{\mathcal{R}}$ are given by

$$(D_{\mathcal{R}})_{ab} = \frac{1}{\sqrt{M_a M_b}} \left\langle \frac{\partial^2 V^{BO}}{\partial \mathcal{R}^a \partial \mathcal{R}^b} \right\rangle_{\rho_{\mathcal{R}}, \Phi_{\mathcal{R}}} = \frac{(\Phi_{\mathcal{R}})_{ab}}{\sqrt{M_a M_b}}, \tag{2.70}$$

$$\overset{(3)}{(D_{\mathcal{R}})}_{abc} = \frac{1}{\sqrt{M_a M_b M_c}} \left\langle \frac{\partial^3 V^{BO}}{\partial \mathcal{R}^a \partial \mathcal{R}^b \partial \mathcal{R}^c} \right\rangle_{\rho_{\mathcal{R}}, \Phi_{\mathcal{R}}} = \frac{\overset{(3)}{(\Phi_{\mathcal{R}})}_{abc}}{\sqrt{M_a M_b M_c}}, \tag{2.71}$$

$$\overset{(4)}{(D_{\mathcal{R}})}_{abcd} = \frac{1}{\sqrt{M_a M_b M_c M_d}} \left\langle \frac{\partial^4 V^{BO}}{\partial \mathcal{R}^a \partial \mathcal{R}^b \partial \mathcal{R}^c \partial \mathcal{R}^d} \right\rangle_{\rho_{\mathcal{R}}, \Phi_{\mathcal{R}}} = \frac{\overset{(4)}{(\Phi_{\mathcal{R}})}_{abcd}}{\sqrt{M_a M_b M_c M_d}}, \tag{2.72}$$

and $\Lambda_{\mathcal{R}}[z]$ is a fourth-order negatively defined tensor

$$\begin{cases} (\Lambda_{\mathcal{R}}[z])^{abcd} = \sum_{\mu\nu} \mathcal{J}(z, \omega_\mu, \omega_\nu)\, e^a_\nu e^b_\mu e^c_\nu e^d_\mu, \\ \mathcal{J}(z, \omega_\mu, \omega_\nu) = \frac{\hbar}{4\omega_\mu \omega_\nu} \left[\frac{(\omega_\mu - \omega_\nu)(n_\mu - n_\nu)}{(\omega_\mu - \omega_\nu)^2 - z^2} - \frac{(\omega_\mu + \omega_\nu)(1 + n_\mu + n_\nu)}{(\omega_\mu + \omega_\nu)^2 - z^2} \right], \end{cases} \tag{2.73}$$

where ω_μ and e^a_ν are the eigenvalues and eigenvectors of $D_{\mathcal{R}}$, n_μ are the Bose-Einstein occupations and the $\overset{(n)}{\Phi}_{\mathcal{R}}$ are the n-th order SSCHA force constants.

Overall, each term appearing in equation (2.70) is a complex object that contains a dependence of derivatives of the Born-Oppenheimer energy surface averaged over the density $\rho_{\mathcal{R}}$. While $\overset{(2)}{D}_{\mathcal{R}}$ is positive defined, both $\overset{(3)}{D}_{\mathcal{R}}$ and $\overset{(4)}{D}_{\mathcal{R}}$ can be negative. This implies that the free energy hessian (2.69) can have negative values and describe second order phase transitions in which frequencies collapse to zero.

2.4.4 *Dynamical theory, SSCHA self-energy and spectral function*

In order to build a quantum anharmonic dynamical theory, Bianco et al [63] formulated and *ansatz* for the one-phonon Green function $G(z)$, which was later proved by Monacelli et al [65]

$$G^{-1}(z) = z^2 - \left(D^{(\mathcal{H})} + \Pi(z) \right), \tag{2.74}$$

where $D^{(\mathcal{H})}$ is the dynamical matrix of the SSCHA effective harmonic Hamiltonian $\mathcal{H}$ and $\Pi(z)$ is the SSCHA self-energy given by

$$\Pi(z) = \overset{(3)}{D}_{eq} : \Lambda_{eq}[z] : \left[1 - \overset{(4)}{D}_{eq} : \Lambda_{eq}[z] \right]^{-1} : \overset{(3)}{D}_{eq}, \tag{2.75}$$

where $\overset{(3)}{D}_{eq}$ and Λ_{eq} are taken in the equilibrium positions $\mathcal{R}_{eq}$ and defined in equations (2.70) and (2.73).

Then, hessian of the free energy (2.69) in equilibrium $D^{(F)}$ can be rewritten in terms of the self-energy $\Pi(z)$ as

$$D^{(F)} = D^{(\mathcal{H})} + \Pi(0), \tag{2.76}$$

where $(z = 0)$ corresponds to the so-called static approximation.

2.4.4.1 *The static bubble approximation*

Within the static limit, we can apply the bubble approximation and compute the free energy Hessian $D^{(F)}(\mathbf{q})$ at any reciprocal space $\mathbf{q}$-point (not necessarily commensurate with the supercell). The bubble approximation consists on dropping the fourth order terms $\overset{(4)}{D}$ in the SSCHA self-energy (2.75). Then, effectively you only are left with the bubble term in the corresponding Feynman diagrams and the bubble self-energy reads

$$\overset{(B)}{\Pi}(z) = \overset{(3)}{D}_{eq} : \Lambda_{eq}[z] : \overset{(3)}{D}_{eq} . \tag{2.77}$$

The code can then compute the Fourier transform of the static bubble self-energy $\overset{(B)}{\Pi}(\mathbf{q}, 0)$ at any $\mathbf{q}$-point as a Fourier interpolation in reciprocal space as

$$\begin{aligned}\overset{(B)}{\Pi}_{\mu\nu}(\mathbf{q}, 0) = \frac{1}{N_k} \sum_{\mathbf{k}_1, \mathbf{k}_2, \rho_1, \rho_2} \sum_{\mathbf{G}} \delta_{\mathbf{G}, \mathbf{q}+\mathbf{k}_1+\mathbf{k}_2} \mathcal{J}(0, \omega_{\rho_1}(\mathbf{k}_1), \omega_{\rho_2}(\mathbf{k}_2)) \\ \times \overset{(3)}{D}_{\mu\rho_1\rho_2}(-\mathbf{q}, -\mathbf{k}_1, -\mathbf{k}_2) \overset{(3)}{D}_{\rho_1\rho_2\nu}(\mathbf{k}_1, \mathbf{k}_2, \mathbf{q}),\end{aligned} \tag{2.78}$$

where the sum is over a mesh of N_k different $\mathbf{k}_i$ vectors over the Brillouin zone; $\overset{(3)}{D}_{\mu\rho_1\rho_2}(\mathbf{k}_1, \mathbf{k}_2, \mathbf{q})$ are the Fourier transform of $\overset{(3)}{D}_{eq}$, $\omega_\rho(\mathbf{k})$ are the frequencies of $D^{\mathcal{H}}(\mathbf{k})$, the function $\mathcal{J}$ is defined in equation (2.73), and $\mathbf{G}$ are reciprocal lattice vectors. Notice how, in this formula neither $\mathbf{q}$ or $\mathbf{k}_i$ are confined to the commensurate grid of the supercell, which allows us to obtain SSCHA free energy Hessians at any $\mathbf{q}$ after converging for a sufficiently dense $\mathbf{k}_i$ grid.

2.4.4.2 *The SSCHA spectral function*

With the Green function defined in (2.74) we can obtain the spectral function $\sigma(q, \Omega)$, which is proportional to the measured signal in Raman, infrared or inelastic diffraction experiments. The spectral function is given by

$$\sigma(\Omega) = -2 \operatorname{Im} \operatorname{Tr}\left[G(\Omega + i0^+)\right], \tag{2.79}$$

where 0^+ is an infinitesimally small positive real number and Ω is the energy. Then, taking advantage of the translational symmetry one can Fourier transform to

$$\sigma(\mathbf{q}, \Omega) = -\frac{\Omega}{\pi} \operatorname{Im} \operatorname{Tr}\left[G(\mathbf{q}, \Omega + i0^+)\right], \tag{2.80}$$

or equivalently

$$\sigma(\mathbf{q},\Omega) = -\frac{\Omega}{\pi}\,\mathrm{Im}\,\mathrm{Tr}\left[(\Omega+i0^+)^2\mathbb{1} - (D^{(\mathcal{H})}(\mathbf{q}) + \Pi(\mathbf{q},\Omega+i0^+))\right]^{-1} \tag{2.81}$$

Within the **static approximation**, the full SSCHA self-energy $\Pi(z)$ is replaced by the static limit $\Pi(0)$. Which will result in a spectral function given by delta peaks at the eigenvalues of the free energy Hessian $D^{(F)}(\mathbf{q})$ given in (2.76)

$$\begin{aligned}\overset{(\mathrm{stat})}{\sigma}(\mathbf{q},\Omega) &= -\frac{\Omega}{\pi}\,\mathrm{Im}\,\mathrm{Tr}\left[(\Omega+i0^+)^2\mathbb{1} - (D^{(\mathcal{H})}(\mathbf{q}) + \Pi(\mathbf{q},0))\right]^{-1} \\ &= -\frac{\Omega}{\pi}\,\mathrm{Im}\,\mathrm{Tr}\left[(\Omega+i0^+)^2\mathbb{1} - D^{(F)}(\mathbf{q}))\right]^{-1}.\end{aligned} \tag{2.82}$$

The **full dynamical SSCHA self-energy** ($z \neq 0$) can only be computed within the bubble approximation defined by (2.77), but in this case with $z \neq 0$. Then, the resulting self-energy $\overset{(B)}{\Pi}(z)$ in the $D^{(\mathcal{H})}(\mathbf{q})$'s eigenbasis is given by

$$\begin{aligned}\overset{(B)}{\Pi}_{\mu\nu}(\mathbf{q},\Omega+i\delta_{se}) = \frac{1}{N_k}\sum_{\mathbf{k}_1,\mathbf{k}_2,\rho_1,\rho_2}\sum_{\mathbf{G}}\delta_{\mathbf{G},\mathbf{q}+\mathbf{k}_1+\mathbf{k}_2}\mathcal{J}(\Omega+i\delta_{se},\omega_{\rho_1}(\mathbf{k}_1),\omega_{\rho_2}(\mathbf{k}_2)) \\ \times \overset{(3)}{D}_{\mu\rho_1\rho_2}(-\mathbf{q},-\mathbf{k}_1,-\mathbf{k}_2)\overset{(3)}{D}_{\rho_1\rho_2\nu}(\mathbf{k}_1,\mathbf{k}_2,\mathbf{q}),\end{aligned} \tag{2.83}$$

where the meaning of the different variables is the same as in equation (2.78), and δ_{se} is an infinitely small positive number (akin to the 0^+ used previously times). This self energy should be then converged with respect to a support $\mathbf{k}$-grid, and the infinitely small positive value δ_{se}. Thus, the SSCHA method allows also to compute the equivalent to the measured total spectral function $\sigma(\mathbf{q},\Omega)$, which can be used to compute the phonon anharmonic linewidths and compare with experiments.

2.4.4.3 *No-mode mixing approximation*

The no-mode mixing approximation consists in discarding the off-diagonal elements of the computed self-energy $\Pi(z)$ in equation (2.83). This not only saves computational cost, but implies that the total spectral function is given as a sum of individual spectral functions

$$\sigma(\mathbf{q},\Omega) = \sum_{\mu}\sigma_\mu(\mathbf{q},\Omega), \tag{2.84}$$

which allows to track the individual anharmonic corrections of each mode individually. Each of the individual spectral functions $\sigma_\mu(\mathbf{q},\Omega)$ are given by

$$\begin{aligned}\sigma_\mu(\mathbf{q},\Omega) = \frac{1}{2\pi}\Bigg[&\frac{-\mathrm{Im}\mathcal{Z}_\mu(\mathbf{q},\Omega)}{[\Omega-\mathrm{Re}\mathcal{Z}_\mu(\mathbf{q},\Omega)]^2+[\mathrm{Im}\mathcal{Z}_\mu(\mathbf{q},\Omega)]^2} \\ &+\frac{\mathrm{Im}\mathcal{Z}_\mu(\mathbf{q},\Omega)}{[\Omega+\mathrm{Re}\mathcal{Z}_\mu(\mathbf{q},\Omega)]^2+[\mathrm{Im}\mathcal{Z}_\mu(\mathbf{q},\Omega)]^2}\Bigg],\end{aligned} \tag{2.85}$$

where $\mathcal{Z}_\mu(\mathbf{q}, \Omega)$

$$\mathcal{Z}_\mu(\mathbf{q}, \Omega) = \sqrt{\omega_\mu^2(\mathbf{q}) + \Pi_{\mu\mu}(\mathbf{q}, \Omega + i\delta_{se})}. \tag{2.86}$$

2.4.4.4 *Lorentzian approximation*

In some cases, each mode-individual spectral function $\sigma_\mu(\mathbf{q}, \Omega)$ computed in the no-mode mixing approximation can be approximated by a true Lorentzian function, meaning that the quasiparticle picture is still valid. Then, the individual spectral functions can be approximated as

$$\begin{aligned}\sigma_\mu(\mathbf{q}, \Omega) = \frac{1}{2\pi}\Bigg[&\frac{\Gamma_\mu(\mathbf{q})}{[\Omega - \Omega_\mu(\mathbf{q})]^2 + [\Gamma_\mu(\mathbf{q})]^2} \\ &+ \frac{\Gamma_\mu(\mathbf{q})}{[\Omega + \Omega_\mu(\mathbf{q})]^2 + [\Gamma_\mu(\mathbf{q})]^2}\Bigg],\end{aligned} \tag{2.87}$$

where $\Omega_\mu(\mathbf{q})$ is the quasiparticle frequency and $\Gamma_\mu(\mathbf{q})$ is the half-width half-maximum (HWHM) linewidth defining the Lorentzian. The frequency shift $\Delta_\mu(\mathbf{q})$ is defined as the difference of the Lorentzian centers from the "bare" SSCHA frequencies (coming from the auxiliary Hamiltonian $\mathcal{H}$) $\Delta_\mu(\mathbf{q}) = \Omega_\mu(\mathbf{q}) - \omega_\mu(\mathbf{q})$. More importantly, a phonon lifetime τ can also be defined, which is given by $\tau = 1/2\Gamma_\mu(\mathbf{q})$.

Within the Lorentzian approximation, the SSCHA code can estimate frequencies and HWHMs in different ways. While the self-consistent equations that one should solve are well defined, effectively these are solved in two possible ways:

1. The One-shot approximation, in which the frequencies and linewidths are given by

$$\begin{aligned}\overset{(os)}{\Omega}_\mu(\mathbf{q}) &= \mathrm{Re}\mathcal{Z}_\mu(\mathbf{q}, \omega_\mu(\mathbf{q})), \\ \overset{(os)}{\Gamma}_\mu(\mathbf{q}) &= -\mathrm{Im}\mathcal{Z}_\mu(\mathbf{q}, \omega_\mu(\mathbf{q})).\end{aligned} \tag{2.88}$$

2. If the SSCHA self-energy $\Pi(z)$ is small, it can use lowest order perturbation theory to get the Lorentzian center and linewidths as

$$\begin{aligned}\overset{(pert)}{\Omega}_\mu(\mathbf{q}) &= \frac{1}{2\omega_\mu(\mathbf{q})}\mathrm{Re}\ \Pi_{\mu\mu}(\mathbf{q}, \omega_\mu(\mathbf{q})), \\ \overset{(pert)}{\Gamma}_\mu(\mathbf{q}) &= \frac{-1}{2\omega_\mu(\mathbf{q})}\mathrm{Im}\ \Pi_{\mu\mu}(\mathbf{q}, \omega_\mu(\mathbf{q}) + i\delta_{se}).\end{aligned} \tag{2.89}$$

In summary, the SSCHA code can provide with a different set of "frequencies". The frequencies $\omega_\mu(\mathbf{q})$ from the auxiliary Hamiltonian $\mathcal{H}$ are used to define the density matrix that minimizes the free energy. On the other hand, the frequencies from the free energy Hessian $D^{(F)}(\mathbf{q})$ can be used to analyze second-order phase transitions, as a zero value corresponds to an structural instability. Finally, while the full spectral functions is what is experimentally measured, the frequencies $\Omega_\mu(\mathbf{q})$ of the Lorentzian approximation are the closest to a true physical quantity while maintaining a quasiparticle picture.

3

GROUP THEORY AND TOPOLOGY

3.1 BASIC CONCEPTS OF GROUP THEORY

The beauty of group theory lies in its ability to extract the physical consequences of symmetries across systems, regardless of their complexity, through a straightforward application of basic algebraic rules. In this section we will summarize the most basic group theory concepts that will be later used during this thesis.

3.1.1 *Definition of Group*

A **group G** can be defined as a set of objects together with a binary operation, often called the **group operation**, that will be denoted as $\circ$. This set of elements and operations must satisfy the four fundamental properties of closure, associativity, the identity property, and the inverse property:

- Closure:
$$\forall \{A, B\} \in G \Rightarrow C = A \circ B \in G. \tag{3.1}$$
- Associativity: The group operation is associative
$$(A \circ B) \circ D = A \circ (B \circ D). \tag{3.2}$$
- Identity: there is a unique identity element E such that for every element $A \in G$.
$$E \circ A = A \circ E = A \tag{3.3}$$
- Inverse: There must be an inverse for each element. Therefore, $\forall A \in G$, the set contains an element $B = A^{-1}$ such that
$$A \circ A^{-1} = A^{-1} \circ A = E. \tag{3.4}$$

In the following, in order to simplify the notation we will get rid of the $\circ$ symbol assuming that $g_1 g_2 \equiv g_1 \circ g_2$. Some other useful definitions are:

- The **order of a group** is the number of elements in G.
- The **order of a group element** g is the minimum value of h such that $g^h = E$.
- A subset of elements H belonging to the group G, which itself satisfies the group structure, is called a **subgroup** of G.

3.1.2 *Conjugate elements and classes*

If two elements g and g_i belong to the group G, let us define g' as $g' = g_i g g_i^{-1}$. Then g and g' are said to be **conjugate** elements.

Now, as we let g_i run over G, we obtain n conjugate elements (the order of G) of which some might be equal. Assume there are k distinct elements, which by construction are mutually conjugate. The set of these mutually conjugate elements forms a **class**. Notice that:

- A class is fully defined by one of his elements.
- A finite group can be divided into classes.
- All the elements of a class have the same order.
- The set of group operations of the elements of two classes consists of whole classes

$$C_i C_j = \sum_k h_{ijk} C_k, \tag{3.5}$$

where C_i is the set of elements of class i and h_{ijk} are integers.

3.1.3 *Isomorphism and homomorphism*

Homomorphism: A homomorphism is a structure-preserving map between two algebraic structures of the same type. So that if to each element of a group G there corresponds only one definite element of the group G', and to each element of G' there corresponds a number of elements of G and, moreover, this correspondence is preserved under the group operation, then the group G' is homomorphic to G.
Isomorphism: An isomorphism is a homomorphism that is also a bijection. So that when between the elements of two groups there is a one-to-one correspondence, which preserves the group operation, then the groups are isomorphic.

3.2 REPRESENTATION THEORY

The theory of representations is one of the most important parts of group theory for a physicist, since it provides a great insight into qualitative properties of matrices such as eigenvectors or degeneracy of eigenvalues. Essentially, representations elucidate the abstract algebraic concept of a group by mapping its elements to matrices and expressing group operations through matrix multiplication, thereby rendering them more tangible.

A **representation** of a group G can be understood as an homomorphism between a group G and a group T of linear **operators** $\hat{T}_g$ that act in a space $\mathbb{R}^n$ and follow the relation:

$$\hat{T}_{g_i} \hat{T}_{g_k} = \hat{T}_{g_i g_k}. \tag{3.6}$$

The operator $\widehat{T}_g$ will be defined if we specify its action on the unit vectors $\mathbf{e}_k$ forming the basis of $\mathbb{R}^n$

$$\widehat{T}_g \mathbf{e}_k = \sum_{r=1}^{n} D_{rk}(g)\mathbf{e}_r. \tag{3.7}$$

Then, to each element of the group g_i we can assign a matrix $D_{rk}(g_i)$ such that

$$\begin{aligned} g_i &\longrightarrow D_{rk}(g_i), \\ D(g_i)D(g_j) &= D(g_i g_j). \end{aligned} \tag{3.8}$$

The matrices $D(g_i)$ are a representation of order n of the group G.

3.2.0.1 *Transformation of representations under a change of basis*

Let us now consider the change in the representation matrix which occurs when a new basis $\{\mathbf{e}'_i\}$ is taken in the space $\mathbb{R}^n$. The new basis will be related to $\{\mathbf{e}'_k\}$ by the linear transformation

$$\mathbf{e}'_i = \sum_k V_{ki}\mathbf{e}_k \quad ; \quad \mathbf{e}_i = \sum_k [V]^{-1}_{ki}\mathbf{e}'_k. \tag{3.9}$$

To this end, we will apply the operator $\widehat{T}_g$ to the new basis vector $\mathbf{e}'_j$. Using (3.9) we have

$$\begin{aligned} \widehat{T}_g \mathbf{e}'_j &= \sum_k \widehat{T}_g V_{kj}\mathbf{e}_k = \sum_{rk} D_{rk}(g)V_{kj}\mathbf{e}_r = \\ &= \sum_{rks} D_{rk}(g)V_{kj}[V]^{-1}_{sr}\mathbf{e}'_s = \sum_s \left\{ \sum_{rk} [V]^{-1}_{sr} D_{rk}(g)V_{kj} \right\} \mathbf{e}'_s = \\ &= \sum_s \left[[V]^{-1} D(g) V \right] \mathbf{e}'_s. \end{aligned} \tag{3.10}$$

Hence, the representation matrices transform as $D \to V^{-1}DV$ when we change basis. Some useful properties and definitions we will use are the following:

- Representations D and $V^{-1}DV$ are said to be **equivalent**.
- If all the representation matrices are unitary the representation is said to be **unitary**.
- It can be proved that any representation of a finite group is equivalent to a unitary representation.
- If the group of matrices $\{D(g_i)\}$ is isomorphic to G the representation is said to be a **faithful**.

3.2.1 *Reducible and irreducible representations of a group*

In order to define the concepts of reducible and irreducible representations is useful to first define the concept of **invariant subspace**. Motivated by the

action of the operators over the basis of our space described in (3.7), we can think of a subspace of dimension k with basis $\{\mathbf{e}_1, \mathbf{e}_2, ..., \mathbf{e}_k\}$ such that

$$\widehat{T}_g \mathbf{e}_i = \sum_{r=1}^{k} D_{ri}(g)\mathbf{e}_r \quad \forall g \in G \,; i \in [1,k]\,. \tag{3.11}$$

In other words, any vector belonging to this subspace will stay in the same subspace under group transformations. We say then that $\mathbb{R}^k$ is an invariant subspace under this representation.

Now, let D be a representation of G acting on $\mathbb{R}^n$. If there is a subspace $\mathbb{R}^k$ which is invariant under all the transformations D we can say that the representation is **reducible**. On the other hand, if such subspace does not exist, the representation is **irreducible** (irrep). For example, if the subspace $\{\mathbf{e}_1, ..., \mathbf{e}_k\}$ is an invariant subspace then:

$$D = \begin{pmatrix} D_{1,1} & ... & D_{1,k} & D_{1,k+1} & ... & D_{1,n} \\ ... & \ddots & ... & ... & ... & ... \\ D_{k,1} & ... & D_{k,k} & ... & ... & ... \\ 0 & 0 & 0 & D_{k+1,k+1} & ... & ... \\ 0 & 0 & 0 & ... & \ddots & ... \\ 0 & 0 & 0 & D_{n,k+1} & ... & D_{n,n} \end{pmatrix}, \tag{3.12}$$

but it can be proved that if D is a unitary representation and $\mathbb{R}^k$ is an invariant subspace, the complement $\mathbb{R}^{n-k}$ is also invariant, which leads to a block-diagonal form for the matrices of the representation

$$D = \begin{pmatrix} D_{1,1} & ... & D_{1,k} & 0 & 0 & 0 \\ ... & \ddots & ... & 0 & 0 & 0 \\ D_{k,1} & ... & D_{k,k} & 0 & 0 & 0 \\ 0 & 0 & 0 & D_{k+1,k+1} & ... & D_{k+1,n} \\ 0 & 0 & 0 & ... & \ddots & ... \\ 0 & 0 & 0 & D_{n,k+1} & ... & D_{n,n} \end{pmatrix}. \tag{3.13}$$

We could say then that a representation D is reducible if there exists a non-singular matrix V, such that the equivalent representation $V^{-1}DV$ is block-diagonal. Hence a reducible representation may be written as

$$D(g) = \sum_{i}^{\oplus} E_{r_i} \otimes D^{(i)}(g), \tag{3.14}$$

where E_{r_i} is the identity matrix of order r_i (the multiplicity of the representation i), $D^{(i)}(g)$ is the i-th irreducible representation of the group element $g \in G$, $\otimes$ is the Kroenecker product and the symbol $\oplus$ reminds us that the expression on the right-hand side of the equation is the direct sum of matrices.

$$D = \bigoplus_i r_i D^{(i)}. \tag{3.15}$$

3.2.1.1 *Symmetry adapted coordinates*

The symmetry adapted coordinates transform under the action of group elements according to the irreducible representations of the group. These coordinates are directly related to the invariant subspaces defined by (3.11). Hence, changing from regular coordinates to symmetry adapted coordinates implies the decomposition of the representation D into irreducible representations described at (3.14) and (3.15).

3.2.2 *Schur's lemmas*

In representation theory, Schur's two lemmas are concerned with the properties of matrices that commute with all of the matrices of an irreducible representations. Thus, they provide elementary but extremely useful statements.

Lemma 1 ***(Schur's first lemma):*** A matrix which commutes with all the matrices of an irreducible representation is a multiple of the identity.

Hence, if a representation is reducible and therefore can be written as (3.15), each of the irreducible representations $D^{(i)}$ will commute only with a multiple of the identity $\alpha_{m_i} E_{l_i}$, where l_i is the order or the i-th representation, α is a constant and $m_i \in [1, r_i]$ labels the multiplicity. Thus, if we construct a B matrix such as

$$B = \bigoplus_{i,m_i} \alpha_{m_i} E_{l_i}, \tag{3.16}$$

the matrix D of the reducible representation will commute with B, which is not a multiple of the identity.

Thus, one may be conclude that if the only matrix which commutes with all the matrices of a representation of a group is a multiple of the identity, then this representation is irreducible.

Lemma 2 ***(Schur's second lemma):*** Let $D^{(1)}(g)$ and $D^{(2)}(g)$ be the matrices of two irreducible non-equivalent representations of the group G of orders n_1 and n_2 respectively. Then, any rectangular matrix M with n_1 columns and n_2 rows which satisfies the equation

$$MD^{(1)}(g) = D^{(2)}(g)M \qquad \forall g \in G, \tag{3.17}$$

must be the null matrix.

3.2.3 *Character of a representation*

In group theory, the character or a group representation $D(g)$ is defined as the function that associates to each element of the group the trace of the corresponding matrix:

$$\chi(g) = \sum_i D_{i,i}(g). \tag{3.18}$$

Since the trace of a matrix is invariant under a change of basis, characters encode the invariant properties of a representation. Here, we describe some of the main properties of characters (and traces):

- Equivalent representations have identical characters. Since the trace of a matrix is invariant under a change in basis and, consequently $\mathrm{Tr}(D(g)) = \mathrm{Tr}(V^{-1}D(g)V)$.
- Traces are class functions. Thus, traces of a given representation corresponding to the elements of the same class are identical.
- The characters of the irreducible representations satisfy an orthogonality condition.
$$\sum_{g\in G} \chi^{(i)}(g)\chi^{*(j)}(g) = m\delta_{ij}, \tag{3.19}$$
where $\chi^{(i)}(g)$ and $\chi^{(j)}(g)$ are the characters of the irreducible representations $D^{(i)}$ and $D^{(j)}$, respectively. And m is the order of the group G.
- Most importantly, the character of a reducible representation D is equal to the sum of characters of irreducible representations into which it can be decomposed:
$$\chi(g) = \sum_j r_j\chi^{(j)}(g), \tag{3.20}$$
where again r_j is the multiplicity of the irrep $D^{(j)}$ and $\chi^{(j)}$ is the character of the j-th irreducible representation. This property will be used to decompose reducible representations.

With these properties one can find what is called the **magic formula**. First multiplying by $\chi^{*(i)}(g)$ and summing over all elements in G the expression (3.20); and then making use of the orthogonality condition (3.19)

$$\sum_g \chi^{*(i)}(g)\chi(g) = \sum_{g,j} r_j\chi^{*(i)}(g)\chi^{(j)}(g) = \sum_j r_j m\delta_{ij} = r_i m. \tag{3.21}$$

The magic formula tells us how many times a given irreducible representation appears in the decomposition of a reducible representation

$$r_i = \frac{1}{m}\sum_{g\in G} \chi^{*(i)}(g)\chi(g). \tag{3.22}$$

Hence, it follows that the decomposition of a reducible representation into irreducible parts (3.15) can be carried out uniquely as described in equation (3.22).

3.2.4 *Useful theorems*

In this last subsection about representation theory we will introduce some useful theorems that will come handy in the following chapters:

- The number of non-equivalent irreducible representations of a group G is equal to the number of classes.
- The sum over the squares of the dimensions n_j of the non-equivalent irreducible representations of a group G must be equal to the order of the group m

$$\sum_j n_j^2 = m. \tag{3.23}$$

- In abelian groups each element is its own class. Therefore, there must be m non-equivalent irreducible representations and their squares must sum m, hence they all must be unidimensional.

3.2.5 *Wigner's theorem*

Wigner's theorem determines the shape of a matrix that commutes with a particular representation of a group. This is an extremely powerful result, as any physical observable of the system must obey the symmetries and thus commute with certain representation of the symmetry group. For example, when applied to the Hamiltonian implies that just by looking at the irreps allows us to analyse the degeneracy of the energy levels and how they transform along the Brillouin zone; all without solving explicitly the Hamiltonian.

Theorem 6 ***(Wigner's theorem):*** Let $D(g)$ be a representation (in general, reducible) of the group G. We take the basis elements so that it splits into blocks corresponding to the different irreducible representations:

$$D(g) = \left\{ \begin{array}{ccccccc} D^{(1)}(g) & & & & & & \\ & D^{(2)}(g) & & & & & \\ & & \ddots & & & & \\ & & & D^{(i)}(g) & & & \\ & & & & \ddots & & \\ & & & & & D^{(n)}(g) & \end{array} \right\}, \tag{3.24}$$

where $D^{(i)}(g)$ is the matrix of the i-th irreducible representation of G, with multiplicity r_i. Hence, we can write $D(g)$ as:

$$D(g) = \sum_i^{\oplus} E_{r_i} \otimes D^{(i)}(g). \tag{3.25}$$

Let us suppose that a matrix H commutes with $D(g)$, then H must be of the form:

$$H = \sum_i^{\oplus} H^{(i)} \otimes E_{l_i}, \tag{3.26}$$

where $H^{(i)}$ is a matrix of order r_i and l_i is the order of the irreducible representation $D^{(i)}$.

The beauty of this theorem lies in that it allows to predict degenerate eigenvalues whenever we have non-unidimensional irreducible representations. Note that the number of different eigenvalues associated with an irrep i is equal to its multiplicity r_i, while the degeneracy of each eigenvalue equals the dimension of the corresponding irrep.

Moreover, this theorem gives us a recipe to block-diagonalize any matrix describing a physical observable, which greatly simplifies the process of full diagonalization. One just needs to find the group that commutes with the matrix and change to the symmetry adapted coordinates (adequately ordered) of such group by finding the invariant subspaces under the group transformations.

3.3 POINT GROUPS AND SPACE GROUPS

In physical applications, point groups are used to describe the symmetry of molecules since they are closely related with our immediate ideas about symmetry of geometrical figures such as spheres, cubes or prisms.

Mathematically speaking a **point group** is a finite subgroup of the group $\mathbb{O}(3)$ described by orthogonal 3×3 matrices. Their elements are written as C_n for the n-fold axis rotation, I for the inversion, σ_k for reflection planes and S_k for mirror rotations. Some really useful properties of point groups are: (i) each class of a point group consists of rotations or mirror rotations through the same angle. (ii) Each class contains only those rotations, or mirror rotations for which the axes can be mapped into each other with transformations belonging to the group.

However, in condensed matter we are often interested in the **space group** G, which describes any of the ways in which a crystal can be transformed without seeming to change the position of its atoms. Unlike point groups, which consist solely of rotations and rotoinversions, space groups also can include translations along crystallographic axes, point group and non-symmorphic operations (combinations of point group operation with fractional lattice translation).

3.3.1 *Irreducible representations of the translation group*

The set of Bravais lattice translations is always a subgroup of the space group. In this section we consider the irreducible representations of the translation group. Since the translation group $T_{\mathbf{a}}$ is abelian, we already discussed (Sec. 3.2.4) that the number of irreducible representations is equal to the number of elements in the group while all being unidimensional. If we denote translations along the basic lattice vectors by

$$t_{\mathbf{a}_1},\ t_{\mathbf{a}_2},\ t_{\mathbf{a}_3}, \tag{3.27}$$

then, an arbitrary element of the group $T_{\mathbf{a}}$ can be represented as

$$t_{\mathbf{a}} = t_{\mathbf{a}_1}^{n_1} t_{\mathbf{a}_2}^{n_2} t_{\mathbf{a}_2}^{n_2}, \tag{3.28}$$

where

$$\mathbf{a} = n_1\mathbf{a}_1 + n_2\mathbf{a}_2 + n_2\mathbf{a}_2. \tag{3.29}$$

The translation group $T_{\mathbf{a}}$ is a direct product of the three groups $T_{\mathbf{a}_i}$ corresponding to translations through the three crystallographic axes. In these groups, we can impose cyclic conditions, which are nothing more than the usual Born-von Karman periodic boundary conditions, as

$$t_{\mathbf{a}_i}^{L_i+1} = t_{\mathbf{a}_i}, \tag{3.30}$$

where L_i and $\mathbf{a}_i$ are the number of unit cells and the lattice unit vector on the i direction, respectively. Since $T_{\mathbf{a}_i}$ is abelian and must satisfy the cyclic property, the corresponding irreducible representations must be given by

$$e^{2\pi i \frac{m}{L_i} n}, \tag{3.31}$$

where m labels one of the L_i irreducible representations, and n is the representation for each of the L_i elements on such representation. Therefore, the irreducible representations of the group T_a with elements (3.28) are the numbers

$$e^{2\pi i(\frac{m_1}{L_1} n_1 + \frac{m_2}{L_2} n_2 + \frac{m_2}{L_2} n_2)}. \tag{3.32}$$

When defining the reciprocal lattice base at the usual form $\mathbf{a}_i \cdot \mathbf{b}_j = 2\pi\delta_{ij}$ each representations k can be written as:

$$\Gamma^k = e^{i\mathbf{k}\cdot\mathbf{a}}, \tag{3.33}$$

where $\mathbf{a}$ is a Bravais lattice vector associated with the translation and $\mathbf{k}$ is the point on the first Brilliant zone of the reciprocal space that labels the irreducible representation.

Finally, we can define the **unit vector** $\mathbf{q}_\mathbf{k}$ of a representation Γ^k as a vector that transforms under a given translation a as

$$\hat{t}_a \mathbf{q}_\mathbf{k} = e^{i\mathbf{k}\cdot\mathbf{a}} \mathbf{q}_\mathbf{k}, \tag{3.34}$$

These unit vectors are essentially Bloch functions (Sec. 1.4). Thus, here we provide an alternative proof of the Bloch's theorem from group theory arguments, where the $\mathbf{q}_\mathbf{k}$ vectors, characterized by the particular $\mathbf{k}$-irrep of the translation group under which they transform play the role of Bloch functions.

Although we have demonstrated here, for pedagogical purposes, how the irreducible representations for the translational group can be derived, fortunately, the irreps of all crystallographic point groups and space groups have already been computed and tabulated, and can be found in numerous references [66–70].

3.3.2 *Additional definitions*

This last subsection is devoted to simple, but useful definitions we will be referring during the thesis and that are related to space groups.

3.3.2.1 *The little group and the star of* **k**

The set of transformations in G which leave **k** invariant is the **little group of the vector k**, It also constitutes a subgroup of G and will be denoted as H_k. On the other hand, the set of $\{\mathbf{k_i}\}$ reciprocal vectors that are related by symmetry to **k**

$$\{\mathbf{k}_i\} \mid g\mathbf{k} = \mathbf{k}_i,\ g \in G \tag{3.35}$$

is defined as the **start of k**.

3.3.2.2 *Maximal symmetry Wyckoff position*

Wyckoff positions label the **site-symmetry group** of a point in real space akin to little group for reciprocal space. **Maximal symmetry Wyckoff positions** are those whose site-symmetry groups are maximal subgroups of the point group of the crystal. Finally, a **maximal subgroup** H of a group G is a proper subgroup, such that no proper subgroup K of G contains H strictly.

3.4 TOPOLOGY

3.4.1 *Adiabatic transport*

The adiabatic evolution introduced in section 1.1.1 can be reformulated in terms of geometry and projector operators as was first shown by Kato et al [71]. As we will see, this formulation of the adiabatic theorem allows to obtain and define topological invariants for the adiabatic evolution of a system under certain conditions.

Let us assume a Hamiltonian H, which depends on a set of *parameters* $(\lambda_i) \equiv \boldsymbol{\lambda}$, that belongs to a smooth *parameter space* $\mathcal{M}$. Thus, we can consider a **family of parametric Hamiltonians** $H(\boldsymbol{\lambda})$, which we assume has a discrete energy spectrum $E_n(\boldsymbol{\lambda})$ and eigenstates $|\psi_n(\boldsymbol{\lambda})\rangle$

$$H(\boldsymbol{\lambda})\,|\psi_n(\boldsymbol{\lambda})\rangle = E_n(\boldsymbol{\lambda})\,|\psi_n(\boldsymbol{\lambda})\rangle\,, \tag{3.36}$$

for every $\boldsymbol{\lambda}$.

Let us now assume that there exists a *collection of eigenstates* $\mathcal{R}(\boldsymbol{\lambda})$

$$\mathcal{R}(\boldsymbol{\lambda}) = \{|\psi_n(\boldsymbol{\lambda})\rangle\}, \tag{3.37}$$

so that there exists a gap $\Delta > 0$ for every $\boldsymbol{\lambda}$, implying that the spectrum of the states $\mathcal{R}(\boldsymbol{\lambda})$ are *gapped from the rest of states*. It is also useful to define the hermitian *projection operator* $P(\boldsymbol{\lambda})$ as

$$P(\boldsymbol{\lambda}) = \frac{1}{2\pi i}\oint_{C(\boldsymbol{\lambda})} \frac{1}{z - H(\boldsymbol{\lambda})}\,dz, \tag{3.38}$$

where $C(\boldsymbol{\lambda})$ is a contour in the complex plane enclosing only the $E_n(\boldsymbol{\lambda})$ energies; it is easy to check that indeed $P(\boldsymbol{\lambda})$ is a projector operator since

$$P(\boldsymbol{\lambda})\,|\psi_n(\boldsymbol{\lambda})\rangle = \frac{1}{2\pi i}\oint_{C(\boldsymbol{\lambda})} \frac{dz}{z - E_n(\boldsymbol{\lambda})}\,|\psi_n(\boldsymbol{\lambda})\rangle = \begin{cases} |\psi_n(\boldsymbol{\lambda})\rangle & \text{if } E_i(\boldsymbol{\lambda}) \in C(\boldsymbol{\lambda}), \\ 0 & \text{otherwise,} \end{cases} \tag{3.39}$$

which is clear when using Cauchy's residue theorem. Another equivalent and more direct definition for $P(\boldsymbol{\lambda})$ is:

$$P(\boldsymbol{\lambda}) = \sum_{n=1}^{N} |\psi_n(\boldsymbol{\lambda})\rangle \langle \psi_n(\boldsymbol{\lambda})| . \tag{3.40}$$

Finally, $\mathcal{R}(\boldsymbol{\lambda})$ can be related to $P(\boldsymbol{\lambda})$ as $\mathcal{R}(\boldsymbol{\lambda})$ spans the image of $P(\boldsymbol{\lambda})$:

$$\mathcal{R}(\boldsymbol{\lambda}) = \mathrm{Im}[P(\boldsymbol{\lambda})]. \tag{3.41}$$

So far, we have a well defined family of states (gapped from the rest) and a projection operator over such subspace.

3.4.1.1 *The adiabatic evolution*

Now, lets assume a path $\boldsymbol{\lambda}(t)$, with $t \in [0, \tau]$ with $\tau \to \infty$. Then, the **quantum adiabatic theorem** states that the projector $P(t)$ is approximately $P(\boldsymbol{\lambda}(t))$:

$$P(t) = U(t)P(0)U^{\dagger}(t) \approx P(\boldsymbol{\lambda}(t)), \tag{3.42}$$

where $U(t)$ *is the evolution operator*. The difference between this two operators would imply that for a time t, there is a probability of the operator $P(t)$ to contain states not in $\mathcal{R}(\boldsymbol{\lambda}(t))$. Thus, the **quantum adiabatic theorem** consists in assuming that as the system evolves, the projector $P(t)$ is always restricted to the subspace $\mathcal{R}(\boldsymbol{\lambda}(t))$.

We can now introduce an **adiabatic evolution operator** $U_A(t)$ (which drives the evolution of $P(\boldsymbol{\lambda}(t))$:

$$P(\boldsymbol{\lambda}(t)) = U_A(t)P(0)U_A^{\dagger}(t), \tag{3.43}$$

and differentiating (3.43) one can get the differential equation that $U_A(t)$ must satisfy, given by

$$i\dot{P} = \left[i\dot{U}_A U_A^{\dagger}, P \right], \tag{3.44}$$

and after using $P\dot{P}P = 0$ it can be shown that this implies:

$$\dot{U}_A U_A^{\dagger} = [\dot{P}, P] + f(H(\boldsymbol{\lambda})), \tag{3.45}$$

where f is an arbitrary function of $H(\boldsymbol{\lambda})$.

3.4.1.2 *Choice* $f(x) = x$*:*

If we choose $f(x) = x$ and solve equation (3.45), it can be shown that the difference between $U_A(t)$ and $U(t)$ is given by

$$U(t) - U_A(t) = U_A(t)\mathcal{O}\left(\frac{1}{\tau}\right), \tag{3.46}$$

which implies that if $\tau \to \infty$ both evolutions are equal, and thus (3.42) satisfies an exact equality. This, constitutes a **demonstration** of the **quantum adiabatic theorem** and also gives an explicit sense of the approximation.

3.4.1.3 *Choice* $f(x) = 0$*:*

In the following, we will use the simpler choice of $f(x) = 0$, which simplifies the equation (3.45) with solution

$$U_A(t) = \mathcal{P}\exp\left[\int_0^t \mathcal{A}_s\, dt'\right] \equiv \lim_{\Delta t\to 0} e^{\mathcal{A}_s(t_N)\Delta t} e^{\mathcal{A}_s(t_{N-1})\Delta t} \dots e^{\mathcal{A}_s(t_1)\Delta t}, \tag{3.47}$$

$$\mathcal{A}_s \equiv [\dot{P}, P], \tag{3.48}$$

where $\mathcal{P}$ means path-ordering, and as we will see $\mathcal{A}_s$ is the Berry connection. An important feature of U_A is that it is purely geometric, as can be seen from expanding the exponential in (3.47)

$$\mathcal{A}_s dt = [\dot{P}, P]dt = [\dot{\boldsymbol{\lambda}}(t)\partial_{\boldsymbol{\lambda}} P, P]dt = [\partial_{\boldsymbol{\lambda}} P, P]\dot{\boldsymbol{\lambda}}(t)dt = [\partial_{\boldsymbol{\lambda}} P, P]d\boldsymbol{\lambda}. \tag{3.49}$$

Thus, $U_A(t)$ is independent of the rate at which t is varied and only depends on the particular adiabatic path (**purely geometric quantity**), thus we can exchange $U_A(t) \leftrightarrow U_A(\boldsymbol{\lambda})$.

3.4.1.4 *Parallel transport equation*

If we restrict ourselves to states $|\phi(\boldsymbol{\lambda})\rangle \in \mathrm{Im}[P(\boldsymbol{\lambda})]$, but not necessarily eigenstates we have that

$$|\phi(\boldsymbol{\lambda})\rangle = U_A\,|\phi(0)\rangle\,, \tag{3.50}$$

from the fact that $P(\boldsymbol{\lambda})\,|\phi(\boldsymbol{\lambda})\rangle = |\phi(\boldsymbol{\lambda})\rangle$. Differentiating (3.50) we get:

$$\partial_{\boldsymbol{\lambda}}\,|\phi(\boldsymbol{\lambda})\rangle = [\partial_{\boldsymbol{\lambda}} P, P]\,|\phi(\boldsymbol{\lambda})\rangle = [\partial_{\boldsymbol{\lambda}} P, P]P\,|\phi(\boldsymbol{\lambda})\rangle\,, \tag{3.51}$$

where in the third equality we introduced a projector P (with no effect), which allows us to rewrite (3.51) as

$$[\partial_{\boldsymbol{\lambda}} - (\partial_{\boldsymbol{\lambda}} P)P]\,|\phi(\boldsymbol{\lambda})\rangle = 0. \tag{3.52}$$

Equation (3.51) is the **parallel transport equation** and it tells us that under adiabatic evolution, the projection of states into the subspace of interest does not change. The quantity $[\partial_{\boldsymbol{\lambda}} P, P]P = (\partial_{\boldsymbol{\lambda}} P)P$ is the **adiabatic (Berry) connection**, which precisely coincides with $\mathcal{A}_s$ presented in (3.48).

The Berry connection, can be written in a more conventional form in a basis given by $\{|\psi_n(\boldsymbol{\lambda})\rangle\}$, so that $P(\boldsymbol{\lambda})$ can be written as in (3.40) and $|\phi(\boldsymbol{\lambda})\rangle$ is given by

$$|\phi(\boldsymbol{\lambda})\rangle = \sum_n a_n(\boldsymbol{\lambda})\,|\psi_n(\boldsymbol{\lambda})\rangle\,. \tag{3.53}$$

Then, we can write equation (3.52) as

$$\partial_{\boldsymbol{\lambda}} a_n - i\sum_{m=1}^{N} \mathbf{A}_{nm}(\boldsymbol{\lambda})a_m = 0, \tag{3.54}$$

$$\mathbf{A}_{nm}(\boldsymbol{\lambda}) \equiv i\,\langle\psi_n(\boldsymbol{\lambda})|\partial_{\boldsymbol{\lambda}}\psi_m(\boldsymbol{\lambda})\rangle \tag{3.55}$$

where $\mathbf{A}_{nm}(\boldsymbol{\lambda})$ is the **Berry connection** in the form that is usually presented. This equation, tells use how the coefficients $a_n(\boldsymbol{\lambda})$ that define certain state $|\phi(\boldsymbol{\lambda})\rangle$ change along the adiabatic evolution. Whether to use $\mathcal{A}_s(\boldsymbol{\lambda})$ or $\mathbf{A}_{nm}(\boldsymbol{\lambda})$ depends on whether one considers that the adiabatic transformation acts on the basis or on the coordinates.

3.4.1.5 *Holonomy*

Now that we have and explicit expression for the evolution of the coefficients that define a state $|\phi(\boldsymbol{\lambda})\rangle$, we can solve (3.54) and get an explicit expression for $a_n(\boldsymbol{\lambda})$

$$\begin{aligned} W_{nm}(\boldsymbol{\lambda}) &\equiv \mathcal{P} e^{i\int_0^{\boldsymbol{\lambda}} \mathbf{A}_{nm}(\boldsymbol{\lambda}')\, d\boldsymbol{\lambda}'} \\ a_n(\boldsymbol{\lambda}) &= \mathcal{P} e^{i\int_0^{\boldsymbol{\lambda}} \mathbf{A}_{nm}(\boldsymbol{\lambda}')\, d\boldsymbol{\lambda}'} a_m(0) \equiv W_{nm}(\boldsymbol{\lambda}) a_m(0), \end{aligned} \tag{3.56}$$

where the matrix $W_{nm}(\boldsymbol{\lambda})$ defines the evolution of the coefficients, and therefore, the evolution of the state. Moreover, it can be shown that if we choose $|\phi(0)\rangle = |\psi_m(0)\rangle$ in (3.53), together with (3.56) we have that W_{nm} is given by

$$W_{nm}(\boldsymbol{\lambda}) = \langle \psi_n(\boldsymbol{\lambda}) | U_A | \psi_m(0) \rangle \,, \tag{3.57}$$

and thus can be essentially understood as the matrix form of the **adiabatic evolution operator** introduced in equation (3.43) in a particular basis, which evolves the system constrained to the subspace $\mathcal{R}(\boldsymbol{\lambda})$.

However, this matrix is not invariant under a basis rotation $U(N)$ unless we consider a closed path. This specific case of the adiabatic evolution matrix W_{nm} along a closed path is called the **holonomy** of the adiabatic connection around that path, with the spectrum of the holonomy being basis independent.

It is useful to define an auxiliary way of defining W that does not depend on the basis states. Thus, we define the operator $\mathcal{W}(\boldsymbol{\lambda})$

$$\mathcal{W}(\boldsymbol{\lambda}) \equiv P(\boldsymbol{\lambda}) U_A P(0), \tag{3.58}$$

which can be shown that is equivalently written as

$$\mathcal{W}(\boldsymbol{\lambda}) = \prod_{\boldsymbol{\lambda}'}^{\boldsymbol{\lambda} \leftarrow 0} P(\boldsymbol{\lambda}'), \tag{3.59}$$

and where the product is path-ordered, which forces the parallel transport on $\mathcal{R}$. It can be shown with (3.57) that $\mathcal{W}$ and W share the same spectrum, and W_{nm} can be understood as a matrix element of $\mathcal{W}$ in the subspace $\mathcal{R}(\boldsymbol{\lambda})$.

3.4.2 *Parametrization of the Bloch Hamiltonians*

So far, we have discussed the adiabatic evolution of quantum states under a Hamiltonian that changes by means of a varying parameter $\hat{H}(\boldsymbol{\lambda})$. However, as we are interested in applying this formalism to particles (electrons, phonons,

etc.) in crystals, we must identify which is the parameter that defines the family of parametric Hamiltonians. As we will see, the parameter of interest in this cases is rooted in the intrinsic periodicity of crystals.

As introduced in section 1.4 and demonstrated in 3.3.1, when the Hamiltonian is periodic in real-space, the Bloch's theorem allows to label the eigenstates of the Hamiltonian $\hat{H}$ with the quantum numbers $(n, \mathbf{k})$, where n labels the band-index and $\mathbf{k}$ is a reciprocal space vector belonging to the first Brillouin zone. Hence, the eigenstate problem of the Hamiltonian can be written

$$\hat{H}\psi_{n\mathbf{k}}(\mathbf{r}) = E_{n\mathbf{k}}\psi_{n\mathbf{k}}(\mathbf{r}), \tag{3.60}$$

where the eigenstates $\psi_{n\mathbf{k}}(\mathbf{r})$ can be decomposed as (1.105). This allows us to define the **Bloch Hamiltonian** as

$$\hat{H}(\mathbf{k}) \equiv e^{-i\mathbf{k}\cdot\mathbf{r}}\hat{H}e^{i\mathbf{k}\cdot\mathbf{r}}, \tag{3.61}$$

which satisfies the new eigenvalue problem

$$\hat{H}(\mathbf{k})u_{n,\mathbf{k}} = E_{n,\mathbf{k}}u_{n,\mathbf{k}}. \tag{3.62}$$

It can be shown that the specific form of $\hat{H}(\mathbf{k})$ is given by

$$\begin{aligned}\hat{H}(\mathbf{k}) &= \frac{1}{2m}(\hbar\mathbf{k} + \hat{\mathbf{p}})^2 + V(\hat{\mathbf{r}}) \\ &= \frac{\hat{\mathbf{p}}^2}{2m} + \frac{\hbar\mathbf{k}\cdot\hat{\mathbf{p}}}{m} + \frac{(\hbar\mathbf{k})^2}{2m} + V(\hat{\mathbf{r}}),\end{aligned} \tag{3.63}$$

which comes as a direct consequence of acting with $\hat{\mathbf{p}}$ over $e^{i\mathbf{k}\cdot\mathbf{r}}$ in equation (3.61).

It is often convenient to work in a fixed basis of orbitals. If we define the ket $|u_{n\mathbf{k}}\rangle$ as the column vector obtained by projecting $u_{n\mathbf{k}}(\mathbf{r})$ over the basis of orbitals, we can rewrite (3.62) as

$$\hat{H}(\mathbf{k})\,|u_{n\mathbf{k}}\rangle = E_{n\mathbf{k}}\,|u_{n\mathbf{k}}\rangle\,, \tag{3.64}$$

which naturally splits the original Hamiltonian in $\mathbf{k}$-blocks. However, we can also consider the Bloch Hamiltonian $\hat{H}(\mathbf{k})$ as a family of Hamiltonians that depend on the parameter $\mathbf{k}$ belonging to the 1BZ, as the one studied in section 3.4.1. This allows to study geometrical aspects of the adiabatic evolution of a quantum state as $\mathbf{k}$ is varied. A fair question would be whether such adiabatic evolution occurs in a real system or if it is merely a mathematical abstraction. As we will see, it turns out it does. For example, the electronic response to an electric field (the polarization) is described by a Hamiltonian $\hat{H}$ that evolves precisely in this manner.

3.4.3 *The Berry phase and polarization*

There is a direct connection between the adiabatic variation of $\mathbf{k}$ of the Bloch Hamiltonian Bloch's (3.61) and the response of the real-space charge distribution when in presence of an electric field, or said in other words, between the adiabatic evolution and the polarization.

Let us assume a one-dimensional periodic potential $V(x+a) = V(x)$ in a Bloch Hamiltonian as (3.63) with a projector over the N occupied bands $P(k)$ defined as:

$$P(k) = \sum_{n=1}^{N} |\psi_{nk}\rangle \langle \psi_{nk}| . \tag{3.65}$$

Now, lets consider the effect of a small uniform electric field E, that can be attributed to a vector potential of the form $A(t) = -Et$. This, vector potential appears in the Hamiltonian $\hat{H}(k)$ at minimal coupling as

$$\hat{H}(k,t) = \frac{1}{2m}[\hat{p} + k - qA(t)]^2 + V(x) \equiv \frac{1}{2m}[\hat{p} + k(t)]^2 + V(x) = \hat{H}(k(t)), \tag{3.66}$$

where we have redefined $k(t) \equiv k - qA(t) = k + qEt$.

Thus, we have successfully **mapped** the problem of an electron moving under the influence of an electric field E to a problem of evolution within a parametric family of Hamiltonians $\hat{H}(k(t))$.

If we want to compare to the general scenario, where we had $\boldsymbol{\lambda}(t)$, with $t \in [0,\tau]$. Now, $k(t') = k(qEt)$, and since $t' \in [0,\tau]$, then τ/qE, plays the role of τ for t in this case. This implies that if we recall expression (3.46), we need for the field to be small enough for the adiabatic approximation to hold.

Now, we can infer how an initial state $\psi_n(x, t=0) = e^{ikx}u_{nk}(x)$ evolves under the presence of an electric field. Since $\psi_n(x,t)$ is totally determined by its coefficients when written as (3.53), and the evolution of the coefficient is given by expression (3.56). We can write $\psi_n(x,t)$ as

$$\psi_n(x,t) = e^{ik(t)x}W_{nm}(t)u_{mk(t)}(x) \tag{3.67}$$

where W is given by (3.56) and is equivalent to the **non-abelian Berry phase**. In summary, we have showed how something as physical as the evolution of a quantum state under the presence of an electric field E, is defined by the geometric properties of the eigenvectors of $\hat{H}(k)$.

3.4.3.1 *Relation between Berry phase and position operator*

It can be also shown that $W(t)$ is related to the position operator. In a system of length L (with periodic boundary conditions) the average position can be related to the operator $\mathfrak{B}$ defined as

$$\mathfrak{B} = e^{2\pi i\hat{X}/L}. \tag{3.68}$$

It can be shown, that the mean value of $\mathfrak{B}$ for a ground state given by a Slater determinant of the occupied states is given by

$$\langle \mathfrak{B} \rangle = \prod_k \det\left[\int_0^L dx\, u^*_{nk}u_{m(k-2\pi/L)}\right] = \det(W(2\pi/a)). \tag{3.69}$$

Thus, the gauge-invariant determinant of W across a closed path is related to the center of mass within the unit cell. This relationship underscores the

profound link between the geometry of adiabatic evolution and electron localization.

This can be seen more clearly in terms of polarization P_e, which from Maxwell's equations must satisfy

$$\dot{P}_e = q \langle v \rangle , \tag{3.70}$$

where $\langle v \rangle$ is the mean velocity. It is shown in [72], that the mean velocity is precisely given by

$$\frac{d}{dt}\frac{1}{2\pi}\mathrm{Im}\left[\log \langle \mathfrak{B} \rangle\right] = \langle v \rangle . \tag{3.71}$$

An therefore, putting together equations (3.70) and (3.71) , one can see that

$$P_e = \frac{q}{2\pi}\mathrm{Im}\left[\log \langle \mathfrak{B} \rangle\right] = \frac{q}{2\pi}\mathrm{Im}\left\{\log\left[\det(W(2\pi/a))\right]\right\}, \tag{3.72}$$

so that the polarization is given by the holonomy (the evolution across a closed path in the BZ), which as shown is determined by the Berry phase.

3.4.4 *Wannier functions and charge localization*

In the previous section we discussed how the geometry of the eigenstate space is related to the mean charge localization in real space, by establishing a relation between Berry phase and polarization. On the other hand, we already discussed in section 1.5, that Wannier functions constitute an ideal basis for analyzing real space properties. While we already introduced the basic aspects of Wannier functions in section 1.5, we focus now in studying different kinds of real space localization and their implications.

3.4.4.1 *Exponentially localized Wannier functions*

From equation (1.120) it can be shown that the n-derivative $\partial^n_{k_i}$ with respect to k_i of a Bloch-like function $\psi_{n\mathbf{k}}(\mathbf{r})$ (it does not matter whether is rotated with $U(\mathbf{k}) \to \tilde{\psi}_{n\mathbf{k}}$ or not) holds

$$\left|\partial^n_{k_i}\tilde{\psi}_{n\mathbf{k}}(\mathbf{r})\right| = \left|\sum_{\mathbf{T}} (iT_i)^n e^{i\mathbf{k}\cdot\mathbf{T}} w_n(\mathbf{r}-\mathbf{T})\right| \leqslant \sum_{\mathbf{T}} |T_i^n w_n(\mathbf{r}-\mathbf{T})| , \tag{3.73}$$

which implies that if $w_n(\mathbf{r}-\mathbf{T})$ decays faster than any power of $(\mathbf{r}-\mathbf{T})$, $\psi_{n\mathbf{k}}$ will be smooth in $\mathbf{k}$ to any order. Thus, the *exponential localization* of Wannier functions is a necessary condition for obtaining smooth functions $\psi_{n\mathbf{k}}$ in reciprocal space.

It also was shown in [73, 74] that the opposite is true. Given that $\psi_{n\mathbf{k}}$ is an analytic function of $\mathbf{k}$, then the Wannier functions $w_n(\mathbf{r}-\mathbf{T})$ will decay exponentially as $|\mathbf{r}-\mathbf{T}| \to \infty$.

Thus, the problem of finding a smooth gauge $U(\mathbf{k})$ in reciprocal space is equivalent to finding the gauge that produces exponentially localized Fourier transforms in real space.

3.4.4.2 *Charge localization*

The relation between Berry phase and polarization we have shown in section 3.4.3.1 can be reinterpreted in terms of Wannier functions. Recovering the relation (3.69) an using the definition for W given in (3.56) and for A given in (3.55) the following relation is obtained

$$\text{Im } \log\langle\mathfrak{B}\rangle = \text{tr}\oint dk A(k) = \sum_{n=1}^{N_{occ}} \int_0^{2\pi} dk \overbrace{\int_{cell} i\, u_{nk}^*(x)\partial_k u_{nk}(x)\, dx}^{A_{nn}(k)}. \tag{3.74}$$

Then, by transforming $u_{n\mathbf{k}}$ as described in (1.123) it can be shown that

$$\text{Im}\log\langle\mathfrak{B}\rangle = 2\pi \sum_{m=1}^{N_{occ}} \langle w_m(\mathbf{r})|x|w_m(\mathbf{r})\rangle + 2\pi n, \tag{3.75}$$

and hence, by recovering equation (3.72) we can now write the polarization as

$$P_e = q\left(\sum_{m=1}^{N_{occ}} \langle w_m(\mathbf{r})|x|w_m(\mathbf{r})\rangle + n\right), \tag{3.76}$$

so that it is explicitly related to the average charge center displacement with respect to the origin of the unit cell (written in terms of Wannier functions).

The integer n is given by the particular choice of the unitary transformation $U(\mathbf{k})$ from the $u_{n\mathbf{k}}$ basis to the rotated basis $u_{n\mathbf{k}}^W$ and signals that the Berry phase is only define modulus 2π. However, there is no contradiction here since the same is true for the charge center, which is only defined up to a translation of n unit cells.

3.4.4.3 *Hybrid Wannier functions*

As we will see, the concept of hybrid Wannier functions will be useful when analyzing the spectrum of an holonomy across a closed path. Akin to regular Wannier functions, they are related to smooth states $\tilde{\psi}_{n\mathbf{k}}(\mathbf{r})$ via the following transformation

$$w_{n\mathbf{T}_\perp}(\mathbf{r}, \mathbf{k}_\parallel) = \frac{1}{\sqrt{N_\perp}} \sum_{\mathbf{k}_\perp} e^{-i\mathbf{k}_\perp\cdot\mathbf{T}_\perp} \tilde{\psi}_{n\mathbf{k}}(\mathbf{r}). \tag{3.77}$$

However, in contrast to regular Wannier functions, which are localized in all directions, hybrid Wannier functions are localized along the perpendicular direction $\perp$ to certain $\mathbf{k}_\parallel$ vector, while still being Bloch like or delocalized in direction $\parallel$.

3.4.5 *The projected position operator*

In the previous section 3.4.3 we used the average position operator $\hat{X}$ in order to establish a relation between the Berry phase and the polarization, we

are now instead interested of what can be said from the individual particle position operators $\hat{x}$, or at least, their projected form

$$P\mathbf{x}P, \tag{3.78}$$

which as we will see, has an intimate relation with the holonomy along a closed path in parameter space.

If we take an state $|f\rangle$ that belongs to the image of $P(\mathbf{k})$ so that

$$|f\rangle = \sum_{n\mathbf{k}} f_{n\mathbf{k}} |\psi_{n\mathbf{k}}\rangle , \tag{3.79}$$

and we act over it with the projector position operator (later projected over $\langle\psi_{n\mathbf{k}'}|$) it is shown in [72] that this can be written as

$$\langle\psi_{n\mathbf{k}'}|Px_iP|f\rangle = i\partial_{k_i'} f_{n\mathbf{k}'} + A^i_{nm}(\mathbf{k}')f_{m\mathbf{k}'}, \tag{3.80}$$

where $A^i_{nm}(\mathbf{k})$ is the Berry connection in the k_i direction introduced in (3.55) and now takes the form

$$A^i_{nm}(\mathbf{k}) = i\langle u^*_{n\mathbf{k}}|\partial_{k_i} u_{m\mathbf{k}}\rangle = \int_{\text{cell}} u_{n\mathbf{k}}(\mathbf{r})\partial_{k_i} u_{m\mathbf{k}}(\mathbf{r})\, d\mathbf{r}. \tag{3.81}$$

Notice how equation (3.80) is closely related to the parallel transport equation (3.54), which can be rewritten as $-iP\mathbf{x}P|f\rangle = 0$, and hence must be intimately related to the adiabatic evolution operator $\mathcal{W}$.

Now that we know how $P\mathbf{x}P$ acts on states, we can inquire about its eigenvectors. We are therefore interested in eigenstates $|\phi\rangle$ of $Px_\perp P$ that satisfy

$$Px_\perp P|\phi\rangle = \phi|\phi\rangle . \tag{3.82}$$

We take a trial solution of the form

$$|\phi\rangle = e^{ik_\perp \phi} W_{mn}(k_\perp) f_{n_0} |\psi_{n\mathbf{k}}\rangle , \tag{3.83}$$

where $k_\perp$ is a particular direction defining a path in $\mathbf{k}$-space from $\mathbf{k}_0 = 0$ to $(k_\perp/2\pi)\mathbf{G}_\perp$, with $\mathbf{G}_\perp$ a reciprocal lattice vector in direction $\perp$; and $W_{nm}(k_\perp)$ is the holonomy matrix of the form (3.57).

By introducing the trial (3.83) in the eigenvalue problem (3.82) and knowing the action of $Px_\perp P$ over the coefficients f_{n0} given by (3.80), it can be shown that the conditions for the coefficients defining our trial solution reduce to

$$W_{mn}(2\pi)f_{n0} = e^{i2\pi\phi} f_{m0}. \tag{3.84}$$

Thus, $\{f_{n0}\}$ in (3.83) must be an eigenvector of $W(2\pi)$ with eigenvalue $e^{i2\pi\phi}$. We may conclude then that the spectrum $\{\phi\}$ of Px_iP matches the spectrum of $(1/2\pi)\text{Im}\ \log W_{mn}(\mathbf{k}_0 \to \mathbf{k}_0 + \mathbf{G}_i)$. Hence, *the spectrum of the holonomy is related to the spectrum of the "positions" (projected positions) of the electrons in the crystal*.

Moreover, it can be shown that the coefficients that satisfy the redefined eigenvalue problem (3.84), imply that functions of the form (3.83) are hybrid

Wannier functions (3.77). Since eigenstates of Px_iP are maximally localized in x_i, also are the resulting hybrid Wannier functions, implying that the corresponding antitransformed Bloch wavefunctions are smooth with respect to k_i.

In summary, while the Berry phase included information about the average electronic position, the holonomy has information about the position of individual electrons.

3.4.6 *Wilson loops*

In the previous sections we have shown that there exists a close relation between the adiabatic evolution of Bloch functions in reciprocal space, and the localization properties of the real-space Wannier functions. This relationship between the geometry of reciprocal space and real-space localization can be more thoroughly described in terms of Wilson loops. In order to do so, we will start from a set of tight-binding orbitals in reals space in order to carefully construct the necessary ingredients to define the Wilson loop.

Let us consider a set of orthogonal orbitals $\{|\phi_{\sigma\mathbf{T}}\rangle\}$ such that

$$\langle \mathbf{r}|\phi_{\sigma\mathbf{T}}\rangle = \phi_{\sigma\mathbf{T}}(\mathbf{r}) = \phi_\sigma(\mathbf{r}-\mathbf{T}-\mathbf{r}_\sigma), \tag{3.85}$$

where $\mathbf{r}_\sigma$ is the position of the orbital within the primitive cell, and σ denotes a collection of quantum numbers describing the different orbitals. The Bloch functions $\{|\chi_{\sigma\mathbf{k}}(\mathbf{r})\rangle\}$ corresponding to this orbitals can be built as

$$\chi_{\sigma\mathbf{k}}(\mathbf{r}) = \frac{1}{\sqrt{N}}\sum_{\mathbf{T}} e^{i\mathbf{k}\cdot(\mathbf{T}+\mathbf{r}_\sigma)}\phi_{\sigma\mathbf{T}}(\mathbf{r}), \tag{3.86}$$

where N is the number of cells and their cell periodic part defined as

$$\phi_{\sigma\mathbf{k}}(\mathbf{r}) \equiv e^{-i\mathbf{k}\cdot\mathbf{r}}\chi_{\sigma\mathbf{k}}(\mathbf{r}) = \frac{1}{\sqrt{N}}\sum_{\mathbf{T}} e^{i\mathbf{k}\cdot(\mathbf{T}+\mathbf{r}_\sigma-\mathbf{r})}\phi_{\sigma\mathbf{T}}(\mathbf{r}). \tag{3.87}$$

Then, the eigenfunctions $\{\psi_{n\mathbf{k}}\}$ of the Hamiltonian can be expanded in this basis as linear combinations of these Bloch waves as

$$\psi_{n\mathbf{k}}(\mathbf{r}) = \sum_\sigma u^\sigma_{n\mathbf{k}}\chi_{\sigma\mathbf{k}}(\mathbf{r}) = \frac{1}{\sqrt{N}}\sum_{\sigma\mathbf{T}} e^{i\mathbf{k}\cdot(\mathbf{T}+\mathbf{r}_\sigma)}\phi_{\sigma\mathbf{T}}(\mathbf{r}), \tag{3.88}$$

with the cell periodic part $u_{n\mathbf{k}}(\mathbf{r})$ of $\psi_{n\mathbf{k}}(\mathbf{r})$ given by

$$u_{n\mathbf{k}}(\mathbf{r}) = e^{-i\mathbf{k}\cdot\mathbf{r}}\sum_\sigma u^\sigma_{n\mathbf{k}}\chi_{\sigma\mathbf{k}}(\mathbf{r}) = \sum_\sigma u^\sigma_{n\mathbf{k}}\phi_{\sigma\mathbf{k}}(\mathbf{r}). \tag{3.89}$$

A final constraint must be imposed for the eigenstates $\psi_{n\mathbf{k}}(\mathbf{r})$ to be periodic for $\mathbf{k}\to\mathbf{k}+\mathbf{G}$ which implies that

$$u^\sigma_{n\mathbf{k}+\mathbf{G}} = e^{-i\mathbf{G}\cdot\mathbf{r}_\sigma}\delta_{\sigma\sigma'}u^{\sigma'}_{n\mathbf{k}} \equiv \left[V^{-1}(\mathbf{G})\right]_{\sigma\sigma'}u^\sigma_{n\mathbf{k}}. \tag{3.90}$$

Now, the parametric family of Hamiltonians $h(\mathbf{k})$ can be written in the basis $\{\phi_{\sigma\mathbf{k}}\}$ as:

$$h_{\sigma\sigma'}(\mathbf{k}) = \langle \phi_{\sigma\mathbf{k}} | \hat{H}(\mathbf{k}) | \phi_{\sigma'\mathbf{k}} \rangle \,, \tag{3.91}$$

where $\hat{H}(\mathbf{k})$ is defined as (3.61). Then, the Schrodinger equation can be written as

$$h(\mathbf{k}) \, |u_{n\mathbf{k}}\rangle = E_{n\mathbf{k}} \, |u_{n\mathbf{k}}\rangle \,, \tag{3.92}$$

where the ket $|u_{n\mathbf{k}}\rangle$ is the column vector of coefficients $u^{\sigma}_{n\mathbf{k}}$ introduced in equations (3.88) and (3.89).

Now that we have defined a proper basis for the problem we can easily define the projector over the subspace of interest

$$P(\mathbf{k}) \equiv \sum_{n=1}^{N} |u_{n\mathbf{k}}\rangle \, \langle u_{n\mathbf{k}}| \,, \tag{3.93}$$

which allows us to consider the holonomy matrix $W_{\mathcal{C}}$ over a smooth contour $\mathcal{C}$ in reciprocal space from $\mathbf{k}_0$ to $\mathbf{k}_f$. Using the expression (3.59) for the holonomy, the matrix elements in this basis are given by

$$W^{nm}_{\mathcal{C}} = \langle u_{n\mathbf{k}_f} | \mathcal{W}_{\mathcal{C}} | u_{m\mathbf{k}_0} \rangle = \langle u_{n\mathbf{k}_f} | \prod_{\mathbf{k}}^{\mathcal{C}} P(\mathbf{k}) | u_{m\mathbf{k}_0} \rangle \,. \tag{3.94}$$

If we recall, by construction $\mathcal{W}_{\mathcal{C}}$ was introduced mainly because of its interest for being basis (gauge) invariant, however, the final and initial states are not and thus, under gauge transformations of the form $|u'_{n\mathbf{k}}\rangle = U_{nm}(\mathbf{k}) \, |u_{m\mathbf{k}}\rangle$, $W_{\mathcal{C}}$ transforms as

$$W'_{\mathcal{C}} = U^{\dagger}(\mathbf{k}_f) W_{\mathcal{C}} U(\mathbf{k}_0), \tag{3.95}$$

which implies that the spectrum of $W_{\mathcal{C}}$ is only gauge invariant when $\mathcal{C}$ is closed loop.

Thus, the adiabatic evolution $\mathcal{W}_{\mathcal{C}}$ for a closed loop is referred as the holonomy of the closed loop or **Wilson loop**. As a direct consequence, the eigenvectors of the Wilson loop are also directly related to the ones of the projected position operator and hence, the spectrum related to the charge centers of hybrid Wannier functions.

3.4.6.1 *Effects of symmetry*

The symmetries of Wilson loops can be studied by noting that under a space group symmetry operation of the form $h = \{R, \mathbf{t}\}$ the coefficients $u^{\sigma}_{n\mathbf{k}}$ change as

$$u^{\sigma}_{n\mathbf{k}} \to M_{\sigma\sigma'}(R) u^{\sigma'}_{n(R\mathbf{k})} e^{-i(R\mathbf{k})\cdot\mathbf{t}} \equiv S^{\sigma\sigma'}_{\mathbf{k}} u^{\sigma'}_{n(R\mathbf{k})}, \tag{3.96}$$

where $M(R)$ is the appropriate representation of R that describes the transformation of the basis $\phi_{n\mathbf{k}}(\mathbf{r})$. By doing such analysis it can be shown that under two of the most fundamental symmetries, inversion and time reversal symmetry, the following Wilson loops are related by symmetry

$$I \, \mathcal{W}_{\mathbf{g}}(\mathbf{k}_\perp) I^{\dagger} = \mathcal{W}^{\dagger}_{\mathbf{g}}(-\mathbf{k}_\perp), \tag{3.97}$$

$$\mathcal{T} \mathcal{W}_{\mathbf{g}}(\mathbf{k}_\perp) \mathcal{T}^{-1} = \mathcal{W}_{-\mathbf{g}}(-\mathbf{k}_\perp), \tag{3.98}$$

where the subindex $\mathbf{g}$, is the primitive reciprocal lattice vector that defines the closed loop $\mathbf{k}_0 \to \mathbf{k}_0 + \mathbf{g}$. The Wilson loop does not depend on shifts of the basepoint $\mathbf{k}_0$ parallel to $\mathbf{g}$, but it does depend of shifts perpendicular $\perp$ to $\mathbf{g}$, thus the dependence on $\mathbf{k}_\perp$.

3.4.7 *Wilson loop of topological bands and Chern number*

While in 1D the concept of "regular" Wannier functions and hybrid Wannier Functions coincide, implying that the Wannier centers are related to the spectrum of the Wilson loop $W_{\mathbf{g}}$ as shown in (3.84), in higher dimensions this is generally not true since the projected position operators along different directions do not commute

$$\left[P x_i P, P x_j P\right] \neq 0. \tag{3.99}$$

Therefore, in general there is not a set of common eigenstates. To analyze in which specific cases such set of eigenstates exists we analyze the action of the commutator over a general trial state $|f\rangle = \sum_{n\mathbf{k}} f_{n\mathbf{k}} |\psi_{n\mathbf{k}}\rangle$, where $\{|\psi_{n\mathbf{k}}\rangle\}$ are the eigenfunctions of the Hamiltonian.

$$\left[P x_i P, P x_j P\right] |f\rangle = i \sum_{\mathbf{k},mn} \Omega^{ij}_{nm}(\mathbf{k}) f_{m\mathbf{k}} |\psi_{n\mathbf{k}}\rangle\,, \tag{3.100}$$

$$\begin{aligned} \Omega^{ij}_{nm}(\mathbf{k}) &\equiv \partial_i A^j_{nm}(\mathbf{k}) - \partial_j A^i_{nm}(\mathbf{k}) - i\left[A^i(\mathbf{k}), A^j(\mathbf{k})\right]_{nm}, \\ &= [\nabla_{\mathbf{k}} \times \mathbf{A}_{nm}(\mathbf{k})]^{ij} - i\left[A^i(\mathbf{k}), A^j(\mathbf{k})\right]_{nm}, \end{aligned} \tag{3.101}$$

where the tensor $\Omega^{ij}_{nm}(\mathbf{k})$ is denoted as the **Berry curvature** and $A_{nm}(\mathbf{k})$ the non-abelian Berry connection. Thus, in order for a common basis to exist for $P x_i P$ and $P x_j P$, the Berry curvature must vanish for every value $\mathbf{k}$.

We can conclude that in general, hybrid Wannier functions (eigenstates of projected position operator), will not coincide with maximally localized Wannier functions (designed to be localized in all directions). Moreover, while unique hybrid Wannier functions exist for any gapped projector $P(\mathbf{k})$, Wannier functions are not unique (they are not eigenvalues of a well defined problem as the case for the hybrid ones) and may not be exponentially localizable.

From the relation (3.100), one can already sense that there must be a relation between topology and the possibility for finding hybrid Wannier functions that are exponentially localized in different directions.

3.4.7.1 *Relation between the Wilson loop and the Berry curvature*

The relation between the holonomy (the Wilson loop) of the connection and its curvature is given by the Ambrose-Signer theorem. When, considering a closed loop defined by an infinitesimal parallelogram

$$\partial\mathcal{M} = \{\mathbf{k}_0 \to \mathbf{k_0} + \delta\mathbf{k}_1 \to \mathbf{k}_0 + \delta\mathbf{k}_1 + \delta\mathbf{k}_2 \to \mathbf{k}_0 + \delta\mathbf{k}_2 \to \mathbf{k}_0\} \tag{3.102}$$

in reciprocal space, the Ambrose-Signer theorem relates the Wilson loop along the boundary to the Berry curvature

$$i\Omega^{12}_{nm}(\mathbf{k}_0)\delta\mathbf{k}_1\delta\mathbf{k}_2 = \log W_4W_3W_2W_1 + \mathcal{O}(\delta\mathbf{k}^3), \tag{3.103}$$

where the W_i refer to the four sides of the parallelogram. Then, it is useful to take the trace of (3.103) as it reduces the Berry curvature to the curl of the Berry connection as well as allowing the commutation of the W_i evolutions.

$$i\,\mathrm{tr}\left[\Omega^{12}_{nm}(\mathbf{k}_0)\delta\mathbf{k}_1\delta\mathbf{k}_2\right] = \mathrm{tr}\left[\log W_4W_3W_2W_1\right] = \log\left[\det W_4W_3W_2W_1\right]. \tag{3.104}$$

3.4.7.2 *The Chern number*

We first focus on the left hand side of (3.104) and by considering a closed path across a finite region $\mathcal{M}$ in the Brillouin zone, we can break down the region in small patches and get

$$\begin{aligned}\frac{1}{2\pi}\int_{\mathcal{M}} \mathrm{tr}(\Omega^{12}_{nm})\,dk_1\,dk_2 &= \frac{1}{2\pi}\int_{\mathcal{M}} \partial_{k_1}\mathrm{tr}A^2_{nm} - \partial_{k_2}\mathrm{tr}A^1_{nm}\,dk_1\,dk_2 \\ &= \frac{1}{2\pi}\oint_{\partial\mathcal{M}} \mathrm{tr}\mathbf{A}_{nm}\cdot d\mathbf{l},\end{aligned} \tag{3.105}$$

where we have used stokes theorem, to turn the integral of the flux of the Berry curvature Ω through the surface $\mathcal{M}$ into an integral of the connection $\mathbf{A}$ across the boundary of the surface $\partial\mathcal{M}$. Thus, if $\mathcal{M}$ is a closed surface within the first Brillouin zone, the integral vanishes unless there are discontinuities in $\mathrm{tr}\mathbf{A}(\mathbf{k})$.

For example, if we consider $\mathcal{M}$ to be a *closed* region in the 1BZ (as a sphere), in order to apply the same procedure as in (3.105), we need to divide the sphere in two subsections $\mathcal{M}_1$ and $\mathcal{M}_2$. Then, the set of functions defined for both surfaces has to match at the boundary between them (for example the equator) up to a unitary transformation $U(\mathbf{k})$

$$|\psi^{\mathcal{M}_2}_{n\mathbf{k}}\rangle = U_{nm}(\mathbf{k})\,|\psi^{\mathcal{M}_1}_{n\mathbf{k}}\rangle\,. \tag{3.106}$$

This implies that the Berry connections for both sets of functions are related by

$$\mathbf{A}^{\mathcal{M}_2} = U^\dagger\mathbf{A}^{\mathcal{M}_1}U + iU^\dagger\nabla U \tag{3.107}$$

and hence, their traces by

$$\mathrm{tr}\mathbf{A}^{\mathcal{M}_2} = \mathrm{tr}\mathbf{A}^{\mathcal{M}_1} - \nabla\overbrace{(\mathrm{Im}\log\det U)}^{\equiv\varphi} = \mathrm{tr}\mathbf{A}^{\mathcal{M}_1} - \nabla\varphi, \tag{3.108}$$

where the difference between the traces has been gathered in the $\boldsymbol{\nabla}\varphi(\mathbf{k})$ term.

The integral of the Berry curvature to the full sphere $\mathcal{M}$ can be now written as

$$\begin{aligned}\frac{1}{2\pi}\int_{\mathcal{M}} \mathrm{tr}(\Omega)\,d^2k &= \frac{1}{2\pi}\int_{\mathcal{M}_1} \mathrm{tr}(\Omega)\,d^2k + \frac{1}{2\pi}\int_{\mathcal{M}_2} \mathrm{tr}(\Omega)\,d^2k \\ &= \frac{1}{2\pi}\oint_{\partial\mathcal{M}} \mathrm{tr}(\mathbf{A}^{\mathcal{M}_1})\cdot d\mathbf{l} - \frac{1}{2\pi}\oint_{\partial\mathcal{M}} \mathrm{tr}(\mathbf{A}^{\mathcal{M}_2})\cdot d\mathbf{l} \\ &= \frac{1}{2\pi}\oint_{\partial\mathcal{M}} \nabla\varphi\cdot d\mathbf{l}\end{aligned} \tag{3.109}$$

Hence, the integral of the Berry curvature for a closed regions vanishes unless there is a discontinuity in the gauge $U(\mathbf{k})$ across $\partial\mathcal{M}$. If we include the fact that the gauge $U(\mathbf{k})$ must be periodic in the reciprocal space, it can be shown that this integral is forced to be an integer number ν. This is the so-called **Chern number** defined as:

$$Ch \equiv \frac{1}{2\pi}\int_{\mathcal{M}} \mathrm{tr}(\Omega)\, d^2k = \nu \in \mathbb{Z}. \tag{3.110}$$

The Chern number is a topological invariant of states defined in a closed manifold $\mathcal{M}$, so that the only way to change the value it takes is by closing the gap between the manifold $\mathcal{M}$ (image of $P(\mathbf{k})$) and the rest of the states. Therefore, the Chern number is a topological invariant directly related to the Berry curvature and protected by the gap between the states on the manifold of interest and the rest. This topological invariant defines the classes of insulating (gapped) Hamiltonians which cannot be deformed into each other without closing the gap. Or in layman's terms, two set of bands with different Chern number, can not be deformed into each other without closing the gap.

3.4.7.3 *Relation between the Wilson loop and the Chern number*

After concluding that the left-hand side of (3.104) is related to the Chern number, it is obvious then that Wilson loops must be related to the topology of the system. Hence, we now focus on the right-hand side of the equality (3.104) and consider a 2D plane $\{(k_1\mathbf{g}_1, k_2\mathbf{g}_2)\ |k_1, k_2 \in [0,1]\}$ and Wilson loops $\mathcal{W}_{\mathbf{g}_2}(k_1)$ and $\mathcal{W}_{\mathbf{g}_2}(k_1 + \delta k)$, where we are using the notation introduced in (3.97).

If we now define $\mathcal{M}$ as the area between both loops, then divide the area in infinitesimal parallelograms in the k_1 direction, and take the limit $\delta k \to 0$, one can arrive at the relation

$$\partial_{k_1} \log\det W_{\mathbf{g}_2}(k_1) = i\int_0^{\mathbf{g}_2} \Omega^{12}(\mathbf{k})\, dk_2. \tag{3.111}$$

With this expression we can now integrate the Berry curvature across the hole 2D plane and relate it to the Chern number via equation (3.110)

$$\frac{1}{2\pi i}\int_0^{\mathbf{g}_1} \partial_{k_1}\, dk_1 \log\det W_{\mathbf{g}_2}(k_1) = Ch. \tag{3.112}$$

It can be shown that the left hand side of (3.112) is equal to the number of times the sum of hybrid Wannier centers, the imaginary part of the logarithm of the spectrum of $W_{\mathbf{g}_2}(k_1)$, wind as we vary k_1 in a closed loop $k_1\mathbf{g}_1\ |k_1 \in [0,1]$. Therefore, by plotting the Wilson loop spectrum and just counting the number of times hybrid Wannier functions wind we can extract the Chern number of a subset of bands.

3.4.7.4 *Chern number as an obstruction to Wannier localization*

The Chern number can also be interpreted as an obstruction to charge localization or stated in another way, as an obstruction to the formation of exponentially localized Wannier functions.

This can be intuited if we recall that on the one side, the problem for finding exponentially localized Wannier functions, is related to the one of finding a smooth gauge $U(\mathbf{k})$ in reciprocal space that leads to analytic functions $\{\tilde{\psi}_{n\mathbf{k}}(\mathbf{r})\}$ in reciprocal space (see section 3.4.4.1). While, on the other hand, we showed that the non-zero Chern number is related to the lack of a smooth gauge as shown in (3.109), which translates into a winding of the gauge transformation $U(\mathbf{k})$.

In conclusion, a non-zero Chern number can be interpreted as an obstruction to forming exponentially localized Wannier functions.

3.5 TOPOLOGICAL QUANTUM CHEMISTRY

The formalism of Topological Quantum Chemistry (TQC) establishes a link between topology and the symmetry properties of bands in reciprocal space. This can be established in the following way. First, we showed how topology in condensed matter physics is deeply related to the study of adiabatic evolution of states (3.56). However, we also showed that there exists a link between this adiabatic evolution and real space properties as the polarization (3.72) or the charge localization of individual states (3.84). It turns out, that the symmetry properties of these localized states in real space transfer to reciprocal space (band structures). Hence, we can describe TQC as a formalism that studies topology based on the analysis of the symmetries of band structures.

One of the main benefits of this method is that compared to computing Berry curvatures or Wilson loops, the calculation of bandstructures and their symmetries is much easier from an *ab initio* perspective. This opened the door to high-throughput investigations using large material-databases [18, 19, 75, 76] that have unveiled thousands of topological materials.

The original works from Zak [77–79] in the 1980s studied how Wannier functions in real space lead to bands in reciprocal space. Particularly, he introduced the concept of band representation, which states how the symmetry properties of bands are inherited from the ones of Wannier functions.

Later, the formalism was expanded by Bradlyn *et al* [13, 14, 16] to establish the link with topology. The main idea is that trivial topology corresponds to a smooth gauge in reciprocal space, which implies the possibility of forming exponentially localized Wannier functions in real space. While, at the same time, the symmetries of this Wannier functions define the symmetries of bands. Thus, by studying the symmetries of band structures one can diagnose whether such set of localized basis exists (and therefore whether or not the subset of bands is topologically trivial).

3.5.1 *Band representations*

A key concept of TQC is that of band representation. Roughly speaking, a band representation describes how the set of all atomic orbitals in the crystal transform when symmetry operations are applied. As the number of atoms in

an ideal crystal is infinite, the representation itself is also infinite dimensional. The concept of band representation is not limited to only electronic orbitals and can be also extended to atomic vibrations (phonons) (see Chapter 4) [80, 81] or photonic crystals [82, 83].

3.5.1.1 *Band representation in real space*

The first ingredient for a real-space representation of the space group G is a closed basis under the action of G. This basis will be built of Wannier functions $\{|i, \mathbf{q}, \mathbf{T}\rangle\}$, where i labels the orbital degree of freedom, $\mathbf{q}$ the site or the orbital within the primitive cell and $\mathbf{T}$ the cell in which the orbital is centered.

In order to build the basis, let us start by defining how sites transform under symmetry operations. For this, we will rewrite $\mathbf{q} \to q_\alpha$, where now q labels the Wyckoff position (WP), and α is the orbit within the WP. Since, we only care for the site transformation we will (for now) drop the orbital degree of freedom $|i, q_\alpha, \mathbf{T}\rangle \to |q_\alpha, \mathbf{T}\rangle$.

We define the site-symmetry group G_{q_1} as the symmetry operations that leave q_1 invariant

$$g\,|q_1, \mathbf{o}\rangle = |q_1, \mathbf{o}\rangle\,, \quad \text{with } g \in G_{q_1}. \tag{3.113}$$

Then, we can always find an element $g_\alpha \in G$, that does not belong to G_{q_1} that maps q_1 to q_α in the primitive cell (i.e. $g_\alpha\,|q_1, \mathbf{o}\rangle = |q_\alpha, \mathbf{o}\rangle$. However, in general an element $h = \{R|\mathbf{t}\}$ will map q_α to q_β in another cell.

$$h g_\alpha\,|q_1, \mathbf{o}\rangle = h\,|q_\alpha, \mathbf{o}\rangle = |q_\beta, \mathbf{t}_{\beta\alpha}\rangle \equiv \left\{E|\mathbf{t}_{\beta\alpha}\right\}|q_\beta, \mathbf{o}\rangle = \left\{E|\mathbf{t}_{\beta\alpha}\right\} g_\beta\,|q_1, \mathbf{o}\rangle \tag{3.114}$$

$$\mathbf{t}_{\beta\alpha} \equiv h\,|q_\alpha, \mathbf{o}\rangle - |q_\beta, \mathbf{o}\rangle \tag{3.115}$$

Additionally, from (3.114) we can see that

$$g_\beta^{-1}\left\{E|-\mathbf{t}_{\beta\alpha}\right\} h g_\alpha\,|q_1, \mathbf{o}\rangle = |q_1, \mathbf{o}\rangle\,, \tag{3.116}$$

which implies that

$$g_\beta^{-1}\left\{E|-\mathbf{t}_{\beta\alpha}\right\} h g_\alpha \equiv g \in G_1, \tag{3.117}$$

and hence, h can be written as

$$h = \left\{E|\mathbf{t}_{\beta\alpha}\right\} g_\beta g g_\alpha^{-1} \quad \text{with } g \in G_1. \tag{3.118}$$

Now that we have a clear understanding of how atomic sites transform, we can introduce back the orbital degrees of freedom and start with a set of Wannier functions in the primitive cell $\{|i, q_1, \mathbf{o}\rangle\}$ that transform as the representation ρ of their site-symmetry group groups G_{q_1}. Thus, we have that

$$g\,|i, q_1, \mathbf{o}\rangle = \sum_j^{\dim(\rho)} \rho_{ji}\,|j, q_1, \mathbf{o}\rangle\,, \quad \text{with } g \in G_{q_1}. \tag{3.119}$$

Then, we can use g_α to expand the basis to other sites in the primitive cell as

$$|i, q_\alpha, \mathbf{o}\rangle \equiv g_\alpha\,|i, q_1, \mathbf{o}\rangle\,. \tag{3.120}$$

Finally, the rest of states can be formed by using the translation subgroup $\hat{\mathbf{t}} \in T \subset G$ and expanding the basis as

$$\hat{\mathbf{t}} \, |i, q_\alpha, \mathbf{o}\rangle = |i, q_\alpha, \mathbf{t}\rangle \, . \tag{3.121}$$

We are left now with a closed basis since every element of the group G can be written as $\{E|\mathbf{t}\} \, g_\alpha g$, with $g \in G_1$.

To conclude, we study the action of an arbitrary element $h = \{R|\mathbf{t}\} \in G$ acting over a general element of the basis (making use of relation (3.118))

$$\begin{aligned} h \, |i, q_\alpha, \mathbf{T}\rangle &= h \{E|\mathbf{T}\} \, g_\alpha \, |i, q_1, \mathbf{o}\rangle = \{E|R\mathbf{T}\} \, h g_\alpha \, |i, q_1, \mathbf{o}\rangle \\ &= \{E|R\mathbf{T}\} \left\{E|\mathbf{t}_{\beta\alpha}\right\} g_\beta g \, |i, q_1, \mathbf{o}\rangle = \left\{E|R\mathbf{T} + \mathbf{t}_{\beta\alpha}\right\} g_\beta \sum_j^{\dim(\rho)} \rho_{ji}(g) \, |j, q_1, \mathbf{o}\rangle \\ &= \sum_j^{\dim(\rho)} \rho_{ji}(g) \, |j, q_\beta, R\mathbf{T} + \mathbf{t}_{\beta\alpha}\rangle \, . \end{aligned} \tag{3.122}$$

Notice how we have managed to write the full representation for any symmetry operation $h \in G$ in terms of one representation $\rho(g)$ of the site symmetry group G_1. This representation is called a **band representation** ρ_G and is said to be induced from the representation ρ of the site-symmetry group G_1

$$\rho_G = (\rho \uparrow G)_{WP}, \tag{3.123}$$

where WP stands for the Wyckoff position from which it was induced. Band representations are said to have *atomic limit* as they are induced from exponentially localized Wannier functions.

3.5.1.2 *Band representations in reciprocal space*

So far, we have shown how a band representation is built in real space. However, it is usually better to work in reciprocal space. The concept of band representation is easily transferred by Fourier transforming the basis from $|i, q_\alpha, \mathbf{T}\rangle \to |i, q_\alpha, \mathbf{k}\rangle$ as

$$|i, q_\alpha, \mathbf{k}\rangle = \frac{1}{\sqrt{N}} \sum_{\mathbf{T}} e^{i\mathbf{k}\cdot\mathbf{T}} \, |i, q_\alpha, \mathbf{T}\rangle \, , \tag{3.124}$$

where $\mathbf{k}$ as usual, belongs to the 1BZ. Thus, if we act with $h = \{R|\mathbf{t}\}$ over $|i, q_\alpha, \mathbf{k}\rangle$ and use equations (3.122) and (3.124)

$$\begin{aligned}
h\,|i, q_\alpha, \mathbf{k}\rangle &= h\left(\frac{1}{\sqrt{N}}\sum_{\mathbf{T}} e^{i\mathbf{k}\cdot\mathbf{T}}\,|i, q_\alpha, \mathbf{T}\rangle\right) = \frac{1}{\sqrt{N}}\sum_{\mathbf{T}} e^{i\mathbf{k}\cdot\mathbf{T}}\,(h\,|i, q_\alpha, \mathbf{T}\rangle) \\
&= \frac{1}{\sqrt{N}}\sum_{\mathbf{T}} e^{i\mathbf{k}\cdot\mathbf{T}}\left(\sum_{j}^{\dim(\rho)} \rho_{ji}(g)\,|j, q_\beta, R\mathbf{T} + \mathbf{t}_{\beta\alpha}\rangle\right) \\
&= e^{-iR\mathbf{k}\cdot\mathbf{t}_{\beta\alpha}}\frac{1}{\sqrt{N}}\sum_{\mathbf{T}} e^{iR\mathbf{k}\cdot R\mathbf{T}} e^{iR\mathbf{k}\cdot\mathbf{t}_{\beta\alpha}}\left(\sum_{j}^{\dim(\rho)} \rho_{ji}(g)\,|j, q_\beta, R\mathbf{T} + \mathbf{t}_{\beta\alpha}\rangle\right) \\
&= e^{-iR\mathbf{k}\cdot\mathbf{t}_{\beta\alpha}}\sum_{j}^{\dim(\rho)} \rho_{ji}(g)\left(\frac{1}{\sqrt{N}}\sum_{\mathbf{T}} e^{iR\mathbf{k}\cdot(R\mathbf{T}+\mathbf{t}_{\beta\alpha})}\,|j, q_\beta, R\mathbf{T} + \mathbf{t}_{\beta\alpha}\rangle\right) \\
&= e^{-iR\mathbf{k}\cdot\mathbf{t}_{\beta\alpha}}\sum_{j}^{\dim(\rho)} \rho(g)_{ji}\,|j, q_\beta, R\mathbf{k}\rangle\,,
\end{aligned} \tag{3.125}$$

we get that in reciprocal space the matrices of the band representations are block diagonal in blocks of dimensions $n \times \dim(\rho)$, where n is the size of the orbit or the Wyckoff position. The matrix elements of the band representation in reciprocal space can be directly obtained from (3.125) and are given by

$$\rho^{R\mathbf{k},\mathbf{k}}_{j\beta,i\alpha} = \langle j, q_\beta, R\mathbf{k}|h|i, q_\alpha, \mathbf{k}\rangle = e^{-iR\mathbf{k}\cdot\mathbf{t}_{\beta\alpha}}\rho_{ji}(g). \tag{3.126}$$

In summary, we have seen that when there is an exponentially localized set of Wannier functions (an atomic limit), the symmetry properties of Bloch states can be related to the symmetry properties of Wannier functions.

3.5.1.3 *The representation of the little group* $G_\mathbf{k}$

Finally, if we focus on the little group $G_\mathbf{k}$ of a particular $\mathbf{k}$ point, the representation for the little group can be obtained from the band representation ρ_G and is denoted $G \downarrow G_\mathbf{k}$. In this case we say that the representation $\rho_{G_\mathbf{k}}$ has been *subduced* from the representation ρ_G. In principle the representation $\rho_{G_\mathbf{k}}$ will be reducible in terms of irreps $D^\mathbf{k}_i$ of $G_\mathbf{k}$

$$G \downarrow G_\mathbf{k} = \bigoplus_i m^\mathbf{k}_i D^\mathbf{k}_i, \tag{3.127}$$

where $m^\mathbf{k}_i$ are the multiplicities of each irrep. Since $H(\mathbf{k})$ commutes with $G_\mathbf{k}$, according to Wigner's theorem (section 3.2.5), the degeneracies at each $\mathbf{k}$ point and the transformation properties of the eigenstates can be directly related to the irreducible decomposition (3.127). This showcases the potential of the band representation, which allows us to infer all these properties, just from the symmetries of the original Wannier orbitals in real space.

3.5.2 *The compatibility relations*

A fair question one can ask is whether the connection between irreps in different little groups across the Brillouin zone is enforced by symmetries in any way. As $H(\mathbf{k})$ varies along $\mathbf{k}$-space, the eigenvalues transform according to different irreps every time we change the little group, for example, when $\mathbf{k}$ goes from a high-symmetry point to a high-symmetry line. I turns out, that in this cases, the irrep of the high-symmetry point fixes the irrep of the high-symmetry line. These relations, imply a constraint in the ways in which bands are connected.

Let us consider two points $\mathbf{k}_\alpha$ and $\mathbf{k}_\beta$ with their corresponding little groups G_α and G_β, as well as a vector $\mathbf{k}_\gamma$ that defines a line connecting $\mathbf{k}_\alpha$ and $\mathbf{k}_\beta$. The little group across the line G_γ is a subgroup of both G_α and G_β, therefore, the representations for G_α and G_β have to subduce to the same representation of G_γ. This can be expressed as

$$(\rho_G \downarrow G_\alpha) \downarrow G_\gamma = \left(\rho_G \downarrow G_\beta\right) \downarrow G_\gamma. \tag{3.128}$$

This implies that for example in this case, the irreps across the γ line are completely fixed by either the ones of $\rho^{\mathbf{k}_\alpha}$ or $\rho^{\mathbf{k}_\beta}$.

Moreover, it also happens that the irreps of both $\rho^{\mathbf{k}_\alpha}$ and $\rho^{\mathbf{k}_\beta}$ are constrained by each other. It can be shown that by knowing the irreps in what are called the *maximal k-points* of the BZ, the irreps in the rest of $\mathbf{k}$ points can be determined. The compatibility relations that are established by this rules can be found in the Bilbao Crystallographic Server [68–70].

3.5.3 *Elementary band representations*

If we form a band representation using two closed bases, the resulting representation (for both band structures stacked together) can be written as a sum of the band representations of each of the bases, and is called a **composite band representation**. This can be intuited by the fact that symmetry operations by definition will not mix both basis (since are closed).

On the other hand, when a band representation can not be decomposed into smaller band representations it is called an **elementary band representation** (EBR). Additionally, it can be shown that the only way to form elementary band representations, is to induce them from Wannier functions transforming under irreducible representations of maximal Wyckoff positions. Thus, while the number of possible band representations one can form is infinite, they are all formed by a finite set of building blocks (the EBRs). This finite set of EBRs has been computed for all space groups [13], and can be found in the Bilbao Crystallographic Server.

In other words, the EBRs are the basis from which all atomic limits are formed, therefore the band representation of every atomic limit can be decomposed as

$$\rho_G = \bigoplus_i m_i \rho_G^i, \tag{3.129}$$

where m_i is the multiplicity of each EBR ρ^i_G.

An EBR is said to be *decomposable* if its bands can be separated into two or more disconnected sets of bands while respecting the compatibility relations. Notably, when this occurs, at least one of the subsets cannot be a band representation.

3.5.4 *Topology diagnosis with TQC*

The groundbreaking achievement of the TQC formalism relies on providing an easy way to identify non-trivial topological phases using the previously discussed concepts. By construction, band structures transforming as band representations can be written in terms of exponentially localized Wannier functions, or in other words, can be connected to an atomic limit. On the other hand, we already discussed the relation between a topological set of bands and the Wannier obstruction (section 3.4.6).

Based on these two statements, we can devise a diagnostic method: if, when decomposing the representation ρ_G of an isolated subset of bands into elementary band representations as

$$\rho_G = \bigoplus_i m_i \mathrm{EBR}^i_G, \tag{3.130}$$

any of the coefficients m_i is not a positive integer, this implies that there is an obstruction to forming exponentially localized Wannier functions (there is no atomic limit). Consequently, the subset of bands is topologically non-trivial.

Moreover, using the fact that band representations are totally defined by the irreducible representations of the maximal k-points due to the compatibility relations, the decomposition (3.130) can be done solely knowing the irreps at the maximal k-points.

Two main types of topological bands can be identified from the coefficients in (3.130). When any of the coefficients is a fractional number, the bands are in a **stable topological phase**. In contrast, if only negative integers are found, this corresponds to a **fragile topological phase**. The distinction arises because fragile bands can be trivialized by adding an additional set of trivial bands (derived from an EBR), which is not possible for stable phases.

A final note is necessary to emphasize that the converse of the reasoning presented is not true. The ability to write a representation as a sum of EBRs does not imply the existence of an atomic limit and may still not constitute a band representation. Thus, Topological Quantum Chemistry provides a sufficient condition for topology but not a necessary one. For a more in-depth analysis, one must employ more complex and computationally intensive methods, such as analyzing the Wilson loop spectrum or computing Chern numbers by integration of the Berry curvature.

Part II

PHONON TOPOLOGY

4

TOPOLOGICAL ANALYSIS OF THE PHONON SPECTRA OF THE BUCKLED HONEYCOMB LATTICE

In this chapter, we analyze the topology of the 2D buckled honeycomb lattice phonon spectra using group theory, topological quantum chemistry, first-principles calculations, and Monte Carlo simulations. Taking the pure crystal structure as an input, we show that eleven distinct phases are possible, five of which necessarily have non-trivial topology according to topological quantum chemistry. Another four of them are also identified as topological using Wilson loops in an analytical model that includes all the symmetry allowed force constants up to third nearest neighbors, making a total of nine topological phases. We then compute the ab initio phonon spectra for the two-dimensional crystals of Si, Ge, P, As and Sb in this structure and construct its phase diagram. We found that, despite the large proportion of topological phases found in the analytical model, all of the crystals lie in a trivial phase. By analyzing the force constants space using Monte Carlo calculations, we elucidate why topological phonon phases are physically difficult to realize in real materials with this crystal structure.

4.1 OVERVIEW

Topological materials are known for having exotic electronic properties such as symmetry protected surface states, edge states or unconventional electromagnetic activity [84, 85]. Following the first topological insulator realization [8] in 2007, the concept of symmetry protected topological (SPT) orders [86–88] was extended to all sorts of symmetry settings with the advent of topological crystalline insulators [9, 89–98]. However, with the exception of the Fu-Kane parity criterion [9] and a few other symmetry based diagnosis methods [99–101], there was not a clear link between symmetry and topology for general symmetry settings. As a result, the calculation of most topological band invariants used in the prediction and diagnosis of topological materials had to be carried out numerically with computationally expensive *ab initio* methods, and the rate of discovery of new materials was consequently rather slow. Recently, as shown in Chapter 3, much more powerful links have been established between the topology of the electronic spectrum and the crystal symmetry thanks to the theory of symmetry indicators of band topology [16, 102], band combinatorics [103], and topological quantum chemistry (TQC) [13]. These formalisms have provided a reliable and systematic way to search for all the topologically non-trivial phases compatible with a given crystal structure. This has led to the discovery of thousands of materials with non-

trivial electronic topology, showing that the existence of topological electron bands, previously considered a rarity, is rather frequent in nature. In particular, the systematic application of the methods of TQC have enormously enlarged the number of known topological materials [18, 76] and led to new and more refined methods of classifying their topology [104–107].

Despite recent advances, most research has focused on analyzing electronic topology. However, in principle, many other quasiparticles can also exhibit topological features. In our case, we focus on phonons, which are fundamental to many properties of solids, such as transport, optical and thermal responses, superconductivity, or phase transitions. Despite the fact that finding materials with topological phonons is likely to have a large impact on solid-state physics, the search for non-trivial phonon topology has progressed slowly, while primarily using traditional methods [108–117], or focusing on degeneracies with topological charge, such as Weyl points and nodal lines [118, 119]. When we began this project, only one instance in the literature applied the more modern methods of topological quantum chemistry (TQC) to the search for phonon topology, focusing on the planar honeycomb structure [20]. Inspired by this work, in this chapter we study phonon topology in a more complex structure that couples out-of-plane and in-plane lattice vibrations: the buckled honeycomb lattice. This is an important system since the planar honeycomb lattice is unstable for atoms larger than carbon and two-dimensional materials based on Si, Ge, P, As, and Sb crystallize in the buckled honeycomb lattice. Moreover, the coupling between in- and off- plane modes gives rise to a whole array of phases not present on the planar honeycomb. Notably, parallel to this thesis, a significant advancement has been made with the launch of a high-throughput phonon catalogue applying TQC to 3D materials [19]. This work highlights the almost complete absence of fragile cumulative topology for phonons, which aligns with our findings.

As already discussed in chapter 3, the TQC analysis relies on detecting an obstruction to a localized real space interpretation of isolated subsets of phonon bands. Whenever this obstruction is present, the subset has non-trivial topology. In some cases this obstruction can be diagnosed just from the irreducible representations (irreps) describing how those bands transform at the high symmetry points (HSPs) in the Brillouin zone. In practice, this analysis consists of three steps. First, one finds the irreps describing how phonons transform at the HSPs. Second, a compatibility problem is solved, in which one tries to connect the bands forming isolated subsets separated by gaps in ways that are consistent with the system symmetries and the existence of the acoustic zero frequency modes. Each of these band configurations constitutes a phase. Finally, if the irreps of an isolated subset cannot be obtained from the sum of elementary band representations (EBRs), the corresponding phase is necessarily topological. Note that even if the irreps of all the isolated subsets in a given phase can be obtained from the sum of elementary band representations, the phase could still be topological. Thus, an extra step in order to fully diagnose the topology involves the construction of an analytical model that

reproduces the different phases and the computation of Wilson loop spectra for the different phases.

The chapter is organized as follows. A discussion on how the TQC machinery is adapted to the study of phonon spectra of the BHL is presented in Section 4.2. An analytical model that includes all the symmetry compatible couplings up to third nearest neighbors is constructed in Section 4.3. The model is used to compute Wilson loop spectra and fully classify the topology of all the phases obtained in Section 4.3.4. In Section 4.4 we use Quantum Espresso [120, 121] to compute the phonon spectra for several monoatomic crystals with the buckled honeycomb structure and locate them on the phase diagram. Moreover, we show how the analytical model can be used to study the phase diagram by means of a Monte Carlo method, which provides a plausible explanation to why topological phonon phases are physically difficult to realize in real materials. Finally, the summary and conclusions are presented in Section 4.5.

4.2 TOPOLOGICAL QUANTUM CHEMISTRY APPLICATION TO THE PHONON SPECTRA

4.2.1 *Band representations for phonons*

As explained in Chapter 3, for electronic systems, a band representation (BR) [77, 78, 122] can be understood as a mathematical construction that links the real space orbital description to the reciprocal space momentum picture. Then, one says that the band representation is induced by the set of orbitals. Note that, in order to be closed under the translations in the space group G of the crystal, the set must contain infinitely many orbitals and band representations are always infinite-dimensional, which is at the origin of some counterintuitive properties.

In practice, each band representation induces a collection of little group irreps at every point in the Brillouin zone [13]. Although this collection of irreps can be considered as a footprint of the band representation, it is important to bear in mind that the band representation is not uniquely specified by its footprint, as different (inequivalent) band representations, and even representations that are not BRs, can give rise to identical sets of irreps at all the points in the Brillouin zone [122]. The reason is that the set of irreps at all the points in the Brillouin zone does not exhaust all the information contained in the band representation. This phenomenon has no analogue in the case of ordinary, finite-dimensional representations and has important consequences for the irrep-based detection of topological phases.

The concept of inducing a band representation can be easily extended to the phononic case [20, 80]. Instead of having orbitals or Wannier functions (WFs) as a basis, one has a set of vectors describing the displacements located on every atom in the crystal. These displacements (real space) transform under the vector representation $V(g)$ for symmetry elements g of the site symmetry group G_q. As phonons are a combination of local displacements, one

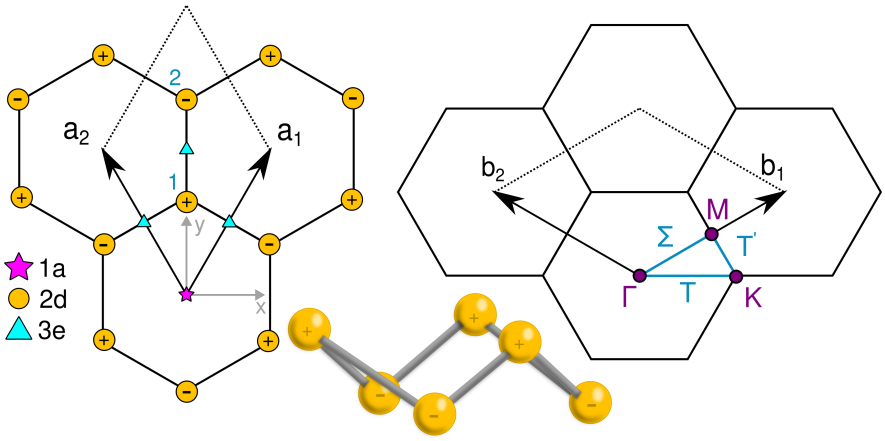

Figure 4.1: Buckled honeycomb lattice with real an reciprocal space lattice vectors. The structure is formed with two atoms per cell, placed at the 2d maximal Wyckoff positions, each displaced along the z axis in opposite directions. The little groups for the Γ, K, M points and T, T′, Σ lines are D_{3d}, D_3, C_{2h} and C_2, C_2, C_{1h}, respectively.

can induce a band representation describing how phonons (reciprocal space) transform under the full space group symmetry operations from the vector representation of one of the site symmetry groups of the occupied Wyckoff positions (WPs).

When inducing the band representation from the displacements centered on the atoms, we obtain *all* the phononic bands for the crystal. But this should not be mistaken with the possibility of inducing connected subsets of bands from 'Wannier like" functions for phonons, even when these WFs are not centered on atomic positions. The matter of defining a localized basis for vibrations was already discussed by W. Kohn [123] and more recently in terms of the position operator in Ref. [124]. This possibility generalizes the concept of EBRs to phonons in an equivalent way to the electronic case, where EBRs are induced from WFs that transform under an irreducible representation of the local site symmetry group G_q of any maximal symmetry Wyckoff position.

4.2.2 *Mechanical BR for the BHL structure*

As shown in Fig. 4.1 the BHL is a 2D structure that can be obtained by giving opposite vertical (perpendicular to the sample plane) displacements to the two atoms in the primitive cell of the planar honeycomb lattice. These displacements break the mirror symmetry with respect to the plane of the sample and are thus responsible for the couplings between off- and in-plane phonons, which are forbidden for the planar honeycomb. The layer group leaving the BHL invariant is LG 72 ($p\bar{3}m1$), which corresponds to the space group SG 164 ($P\bar{3}m1$) with point group D_{3d} ($\bar{3}m$). The direct and reciprocal lattice vectors satisfying $\mathbf{a}_i \cdot \mathbf{b}_j = 2\pi\delta_{ij}$ are shown in Fig 4.1. In this basis, the high symmetry points are located at $\Gamma = (0,0)$, $K = \frac{1}{3}(\mathbf{b}_1 - \mathbf{b}_2)$ and $M = \frac{\mathbf{b}_1}{2}$, while the atoms are located at the Wyckoff position 2d with site-symmetry group C_{3v}.

As mentioned above, the phononic BR for the crystal, also known as the mechanical BR, is induced from the vector representations of the atomic site symmetry groups

$$\rho_G = \bigoplus_q V_{G_q} \uparrow G, \tag{4.1}$$

where q runs over all occupied Wyckoff positions. By decomposing the vector representation into irreducible representations $D^{(i)}_{G_q}$, the mechanical BR can be written as a sum of EBRs

$$\rho_G = \bigoplus_q V_{G_q} \uparrow G = \bigoplus_{q,i} D^{(i)}_{G_q} \uparrow G \tag{4.2}$$

In our case, the vector representation of C_{3v} is reducible, $V = A_1 + E$, and according to Eq. (4.2) the mechanical BR is given by

$$M = V|_{2d} \uparrow G = A_1|_{2d} \uparrow G \oplus E|_{2d} \uparrow G. \tag{4.3}$$

In other words, the mechanical BR can be written as the sum of the EBRs induced from A_1 and E at the WP 2d. We can avoid the actual computation of the mechanical BR by noting that the little group irreps induced by any EBR at any point $\mathbf{k}$ in the BZ are given by the *BandRep* application at the Bilbao Christallographic Server (BCS) [68–70]. For the rest of the analysis we only need the irrep contents at the high symmetry points in the BZ. Adding the irreps given by *BandRep* for the two EBRs in Eq. (4.3) yields

$$\begin{aligned} M(\Gamma) &= \Gamma_1^+(1) + \Gamma_2^-(1) + \Gamma_3^+(2) + \Gamma_3^-(2) \\ M(K) &= 2K_3(2) + K_1(1) + K_2(1) \\ M(M) &= 2M_1^+(1) + M_1^-(1) + M_2^+(1) + 2M_2^-(1), \end{aligned} \tag{4.4}$$

where the numbers in parenthesis give the dimensions of the irreps and lead to band crossings when greater than one. The irreps at the high symmetry lines and the compatibility relations are obtained by subduction from the high symmetry points and are also given by *BandRep* [70].

In order to find all the different gapped phases compatible with the symmetries, we just have to order the irreps at the high-symmetry points in the BZ in such a way that they lead to gaps in the phonon spectrum while respecting the compatibility relations arising from the subduction rules to the high symmetry lines. Moreover, an additional constraint that distinguishes phonon spectra from electron bands is the existence of three acoustic bands, for which the dispersion relation must satisfy $\lim_{\mathbf{k}\to 0} \omega(\mathbf{k}) = 0$. The acoustic modes at $\mathbf{k} = 0$ represent global translations of the crystal and transform under the vector representation Thus, by decomposing the vector representation V_Γ of the little group of Γ, the irreducible representations of the acoustic bands at Γ are obtained. In this case, V_Γ decomposes as $V_\Gamma = \Gamma_2^- + \Gamma_3^-$ and we conclude that three eigenvalues associated with the irreps $\Gamma_2^-(1)$ and $\Gamma_3^-(2)$ must vanish at $\mathbf{k} = 0$. Table 4.1 gives all the irrep orderings that respect the compatibility relations and acoustic band constraints and result in gapped phases in

Phase	Subset 1	Subset 2	Subset 3
1	$\Gamma_3^- + \Gamma_2^-; K_2 + K_3; M_1^+ + M_2^+ + M_2^-$	$\Gamma_1^+; K_1; M_1^+$	$\Gamma_3^+; K_3; M_1^- + M_2^-$
2	$\Gamma_3^- + \Gamma_2^-; K_2 + K_3; M_1^- + 2M_2^-$	$\Gamma_1^+; K_1; M_1^+$	$\Gamma_3^+; K_3; M_1^+ + M_2^+$
3	$\Gamma_3^- + \Gamma_2^-; K_2 + K_3; M_1^+ + M_2^+ + M_2^-$	$\Gamma_3^+; K_3; M_1^- + M_2^-$	$\Gamma_1^+; K_1; M_1^+$
4	$\Gamma_3^- + \Gamma_2^-; K_2 + K_3; M_1^- + 2M_2^-$	$\Gamma_3^+; K_3; M_1^+ + M_2^+$	$\Gamma_1^+; K_1; M_1^+$
Phase	Subset 1	Subset 2	
5	$\Gamma_3^- + \Gamma_2^-; K_2 + K_3; M_1^- + 2M_2^-$	$\Gamma_3^+ + \Gamma_1^+; K_3 + K_1; 2M_1^+ + M_2^+$	
6	$\Gamma_3^- + \Gamma_2^-; K_2 + K_3; M_1^+ + M_2^+ + M_2^-$	$\Gamma_3^+ + \Gamma_1^+; K_3 + K_1; M_1^+ + M_1^- + M_2^-$	
7	$\Gamma_3^- + \Gamma_2^- + \Gamma_3^+; K_2 + 2K_3; M_1^+ + M_1^- + M_2^+ + 2M_2^-$	$\Gamma_1^+; K_1; M_1^+$	
8	$\Gamma_3^- + \Gamma_2^- + \Gamma_1^+; K_1 + K_2 + K_3; 2M_1^+ + M_2^+ + M_2^-$	$\Gamma_3^+; K_3; M_1^- + M_2^-$	
9	$\Gamma_3^- + \Gamma_2^- + \Gamma_1^+; K_1 + K_2 + K_3; M_1^+ + M_1^- + 2M_2^-$	$\Gamma_3^+; K_3; M_1^+ + M_2^+$	
10	$\Gamma_3^- + \Gamma_2^- + \Gamma_1^+; 2K_3; 2M_1^+ + M_2^+ + M_2^-$	$\Gamma_3^+; K_1 + K_2; M_1^- + M_2^-$	
11	$\Gamma_3^- + \Gamma_2^- + \Gamma_1^+; 2K_3; M_1^+ + M_1^- + 2M_2^-$	$\Gamma_3^+; K_1 + K_2; M_1^+ + M_2^+$	

Table 4.1: Irreducible representations decomposition of the isolated subsets at the three high symmetry points in the BZ for all gapped phases. The subsets are ordered in terms of energy from lower to higher. The little groups for the Γ, K, M points and T, T′, Σ lines are D_{3d}, D_3, C_{2h} and C_2, C_2, C_{1h}, respectively.

the phonon spectrum. It is important to note that we refer to these phases as "gapped" because they contain isolated subsets of phonon bands separated by gaps, notwithstanding the existence of gapless excitations in the form of acoustic modes.

4.2.3 *Irrep-based topological analysis*

The next step is to find the isolated subsets of connected bands that can not transform as band representations. As every band representation can be written as a sum of EBRs, if the irreps of an isolated subset can not be induced from any sum of EBRs then, according to TQC, the subset must have nontrivial topology. The result of this analysis is presented in Table 4.2, where we see that phases 1, 3, 8, 10 and 11 *must* have nontrivial topology. As mentioned before, some of the remaining seven phases *might* still be topologically nontrivial, but this cannot be diagnosed solely on the basis of their irrep contents. In the next subsection we will compute Wilson loops to diagnose their topology.

The presence of negative coefficients in Table 4.2 for phases 1, 3, 8, 10 and 11 is usually taken, at least for electronic bands, as a signature of fragile topology [20, 107]. When the irreps of an isolated subset of bands can be obtained as a difference of EBRs, as in phase 1 in Table 4.2, the addition of a trivial band that transforms under $A_1^+ \,|_{1a}$ in that case would "trivialize" the fragile topology. For electrons this band may be found as core orbitals or high energy conduction bands, but for phonons the number of bands is fixed and the

Phase	Subset 1	Subset 2	Subset 3
1	$B^- \vert_{3e}$	$A_1^+ \vert_{1a}$	$A^+ \vert_{3e} - A_1^+ \vert_{1a}$
2	$A_2^- \vert_{1a} + E^- \vert_{1a}$	$A_1^+ \vert_{1a}$	$E^- \vert_{1a}$
3	$B^- \vert_{3e}$	$A^+ \vert_{3e} - A_1^+ \vert_{1a}$	$A_1^+ \vert_{1a}$
4	$A_2^- \vert_{1a} + E^- \vert_{1a}$	$E^+ \vert_{1a}$	$A_1^+ \vert_{1a}$
5	$A_2^- \vert_{1a} + E^- \vert_{1a}$	$A_1^+ \vert_{1a} + E^+ \vert_{1a}$	
6	$B^- \vert_{3e}$	$A^+ \vert_{3e}$	
7	$A_2^- \vert_{1a} + E^+ \vert_{1a} + E^- \vert_{1a}$	$A_1^+ \vert_{1a}$	
8	$A_1^+ \vert_{1a} + B^- \vert_{3e}$	$A^+ \vert_{3e} - A_1^+ \vert_{1a}$	
9	$A_1^+ \vert_{1a} + A_2^- \vert_{1a} + E^- \vert_{1a}$	$E^+ \vert_{1a}$	
10	$A_1^+ \vert_{1a} + E_1^+ \vert_{1a} + E_1^- \vert_{1a} + A_1 \vert_{2d} - A^+ \vert_{3e}$	$A_2^- \vert_{1a} - A_1 \vert_{2d} + A^+ \vert_{3e}$	
11	$E^- \vert_{1a} + A_1 \vert_{2d}$	$A_1^+ \vert_{1a} + A_2^- \vert_{1a} + E^+ \vert_{1a} - A_1 \vert_{2d}$	

Table 4.2: Combinations of EBRs that reproduce the irrep content in Table 4.1 for each of the isolated subsets, with the Wyckoff positions indicated as subscripts. Note that these combinations are in general non-unique, but have been presented as a sum whenever possible. Phases diagnosed as topological by TQC are given in boldface.

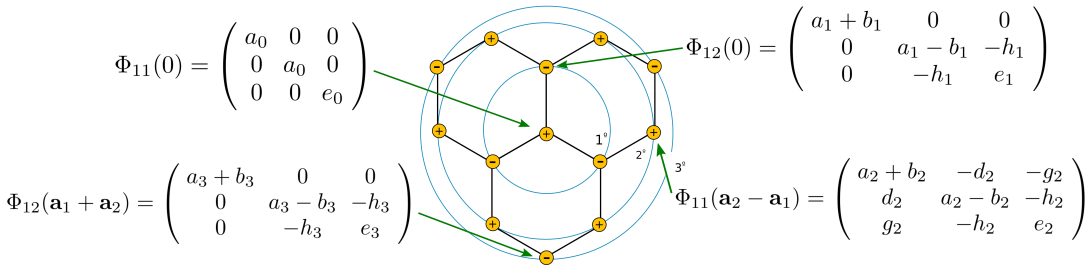

Figure 4.2: Matrices of force constants consistent with the BHL symmetries up to third nearest neighbors. As described in section 4.3.2, all the matrices for neighbors on the same circle are related by symmetry operations to the one given in this figure.

required trivial band may not be available. This is another difference between electronic and phononic systems.

4.3 ANALYTICAL MODEL FOR THE BUCKLED HONEYCOMB LAYER

In this section we present a truncation of the dynamical matrix for the BHL that includes, up to third nearest neighbors, all couplings compatible with the system symmetries. We stop at third nearest neighbors because that is enough to reach all the phases in Tables I and II. The truncated dynamical matrix provides an analytical model that is used below to compute Wilson loops [125–127] for every disconnected subset of bands, identifying thus all the topologically non-trivial phases.

The harmonic potential energy of the crystal can be written as

$$U^{\text{harm}} = \frac{1}{2} \sum_{\mathbf{R}\mathbf{R}',ij} \mathbf{u}_i(\mathbf{R}) \Phi_{ij}(\mathbf{R}-\mathbf{R}') \mathbf{u}_j(\mathbf{R}'), \tag{4.5}$$

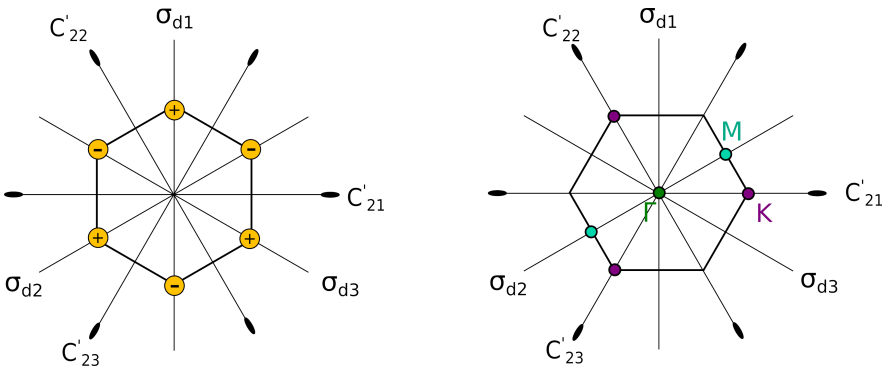

Figure 4.3: Symmetry operations of the D_{3d} group in real and reciprocal space. The threefold rotation axes $C_3^{\pm}$ are perpendicular to the plane of the crystal.

where $\mathbf{R}$ and $\mathbf{R}'$ label two distinct unit cells, $\mathbf{u}$ is a displacement vector, (i, j) are the atom indices and Φ_{ij} is a 3×3 matrix of force constants which must be real by time reversal symmetry. Note that the fact that U^{harm} is a quadratic form in the atomic displacements implies

$$\Phi_{ij}(\mathbf{R}) = \Phi_{ji}^{t}(-\mathbf{R}), \tag{4.6}$$

where t indicates matrix transposition.

4.3.1 *Symmetry constraints on the analytical model*

In this section we compute the four matrices of force constants in Fig. 4.2 and show how to use them to obtain the matrices for symmetry-related neighbors. Then the Fourier transform in Eq. (4.24) yields the most general dynamical matrix $D(\mathbf{k})$ compatible with all the symmetries and including up to third nearest neighbor couplings. A generic force constants matrix is parametrized by nine real constants

$$\Phi_{ij}(\mathbf{R}) = \begin{pmatrix} a+b & -c-d & -f-g \\ -c+d & a-b & -h-i \\ -f+g & -h+i & e \end{pmatrix}, \tag{4.7}$$

where the indices i and j take the values 1 or 2 for the two atoms in the unit cell (see Fig. 4.1), and $\mathbf{R}$ is a lattice vector connecting the origins of the cells to which the two atoms belong.

Besides the constraint in Eq. (4.6), the force constants matrices must satisfy additional relations due to the point group symmetries of the crystal [128]

$$\Phi_{i'j'}(S\mathbf{R}) = V(S)\Phi_{ij}(\mathbf{R})V(S)^{t}, \tag{4.8}$$

where $V(S)$ is the 3×3 matrix for the symmetry operation S in the vector representation; i', j' are the indices for the atoms in the transformed positions; and $S\mathbf{R}$ is the lattice vector connecting the origins of the cells to which the atoms in the transformed positions belong. Note that, in general, $S\mathbf{R} \neq V(S)\mathbf{R}$.

It is important to note that, given that the space group for the BHL is symmorphic, we can restrict ourselves to point group operations. This would not be possible for a nonsymmorphic group, where the point group is *not* a subgroup of the space group.

4.3.1.1 *On-site couplings*

According to Eq. (4.8) the matrix $\Phi_{11}(\mathbf{0})$ must be invariant under any operation belonging to the site symmetry group C_{3v} of atom 1,

$$\Phi_{11}(\mathbf{0}) = V(S)\Phi_{11}(\mathbf{0})V(S)^t \quad \forall\, S \in C_{3v}. \tag{4.9}$$

Applying this equation with S equal to C_3^+ and σ_{d_1} (see Fig. (4.3) for notation), which together generate the group C_{3v}, shows that the on-site matrix must take the form

$$\Phi_{11}(0) = \begin{pmatrix} a_0 & 0 & 0 \\ 0 & a_0 & 0 \\ 0 & 0 & e_0 \end{pmatrix}. \tag{4.10}$$

Noting that the spatial inversion I exchanges atoms 1 and 2 and using Eq. (4.8) for $S = I$ yields

$$\Phi_{22}(\mathbf{0}) = V(I)\Phi_{11}(\mathbf{0})V(I)^t = \Phi_{11}(\mathbf{0}). \tag{4.11}$$

4.3.1.2 *First nearest neighbors*

Here we consider the couplings between atoms 1 and 2 in Fig. 4.1. We can obtain a first constraint on $\Phi_{11}(\mathbf{0})$ by using Eq. (4.8) with $S = \sigma_{d_1}$, which leaves atoms 1 and 2 invariant

$$\Phi_{12}(\mathbf{0}) = V(\sigma_{d_1})\Phi_{12}(\mathbf{0})V(\sigma_{d_1})^t. \tag{4.12}$$

A second constraint is obtained by combining Eq. (4.8) for $S = I$ with Eq. (4.6)

$$\Phi_{12}(\mathbf{0}) = V(I)\Phi_{21}(\mathbf{0})V(I)^t = \Phi_{21}(\mathbf{0}) = \Phi_{12}(\mathbf{0})^t, \tag{4.13}$$

and the two constraints together imply

$$\Phi_{12}(\mathbf{0}) = \begin{pmatrix} a_1 + b_1 & 0 & 0 \\ 0 & a_1 - b_1 & -h_1 \\ 0 & -h_1 & e_1 \end{pmatrix}. \tag{4.14}$$

Finally, using Eqs. (4.6) and (4.8) for $S = C_3^\pm$ yields the remaining nearest neighbor matrices in terms of Eq. (4.14)

$$\begin{aligned} \Phi_{12}(\mathbf{a}_1) &= V(C_3^+)\Phi_{12}(\mathbf{0})V(C_3^+)^t \\ \Phi_{12}(\mathbf{a}_2) &= V(C_3^-)\Phi_{12}(\mathbf{0})V(C_3^-)^t \\ \Phi_{21}(\mathbf{0}) &= \Phi_{12}(\mathbf{0}) \\ \Phi_{21}(-\mathbf{a}_1) &= \Phi_{12}^t(\mathbf{a}_1) \\ \Phi_{21}(-\mathbf{a}_2) &= \Phi_{12}^t(\mathbf{a}_2). \end{aligned} \tag{4.15}$$

4.3.1.3 *Second nearest neighbors*

Using Eq. (4.8) with $S = \sigma_{d_1}$, which exchanges two second neighbors, followed by Eq. (4.6), gives

$$\sigma_{d_1}\Phi_{11}(\mathbf{a}_2-\mathbf{a}_1)\sigma_{d_1}^{-1} = \Phi_{11}(\mathbf{a}_1-\mathbf{a}_2) = \Phi_{11}^{t}(\mathbf{a}_2-\mathbf{a}_1), \tag{4.16}$$

which directly leads to:

$$\Phi_{11}(\mathbf{a}_2-\mathbf{a}_1) = \begin{pmatrix} a_2+b_2 & -d_2 & -g_2 \\ d_2 & a_2-b_2 & -h_2 \\ g_2 & -h_2 & e_2 \end{pmatrix}. \tag{4.17}$$

Then the remaining second nearest neighbor matrices can be obtained using $\Phi_{22}(\mathbf{a}_1-\mathbf{a}_2) = \Phi_{11}(\mathbf{a}_2-\mathbf{a}_1)$ and

$$\begin{aligned}
&\Phi_{11}(-\mathbf{a}_2) = \Phi_{22}(\mathbf{a}_2) = V(C_3^+)\Phi_{11}(\mathbf{a}_2-\mathbf{a}_1)V(C_3^+)^t \\
&\Phi_{11}(\mathbf{a}_1) = \Phi_{22}(-\mathbf{a}_1) = V(C_3^-)\Phi_{11}(\mathbf{a}_2-\mathbf{a}_1)V(C_3^-)^t \\
&\Phi_{11}(\mathbf{a}_1-\mathbf{a}_2) = \Phi_{22}(\mathbf{a}_2-\mathbf{a}_1) = \Phi_{11}^{t}(\mathbf{a}_2-\mathbf{a}_1) \\
&\Phi_{11}(\mathbf{a}_2) = \Phi_{22}(-\mathbf{a}_2) = \Phi_{11}^{t}(-\mathbf{a}_2) \\
&\Phi_{11}(-\mathbf{a}_1) = \Phi_{22}(\mathbf{a}_1) = \Phi_{11}^{t}(\mathbf{a}_1).
\end{aligned} \tag{4.18}$$

4.3.1.4 *Third nearest neighbors*

As seen in Fig. 4.2, the geometry of third nearest neighbors is closely related to the one for first neighbors, with σ_{d_1} and the inversion I playing analogous roles here. Instead of Eqs. (4.12) and (4.13) we have now

$$\Phi_{12}(\mathbf{a}_1+\mathbf{a}_2) = V(\sigma_{d_1})\Phi_{12}(\mathbf{a}_1+\mathbf{a}_2)V(\sigma_{d_1})^t \tag{4.19}$$

and

$$\Phi_{12}(\mathbf{a}_1+\mathbf{a}_2) = \Phi_{21}(-\mathbf{a}_1-\mathbf{a}_2) = \Phi_{12}^{t}(\mathbf{a}_1+\mathbf{a}_2), \tag{4.20}$$

and these two conditions imply

$$\Phi_{12}(\mathbf{a}_1+\mathbf{a}_2) = \begin{pmatrix} a_3+b_3 & 0 & 0 \\ 0 & a_3-b_3 & -h_3 \\ 0 & -h_3 & e_3 \end{pmatrix}. \tag{4.21}$$

The remaining third nearest neighbor matrices are given by

$$\begin{aligned}
&\Phi_{12}(\mathbf{a}_2-\mathbf{a}_1) = V(C_3^+)\Phi_{12}(\mathbf{a}_1+\mathbf{a}_2)V(C_3^+)^t \\
&\Phi_{12}(\mathbf{a}_1-\mathbf{a}_2) = V(C_3^-)\Phi_{12}(\mathbf{a}_1+\mathbf{a}_2)V(C_3^-)^t \\
&\Phi_{21}(-\mathbf{a}_1-\mathbf{a}_2) = \Phi_{12}^{t}(\mathbf{a}_1+\mathbf{a}_2) \\
&\Phi_{21}(\mathbf{a}_1-\mathbf{a}_2) = \Phi_{12}^{t}(\mathbf{a}_2-\mathbf{a}_1) \\
&\Phi_{21}(\mathbf{a}_2-\mathbf{a}_1) = \Phi_{12}^{t}(\mathbf{a}_1-\mathbf{a}_2).
\end{aligned} \tag{4.22}$$

We finish by giving the matrices of the vector representation used in this procedure.

$$V(\sigma_{d_1}) = \begin{pmatrix} -1 & 0 & 0 \\ 0 & 1 & 0 \\ 0 & 0 & 1 \end{pmatrix}, V(C_3^+) = \begin{pmatrix} -\frac{1}{2} & -\frac{\sqrt{3}}{2} & 0 \\ \frac{\sqrt{3}}{2} & -\frac{1}{2} & 0 \\ 0 & 0 & 1 \end{pmatrix}. \tag{4.23}$$

Note also that $V(C_3^-) = V(C_3^+)^t$ and $V(I) = -\mathbb{1}_{3\times 3}$.

4.3.2 *The acoustic sum rule*

As just shown in Section 4.3.1.4, after restricting ourselves to third nearest neighbors and applying all the symmetry constraints, we are left with sixteen independent parameters

$$(\overbrace{a_0, e_0}, \overbrace{a_1, b_1, \underline{h_1}, e_1}, \overbrace{a_2, b_2, e_2, \underline{g_2}, d_2, \underline{h_2}}, \overbrace{a_3, b_3, e_3, \underline{h_3}}),$$

where a subindex n indicates a coupling between nth-nearest neighbors and the underlined parameters describe couplings between on- and off-plane phonons that vanish for the planar honeycomb lattice [20]. The corresponding matrices of coupling constants are shown in Fig 4.2. As we will see, not all the parameters are independent due to the additional constraints imposed by the existence of three acoustic bands.

The dynamical matrix is defined as a Fourier transform in the usual way

$$D_{ij}(\mathbf{k}) = \sum_{\mathbf{R}} \frac{\Phi_{ij}(\mathbf{R})}{\sqrt{M_i M_j}} e^{-i\mathbf{k}\cdot\mathbf{R}}, \tag{4.24}$$

where $\mathbf{k}$ belongs to the first Brillouin zone and M_i is the mass of atom i. After analytically diagonalizing the dynamical matrix at the high symmetry points as shown in section 4.3.3, we take care of the existence of acoustic branches by imposing $w^2(\Gamma_3^-) = w^2(\Gamma_2^-) = 0$, which will be satisfied as long as

$$\begin{aligned} a_0 &= -3(a_1 + 2a_2 + a_3), \\ e_0 &= -3(e_1 + 2e_2 + e_3). \end{aligned} \tag{4.25}$$

This leaves 14 independent parameters that can be tuned to replicate any of the eleven gapped phases or fitted to experimental or DFPT data for real materials:

$$(\overbrace{a_1, b_1, \underline{h_1}, e_1}, \overbrace{a_2, b_2, e_2, \underline{g_2}, d_2, \underline{h_2}}, \overbrace{a_3, b_3, e_3, \underline{h_3}}) \tag{4.26}$$

We close the discussion of the 6×6 dynamical matrix $D(\mathbf{k})$ for the BHL by noting that, in general, we can not expect to diagonalize it analytically, as that requires the solution of a sixth order polynomial equation. However, while this is true for generic points in the BZ, it is actually possible to obtain explicit expressions for all the frequencies and eigenstates the three high symmetry points in the BZ. This is a simple consequence of Wigner's theorem [67],

which applied to the dynamical matrix establishes that changing to a basis of symmetry adapted modes reduces $D(\mathbf{k})$ to a block-diagonal form. Specifically, each irrep of dimension d and multiplicity m gives rise to d identical $m \times m$ blocks in $D(\mathbf{k})$. A look at Eq. (4.4) shows that the largest multiplicity is two, which involves solving at most a quadratic equation. The process of diagonalization using Wigner's theorem requires the construction of symmetry-adapted modes, which are given in section 4.3.3 together with the resulting analytic formulas for the frequencies. As according to Table 4.1 the topology of phononic bands is largely determined by the ordering of frequencies at the high symmetry points, having explicit formulas greatly simplifies the study of the phase space.

4.3.3 *Spectrum of the dynamical matrix at the high symmetry points*

Group theory can also be used to simplify the diagonalization of the dynamical matrix by expressing it in a basis of symmetry-adapted modes, where it takes a block-diagonal form.

4.3.3.1 *Symmetry adapted modes*

The mechanical representation is induced from the vector representation of C_{3v}, which is the site-symmetry group for the WP 2b. The vector representation is reducible, and according to the BCS

$$V = A_1(z) + E(x, y). \tag{4.27}$$

As a consequence, we may compute separately the off-plane modes, induced from A_1 and involving atomic displacements OZ direction, and the n-plane modes, induced from E, in the OXY plane of the sample. In other words, the mechanical band representation can be split into two BRs, $M = M_z \oplus M_{xy}$, with

$$\begin{aligned} M_z(\Gamma) &= \Gamma_1^+(1) + \Gamma_2^-(1) \\ M_z(K) &= K_3(2) \\ M_z(M) &= M_1^+(1) + M_2^-(1) \end{aligned} \tag{4.28}$$

and

$$\begin{aligned} M(\Gamma) &= \Gamma_3^+(2) + \Gamma_3^-(2) \\ M(K) &= K_3(2) + K_1(1) + K_2(1) \\ M(M) &= M_1^+(1) + M_1^-(1) + M_2^+(1) + M_2^-(1). \end{aligned} \tag{4.29}$$

This facilitates the computation of the symmetry-adapted modes and clarifies their geometrical nature.

All the irreps at the Γ point have multiplicity one and according to Wigner's theorem the dynamical matrix is fully diagonalized in a basis of symmetry-

adapted modes, which therefore are automatically normal modes. The odd-parity (acoustic) modes are given by

$$\begin{aligned}
\vec{\varepsilon}_{\text{off}}(\Gamma_2^-) &= (0,0,\frac{1}{\sqrt{2}},0,0,\frac{1}{\sqrt{2}}) \\
\vec{\varepsilon}_{\text{in}}(\Gamma_3^-,1) &= (\frac{1}{2},-\frac{i}{2},0,\frac{1}{2},-\frac{i}{2},0) \\
\vec{\varepsilon}_{\text{in}}(\Gamma_3^-,2) &= (\frac{1}{2},\frac{i}{2},0,\frac{1}{2},\frac{i}{2},0).
\end{aligned} \tag{4.30}$$

while the optical modes are

$$\begin{aligned}
\vec{\varepsilon}_{\text{off}}(\Gamma_1^+) &= (0,0,\frac{1}{\sqrt{2}},0,0,-\frac{1}{\sqrt{2}}) \\
\vec{\varepsilon}_{\text{in}}(\Gamma_3^+,1) &= (\frac{1}{2},-\frac{i}{2},0,-\frac{1}{2},\frac{i}{2},0) \\
\vec{\varepsilon}_{\text{in}}(\Gamma_3^+,2) &= (\frac{1}{2},\frac{i}{2},0,-\frac{1}{2},-\frac{i}{2},0).
\end{aligned} \tag{4.31}$$

The situation changes at the K point, where the irrep K_3 has multiplicity two and the corresponding normal modes are linear combinations of the symmetry-adapted modes, while for K_1 and K_2 the modes are automatically normal. The off-plane modes are given by

$$\begin{aligned}
\vec{\varepsilon}_{\text{off}}(K_3,1) &= (0,0,1,0,0,0) \\
\vec{\varepsilon}_{\text{off}}(K_3,2) &= (0,0,0,0,0,1).
\end{aligned} \tag{4.32}$$

and the in-plane modes by

$$\begin{aligned}
\vec{\varepsilon}_{\text{in}}(K_1) &= (\frac{1}{2},\frac{i}{2},0,\frac{1}{2},-\frac{i}{2},0) \\
\vec{\varepsilon}_{\text{in}}(K_2) &= (\frac{1}{2},\frac{i}{2},0,-\frac{1}{2},\frac{i}{2},0) \\
\vec{\varepsilon}_{\text{in}}(K_3,1) &= (0,0,0,\frac{1}{2},\frac{i}{2},0) \\
\vec{\varepsilon}_{\text{in}}(K_3,2) &= (\frac{1}{2},-\frac{i}{2},0,0,0,0).
\end{aligned} \tag{4.33}$$

At the M-point only the modes for M_1^- and M_2^+ are automatically normal. The off-plane modes are given by

$$\begin{aligned}
\vec{\varepsilon}_{\text{off}}(M_1^+) &= (0,0,\frac{1}{\sqrt{2}},0,0,\frac{1}{\sqrt{2}}) \\
\vec{\varepsilon}_{\text{off}}(M_2^-) &= (0,0,\frac{1}{\sqrt{2}},0,0,-\frac{1}{\sqrt{2}}),
\end{aligned} \tag{4.34}$$

while the off-plane modes are

$$\begin{aligned}
\vec{\varepsilon}_{in}(M_1^+) &= (\frac{\sqrt{3}}{2\sqrt{2}}, \frac{1}{2\sqrt{2}}, 0, \frac{\sqrt{3}}{2\sqrt{2}}, \frac{1}{2\sqrt{2}}, 0) \\
\vec{\varepsilon}_{in}(M_2^-) &= (\frac{\sqrt{3}}{2\sqrt{2}}, \frac{1}{2\sqrt{2}}, 0, -\frac{\sqrt{3}}{2\sqrt{2}}, -\frac{1}{2\sqrt{2}}, 0) \\
\vec{\varepsilon}_{in}(M_1^-) &= (\frac{1}{2\sqrt{2}}, -\frac{\sqrt{3}}{2\sqrt{2}}, 0, -\frac{1}{2\sqrt{2}}, \frac{\sqrt{3}}{2\sqrt{2}}, 0) \\
\vec{\varepsilon}_{in}(M_2^+) &= (\frac{1}{2\sqrt{2}}, -\frac{\sqrt{3}}{2\sqrt{2}}, 0, \frac{1}{2\sqrt{2}}, -\frac{\sqrt{3}}{2\sqrt{2}}, 0).
\end{aligned} \tag{4.35}$$

4.3.3.2 *Eigenvalues of the model dynamical matrix* $D(\boldsymbol{k})$

Changing to the symmetry-adapted basis turns the dynamical matrix into a block-diagonal form, where the dimension of each block equals the multiplicity of the corresponding irrep. Thus the change of basis yields the eigenvalues for all the multiplicity one irreps, while to compute the frequencies associated with a multiplicity two irrep one has to diagonalize a 2×2 matrix. At the Γ point the resulting frequencies depend linearly on the coupling constants

$$\begin{aligned}
\omega^2(\Gamma_3^-) &= \omega^2(\Gamma_2^-) = 0 \\
\omega^2(\Gamma_3^+) &= -6(a_1 + a_3) \\
\omega^2(\Gamma_1^+) &= -6(e_1 + e_3).
\end{aligned} \tag{4.36}$$

This is no longer true at the K and M points, where computing the K_3, M_1^+ and M_2^- frequencies requires the solution of a quadratic equation due to couplings between off- and in-plane modes. The results are

$$\begin{aligned}
\omega^2(K_1) &= -3(a_1 + 3a_2 + a_3 - b_1 - b_3 + \sqrt{3}d_2) \\
\omega^2(K_2) &= -3(a_1 + 3a_2 + a_3 + b_1 + b_3 + \sqrt{3}d_2), \\
\omega^2(K_3, \pm) &= \frac{1}{2}\Bigg\{-3(a_1 + 3a_2 + a_3 - \sqrt{3}d_2 + e_1 + 3e_2 + e_3) \\
&\quad \pm \left[(-3(a_1 + 3a_2 + a_3 - \sqrt{3}d_2 - e_1 - 3e_2 - e_3))^2 + 18(h_1 + h_3)^2\right]^{\frac{1}{2}}\Bigg\}.
\end{aligned} \tag{4.37}$$

and

$$\begin{aligned}
&\omega^2(M_1^-) = 2(-2a_1 - 4a_2 + b_1 + 2b_2),\\
&\omega^2(M_2^+) = -2(a_1 + 4a_2 + 3a_3 + b_1 - 2b_2),\\
&\omega^2(M_1^+, \pm) = -a_1 - 4a_2 - 3a_3 + b_1 - 2b_2 - e_1 - 4e_2 - 3e_3\\
&\qquad \pm\left\{(-a_1 - 4a_2 - 3a_3 + b_1 - 2b_2 + e_1 + 4e_2 + 3e_3)^2 + 4(-h_1 + 2h_2)^2\right\}^{\frac{1}{2}},\\
&\omega^2(M_2^-, \pm) = -2a_1 - 4a_2 - b_1 - 2b_2 - 2e_1 - 4e_2\\
&\qquad \pm\left\{(-2a_1 - 4a_2 - b_1 - 2b_2 + 2e_1 + 4e_2)^2 + 4(h_1 + 2h_2)^2\right\}^{\frac{1}{2}}.
\end{aligned} \tag{4.38}$$

4.3.4 *Wilson loop windings*

Another benefit of having an analytical model is that Wilson loops (WL) can be easily computed using a tight binding code such as PythTB [129]. The existence of windings in the WL spectrum that cannot be eliminated by any perturbation that respects the symmetries of the system and does not close a gap guarantees that the subset of bands has nontrivial topology. We will consider a $\mathbf{b_1}$-oriented Wilson loop [125, 126] defined by

$$W(k_2) = P\ e^{-\int_0^{2\pi} dk_1 A_{i,j}(\mathbf{k})}, \tag{4.39}$$

where P means that the integral is path-ordered and $A_{i,j}(\mathbf{k}) = \langle u_i(\mathbf{k})|\partial_{k_1}|u_j(\mathbf{k})\rangle$ is the non abelian Berry connection built from the normal modes $u_i(\mathbf{k})$ of a subset of isolated bands. The eigenvalues of this WL matrix are of the form $e^{i2\pi x_1(k_2)}$, where $x_1(k_2)$ are the positions of the hybrid Wannier functions [130] along $\mathbf{a_1}$. As k_2 moves along a closed path (Γ-M-Γ), these Wannier centers move along the $\mathbf{a_1}$ direction as shown in Fig 4.4.

According to the results in Table 4.2, most of the subsets of bands *might* transform as a band representation and therefore the corresponding phases could have trivial topology. However, after realizing all the phases within the model, we were able to compute the Wilson loop spectrum for all the subsets as shown in Appendix B.1. The results imply that nine out eleven gapped phases have subsets of bands with winding in the WL spectrum and are thus topologically nontrivial, as shown in Table 4.3. Notice also that all the phases predicted to be topological with TQC techniques in Table 4.2 have indeed non-zero windings in the WL spectra.

4.4 MERGING THE AB INITIO AND ANALYTICAL MODEL RESULTS

4.4.1 *DFPT results*

In this section we relate our previously developed model to the phonon spectra of real materials with the buckled honeycomb lattice. To search for

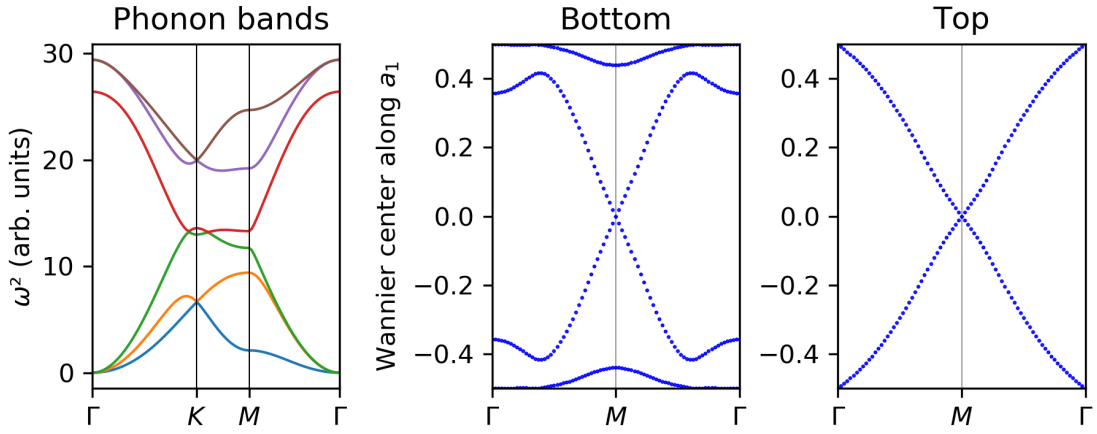

Figure 4.4: Wilson loop analysis for phase 8 in Tables 4.1 and 4.2. Phonon bands (left) and Wannier centers for the bottom (middle) and top (right) subsets of bands. The WL spectrum of the bottom bands shows trivial topology, while being non-trivial (winding) at the top subset.

Phase	**1**	**2**	**3**	**4**	**5**	**6**	**7**	**8**	**9**	**10**	**11**
Subset 1	0	0	0	2	0	0	0	0	0	0	2
Subset 2	0	0	1	2	2	0	0	1	2	1	2
Subset 3	1	2	0	0	—	—	—	—	—	—	—

Table 4.3: Windings in the WL spectrum of the isolated subsets of bands in the eleven phases. All phases with non-zero winding are topological.

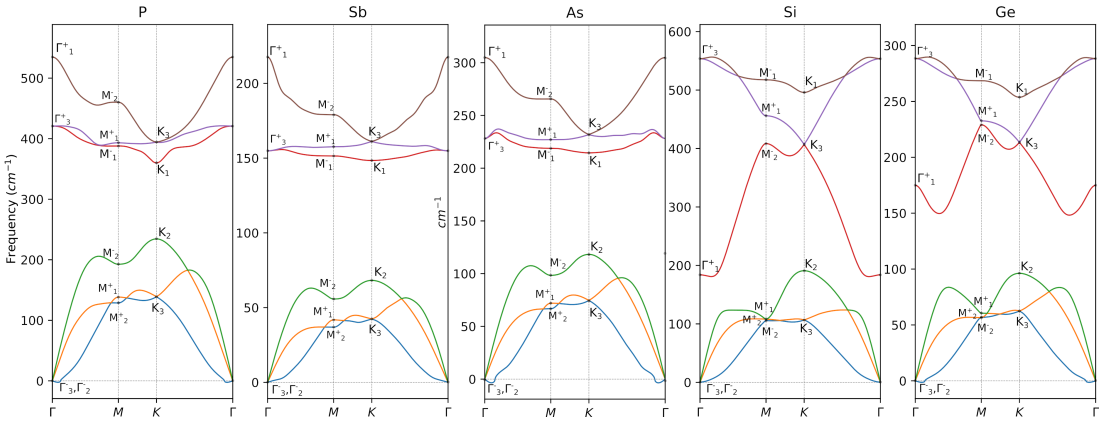

Figure 4.5: DFPT phonon dispersion bands of P, Sb, As, Si and Ge in the BHL. The irrep content of each subset of bands corresponds with phase 6 in Table 4.1 for all cases, which is not topological according to the results in Table 4.3.

phononic topological phases we use a procedure based on the following steps: (i) relax the structure, (ii) compute the phonon spectrum with DFPT and check whether it is gapped, (iii) place the material on the phase diagram by comparing the irreps of the computed dispersion bands with the ones in Table 4.1.

All DFPT [131] calculations were done using the QUANTUM ESPRESSO package [120, 121]. We parametrized the exchange-correlation functional assuming the Perdew-Burke-Ernzerhof [132] parametrization and model the electron-ion interaction with projector augmented wave pseudopotentials [133, 134] including four electrons in the valence for Si and Ge, and three electrons for P, As, and Sb. We used a kinetic energy cutoff of 60 Ry for the plane-wave basis and 600 Ry for the charge density. Brillouin zone integrals in the DFPT self-consistent loop were calculated with a $20 \times 20 \times 1$ grid and the occupancies have a Methfessel-Paxton first-order spreading [135] of 0.02 Ry. As said, prior to the phonon calculation, the structures were relaxed to the Born-Oppenheimer minimum. Then, we calculated the the force constants in a $12 \times 12 \times 1$ grid and obtained the phonon spectra by Fourier interpolation.

We searched for topological behaviour in Si, Ge, P, As, and Sb. The calculated phonon spectra and irreps are displayed in Fig 4.5, and a comparison with Table 4.1 shows that all of them are in phase 6, which is topologically trivial. However, given that nine out of eleven possible phases are topologically nontrivial, a natural question is whether a transition to a topological phase could be induced by some kind of symmetry preserving method such as isotropic strain, doping and photoexcitation. To test this possibility we numerically simulated stretching or compressing the lattice by up to a 7%, which is already a rather large deformation for experimental setups [136], but found that the materials remained in the topologically trivial phase 6. Indeed, as seen for example in Fig. 4.7 for Germanium, even such large deformations are unable to close any of the gaps at the HSPs and cause a band inversion, which would be necessary in order to change the band topology. This is due to the fact that all the gaps at the HSPs are a large fraction of the total span of the bands, so that any band inversion would require large relative changes in the frequencies, which are very hard to achieve experimentally. In other words, all five materials are physically very far from any topologically nontrivial phase.

4.4.1.1 *Mapping DFPT data to the model*

By inspecting the DFPT phonon spectrums in Figs. 4.5, it is easy to spot two groups with similar phonon spectrums. These groups correspond to the families of pentavalent (P,Sb,As) and tetravalent (Si,Ge) materials. Moreover, one can double check this assumption by comparing the force constants extracted by our DFPT calculations. As shown in Fig 4.6, the properly rescaled DFPT force constants defined in Fig 4.2 tend to cluster around two points in parameter space. In what follows we will refer to the two groups as the P and Si families.

In order to map the DFPT data to the analytical model one should notice that we can describe a material with the BHL symmetries by 14 independent

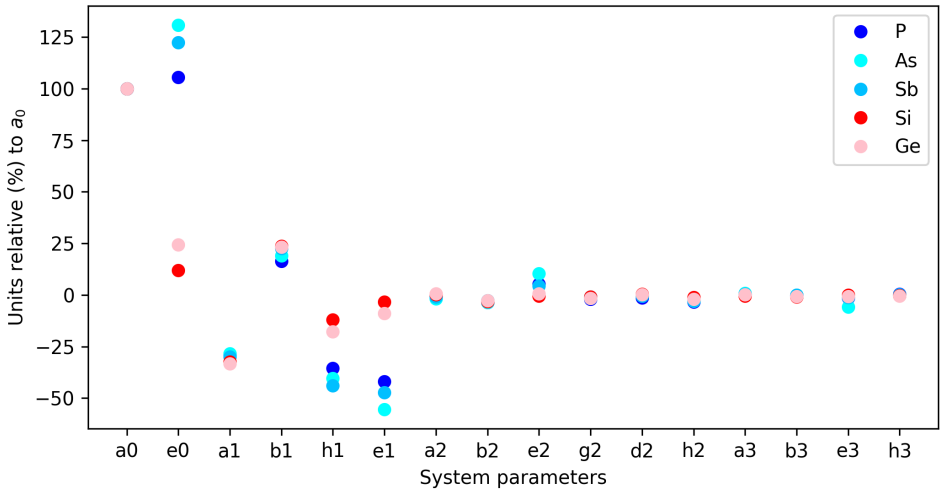

Figure 4.6: Non-zero force constants up to third nearest neighbors as defined in Fig 4.2. Dividing the force constants by a_0 is equivalent to making a change of units to the squared frequencies and is irrelevant for the topological analysis.

force constants $(a_1, b_1, ..., h_3)$, as shown in section 4.3.2. Thus, we can think of these parameters as coordinates in a 14-dimensional space where each point will correspond to a crystal with the BHL structure within our model. By inspecting the phonon spectra and irreps in Fig 4.5 one can check that phases 1 and 3 are the closest topological phases to phase 6 for the Si and P families respectively.

4.4.2 *Monte Carlo analysis*

In order to understand why all the materials studied by DFPT are so far from any topologically nontrivial phase we carried out a Monte Carlo study of the phase space of the analytical model. This is possible because we have analytic expressions for the frequencies at the HSPs as functions of the force constants, as given explicitly in section 4.3.3. Thus, to any point in the phase space specified by the values of the fourteen independent coupling constants $(a_1, b_1, ..., h_3)$ in equation (4.26) we can associate another point with frequencies $(\omega_{\Gamma_3^+}, \omega_{\Gamma_3^+}, \omega_{K_{3,1}}, \omega_{K_{3,2}}, ..., \omega_{M_2^-})$ in the space of nonzero frequencies at the HSPs. Note that we are discarding the acoustic phonon frequencies $(\omega_{\Gamma_3^-}, \omega_{\Gamma_2^-})$, as they must vanish at the Γ point.

It is important to note that the map from the fourteen independent parameters to the twelve nonzero frequencies at the HSPs is *not* invertible. Thus, there is no direct way to find a model specified by a given set of frequencies. Instead, we must do a Monte Carlo sampling of parameter space, compute the associated frequencies and select the point that most closely satisfies our requirements. This is precisely the method we followed to find model realizations for the eleven gapped phases in Table 4.1, with the resulting phonon

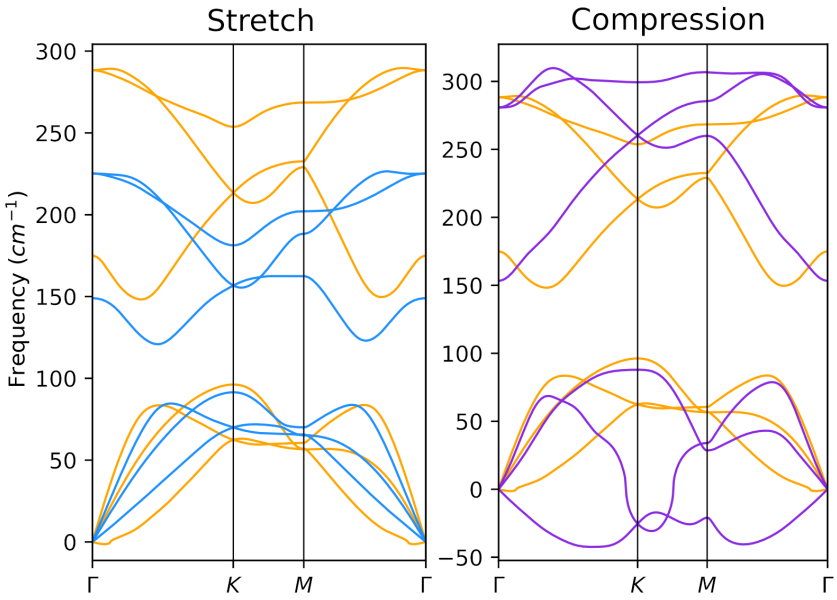

Figure 4.7: Phonon dispersion bands for Germanium BHL (orange), with a 7 % stretch (blue) and 7 % compression (purple).

bands and Wilson loops given in Appendix B.1. Comparing the computed frequencies with the irreps in Table 4.1 would immediately assign a phase to the model.

The method can also be used to find the model that best fits a real material. First, we define the following distance in the space of frequencies

$$r \equiv \frac{1}{12}\sum_{i=1}^{12}\frac{|\omega_i^2-\lambda_i^2|}{\omega_i\lambda_i}, \tag{4.40}$$

where ω_i are the frequencies at the HSPs for the real material, λ_i the frequencies for a model obtained by Monte Carlo sampling, and i labels the twelve nonzero frequencies at the HSPs. Therefore, this distance r measures the overall relative difference between the frequencies of the real material and a particular model. Once a model with sufficiently small r is obtained by random sampling of parameter space, we can use the gradient method to minimize the value of r and improve the fit. For example, the best fit ($r = 0.054$) for phosphorous is shown in Fig. 4.8.

4.4.3 *Relation between topology and long-range hoppings*

Finally, a relation can be established between the existence of topological phases and the need for sizeable couplings between far apart neighbors. In any real material the couplings between different neighbors are bound to decrease as the distance is increased, due to the localized nature of the atomic wavefunctions. In the case of the planar honeycomb lattice, where the boundaries between different phases can be given analytically, it was found that the

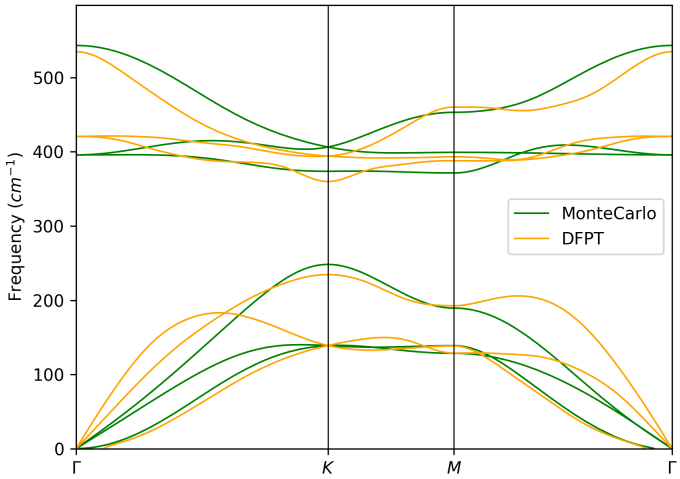

Figure 4.8: DFPT dispersion phonons for the "blue phosphorus" structure compared with the dispersion bands of a model with $r = 0.054$.

existence of two out of four possible topological phases required a relatively large third nearest neighbor force constant [20].

In order to define the average decay of the force constants as we go to further neighbours we do the following. First, we take the mean absolute values of the nonzero elements of the matrices of force constants in Fig. 4.2 for each neighbour, which are then defined as

$$\begin{aligned} m_0 &= \frac{1}{3}\left(2|a_0| + |e_0|\right) \\ m_1 &= \frac{1}{5}\left(|a_1 + b_1| + |a_1 - b_1| + |e_1| + 2|h_1|\right) \\ m_2 &= \frac{1}{9}\left(|a_2 + b_2| + |a_2 - b_2| + |e_2| + 2|d_2| + 2|g_2| + 2|h_2|\right) \\ m_3 &= \frac{1}{5}\left(|a_3 + b_3| + |a_3 - b_3| + |e_3| + 2|h_3|\right) \ . \end{aligned} \tag{4.41}$$

And later, since we are only interested in the decay ratio, we normalize by multiplying by $100/m_0$.

$$(100 : 100\,\frac{m_1}{m_0} : 100\,\frac{m_2}{m_0}, 100\,\frac{m_3}{m_0}), \tag{4.42}$$

which defines the decay ratio with respect to the on-site energies as we go to further neighbours.

By fitting our DFPT results to the analytical model, as explained above, we find that in all cases the force constants decay faster than a ratio of (100:35:4) for onsite, first and second neighbors respectively. We have explored the parameter space of the model using different decay ratios as thresholds and computed the percentage of space occupied by each phase. The results in Table 4.4 show that some of the predicted phases may be almost impossible to realize for force constants restricted to decay as in real materials, although

Ratio	100:50:10	100:40:7	100:35:4
Phase 1	1.11%	1.361%	4.81%
Phase 2	0.06%	0.05%	0%
Phase 3	9.71%	11.9%	3.09%
Phase 4	0.15%	0.14%	0%
Phase 5	0.19%	0.17%	0%
Phase 6	30.03%	49.85%	89.05%
Phase 7	10.14%	5.88%	0.06%
Phase 8	1.89%	1.22%	2.71%
Phase 9	19.87%	15.06%	0.03%
Phase 10	1.47%	0.43%	0.73%
Phase 11	25.31%	13.89%	0.02%

Table 4.4: Percentage of randomly sampled points belonging to each gapped phase. For each column the force constants are constrained to decay faster than the indicated decay ratio, which compares the mean absolute values of non-zero force constants for onsite, first and second neighbors. The mean value of third nearest neighbor constants is constrained to be smaller than that of second neighbors.

this does not exclude the possibility of metamaterial realizations. Moreover, it shows that as we approach realistic decay ratios (third column), the volume occupied by the trivial phase 6 increases. This is is consistent with the fact that all the materials considered in this paper happen to be in phase 6.

We close this analysis by noting that the phases that are most suppressed for fast decay ratios (column three in Table 4.4) are precisely the ones with higher WL windings in table 4.3. This correlation admits a simple heuristic explanation. The dynamical matrix $D_{ij}(\mathbf{k})$ is periodic in reciprocal space and therefore admits a Fourier series representation, with force constants between far away neighbors contributing to higher harmonics. On the other hand, WL windings measure the extend to which the eigenvectors of the dynamical matrix twist around as we move across de BZ, and this twisting is obviously related to the harmonics in the in $D_{ij}(\mathbf{k})$. Thus, high WL windings are favored by strong force constants between far away neighbors.

4.5 CONCLUSIONS

We have predicted all the possible topological phases for phonons on the buckled honeycomb lattice. To this end we have used TQC group theory techniques and discussed how they may be applied to phonons. Eleven gapped phases where found with nine of them being topological. This result, together with the ones for the planar honeycomb lattice [20], suggests that a huge array of topological phases exist for distinct structures. This has been confirmed

in the recently launched catalogue of 3D materials with topological phonons [19].

Finally, we have constructed the most general dynamical matrix for the buckled honeycomb lattice including all couplings compatible with the symmetries up to third nearest neighbors. The model has been used to fully characterize the topology of the possible phases using Wilson loops and to analyze the complete phase space under conditions resembling real materials. We have studied the possibility of having topological phononic phases in Si, Ge, P, As, and Sb in the buckled honeycomb structure and explained why inducing topological phases in these systems is difficult.

Part III

CHARGE-DENSITY WAVE MATERIALS

5

TOPOLOGY AND ANHARMONICITY OF THE CHARGE-DENSITY WAVE IN MONOLAYER SnP

This chapter discusses the possibility of a topological phase transition mediated by a charge-density wave (CDW) in a new 2D monolayer material, SnP. Following this idea, we explore the behavior of three different CDWs in SnP, using both density functional theory calculations and experimental synthesis to study its stability. The layered structure of its bulk counterpart, Sn_4P_3, suggests that the structure can be synthesized down to the monolayer by chemical means. However, despite the stability of the bulk, the monolayer shows unstable phonons at Γ, K, and M points of the Brillouin zone, which lead to three possible charge-density-wave phases. All three CDWs lead to metastable insulating phases, with the one driven by the active phonon in the K point being topologically non-trivial under strain. Strikingly, the ground-state structure is only revealed due to the presence of strong anharmonic effects. This, underscores the importance of studying CDWs beyond the conventional harmonic picture, where the system's ground state can be elucidated solely from the anharmonic phonon spectra.

5.1 OVERVIEW

Charge density waves are characterized by a ground state in which both the charge density and ionic positions exhibit periodic modulation relative to a high-symmetry phase [21]. As a result of their periodic modulation, CDWs can lead to changes in electrical transport properties [27, 137, 138], the thermal conductivity [139, 140], and the optical absorption [21, 141]. Particularly, CDWs in two-dimensional (2D) materials have been a major focus of research in condensed matter physics for several decades due to their potential for quantum-based technologies. More recently, CDWs have been also proposed to play a role in novel topological phenomena such as axion insulators [22], where a CDW couples two Weyl fermions in a Weyl semimetal, driving it into an insulating state [23–25]. In a more general fashion, CDWs can be also used to engineer band structures as they can gap out trivial bands, leaving an ideal Dirac or Weyl semimetal behind [142].

Interested in the relationship between charge-density waves and emerging topological features, we began this study by filtering a recently published database of two-dimensional materials [143]. Our goal was to identify semimetallic compounds with both phonon instabilities and relatively clean Fermi surfaces, as we were particularly interested in metal-insulator transi-

tions that could result in the emergence of topological phases. From the available materials, we narrowed our search to five promising candidates: AgTl, Br_2C_3Si, MoS_2, P_2Sn_2, and Sn.

The band structures and phonon spectra, as provided by the database, can be found in Fig. 5.1. These materials exhibit both phonon instabilities and a manageable number of bands crossing the Fermi level. For each of the five candidates, we analyzed the structures resulting from the most prominent unstable modes: three for AgTl, two for P_2Sn_2, and one each for Ba_2C_3Si, MoS_2, and Sn. These results, detailed in Appendix B.2, indicate that only P_2Sn_2 exhibited both insulating and stable low-symmetry phases. Further investigation into this compound revealed that its structure was derived from its bulk counterpart, Sn_4P_3. Given that Sn_4P_3 is a bilayer compound, another monolayer could also be inferred from the same compound. Thus, Sn_4P_3 and its monolayers presented to us as a promising family of compounds for studying the interactions between topology and CDWs.

In this chapter, we focus on the study of this family of tin phosphide compounds exhibiting a wide range of stable and metastable phases [144, 145]. This is largely due to their layered structure, which allows different layers to be ordered and distorted in various way. Sn_4P_3, in particular, has been reported to be a Dirac semimetal [13, 18, 76] . However, it still exists the possibility that the Dirac fermions couple through a CDW, leading to the opening of a gap in the single-particle energy spectrum that may give raise to the emergence of a topological insulator [142]. Given the lack of stability analysis in the literature and the intriguing implications of coupling Dirac fermions by means of a CDW, we studied the bulk Sn_4P_3 and its possible monolayers as possible platform for emergence of robust topological insulating phases through CDW instabilities.

It is worth noting that the treatment of CDWs is delicate to say the least. A CDW instability is usually predicted from theoretical first-principles calculations by computing the harmonic phonon spectrum and searching for unstable phonon modes. The active phonons are then tracked into the possible CDW phases. Even if the harmonic approximation may hint the order of the CDW and its associated symmetry breaking, it inevitably fails in the description of CDW physics, since, considering that phonons are temperature independent in this approximation, it can never explain when the CDW melts forming the high-symmetry structure at high temperature. In fact, a CDW transition can be detected experimentally by measuring the phonons of the high temperature phase and determining which is the phonon mode that collapses with decreasing temperature driving the CDW transition [146–148]. Therefore, a first-principles understanding of CDW physics, including the CDW order, requires non-perturbative anharmonic calculations [148–153].

The chapter is organized as follows. In Section 5.2 , by employing first-principles calculations within density-functional theory (DFT) we analyze the stability and layered structure of the bulk Sn_4P_3. In Section 5.3, we determine that two distinct monolayers can be derived from bulk Sn_4P_3, SnP and Sn_2P. Of the two monolayers, SnP displays intriguing phonon instabilities at the K

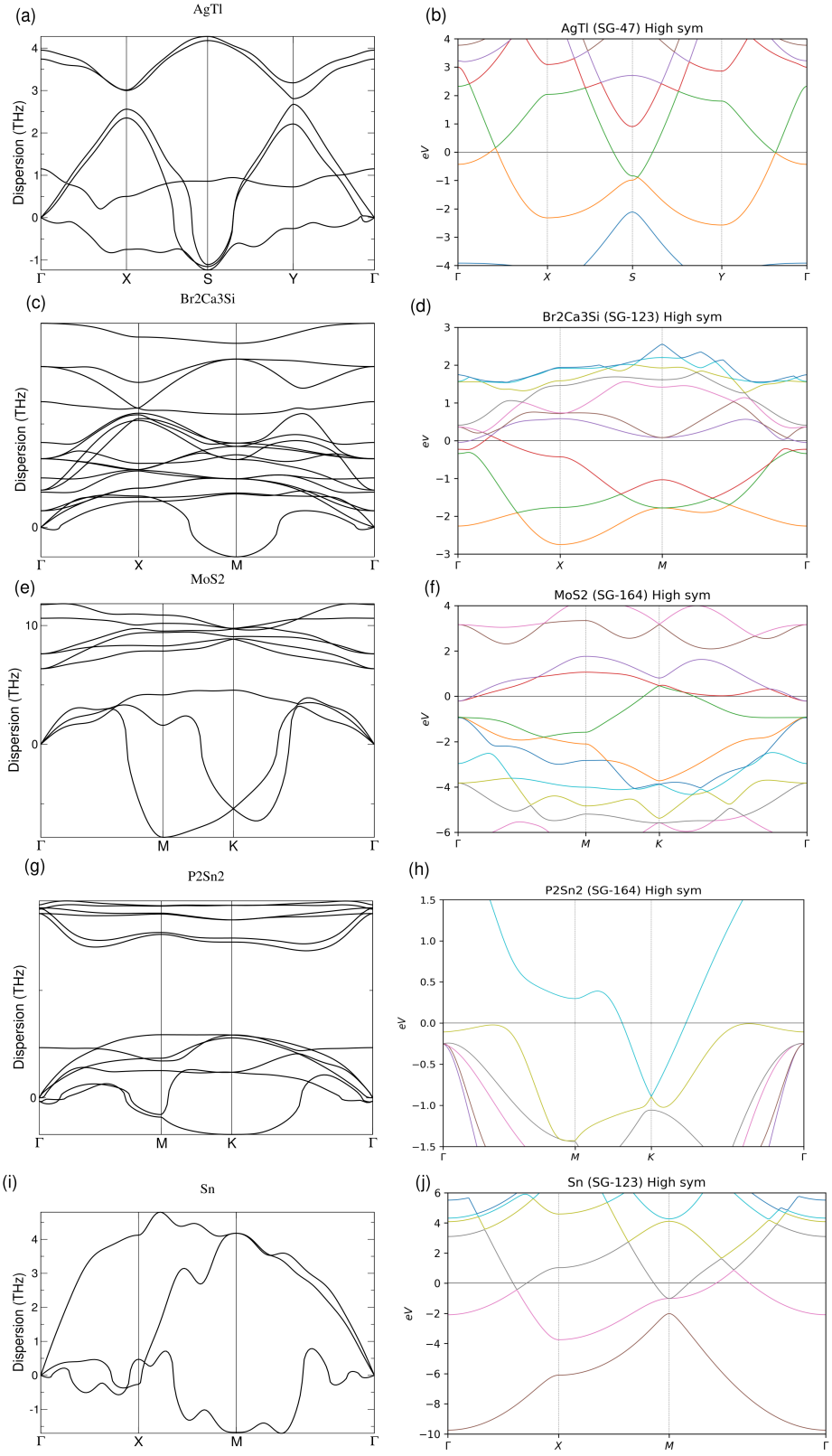

Figure 5.1: **Band structures and phonon spactra of the five initial candidates. a,b.** Phonon and electronic spectra of AgTl. **c,d.** Phonon and electronic spectra of Br_2Ca_3Si. **e,f.** Phonon and electronic spectra of MoS_2. **g,h.** Phonon and electronic spectra of P_2Sn_2. **i,j.** Phonon and electronic spectra of Sn.

and M points, presenting opportunities for the engineering of new materials with specific properties [142] by coupling and annihilating the band crossings to achieve an insulating phase. Our analysis of these instabilities yielded two distinct insulating phases, one of which could transition into a topological phase under tensile strain. Finally, in Section 5.4, we performed a full anharmonic treatment of the phonon spectra revealing a further instability at the Γ point. While the K and M phonons are stabilized by anharmonic corrections at higher temperatures, the Γ mode remains unstable, indicating the true ground state. These results emphasize the crucial role of anharmonic corrections, both in their quantity and quality, in CDW systems.

5.2 BULK Sn_4P_3

The bulk structure of the Sn_4P_3 metal (see Fig. 5.2) has a bilayered structure (space group $R\bar{3}m$) held together by strong intralayer and weak interlayer forces. This weaker interlayer coupling, together with the fact that the structure holds an odd number of electrons, could favour a layer rearrangement (a CDW) into an insulating phase at sufficiently low temperatures. To investigate this possibility, we perform first-principles calculations starting from the structure proposed by Olofsson [154].

First-principles density functional theory (DFT) calculations presented in this chapter were carried out using QUANTUM ESPRESSO (QE) [120, 121], ultrasoft pseudopotentials and a kinetic energy cutoff of 70 Ry with the Perdew-Burke-Ernzerhof parameterization (PBE) approximation for the exchange correlation functional [48] and a $13 \times 13 \times 13$ grid for the 1BZ integrals.

In order to confirm the bilayer structure, we first performed an structural relaxations until pressure fell below 0.01 kBar, to subsequently compute the electron localization function (ELF). The ELF was developed for the analysis of electron localization in real space [155, 156]. In order to define it, it is useful to first define the ratio χ as

$$\chi = \frac{t_p}{t_{HEG}}, \tag{5.1}$$

where t_p is the Pauli kinetic energy density and t_{HEG} is the homogeneous electron gas kinetic energy density [157]. Then, the ELF can be defined as,

$$\mathrm{ELF} = \frac{1}{1+\chi^2} \tag{5.2}$$

so that the ELF is mapped to run from 0 to a maximum value of 1. Values close to 1 appear in places where the electrons are very localized (with very low Pauli kinetic energy), while values of ELF = 0.5 are associated with the distribution in a homogeneous electron gas of the same density as the point of study. Thus, metals are often characterized by very flat ELF profiles of around 0.5. As shown in Fig. 5.2(a), the absence of electronic localization in the interlayer space indicates a weak bonding between the SnP and Sn_2P monolayers.

To test the stability of the compound, we computed harmonic phonons using density functional perturbation theory within a $3 \times 3 \times 3$ supercell in the

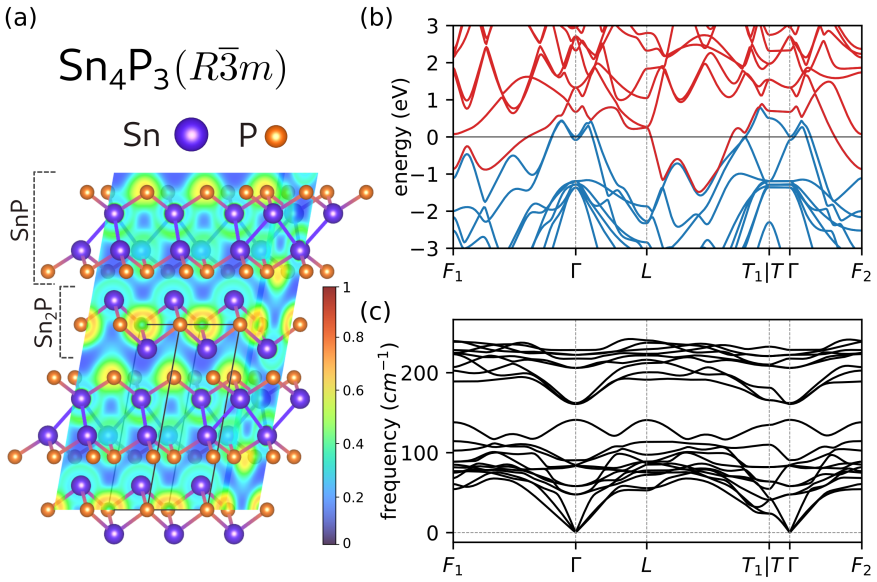

Figure 5.2: **Bulk Sn_4P_3. a.** The figure displays the bi-layered structure of Sn_4P_3, along with an Electron Localization Function (ELF) that reveals the weak Van der Waals coupling between the layers. The two potential monolayers, SnP and Sn_2P, have been marked for clarity. **b.** The accompanying electronic band structure displays a unique Dirac crossing at the L high-symmetry point (blue/red colours have been used for valence/conduction bands respectively). **c.** The stability of the system is further confirmed through the harmonic phonon spectra, which shows no indications of a charge-density wave.

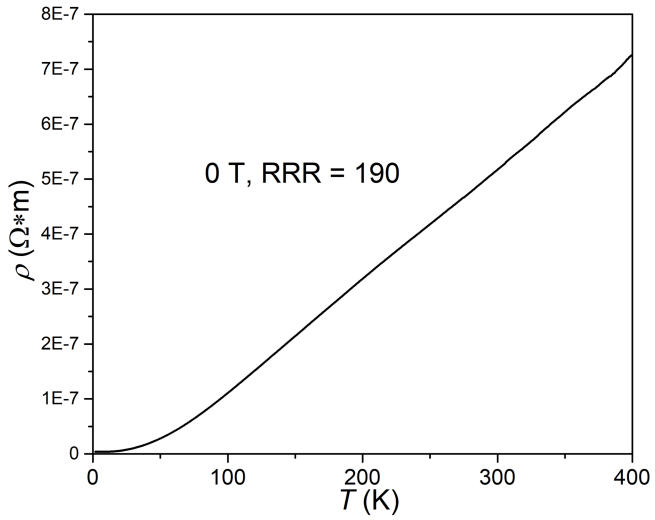

Figure 5.3: **Temperature-dependent resistivity of Sn_4P_3** single crystal, showing a residual resistance ratio (RRR) value of 190.

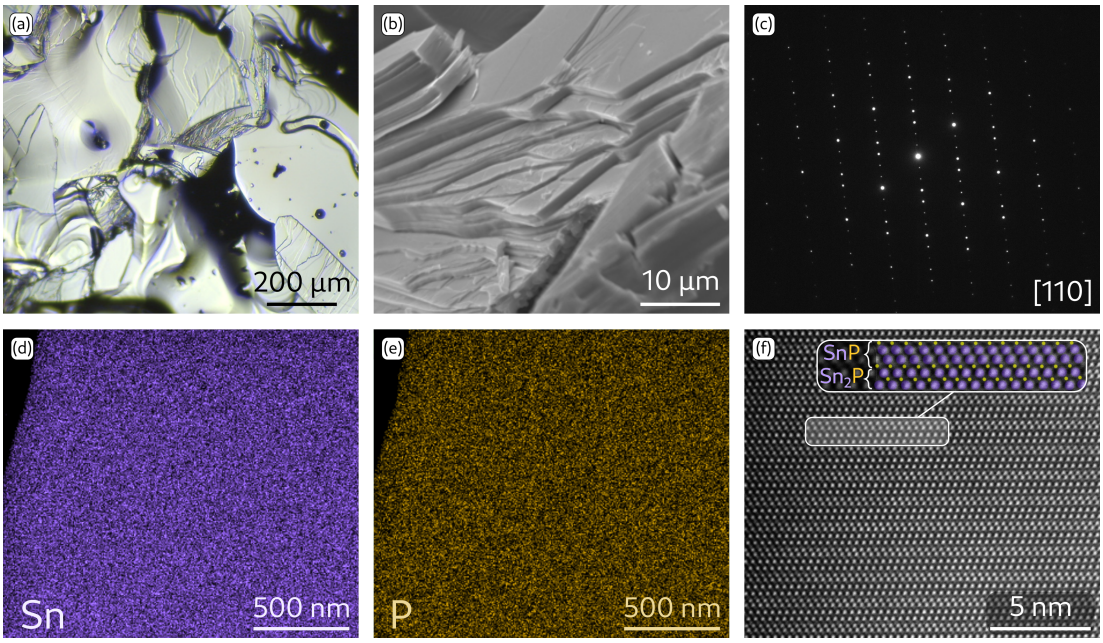

Figure 5.4: **Experimental Result of Sn_4P_3. a, b.** Optical microscope and scanning electron microscope image of Sn_4P_3 crystals, showing the layered structure. **c.** Selected area electron diffraction pattern along [110] axis, suggesting good crystalline quality. **d, e.** Elemental mapping showing homogeneous Sn and P distribution. **f.** Atomic-resolution HAADF-STEM image viewed along [110] axis; the inset shows alternating SnP and Sn_2P structures.

absence of SOC (in order to avoid unnecessary computational cost). The computed phonon spectrum of the bulk in the harmonic approximation (see Fig. 5.2(c)) reveals that the single-band crossing between the valence and conduction bands at the L point (see Fig. 5.2(b)) remains stable and the bulk does not seem to be prone to a CDW formation. It is worth noting, that while we skip SOC for the phonon calculations, the effect of spin-orbit coupling is included in electronic calculations.

In order to test the theoretical analysis outlined, our collaborators successfully synthesized Sn_4P_3 crystals by heating a mixture of Sn and P in sealed, evacuated quartz tube. Single-crystal x-ray diffraction indicates the space group $R\bar{3}m$ (No. 166), which is consistent with the previously reported results [154]. Moreover, the obtained structure by single crystal x-ray measurements is in good agreement with the structure used for the theoretical analysis (see Table B.1). As suggested by the theoretical results, temperature-dependent resistivity measurements confirm that the $R\bar{3}m$ Sn_4P_3 phase is metallic, showing no signs of a CDW from 1.8 to 400 K (Fig. 5.3). The layered structure can be clearly visualized using both optical microscope (OP) and scanning electron microscope (SEM) (Fig. 5.4 (a) and (b)). The high-quality crystalline nature of Sn_4P_3 crystals is confirmed from the selected area electron diffraction (SAED) pattern obtained along the [110] axis using TEM, as illustrated in Fig. 5.4 (c)). Furthermore, the homogeneous distribution of Sn and P within the Sn_4P_3 material is confirmed through energy-dispersive spec-

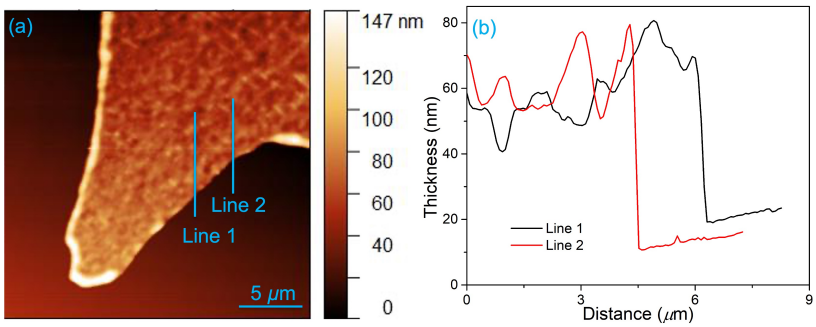

Figure 5.5: **Thickness determination of Sn_4P_3 thin flake obtained using Scotch tape.** **a** AFM image of a typical Sn_4P_3 thin flake. **b.** Height profiles of selected lines on image (a).

troscopy (EDS) mapping, as shown in Fig. 5.4 (d) and (e). Lastly, to confirm the bilayered structure of Sn_4P_3, atomic-resolution high-angle annular dark-field scanning transmission electron microscopy (HAADF-STEM) imaging was conducted, as depicted in (Fig 5.4(f)). The zoom-in inset image reveals that Sn_4P_3 is composed of alternating SnP and Sn_2P layers.

The bilayer structure of bulk Sn_4P_3 suggests that both SnP and Sn_2P monolayers may be synthesized experimentally. Despite the attempt to exfoliate the different monolayers using the scotch-tape technique, the exfoliated flakes could not be thinner than $\sim$ 40 nm. (Fig. 5.5). This thickness corresponds to about $\sim$ 30 bilayers and is therefore far from the monolayer limit. As shown in Fig. 5.4(f), the separation between the layers is too small and, hence, might prevent the bulk from delaminating into monolayers. This is reflected in the relatively high exfoliation energy from the parent layered material (around 100 meV/Å^2) computed with vdw-corrected functionals [143, 158]. However, this does not exclude that these monolayers may be synthesizable by chemical means, as it occurs in for instance in monochalcogenides [159]. Another route to explore might be chemical exfoliation, which can access 2D materials that are unobtainable via the scotch tape method [160–162]. We thus further investigate the dynamical stability of the SnP and Sn_2P monolayers by first principles.

5.3 Sn_2P AND SnP-CDW WITHIN THE HARMONIC APPROXIMATION

The Sn_2P monolayer (see Fig 5.6(a)) belongs to space group SG $P\bar{3}m1$ (No. 164) (see Appendix B.3 for its structural parameters). Our calculations, reveal that the Sn_2P monolayer exhibits a metallic band structure, as illustrated in Fig 5.6(b), while its harmonic phonon spectra (see Fig 5.6(c)) shows some instabilities near Γ, corresponding to the out-of-plane acoustic phonon mode. This result suggests that the Sn_2P monolayer may be subject to a rippling instability [163]. Considering that the band structure of this monolayer is typical of a metal, this rippling instabilities are not expected to yield any significant change to the electronic structure, keeping the structure as metallic.

The band structure of the SnP monolayer is, on the contrary, very interesting. This monolayer belongs to space group SG $P\bar{3}m1$ (No. 164) and consists of tin and phosphorus atoms at 2d and 2c Wyckoff positions, respectively. The structure can be described as a buckled honeycomb of tin atoms sandwiched between two phosphorus triangular lattices, as illustrated in Fig 5.6(d). Its band structure exhibits an interesting single crossing point at the K high-symmetry point, as shown in Fig 5.6(e). Considering that the harmonic phonon spectrum in Fig 5.6(f) shows two instabilities at the K and M points, these modes can act as active phonons through which the CDW could couple the Dirac points at K, thereby leading to an insulating state.

The first-principles calculations for the monolayer materials were performed in the same manner as those for the bulk. Initially, the structures were relaxed, followed by computations of both the band structures and phonons. The parameters used for these calculations were also identical, with the sole difference being the k-grid, which in this case is $20 \times 20 \times 1$, and the supercell for the DFPT calculations is $6 \times 6 \times 1$.

5.3.1 *Electron-phonon linewidth and nesting function*

To delve deeper into the origin of the phonon instabilities, we conducted electron-phonon linewidth and nesting function calculations. The electron-phonon matrix elements $g^{\mu}_{n\mathbf{k},m\mathbf{k}+\mathbf{q}}$ for a phonon mode μ with momentum $\mathbf{q}$ and two electronic states in bands n and m with electronic momenta $\mathbf{k}$ and $\mathbf{k}+\mathbf{q}$ are calculated withing DFPT as in equation (2.45). Then, the electron-phonon contribution to the phonon half-widht-half-maximum ($HWHM_{elph,\mu}$) linewidth for mode μ with momentum $\mathbf{q}$ can be calculated as given in (2.51). Notice that $HWHM_{elph,\mu}$ is independent from the frequency $\omega_{\mu}(\mathbf{q})$, since this term cancels with the one from $g^{\mu}_{n\mathbf{k},m\mathbf{k}+\mathbf{q}}$, which allows us to define it even for negative frequencies. The $HWHM_{elph,\mu}$ was computed using a $48 \times 48 \times 1$ grid and a Gaussian smearing of 0.003 Ry for the Dirac deltas. The nesting function $\zeta(\mathbf{q})$ (2.52) was computed using the same grid and Gaussian smearing.

We conducted computations of the electron-phonon linewidth and nesting function for the high-symmetry SnP phase. As shown in Fig. 5.7(b), the electron-phonon linewidth displays notable peaks for the phonon branch responsible for the charge-density wave. However, these peaks do not correspond to the most significant instabilities observed at the K point. Moreover, neither the nesting function, depicted in Fig. 5.7(d), aligns with the trend of the unstable branch. This discrepancy suggests that neither the nesting function nor the electron-phonon coupling serve as primary instigators of the observed CDW. The contributions to the Born-Oppenheimer energy $V^{BO}(\mathbf{R})$ can be decomposed into distinct components: $T_e + V_{ee} + V_{e-I}(\mathbf{R}) + V_{I-I}(\mathbf{R})$, where $\mathbf{R}$ are the ionic positions and the terms represent the electronic kinetic energy, electron-electron interaction, electron-ion interaction and ion-ion interaction respectively. While the electron-phonon coupling arises from the $V_{e-I}(\mathbf{R})$ term; in this instance, the minimization of the BO energy is predominantly domi-

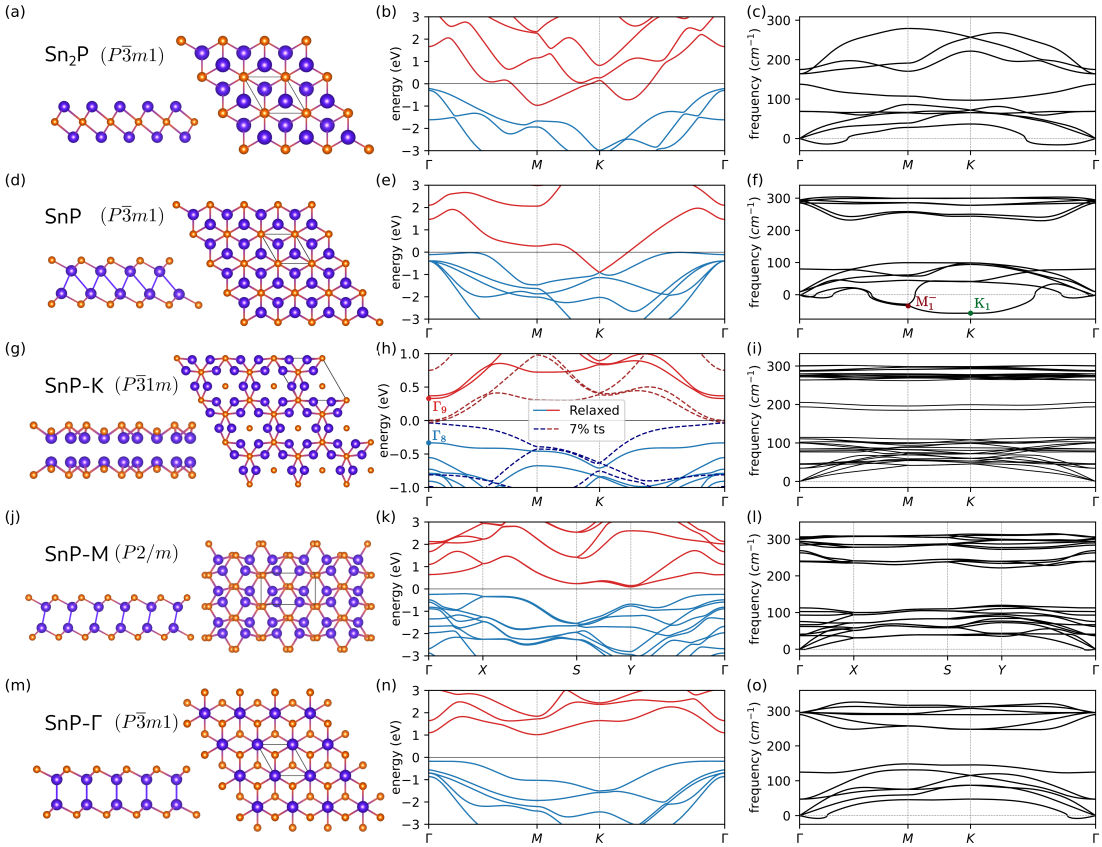

Figure 5.6: **Sn_2P, SnP, SnP-K, SnP-M and SnP-Γ monolayers. a, d, g, j, m.** Represent the atomic structures of the two original monolayers (Sn_2P,SnP) and the CDW phases (SnP-K, SnP-M, SnP-Γ) from the side and top views. **b, e, h, k, n.** Show the corresponding band structures of each of the monolayers. In **h**, we demonstrate that by applying an isotropic tensile strain of 7% the band gap closes, leading to an inversion of Γ9 and Γ8 irreps, and resulting in a topological phase transition. **c, f, i, l, o.** Represent the harmonic phonon spectra of each of the monolayers. As shown in **f**, the SnP monolayer exhibits two active phonons at the M and K points, respectively.

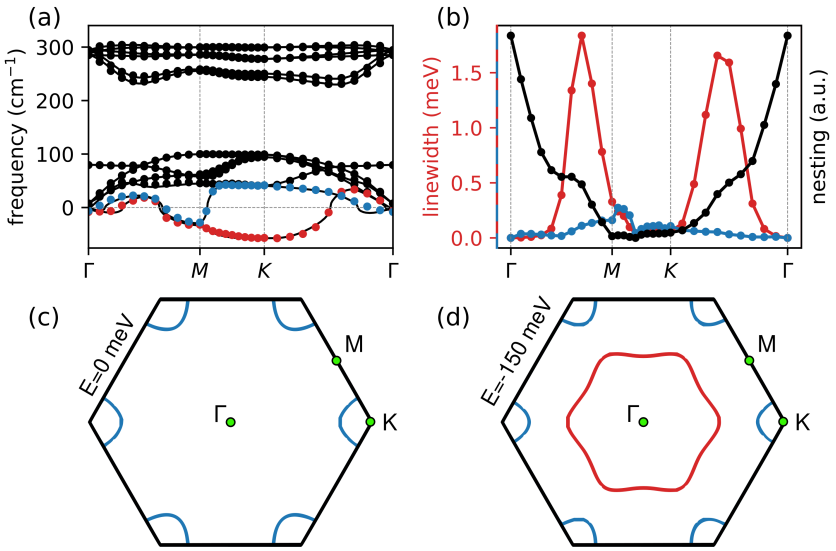

Figure 5.7: **Electron-phonon linewidth, nesting function and Fermi surface of the SnP high-symmetry phase. a.** Phonon spectra of the SnP high-symmetry phase. The continuous line represents the interpolation derived from the 6x6x1 grid, while the dots signify specific DFPT calculations at individual k points. **b.** Shown here are the electron-phonon linewidths for the two most unstable modes highlighted in blue/red in caption **a**. Additionally, the nesting function is represented along the ΓMKΓ path. **c.** The Fermi surface of the SnP high-symmetry phase exhibits a single Fermi pocket at the K point. **d.** Constant energy cut at an energy level of −150 meV. Besides the pocket at K, a new quasi-hexagonal pocket emerges, centered at Γ. This pocket harbors a high density of states due to the band flatness near Γ (Fig. 5.6(e)), and it is responsible for the "saddle-like" points in the nesting function (**b**) along the ΓM and ΓK lines.

nated by the ion-ion interaction $V_{I-I}(\mathbf{R})$, leading to large structural changes between the different phases. Consequently, it is not unexpected that both the nesting function and electron-phonon linewidth peak at different points than those of maximum instabilities.

5.3.2 *The low symmetry structures*

In order to elucidate the low-symmetry structures, we performed a distortion of the SnP monolayer based on the active phonons at the K and M points and relaxed the structure into the minimum of the Born-Oppenheimer energy surface consistent with the symmetry breaking. The resulting structures belonged to space groups $P\bar{3}1m$ and $P2/c$, respectively, in line with the group theory restrictions for phonons transforming under irreducible representations K_1 and M_1^- [66], which are the irreducible representations of the active modes. Then, we computed the band structure and phonon spectra in both cases, which in turn allows us to analyze both the stability and topology. Subsequently, we will refer to the resulting structures from the condensation of the K and M modes as SnP-K ($P\bar{3}1m$) and SnP-M ($P2/c$) (see Fig 5.6 (g and j)).

Both low-symmetry structures turned out to be insulating phases (see Fig 5.6(h,k)), as well as dynamically stable according to the computed harmonic phonon spectra (see Fig 5.6(i,l)). This means that these two structures can be *a priori* stabilized experimentally, showing a large polymorphism of the SnP monolayer.

A topological analysis based on symmetry indicators using topological quantum chemistry (TQC) [13, 18, 76] classified both SnP-K and SnP-M as topologically trivial phases. Nonetheless, it is worth noting that this analysis only verifies for sufficient conditions for topology and not necessary ones. This analysis was done using the IrRep code [164] together with tools provided by the Bilbao Crystallographic Server (BCS) [68–70]. Despite the triviality of the bands of the distorted phases, the insulating gap of SnP-K is remarkably small. This places this monolayer close to a topological transition: a band inversion that interchanges the $\Gamma 8$ and $\Gamma 9$ irreducible representations at the Γ point would lead to a topological phase.

To check this possibility, we perform a more accurate characterization of the gap by carrying out a band structure calculation using an hybrid functional. The bandstructures computed using hybrid functionals were done with VASP [133, 134] in a $9 \times 9 \times 1$ grid under the Heyd–Scuseria–Ernzerhof (HSE) approximation with the HSE06 parametrization [165]. As a result, we found that under an isotropic tensile strain of 7% (see Fig 5.6(h)), the SnP-K monolayer transitions into a topological insulating phase with the topological indices $\mathbb{Z}_{2w,3} = 1$ and $\mathbb{Z}_4 = 2$. Similar strain ranges have previously been realized in different monolayer materials such as graphene [166] and MoS_2 [167]. Conversely, the SnP-M phase is further away from a topological transition, and strain is not expected to give rise to electronically relevant phases.

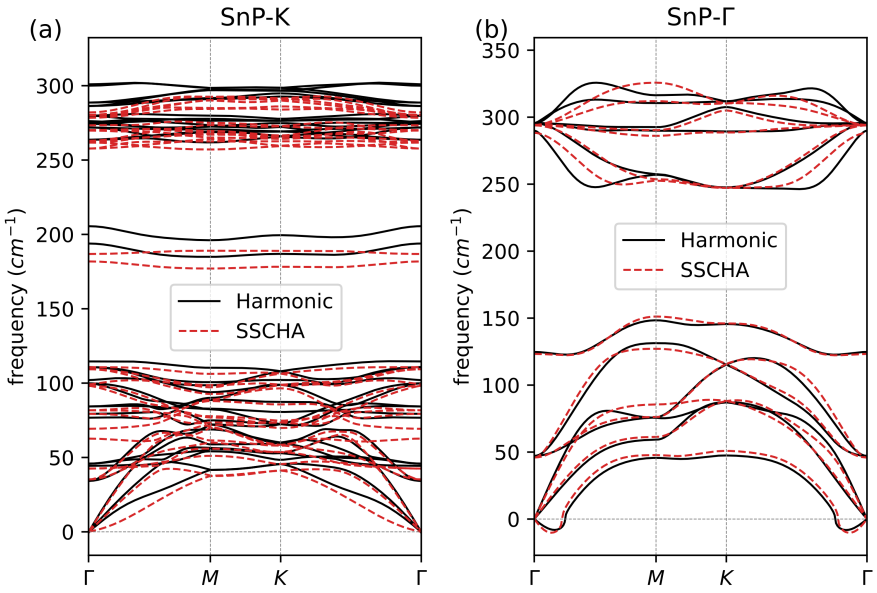

Figure 5.8: **Anharmonic phonon spectra of SnP-K and SnP-Γ monolayers. a** and **b** show the anharmonic (the free energy Hessians) and harmonic phonon spectrums of SnP-K and SnP-Γ respectively. In both cases the SSCHA calculation has been done at T = 0 and the plotted spectra corresponds to the 3x3x1 grid.

5.4 THE IMPACT OF ANHARMONIC EFFECTS

All our analysis so far relies on the harmonic approximation, which is questionable in the vicinity of CDWs. In order to further analyze the stability of the predicted distorted phases, we perform anharmonic first-principles calculations of the phonon spectra of both SnP (high-symmetry phase) and SnP-K (low-symmetry phase) at different temperatures. The anharmonic phonon calculations were done under the Stockastic Self-Consistent Harmonic Approximation (SSCHA) [62, 63, 168] as implemented in the SSCHA code [64]. In order to capture all the relevant high-symmetry points, the free energy Hessians (SSCHA anharmonic phonons) were done in both $2 \times 2 \times 1$ and $3 \times 3 \times 1$ supercells in all cases and with the inclusion of the fourth order terms. As shown in Fig 5.8, the anharmonic results support the idea of the SnP-K phase being stable after the CDW. On the other hand, the anharmonic phonons for the SnP monolayer at different temperatures can be seen in Fig 5.9(a) and present some unexpected outcomes: both the K and M active phonons stabilize with temperature, with the latter stabilizing within the 0 to 200 K range. However, although this seems to support the initial idea of the K phonon leading the CDW, the Γ point, in fact, shows a new negative degenerate phonon frequency transforming under irreducible representation Γ_3^+. This Γ-point instability increases with temperature, contrary to the evolution of K and M modes.

5.4.1 *Calculation of the Born-Oppenheimer energy surface.*

To further understand this behavior and the nature of this purely anharmonic active mode, we explore the Born-Oppenheimer energy surface of the SnP monolayer as we distort the structure according to different active modes.

In order to compute the Born-Oppenheimer (BO) energy surface, we calculate the energy by displacing the ions according to the corresponding active phonons. In the harmonic approximation, the displacement $\mathbf{u}$ of atom i in the unit cell $\mathbf{T}$ can be expressed as

$$\mathbf{u}_i(\mathbf{T}) = \mathrm{Re}\{\sum_{s\mathbf{k}} q_s(\mathbf{k}) \frac{\boldsymbol{\epsilon}_i^s(\mathbf{k})}{\sqrt{M_i}} e^{i\mathbf{k}\cdot\mathbf{T}}\}. \tag{5.3}$$

Here, s labels the mode, M_i represents the ionic mass of atom i, $\boldsymbol{\epsilon}_i^s(\mathbf{k})$ is the polarization vector, and $q_s(\mathbf{k})$ is the order parameter associated with the s mode at wave number $\mathbf{k}$. By plotting the energy against the order parameter q, we obtain the BO energy surface along that specific direction in the order parameter space.

In Fig. 5.9(b) we show the energy dependence as we displace the ions according to the K active phonon. The energy surface displays a double-well shape, which explains both the instability of the phonon within the harmonic approximation as well as the anharmonic hardening of the phonon frequency. Essentially, by increasing the temperature and hence the broadening of the ionic wave function, the potential starts to feel less unstable and more confining. However, this is not the case for the degenerate phonon that develops an instability at Γ within the SSCHA.

As the active phonon is degenerate, this results in a two-dimensional space of deformations that are energetically equivalent just in the harmonic limit. In order to analyze this bidimensional order parameter space (q_1, q_2), we perform calculations in six different directions within this space. To sample this region thoroughly, we evaluate the order parameter along the directions $(\cos(\alpha)q_1, \sin(\alpha)q_2)$, where α takes values of 0, $\frac{\pi}{18}$, $\frac{\pi}{9}$, $\frac{\pi}{6}$, $\frac{2\pi}{9}$, and $\frac{5\pi}{18}$. This sampling strategy effectively covers 120 degrees of the order parameter space. Then, by taking advantage of the system's three-fold symmetry, we can obtain a complete sampling of the (q_1, q_2) space and compute the energies (Fig 5.9(b)). Then, the whole energy surface can be interpolated as seen in Fig 5.9(c). On this occasion, instead of a double-well, the energy surface resembles, rather, a triple saddle point with a small potential well in the middle. This small well explains why this unstable phonon is invisible in the harmonic approximation. However, the quantum nature of the ions, even at zero temperature, is enough to escape the potential well, thus leading to a purely anharmonic CDW. Consequently, the increase of temperature only renders the structure more unstable.

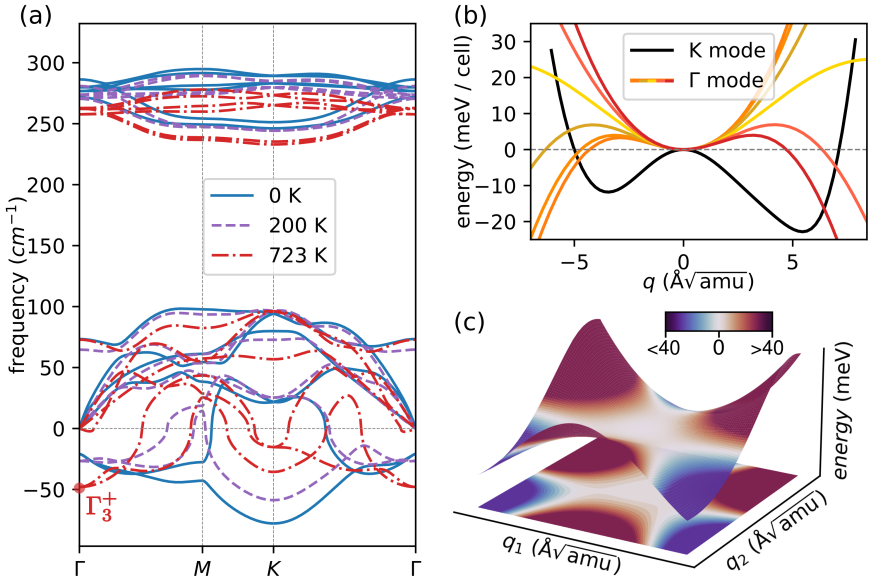

Figure 5.9: **Anharmonic phonons of SnP monolayer and Born-Oppenheimer energy surfaces. a.** The inset shows the anharmonic phonon (free energy Hessians) behavior at various temperatures. The data reveals that the active phonons located at M and K points exhibit greater stability with rising temperatures, while a new purely anharmonic active phonon emerges at Γ, which becomes increasingly unstable as the temperature increases. **b.** Born-Oppenheimer energy surface as the system is displaced according to the K and Γ active phonons. In the case of the degenerate Γ mode, a bidimensional space of deformations is explored through different cuts. The K phonon displays a characteristic "Mexican hat" shape, which becomes more stable as temperature increases, along with quantum fluctuations. Conversely, the Γ mode appears as a saddle point with a small potential well. **c.** The complete energy surface of the Γ active phonon is shown in this inset. The triple saddle point shape with a small minimum at the center explains why the harmonic approximation fails to capture such instability and why the instability increases with temperature.

5.4.2 *The ground state* SnP-Γ

Unlike the active phonons at K and M, the unstable phonon at Γ can not be stabilized with temperature, and thus yields to another possible CDW in the SnP monolayer, showing the polymorphism of this 2D material. We solved the structure arising from the condensation of this degenerate mode by relaxing the lowest energy structure found in the energy surface (Fig 5.9(c)). The irreducible representation Γ_3^+ leads to a structure with space group $C2/m$, which after, relaxes back to space group $P\bar{3}m1$. Despite having the same space group, in the case of SnP-Γ, tin and phosphorus atoms exchange Wyckoff positions in order to minimize the energy of the system (see Fig 5.6(m)), which again leads to an insulating phase (Fig 5.6(n)) classified as trivial according to the TQC analysis. The harmonic phonons shown in Fig 5.6(o) confirm the stability of this SnP-Γ phase (which was also confirmed with anharmonic phonons shown in Fig. 5.8(b)).

Moreover, the energy difference per SnP pair relative to the high-symmetry phase is lowest for SnP-Γ, with $\Delta(\text{SnP}{-}\Gamma) = -296$ meV. In comparison, the energy differences for both $\text{SnP}-\text{K}$ and $\text{SnP}-\text{M}$ are $\Delta(\text{SnP}-\text{K}) = -77$ meV and $\Delta(\text{SnP}-\text{M}) = -37$ meV, respectively. This indicates that SnP-Γ represents the true ground state of the SnP monolayer, while SnP-K and SnP-M are metastable phases.

5.5 CONCLUSIONS

In summary, we have studied the stability and properties of Sn_4P_3 and its monolayers in relation to CDW formations. The stability of bulk Sn_4P_3 is confirmed through both density functional theory calculations and experimental synthesis. The two possible monolayers that this bulk material can yield, SnP and Sn_2P, show phonon instabilities that may lead to metal-insulator transitions. The Sn_2P monolayer is not expected to change its electronic properties, as it is only subject to rippling instabilities. However, the SnP monolayer shows a large polymorphism with the formation of different stable and metastable insulating CDW phases, all of which couple the Dirac points of the parent structure. Remarkably, one of the described phases can be turned into a topological insulator by strain, and the true ground state of the SnP monolayer only is identified thanks to anharmonic effects. Despite, the predicted polymorphism of SnP could not be identified by exfoliating the bulk, chemical methods in the few-layers limit may be able to synthesize the anticipated different phases.

6

CHARGE-DENSITY WAVE IN THE CsV_3Sb_5 KAGOME METAL

This chapter is dedicated to the study of lattice effects beyond the harmonic approximation in the charge-density wave state of the recently discovered AV_3Sb_5 family of kagome metals. By employing a non-perturbative treatment of anharmonicity from first-principles calculations, we reveal that the charge-density transition in CsV_3Sb_5 is driven by the large electron-phonon coupling of the material and that the melting of the CDW state is attributed to ionic entropy and lattice anharmonicity. The calculated transition temperature is in very good agreement with experiments, implying that soft mode physics are at the core of the charge-density wave transition. Contrary to the standard assumption associated with a pure kagome lattice, the CDW is essentially three-dimensional as it is triggered by an unstable phonon at the L point. The absence of involvement of phonons at the M point enables us to constrain the resulting symmetries to six possible space groups. The unusually large electron-phonon linewidth of the soft mode explains why inelastic scattering experiments did not observe any softened phonon. We foresee that large anharmonic effects are ubiquitous and could be fundamental to understand the observed phenomena also in other kagome families.

6.1 OVERVIEW

The kagome lattice, composed of three triangular lattices rotated 120 degrees with respect to each other, stands as one of the most thoroughly investigated hexagonal lattices, offering a wealth of intriguing electronic properties linked to its distinct geometry [169]. Its multilattice nature allows for the emergence of flat bands [170–173], which, in turn, lead to high electronic correlation effects provided they fall into the vicinity of the Fermi energy [174–177], while its triangular arrangement provides a natural platform for magnetically frustrated systems [171, 178]. The presence of Dirac cones in the band structure leads also to non-trivial topological effects [174, 179]. Consequently, the recently discovered family of Kagome materials, AV_3Sb_5 with $A = Cs, K, Rb$ [26], has garnered significant attention, as it provides a platform for exploring the interplay between electronic correlations, frustrated geometry, charge-density waves (CDWs), topology, and even superconductivity.

All compounds within the AV_3Sb_5 family exhibit a CDW at a temperature of approximately 90 K [26]. The CDW holds a crucial significance because below T_{CDW} a plethora of novel and intriguing physical phenomena have been reported. These include switchable chiral transport [27, 28], specular

optical rotation [29], or the presence of a chiral flux phase [30–32] accompanied by loop currents. This unconventional nature is also manifested in the superconducting order observed below 2.5 K for CsV_3Sb_5 [180], with reports, for instance, of unconventional superconductivity [181–184], multi-charge flux quantization [185], and chiral superconductivity [186].

The true nature of the CDW and the resulting atomic structure remain open questions. Moreover, it is not clear what the intricate relation between the CDW order and all observed unconventional phenomena is. In fact, the absence of consensus regarding the CDW structure hinders the understanding of the emerging properties, mainly because they might be constrained by symmetry. Just below $T_{CDW} \sim 94$ K, the prevailing experimental evidence supports a three-dimensional $2 \times 2 \times 2$ structure for the CDW [33, 187–189], but without a consensus on whether the CDW breaks six-fold symmetry [176, 187, 190–192]. Some works report a second CDW around $T_{CDW_2} \sim 60$ K [30, 176, 187, 188, 191, 193, 194], in which a $2 \times 2 \times 4$ CDW [195, 196], a mixture of $2 \times 2 \times 2$ with $2 \times 2 \times 4$ orders [197], or a transition between both types of ordering [194] have been reported. The emergence of the second CDW seems to coincide with the onset of unconventional phenomena, including the chiral flux phase [30], activated chiral transport [27], and the disruption of C_6 symmetry [176, 191]. It is important to note that there are also reports which do not observe this second CDW [189]. In fact, it is not clear whether this exotic phenomena is intrinsic to the material or whether it is imposed by external perturbations [177]. Doubts also persist on the conservation of time-reversal symmetry, with contradictory results from muon spin spectroscopy [30, 198, 199] and magneto-optical Kerr effect [29, 190, 200].

The origin and character of the CDW also remains a subject of debate. At first glance, the nesting mechanism [181, 188, 201–206] appears natural, aligning perfectly with the fermiology of the pure kagome lattice and resulting in the widely experimentally confirmed 2×2 modulation within the plane [30, 33, 176, 187–189, 191, 207]. This nesting paradigm has also been employed to account for the reported unconventional character of the CDW [202, 203, 208, 209]. On the other hand, there are also multiple reports suggesting an electron-phonon driven mechanism [189, 207, 210]. With regard to the CDW character, reports concur on the absence of observed softening in the phonon spectrum in Raman [187, 189] and inelastic x-ray scattering [33] experiments, suggesting a first-order transition to the CDW. Despite a discontinuity observed in the lattice parameters at T_{CDW} supports this picture [211], the discontinuity is so minute that a soft phonon mode driven CDW should not be excluded, which would be consistent with the general mechanism in other CDW materials like transition-metal dichalcogenides [147, 148, 150]. Theoretical calculations performed thus far do not clarify these issues as they are mostly limited to phenomenological models [201, 203–206, 212] or to *ab initio* calculations within the standard harmonic approximation for the phonons [181, 187, 213], which is known to break down in CDW systems [148, 150, 151, 214].

With such an enigmatic CDW, and having that in CDW systems anharmonic effects are expected to play a significant role, the AV_3Sb_5 family of Kagome

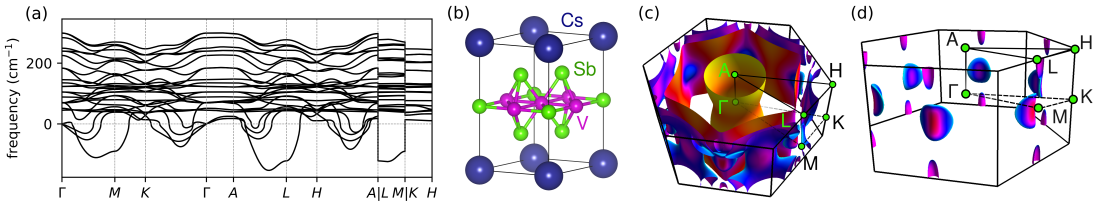

Figure 6.1: **Harmonic phonons and Fermi suface in the high-symmetry phase of CsV_3Sb_5. a.** Calculated harmonic phonon dispersion of CsV_3Sb_5 in the P6/mmm phase. The harmonic spectrum exhibits two main instabilities at the M and L high-symmetry points. **b.** Unit cell for CsV_3Sb_5. The vanadium atoms (pink) form a perfect kagome lattice. **c.** Fermi surface within the first Brillouin zone with labeled high-symmetry points. **d.** While most of the Fermi surface exhibits low dispersion in the z direction, there are closed Fermi surface pockets containing Van Hove singularities situated near the M and L points, indicating the three-dimensional nature of CsV_3Sb_5.

metals stands as an excelent platform to study the implications of lattice effects beyond the harmonic approximation. By incorporating anharmonic effects, it becomes possible to accurately predict phonon softening [148, 150–152], predict the CDW temperature. While in the other hand, it could be that these effects stabilize the high-symmetry structure above T_{CDW} [215]. Thus, in this chapter we make use of first-principles density-functional theory (DFT) calculations including a non-perturbative treatment for lattice anharmonicity to study the CDW in CsV_3Sb_5.

The structure of this chapter is as follows. In Section 6.2, we demonstrate that the CDW melts due to lattice anharmonicity and that soft mode physics play a dominant role in the CDW transition. Moreover, our prediction for the CDW temperature T_{CDW} is in very good agreement with experiments. Conversely, in Section 6.3, we address the opposite question of what triggers the CDW state. We conclude that the softening of the L phonon triggering the CDW, is a consequence of its extraordinary large electron-phonon coupling, discarding pure electronic nesting as the main destabilizing force. This is consistent with a second-order phase transition as well as with a weak first-order character. Then, in Section 6.4 we explain that the phonon softening is not observed experimentally [33] due to its huge broadening, a consequence of the large electron-phonon and anharmonic interactions of the soft mode. To conclude, in Section 6.5, we assume a second-order phase transition alongside the observed absence of condensation in the M mode. This assumption enables the application of Landau formalism, effectively narrowing down the potential space groups that may emerge. To complement this analysis, we present the Raman and infrared spectra for each possible structure.

6.2 THE MELTING OF THE CHARGE-DENSITY WAVE

In order to study the charge-density wave, we conducted first-principles density functional theory (DFT) calculations using the Quantum Espresso package [120, 121]. We used the generalized gradient approximation with the Perdew-Burke-Ernzerhof parameterization [48] together with projector-augmented wave pseudopotentials [216] generated by Dal Corso [217] and considering 9/5/13 valence electrons for cesium/antimony/vanadium. In all cases, we used a energy cutoffs of 60/600 Ry for the wavefunctions/density with a Methfessel-Paxton smearing [135] of 0.002 Ry. The structure was first relaxed using a $16 \times 16 \times 10$ grid, without accounting for spin-orbit coupling (SOC) and was stopped when pressures were below 0.01 kBar. Subsequently, harmonic phonons were computed using a $6 \times 6 \times 4$ phonon grid. Then, SOC was included to compute the electronic band structures. To generate the Fermi surface plots, we employed the Wannierization procedure implemented in Wannier90 [218], along with WannierTools [219]. First, we obtained a tight-binding model with a Wannierization considering d and p orbitals in vanadium and antimony sites. Then, we calculated the Fermi surface as implemented in WannierTools for a $200 \times 200 \times 100$ grid.

The DFT harmonic spectrum of the CsV_3Sb_5 high-symmetry phase exhibits a significant number of lattice instabilities (Fig. 6.1(a)), in agreement with previous works [181, 213]. Two primary instabilities can be observed near the M and L points, coinciding with the nesting vectors of the van Hove Fermi pockets (Fig. 6.1(d)). The most prominent instability occurs at a specific point along the AL line, which we will refer to as the AL mode. However, the instabilities in the phonon spectra of CsV_3Sb_5 are highly sensitive to the electronic temperature used in the DFT calculations to perform integrals over the Brillouin zone [201]. It is important to note that the electronic temperature commonly referred to in *ab initio* calculations is merely a means to smear out the density of states for faster convergence [135], maintaining a relation with the electronic temperature, but without a one-to-one mapping. A more meticulous analysis of the comparison between the L and AL instabilities is presented in Fig. 6.2(a), where we studied the Born-Oppenheimer energy landscape by distorting the structure according to both L and AL modulations independently.

In order to compute the Born-Oppenheimer (BO) energy surface, we calculate the energy by displacing the ions according to the corresponding active phonons. In the harmonic approximation, the displacement $\mathbf{u}$ of an atom s in the unit cell $\mathbf{T}$ can be expressed as

$$u_s^\alpha(\mathbf{T}) = \mathrm{Re}\{\sum_{\mu\mathbf{k}} q_\mu(\mathbf{k}) \frac{\epsilon_{\mu s}^\alpha(\mathbf{k})}{\sqrt{M_s}} e^{i\mathbf{k}\cdot\mathbf{T}}\}. \tag{6.1}$$

Here, α is a Cartesian coordinate, μ labels the mode, M_s represents the ionic mass of atom s, $\epsilon_{\mu s}^\alpha(\mathbf{k})$ is the polarization vector, and $q_\mu(\mathbf{k})$ is the order parameter associated with the μ mode at wave number $\mathbf{k}$. Then, by plotting the energy against the order parameter q, we obtain the BO energy surface along that specific direction in the order parameter space.

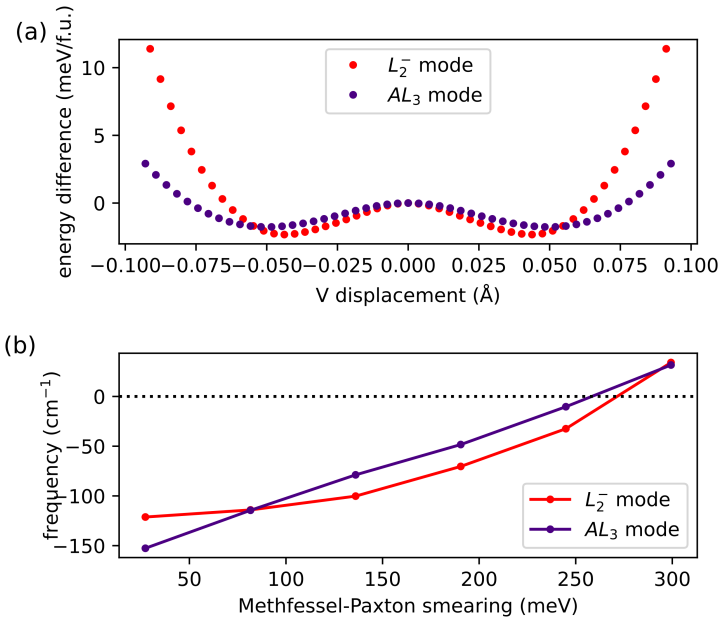

Figure 6.2: **Smearing dependence of** L **and** AL **modes. a.** Born-Oppenheimer energy surfaces as the crystal is distorted according to either the L_{2^-} or the AL_3 mode. As shown, the L mode leads to a lower energy state. **b.** Frequency dependence of both L_2^- and AL_3 modes as a function of a Methfessel-Paxton smearing.

As shown in Fig. 6.2(a), both profiles exhibit a highly anharmonic "Mexican-hat" shape, with the L phonon leading to a lower-energy state. Additionally, Fig. 6.2(b) shows the strong dependence on smearing for both instabilities, indicating that depending on the smearing value, either one could appear as the leading parameter for the charge-density wave. However, it is observed that the L mode stabilizes at higher temperatures, aligning with the findings in existing literature [181, 210, 213].

Considering that when increasing the electronic temperature in the calculations, the L mode stabilizes after the AL one, we can now say that the main instabilities of the system are most likely the soft modes at the M and L points (transforming under L_2^- and M_1^+ irreducible representations), in line with previous findings [181, 210, 213]. Considering that each of these points contributes with three equivalent vectors within the star, we expect the CDW to be described by a six-dimensional order parameter $\mathbf{Q} = (M_1, M_2, M_3, L_1, L_2, L_3)$.

In order to continue with our calculations, we must however select a particular value for the smearing. The beauty of the Methfessel-Paxton (MP) smearing is that while for example, integrals using different Gaussian smearings will converge to different values in general, different MP smearings of order N are supposed to converge to the same result, as long as the integrand is a polynomial of order less than 2N in the width of the smearing. However, when this does not hold, as in this case, there is no a particular reason for choosing one smearing value over the other. To this end, we switch from a MP smearing [135] to a Fermi-Dirac smearing, which has a clear mapping

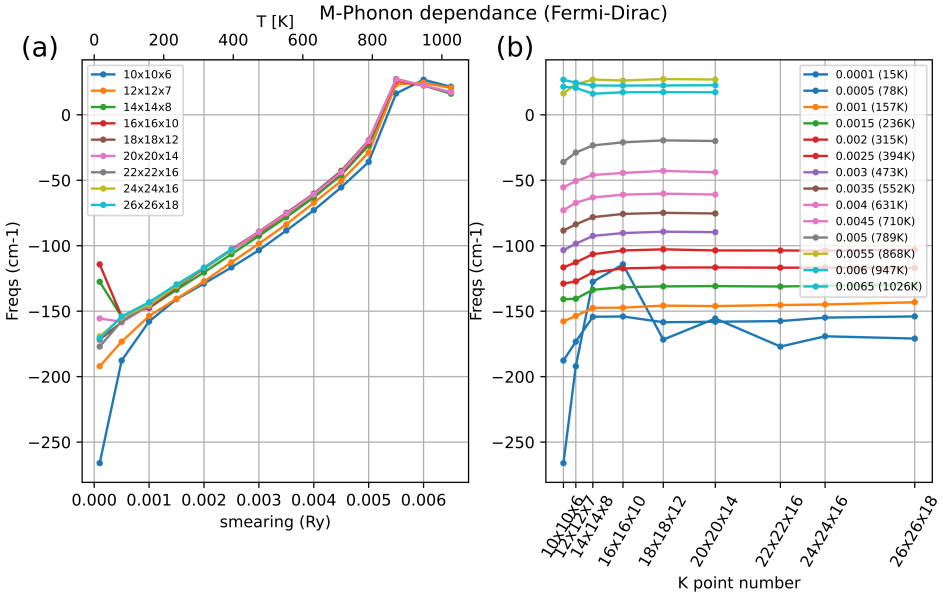

Figure 6.3: **Fermi-Dirac smearing and k-mesh dependence of** M **mode. a.** Frequency dependence of the M_1^+ phonon with respect to Fermi-Dirac smearing (or temperature) for different **k**-grids. **b.** Frequency dependence of the M_1^+ phonon with respect to the $\mathbf{k}-grid$ for different Fermi-Dirac smearings (or temperatures).

with the physical temperature as it is given by the Fermi-Dirac distribution. In Fig. 6.3 we show the frequency dependence of the M_1^+ phonon with respect to both, **k**-grid and Fermi-Dirac smearing. As shown in pane (b), we managed to converge all smearings up to just 15 K, while pane (a) shows how as we decrease the temperature the less dense **k**-grids deviate from our converged results.

In contrast, in Fig. 6.4 we show the equivalent analysis for a MP smearing, notice that here we are not relating the smearing values to temperatures, since the philosophy of MP smearing is not to represent temperature. As shown in pane (b), we successfully converged with small smearings down to 0.002 Ry. However, the fact that even the densest **k**-grids do not plateau in pane (a) suggests that there is no compelling reason to favor one MP smearing over another. Nevertheless, since our smallest smearing of 0.002 Ry provides results close to the Fermi-Dirac smearing at 15 K in Fig. 6.3, while being converged with a less dense **k**-grid, we choose a Methfessel-Paxton smearing of 0.002 Ry with a $16 \times 16 \times 10$ grid for the remainder of the study.

The high sensitivity of both the L_2^- and M_1^+ modes to the electronic temperature has been argued in support of an electron-driven CDW via a nesting mechanism [201]. This concept hinges on the idea that the van Hove singularities at M and L (Fig. 6.1(d)) are coupled by the previously described six-dimensional order parameter **Q**. As temperature increases, it leads to a reduction in the occupied states associated with these van Hove singularities, subsequently diminishing the instability. To test the hypothesis of electronic entropy as a stabilizing factor for the high-symmetry phase, we compute in

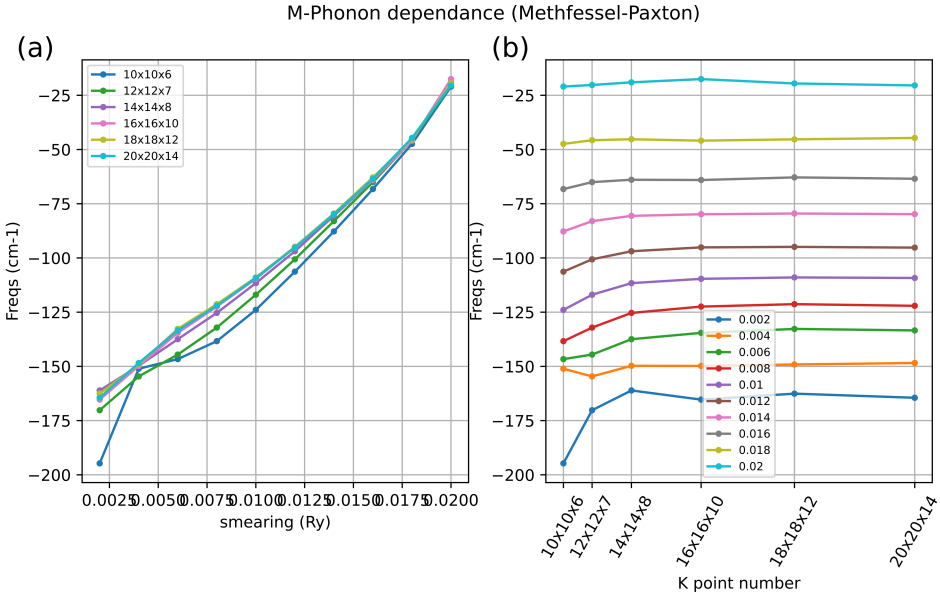

Figure 6.4: **Methfessel-Paxton smearing and k-mesh dependence of M mode. a.** Frequency dependence of the M_1^+ phonon with respect to Methfessel-Paxton smearing (or temperature) for different **k**-grids. **b.** Frequency dependence of the M_1^+ phonon with respect to the $\mathbf{k}-\mathrm{grid}$ for different Methfessel-Paxton smearings (or temperatures).

the harmonic approximation the frequency of the L_2^- and M_1^+ modes as a function of the real electronic temperature described by Fermi-Dirac statistics. In this case, and since Fermi-Dirac smearings are harder to converge, we used a denser grid of $18 \times 18 \times 12$, which is sufficient for convergence (see Fig. 6.4(a)). As shown in Fig. 6.5(d), while the modes do eventually stabilize, the predicted transition temperature of approximately 760 K for the CDW is far from the experimental observations. This, in conjunction with the highly anharmonic Born-Oppenheimer energy landscape illustrated in Fig. 6.5(c), suggests that it is not the electronic entropy, but the ionic entropy that is responsible for the melting of the CDW, as it is the case in transition-metal dichalcogenides [150].

To explore this idea, we compute the static phonon spectra as a function of temperature in the high-symmetry phase of CsV_3Sb_5, taking into account anharmonic effects within the stochastic self-consistent harmonic approximation (SSCHA) [62–64, 168]. In order to capture all the relevant high-symmetry points, the free energy Hessians (SSCHA anharmonic phonons) were done with the inclusion of fourth order force constants in a $2 \times 2 \times 2$ supercell, which naturally captures the Γ, A, M and L points. The Brillouin zone integrals for the supercell calculations were performed with a $7 \times 7 \times 4$ k-grid (equivalent to a $14 \times 14 \times 8$ grid in the primitive cell).

As seen in Fig. 6.5(a), the anharmonic corrections strongly renormalise the phonon spectrum to the point where it is fully stabilized above $T_{CDW} \sim 80$ K, which is in very good agreement with the experimental value of 94 K. This good agreement demonstrates that it is ionic entropy, which is largely affected by anharmonicity, what melts the CDW and that electronic entropy does not

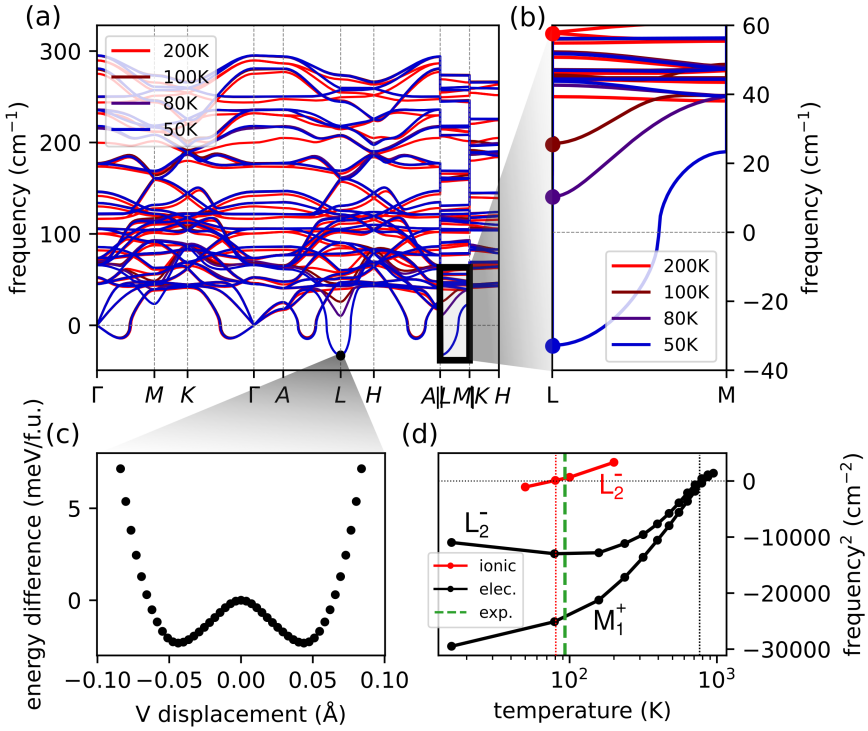

Figure 6.5: **Anharmonic phonon spectrum of CsV_3Sb_5. a.** Calculated anharmonic phonon spectrum for the P6/mmm phase at different temperatures above and below T_{CDW} ~ 94 K. At 80 K the system is entirely stabilized by anharmonic effects, considering that the remaining imaginary frequencies are artifacts of the Fourier interpolation. **b.** Zoomed view of the LM path, showcasing the softening of the L mode. Meanwhile, the M phonon remains fully stabilized across the entire temperature range due to anharmonic effects. **c.** Computed Born-Oppenheimer energies as the structure distorts according to the L_2^- phonon responsible for the CDW. **d.** Effects of electronic and ionic entropy on the stability of the CsV_3Sb_5 high-symmetry phase. The black line shows the squared frequency of the L_2^- and M_1^+ modes with respect to electronic temperature, suggesting that the high-symmetry structure is projected to stabilize at around ~ 760 K. Conversely, the red line considers only the ionic entropy for the L_2^- mode. Our calculations predict that ionic entropy stabilizes the system at ~ 77 K, in agreement with the T_{CDW} ~ 94 K experimental value.

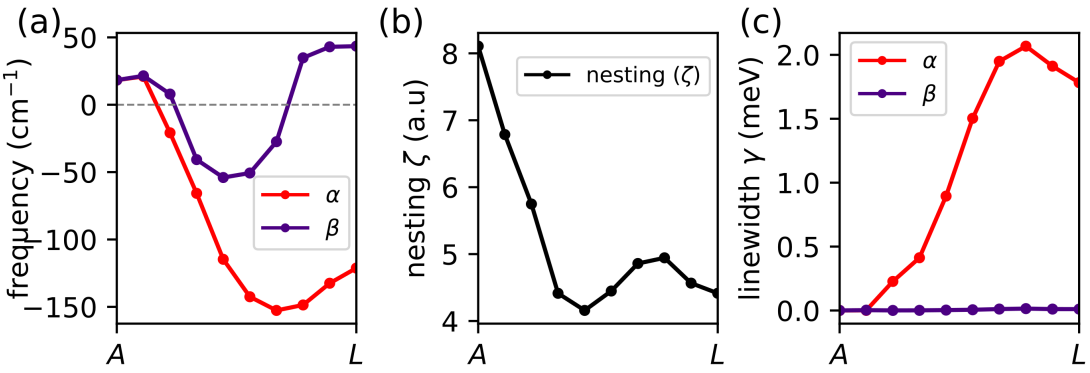

Figure 6.6: **Nesting and electron-phonon linewidth calculations. a.** Harmonic phonon frequencies along the AL high-symmetry line for both the α phonon branch (which contains the L_2^- instability) and the subsequent most unstable branch, β. **b.** The nesting function along the AL high-symmetry line exhibits a peak at A rather than at L, which contradicts expectations for a nesting-driven mechanism. This emphasis on the A point aligns with the highly two-dimensional Fermi surface (Fig. 6.1(c)). **c.** The electron-phonon linewidth of the α and β branches along the AL line shows a large peak at the L point for the α mode.

play any role. Interestingly, the M_1^+ soft mode is no longer almost degenerate with the L_2^- phonon, as it remains stable even at 50 K. This is in agreement with thermal diffuse scattering experiments that do not see any signal at M, only at L [33]. CsV_3Sb_5 deviates thus from the ideal two-dimensional kagome instability picture and indicates that the coupling between kagome layers is strong enough to break the degeneracy between the phonons at M and L. This result is in line with quantum oscillation and magnetotransport experiments underscoring the significance of interlayer coupling [220]. Consequently, a three-dimensional CDW with modulation along the c-axis emerges. This, greatly simplifies the analysis of the CDW from a six-dimensional to a three-dimensional order parameter that now is solely related to the L_2^- instabilities. The clear softening observed at the L point in this static calculation shows that soft phonon physics are triggering the CDW transition and that it has to be of second-order or weak first-order character.

One important conclusion from our results is that the CDW mechanism is independent of the novel physics that emerge below T_{CDW}. In other words, the exotic physics observed are not necessary to explain the CDW. The study of the low-temperature physics of CsV_3Sb_5 becomes, then, more feasible. Instead of dealing with the CDW and the new phenomena in one single problem, one may first solve the CDW structure and then take advantage of the correct symmetries in the next step. Our results suggest as well that anharmonicity cannot be neglected in any model or calculation trying to describe the free energies of the candidate low-symmetry phases, specially given that the Born-Oppenheimer energies of the competing phases are only few meV per formula unit apart [187].

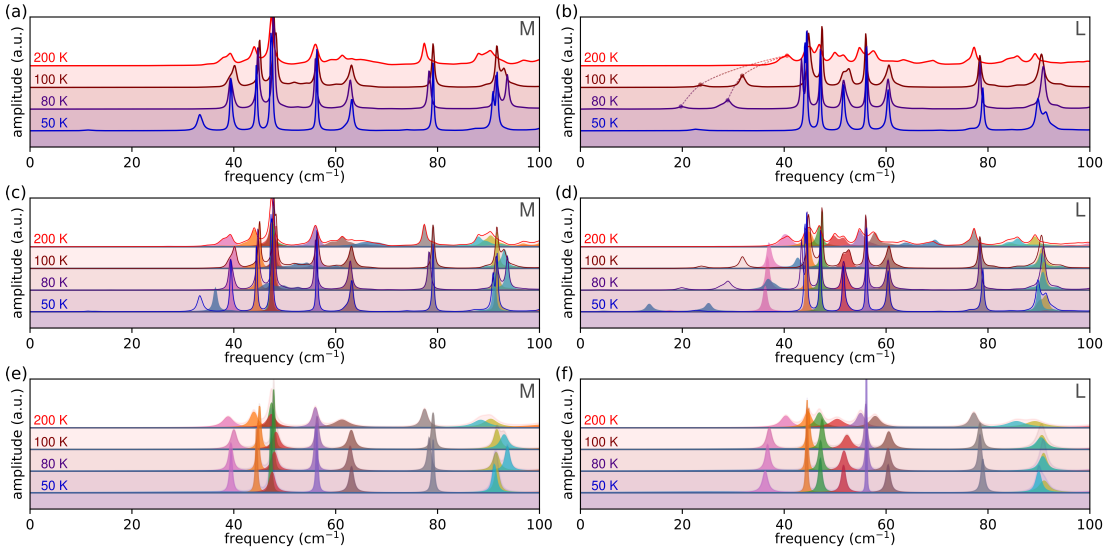

Figure 6.7: **Calculations of the spectral function at the** M **and** L **points. a, b.** Fully anharmonic spectral function for the M and L points at various temperatures. While no evident softening is observed at the M point, the L point exhibits a noticeable softening of a peak at approximately 40 cm^{-1}. Due to the large anharmonic effects, this peak splits into a double-peak as the temperature lowers. **c, d.** Employing a no-mixing approximation by discarding the off-diagonal elements of the self-energy allows for the independent tracking of different modes, as indicated by different colors. The complete anharmonic spectral functions from insets **a** and **b** are also overlaid. **e, f.**Here, we fit a Lorentzian function to each of the individual modes in **c,d** and add the corresponding electron-phonon linewidth to each of the modes.

6.3 THE TRIGGER OF THE CHARGE-DENSITY WAVE

Despite addressing anharmonicity as the primary factor in the CDW melting process, the mechanism responsible for the formation of the CDW in CsV_3Sb_5 remains unclear. In order to unveil this issue, we compute both the nesting function (2.52) and the phonon linewidth given by the electron-phonon (2.51) interaction along the AL high-symmetry line (HSL), which exhibits the most unstable phonons. As shown in Chapter 5, these two magnitudes are very similar, with the difference that the latter includes the electron-phonon matrix elements but not the former. The electron-phonon linewidth $HWHM_{elph,\mu}$ and nesting $\zeta(\mathbf{q})$ were computed using a $24 \times 24 \times 15$ grid and a Gaussian smearing of 0.005 Ry for approximating the Dirac deltas.

In Fig. 6.6(a) we compare these two magnitudes for two modes: the mode responsible for driving the instability (labeled as α) and the next most unstable mode (labeled as β). The nesting function displays a prominent peak at the A point, reflecting the highly two-dimensional Fermi surface of CsV_3Sb_5 (Fig. 6.1(b)), along with a smaller peak around $\frac{3}{4}$ AL, corresponding to the nesting vector of the van Hove pockets at $k_z = 0.5$ (Fig. 6.1(d)). Conversely, the electron-phonon linewidth exhibits a significant increase from nearly zero at the A point to a huge value of approximately 2 meV at the L point for the α mode, while remaining relatively constant for the β mode. These findings further support the idea that the CDW is primarily mediated by the electron-phonon coupling rather than a nesting mechanism, underscoring once again the critical role of lattice effects in this system.

6.4 EXPERIMENTALLY MEASURING THE CDW

Our results indicate either a second-order or a weak first-order character for the phase transition, with the continuous nature imprinted in the softening of the L_2^- phonon (Fig. 6.5(b)). However, multiple instances in the literature point to a first-order nature of the CDW [187, 197], and neither inelastic x-ray scattering [33] or Raman spectroscopy experiments [189, 193] have observed such softening. To understand this apparent contradiction, we compute the spectral function for both the M and L phonons fully accounting for anharmonicity with the methods described in Chapter 2. The calculation was done within the so-called bubble approximation for the self-energy considering phonon-phonon scattering on a $2 \times 2 \times 2$ grid and a 0.1 cm^{-1} Gaussian smearing to approximate the Dirac deltas. In order to assign a particular Lorentzian to each mode we used the no-mixing approximation, consisting on discarding the off-diagonal elements in the computation of the self-energy. Then, the corresponding spectral functions of each of the modes were fitted by a Lorentzian function. Finally, by using the polarization vectors we were able to match the different modes and corresponding linewidths within different temperatures and with the electron-phonon linewidths calculations.

The spectral function, as shown in Fig. 6.7(a,b), not only confirms the absence of phonon collapse at the M point, but also underscores the profoundly

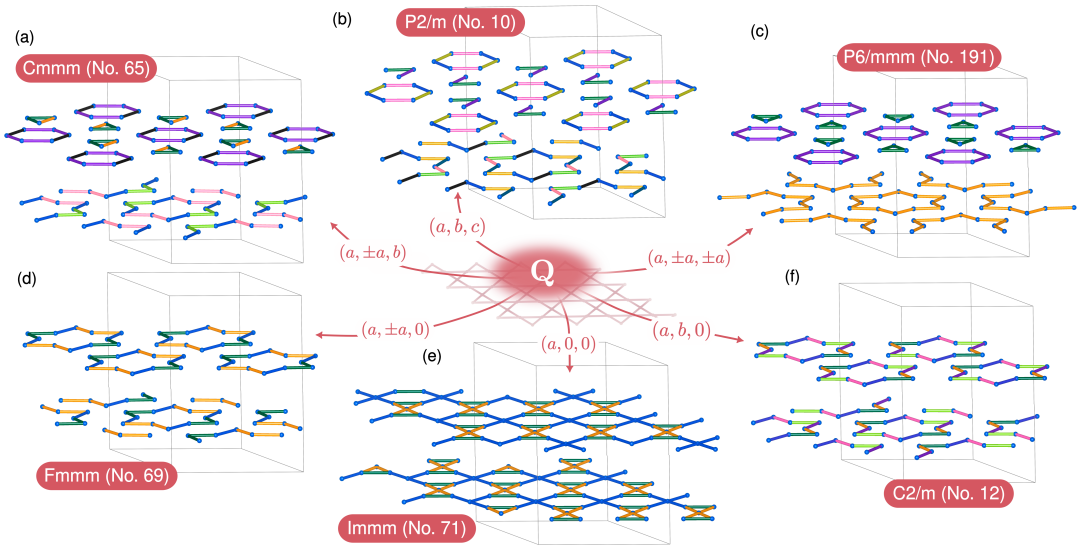

Figure 6.8: **All possible space groups compatible with the order parameter Q** $= (L_1, L_2, L_3)$**.** Different colors distinguish between different bond lengths within the distorted kagome lattices of vanadium atoms. The most symmetric configuration, depicted in inset **c**, corresponds to what is usually referred in the litterature as an stack of star-of-david and tri-hexagonal (inverse-star-of-david) configurations. The remaining distortions either represent distorted versions of **c (a,b)** or an stack of star-of-david configurations, but with the stars being deformed in some form **(d,f)**.

anharmonic nature of the L_2^- phonon that drives the instability. As depicted in Fig. 6.7(b), the unstable L_2^- mode becomes broader and splits into a double peak as the temperature approaches T_{CDW}. Thus, we expect this mode to be exceedingly challenging to observe experimentally. This difficulty arises not only from its double-peak and broadened nature but also because the spectral function is typically fitted using a set of Lorentzians representing different modes experimentally. In order to carry such Lorentzian fitting, we first need to compute the spectral function with a no-mixing approximation by excluding the off-diagonal elements of the anharmonic phonon self-energy. This allows for the independent tracking of different modes, as indicated by different colors in Fig. 6.7(c,d). Nonetheless, for illustrative purposes, the full anharmonic spectral functions are overlaid to demonstrate the impact of this approximation. This approximation works effectively for the M point, except for the softest mode at 50 K, and reveals the softening of a highly anharmonic mode (colored in blue). In the case of L, off-diagonal terms seem to exert a more significant influence overall. Still, we are able to capture the softening of a highly anharmonic mode (colored in blue), which develops a double dome. In Fig. 6.7(e,f) we fit a Lorentzian function to each of the individual modes and add the corresponding electron-phonon linewidth in order to obtain a spectral function that captures both anharmonic and electron-phonon interactions. Both at M and L, the phonon highlighted in blue experiences such a substantial broadening that it becomes imperceptible to the eye. This suggests that the electron-phonon linewidth renders this mode experimentally

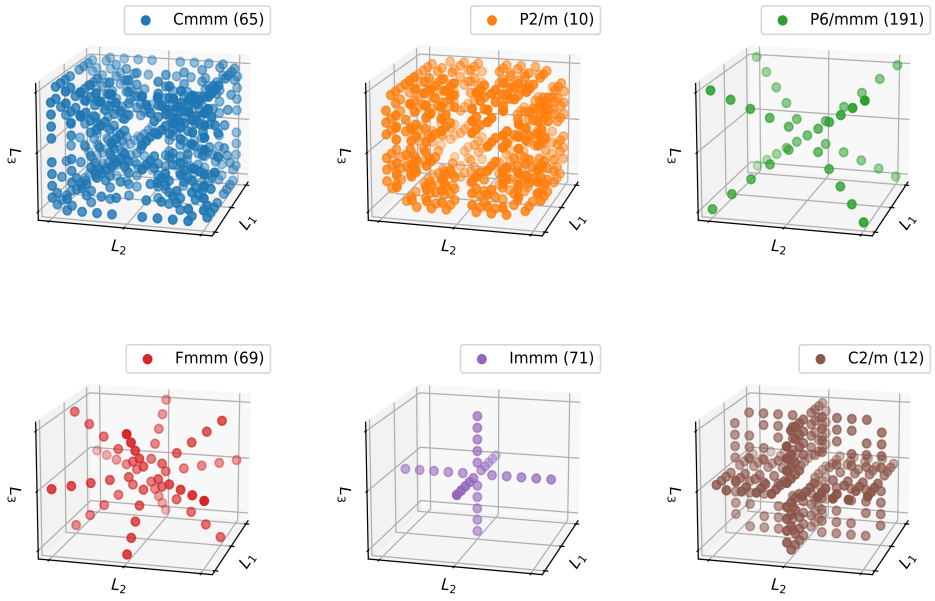

Figure 6.9: **Order parameter space for $\mathbf{Q} = (L_1, L_2, L_3)$.** Each direction in the three-dimensional order parameter space corresponds to a distinct instance of the distorted crystal, characterized by a specific space group and specific set of Wyckoff positions described in Table 6.1. Here the different directions corresponding to each of the space groups are depicted.

inaccessible, implying that the softening goes unnoticed, reconciling our theoretical results with the experiments [33, 189, 193]. The remaining modes at L are well-described by Lorentzian curves, exhibiting a slight broadening as the temperature increases, consistent with the expected impact of anharmonicity.

6.5 SYMMETRY ANALYSIS OF THE CHARGE-DENSITY WAVE

Based on our previous findings, we expect that the CDW transition manifests as either a second-order Landau-type phase transition or a subtle first-order transition. This, together with the observation that the M_1^+ mode is stabilized by anharmonic effects, provides an opportunity to explore the potential phase transitions permitted by group theory [66]. In order to deduce the possible low symmetry structures we explore the possible space groups that span from the three-dimensional order parameter $\mathbf{Q} = (L_1, L_2, L_3)$. We found that six possible space-groups arise for different kinds of linear combinations of the order parameter as depicted in Fig. 6.9. Each of these distortions imprints a characteristic pattern between two adjacent kagome lattices as shown in Fig. 6.8.

6.5.1 *Raman and infrared activities of low-symmetry phases*

The resulting space groups are also expected to exhibit characteristic Raman and infrared spectra, featuring varying numbers of peaks that transform under distinct symmetries. In order to obtain the Raman and infrared activities

Space Group	Order parameter	Cesium	Antimony	Vanadium
P6/mmm (No. 191)	$(0,0,0)$	$1a$	$1b+4h$	$3g$
P6/mmm (No. 191)	$(a,\pm a,\pm a)$	$2e+6i$	$3f+3g+1a+1b+2\times(12o+4h)$	$6l+6j+6m+6k$
Immm (No. 71)	$(a,0,0)$	$4i$	$2a+2c+2\times 8l$	$2b+2d+8n$
Fmmm (No. 69)	$(a,\pm a,0)$	$8f+8h$	$4a+8d+32p+4b+2\times 16m$	$8i+8g+2\times 16n$
Cmmm (No. 65)	$(a,\pm a,b)$	$4k+4l+8m$	$2a+2b+2d+2c+4e+4f+$ $+4\times 8n+2\times 16r$	$4g+4h+4i+4j+2\times(8p+8q)$
C2/m (No. 12)	$(a,b,0)$	$4g+4h$	$2a+2b+2c+2d+4\times 8j$	$6\times 4i$
P2/m (No. 10)	(a,b,c)	$2i+2k+2j+2l$	$1a+1b+1c+1d+1e+1f+$ $+1g+1h+8\times 4o$	$6\times(2m+2n)$

Table 6.1: **Wyckoff positions for all possible subgroups resulting from the condensation of the L_2^- modes.** The first column indicates the resulting space group corresponding to the order parameter $\mathbf{Q}=(L_1,L_2,L_3)$ in the second column. The third fourth and fifth columns specify the Wyckoff possitions for cesium antimony and vanadium atoms in each of the space groups.

of each of this phases we distort the structure according to each of the order parameters and solve the Wyckoff positions of the resulting structures in Table 6.1. Then, one can build the corresponding mechanical representation and decompose it into irreducible representations in the Γ point.

The vibrational modes will be infrared or Raman active depending on whether the corresponding irreducible representations are contained in the vector representation V or its symmetrized square $[V]^2$ respectively (see Table 6.2). Given that the majority of modes do not undergo any softening during the CDW and that the active modes come from either Γ, A, M or L points, a more detailed classification of the resulting frequencies for each Raman and infrared mode could be performed. Moreover, the phonon responsible for the symmetry breaking is always expected to transform under the trivial representation A_g of the low-symmetry group. This is because the symmetries that leave this phonon invariant are precisely the ones preserved in the low-symmetry phase. Given that the identity or trivial representation is always contained in $[V]^2$ (the symmetrized square of the vector representation), the mode responsible for the symmetry breaking will always be Raman active in the low symmetry phase and the softening could be observed. However, as already discussed, its observation may be hindered because of its large phonon broadening.

These distinctions in Raman and infrared activities may offer a robust method for discerning the low-symmetry structure. This stands in contrast to energetic arguments, which can be notably unreliable due to the minute energy differences between phases and the neglect of certain contributions, such as anharmonicity.

6.6 CONCLUSIONS

In summary, our calculations show that the CDW transition in CsV_3Sb_5 is primarily driven by the large electron-phonon coupling within the system, while the melting of the CDW can be attributed to the robust anharmonic effects of

Space Group	Order parameter	Num. modes	Raman active	Infrared active
P6/mmm (No. 191)	$(0,0,0)$	27	$A_{1g}+E_{2g}+E_{1g}$	$4A_{2u}+5E_{1u}$
P6/mmm (No. 191)	$(a,\pm a,\pm a)$	216	$12A_{1g}+17E_{2g}+15E_{1g}$	$16A_{2u}+25E_{1u}$
Immm (No. 71)	$(a,0,0)$	54	$7A_g+4B_{1g}+4B_{2g}+6B_{3g}$	$10B_{1u}+11B_{2u}+9B_{3u}$
Fmmm (No. 69)	$(a,\pm a,0)$	108	$14A_g+10B_{1g}+12B_{2g}+12B_{3g}$	$19B_{1u}+16B_{2u}+17B_{3u}$
Cmmm (No. 65)	$(a,\pm a,b)$	216	$29A_g+23B_{1g}+20B_{2g}+24B_{3g}$	$31B_{1u}+38B_{2u}+34B_{3u}$
C2/m (No. 12)	$(a,b,0)$	108	$26A_g+22B_g$	$24A_u+36B_u$
P2/m (No. 10)	(a,b,c)	216	$52A_g+44B_g$	$48A_u+72B_u$

Table 6.2: **Raman and infrared active modes for all possible subgroups resulting from the condensation of the L_2^- modes.** The first column indicates the resulting space group corresponding to the order parameter $\mathbf{Q}=(L_1,L_2,L_3)$ in the second column. The third column denotes the total number of modes in Γ, while the fourth and fifth columns provide the counts of Raman and infrared active modes along with their respective irreducible representations.

the lattice. The CDW is exclusively triggered by the unstable phonons at the L point, with the M phonons not assuming a pivotal role. Despite the phase transition being of second order or weak first-order character, an examination of the spectral function at the L point suggests that observing this softening experimentally is impossible [33]. All in all, in contrast to the pure Kagome CDW, which is prototypically nesting driven and strictly two-dimensional, the CsV_3Sb_5 CDW exhibits notable deviations being purely three-dimensional and driven by the electron-phonon coupling. The remarkable agreement between our results and experimental data suggests that the CDW mechanism can be studied independently from the phenomena emerging in the CDW phase and that lattice quantum anharmonic effects may also wield a crucial influence on the novel physics in the CDW state. We anticipate a similar impact of the electron-phonon coupling and anharmonicity on other kagome families [221–224], as well as the presence of anomalous phonon spectral functions. For instance, the discrepancy observed in 166 compounds between the phonon collapse and the CDW order [221] might be attributed to the phonon responsible for the CDW order going unnoticed because of its large linewidth. On the other hand, the absence of a CDW in titanium-based $CsTi_3Bi_5$ kagome compounds [222] likely results from a distinct balance between the stabilizing role of anharmonicity and electron-phonon destabilizing forces.

OVERVIEW AND CONCLUSIONS

OVERVIEW AND CONCLUSIONS

While Landau theory has been remarkably successful in elucidating the relationship between lattice effects and traditional phases of matter, the advent of topological matter has revealed a significant insight: symmetries alone are insufficient for classifying phases. This paradigm shift introduces a rich landscape for research, with extensive implications for the future of quantum technologies. Recognizing this, the primary objective of this thesis, as reflected in its title, was to explore the interplay between three specific areas: lattice effects, phase transitions, and topological phases of matter. Each of these fields is already exceedingly vast, encompassing a wide array of projects and ideas at their intersections. From the various projects and collaborations undertaken throughout this thesis, we have selected three particular projects that we believe best illustrate three distinct and specific overlaps between these fields.

In Chapter 4, we combined group theory with topological quantum chemistry to thoroughly characterize the topology of the 2D buckled honeycomb lattice phonon spectra, thereby directly addressing the topology of lattice effects. Utilizing only the pure crystal structure as input, we demonstrated that this system could exhibit eleven distinct phases, nine of which are topological. Furthermore, through a combination of first-principle calculations and analytical modeling, we explained why, despite the potential for various topological phases, real materials adhering to this structure predominantly occupy one of the trivial phases.

A significant open question regarding phonon topology is why it appears to be a rarity, in contrast to electronic topology. Our limited intuition from this single case study suggests a possible relation between long-range interactions and the accessibility of topological phases. This idea can be intuited by analyzing the relationship between force constants and dynamical matrices described by equation (2.17). Longer-range interactions imply higher harmonics in the Fourier expansion of the dynamical matrix $D(\mathbf{k})$, which, in turn, should lead to greater windings of the eigenvectors around a closed loop in the Brillouin zone. However, this is merely a hypothesis that warrants further in-depth study and comparison with the electronic counterpart.

In our pursuit to investigate the interplay between charge-density wave systems and topological order, Chapter 5 delves into the properties of a novel 2D layered material, SnP. Here, we explored the potential of CDWs to induce a metal-insulator transition by coupling two Dirac fermions, giving rise to an emergent topological phase. We investigated three possible CDWs, which resulted in metastable insulating phases, with one proving to be topologically non-trivial under strain.

Strikingly, one of the main outcomes of the study, despite not being the primary intention, was that the ground-state structure only manifested due

to the influence of large anharmonic effects. This underscores the importance of examining CDWs beyond the conventional harmonic framework, as even something as fundamental as the system's ground state would have remained unnoticed under the harmonic approximation. Unfortunately, despite the predicted polymorphism of SnP, the monolayer could not be obtained by exfoliating the bulk. However, chemical methods may succeed in synthesizing the anticipated different phases.

While the potential of CDWs as a tool for manipulating the topology of materials is promising, determining *a priori* the topology of the resulting phase remains a nontrivial challenge. An interesting future direction would be to establish a systematic framework connecting order parameters and topological classifications. Given that the topology of phases can be classified based on the symmetries of the system's quasiparticles (electrons, phonons, etc.), and these symmetries are delineated by the group theory of phase transitions, it is conceivable to devise an algorithm for scrutinizing the potential topological phases emerging from a phase transition governed by a specific order parameter. This approach would parallel how Landau theory discerns potential phases under a particular symmetry of the order parameter, while also extending the characterization of topology based on symmetry information.

Finally, the AV_3Sb_5 family of kagome metals, studied in Chapter 6, provided an ideal platform for exploring lattice effects beyond the harmonic approximation, such as electron-phonon coupling and anharmonic effects, which are expected to be strong in charge-density wave systems. The CDW mechanism and resulting structure of CsV_3Sb_5 have presented an intriguing challenge since their discovery four years ago. However, prior theoretical attempts to dissect the CDW have overlooked the crucial role of anharmonic effects.

Through a non-perturbative approach, we conducted a comprehensive exploration of the mechanisms governing the formation and eventual dissolution of the CDW state in CsV_3Sb_5, addressing some of the primary open questions surrounding this phenomenon. Contrary to previous propositions of a nesting-mediated mechanism, we showed that the electron-phonon coupling drives the CDW, with anharmonicity being responsible for the CDW phase's melting at higher temperatures. Furthermore, our research unveiled that the phonon driving the phase transition operates in a mode distinct from the previous belief within the community. Additionally, we elucidated why spectroscopy measurements fail to capture the softening of the condensing phonon, attributing this to the large electron-phonon and anharmonic linewidths. Lastly, by employing group theory, we listed all space groups compatible with the three-dimensional order parameter instigating the transition. Complementary to these space groups, we put forth spectral properties that may distinguish between different space groups for the low symmetry phase and suggest corresponding spectral measurements as a pathway to resolving the long-sought-after low-symmetry structure.

While this study has answered several questions regarding the CDW, many others remain open. These include determining the actual symmetry of the low-symmetry phase, investigating the first-order character of the phase tran-

sition, or exploring the effects of pressure on the CDW. In principle, many of these questions could be addressed using the same methods described in Chapter 6. However, these inquiries demand more computationally intensive calculations, which are currently beyond our capabilities. One way to tackle this issue is to use machine learning potentials to address the computational challenge of approaching anharmonic effects in a non-perturbative limit. This approach is currently being pursued by other members of our research group with promising results. They have initially reproduced our current results and are now beginning to answer some of the proposed questions.

Altogether, this thesis conveys the vast array of research avenues that the interplay between lattice effects, phase transitions, and topological phases of matter can open. This is especially pertinent given that topology remains a relatively young field, particularly concerning non-electronic systems, and that lattice effects beyond the harmonic approximation are frequently overlooked. I am particularly excited and interested in systems where these two factors play pivotal roles, such as the potential applications of charge-density waves as triggers for topological phases. This interest is further fueled by experimental evidence showing that charge-density wave states can be melted using lasers to stabilize the unstable phonons driving the phase transition, thereby paving the way for technological applications.

Part IV

APPENDICES

A

THEORETICAL FRAMEWORK

A.1 VARIATIONAL PRINCIPLE AND BASIC FUNCTIONAL DERIVATIVES

Theorem 7 ***(Variational theorem):*** Looking for states where the energy is **stationary** ($\delta[\psi] = 0$) is equivalent to finding eigenstates of $\hat{H}$ with eigenvalue $E[\psi]$.

Given a Hamiltonian $\hat{H}$, the energy for a particular wavefunction $|\psi\rangle$ is given by

$$\langle \hat{H} \rangle_\psi = \frac{\langle \psi | \hat{H} | \psi \rangle}{\langle \psi | \psi \rangle} = E[\psi] \ , \tag{A.1}$$

we can now compute $\delta E[\psi]$ as

$$\begin{aligned}
\delta E[\psi] = E[\psi + \delta\psi] - E[\psi] &= \frac{\langle \psi + \delta\psi | \hat{H} | \psi + \delta\psi \rangle}{\langle \psi + \delta\psi | \psi + \delta\psi \rangle} - \frac{\langle \psi | \hat{H} | \psi \rangle}{\langle \psi | \psi \rangle} = \\
&= \frac{\langle \psi | \hat{H} | \psi \rangle + \langle \psi | \hat{H} | \delta\psi \rangle + \langle \delta\psi | \hat{H} | \psi \rangle}{\langle \psi | \psi \rangle + \langle \psi | \delta\psi \rangle + \langle \delta\psi | \psi \rangle} - \frac{\langle \psi | \hat{H} | \psi \rangle}{\langle \psi | \psi \rangle} = \\
&= \frac{\langle \psi | \psi \rangle \left[\cancel{\langle \psi | \hat{H} | \psi \rangle} + \langle \psi | \hat{H} | \delta\psi \rangle + \langle \delta\psi | \hat{H} | \psi \rangle \right] - \langle \psi | \hat{H} | \psi \rangle \left[\cancel{\langle \psi | \psi \rangle} + \langle \psi | \delta\psi \rangle + \langle \delta\psi | \psi \rangle \right]}{\langle \psi | \psi \rangle \left[\langle \psi | \psi \rangle + \langle \psi | \delta\psi \rangle + \langle \delta\psi | \psi \rangle \right]} \ .
\end{aligned} \tag{A.2}$$

Where we have get rid of the second order terms in $\delta\psi$. Taking into account that $\delta\psi$ can be as small as we want, we keep only the higher order terms in both numerator and denominator:

$$\begin{aligned}
\delta E[\psi] &= \frac{\langle \psi | \psi \rangle \left[\langle \psi | \hat{H} | \delta\psi \rangle + \langle \delta\psi | \hat{H} | \psi \rangle \right] - \langle \psi | \hat{H} | \psi \rangle \left[\langle \psi | \delta\psi \rangle + \langle \delta\psi | \psi \rangle \right]}{\langle \psi | \psi \rangle^2} = \\
&= \frac{\langle \psi | \hat{H} | \delta\psi \rangle + \langle \delta\psi | \hat{H} | \psi \rangle}{\langle \psi | \psi \rangle} - \frac{\langle \psi | \hat{H} | \psi \rangle}{\langle \psi | \psi \rangle^2} \left[\langle \psi | \delta\psi \rangle + \langle \delta\psi | \psi \rangle \right] = \\
&= \frac{\langle \psi | \hat{H} | \delta\psi \rangle + \langle \delta\psi | \hat{H} | \psi \rangle - E[\psi] \left[\langle \psi | \delta\psi \rangle + \langle \delta\psi | \psi \rangle \right]}{\langle \psi | \psi \rangle} = \\
&= \frac{\langle \delta\psi | \hat{H} - E[\psi] | \psi \rangle + \{ \langle \delta\psi | \hat{H} - E[\psi] | \psi \rangle \}^*}{\langle \psi | \psi \rangle} \ .
\end{aligned} \tag{A.3}$$

If we now assume the stationary condition for the energy ($\delta E[\psi] = 0$), since this must hold for all $\delta\psi$ in necessarily means that $(\hat{H} - E[\psi])|\psi\rangle = 0$. Thus,

$$\delta E[\psi] = 0 \implies \hat{H} |\psi\rangle = E[\psi] |\psi\rangle \ , \tag{A.4}$$

which is precisely the statement of the variational principle.

A.1.1 *Basic functional derivatives*

In layman terms, a functional F can be seen as a mapping between a function f (vector space) into the field scalar numbers. Or in other words, a function that assings an scalar to another function. For example the energy $E[\psi]$ in equation (A.1) can be thought as a functional that assings a real number (the energy) to any function $|\psi\rangle$. Then, a functional derivative is an evaluation of how such functional varies as we vary the argument:

$$\frac{\delta F}{\delta f} = \frac{F[f+\delta f] - F[f]}{\delta f}\,, \tag{A.5}$$

$$\delta f(r_1, r_2, \dots) \equiv \epsilon\, \eta(r_1, r_2, \dots)\,, \tag{A.6}$$

where ϵ is an infinitesimal number and η is an arbitrary function. We can then Taylor expand $F[f+\epsilon\eta]$ as

$$F[f+\epsilon\eta] = F[f] + \frac{dF[f+\epsilon\eta]}{d\epsilon}\Big|_{\epsilon=0}\epsilon + \frac{1}{2}\frac{d^2F[f+\epsilon\eta]}{d\epsilon^2}\Big|_{\epsilon=0}\epsilon^2 + \dots\,. \tag{A.7}$$

At the same time, we want for the functional derivatives $\delta/\delta f$ to allow for an equivalent definition:

$$\delta F = \int \frac{\delta F[f]}{\delta f(x)}\,\delta f(x)\,dx + \frac{1}{2}\int \frac{\delta^2 F[f]}{\delta f(x_1)\delta f(x_2)}\,\delta f(x_1)\delta f(x_2)\,dx_1 dx_2 + \dots\,. \tag{A.8}$$

Thus, by relating expresions (A.7) and (A.8) one can see the definitions the functional derivatibes must hold:

$$\frac{dF[f+\epsilon\eta]}{d\epsilon}\Big|_{\epsilon=0} = \int \frac{\delta F}{\delta f}(x)\,\eta(x)\,dx \tag{A.9}$$

$$\frac{d^2F[f+\epsilon\eta]}{d^2\epsilon}\Big|_{\epsilon=0} = \int \frac{\delta^2 F[f]}{\delta f(x_1)\delta f(x_2)}\,\eta(x_1)\eta(x_2)\,dx_1 dx_2. \tag{A.10}$$

A.1.2 *Important functional derivatives in density functional theory*

When dealing with condensed matter systems or density functional theory the energies may only depend explicetly on the position operator $\mathbf{r}$, a function of the form $\rho(\mathbf{r})$ that only depends on the position operator, and its derivatives $\nabla\rho(\mathbf{r})$. Let us then define the explicit formula for systems in which the functional $F[\rho]$ is defined as:

$$F[\rho] = \int f(\mathbf{r}, \rho(\mathbf{r}), \nabla\rho(\mathbf{r}))\,d\mathbf{r} \tag{A.11}$$

From the definition of the functional derivative (A.9):

$$\begin{aligned}
\int \frac{\delta F}{\delta\rho}\eta\,d\mathbf{r} &\equiv \frac{d}{d\varepsilon}\Big[\int f(\mathbf{r}, \rho+\varepsilon\eta, \nabla\rho+\varepsilon\nabla\eta)\,d\mathbf{r}\Big]_{\varepsilon=0} = \\
&= \Big[\int \frac{\partial f}{\partial(\rho+\varepsilon\eta)}\frac{\partial(\rho+\varepsilon\eta)}{\partial\varepsilon} + \frac{\partial f}{\partial(\nabla\rho+\varepsilon\nabla\eta)}\frac{\partial(\nabla\rho+\varepsilon\nabla\eta)}{\partial\varepsilon}d\mathbf{r}\Big]_{\varepsilon=0} = \\
&= \Big[\int \frac{\partial f}{\partial\rho}\eta + \frac{\partial f}{\partial\nabla\rho}\nabla\eta\,d\mathbf{r}\Big]_{\varepsilon=0} = \int \Big(\frac{\partial f}{\partial\rho}\eta + \frac{\partial f}{\partial\nabla\rho}\nabla\eta\Big)d\mathbf{r}\,.
\end{aligned} \tag{A.12}$$

Now, using the identity:

$$\nabla \cdot \left(\frac{\partial f}{\partial \nabla \rho}\eta\right) = \frac{\partial f}{\partial \nabla \rho}\nabla\eta + \eta\,\nabla \cdot \frac{\partial f}{\partial \nabla \rho} \implies \frac{\partial f}{\partial \nabla \rho}\nabla\eta = \nabla \cdot \left(\frac{\partial f}{\partial \nabla \rho}\eta\right) - \eta\,\nabla \cdot \frac{\partial f}{\partial \nabla \rho} \tag{A.13}$$

we can replace the second term in equation (A.12) as:

$$\begin{aligned}\int \frac{\delta F}{\delta \rho}\eta\, d\mathbf{r} &\equiv \int \left(\frac{\partial f}{\partial \rho}\eta + \frac{\partial f}{\partial \nabla \rho}\nabla\eta\right) d\mathbf{r} = \int \left(\frac{\partial f}{\partial \rho}\eta + \nabla \cdot \left(\frac{\partial f}{\partial \nabla \rho}\eta\right) - \eta\,\nabla \cdot \frac{\partial f}{\partial \nabla \rho}\right) d\mathbf{r} \\ &= \int \eta \left(\frac{\partial f}{\partial \rho} - \nabla \cdot \frac{\partial f}{\partial \nabla \rho}\right) + \nabla \cdot \left(\frac{\partial f}{\partial \nabla \rho}\eta\right) d\mathbf{r} = \int \eta \left(\frac{\partial f}{\partial \rho} - \nabla \cdot \frac{\partial f}{\partial \nabla \rho}\right) d\mathbf{r}\,,\end{aligned} \tag{A.14}$$

where in the last step we have assumed that both $\rho(\mathbf{r})$ and $\eta(\mathbf{r})$ vanish when $\mathbf{r} \to \infty$ in order to apply the divergence theorem in the second term. This assumption often holds since $\rho(\mathbf{r})$ will represent either a density or a wave-function, which in both cases need to vanish in order to have a fixed number of particles. All and all we can now just remove the $\eta(\mathbf{r})$ function and get the explicity formula for the functional derivative for a functional of the form (A.11):

$$\frac{\delta F}{\delta \rho(\mathbf{r})} = \frac{\partial f}{\partial \rho} - \nabla \cdot \frac{\partial f}{\partial \nabla \rho} \tag{A.15}$$

A.2 INDEPENDENT PARTICLE APPROXIMATION

In general a many-body Hamiltonian for N particles is of the form:

$$\hat{H}(x_1, x_2, \cdots, x_N, t) = \sum_{i=1}^{N} \frac{\hat{p}_i^{\,2}}{2m_i} + \hat{V}(x_1, x_2, \cdots, x_N, t)\,. \tag{A.16}$$

If the particles don not interact with each other the potential term in can be separated as:

$$\hat{V}(x_1, x_2, \ldots, x_N, t) = \sum_{i=1}^{N} \hat{V}(x_i, t)\,, \tag{A.17}$$

and as a consequence, the Hamiltonian (A.16) also seprates as

$$\hat{H}(x_1, x_2, \cdots, x_N, t) = \sum_{i=1}^{N} \hat{H}_i(x_i, t)\,. \tag{A.18}$$

Since the particles are non-interacting we expect their instantaneous positions to be completely uncorrelated. Which implies that the wavefunction Ψ can be written as a product of N independent single-particle wavefunctions:

$$\Psi(x_1, x_2, \cdots, x_N, t) = \psi_1(x_1, t)\,\psi_2(x_2, t)\,\cdots\psi_N(x_N, t) \tag{A.19}$$

Each of this single-particle wavefunctions evolves as

$$\psi_i(x_i, t) = \psi_{E_i}(x_i)\,\exp(-i\,E_i\,t/\hbar) \tag{A.20}$$

, and thus:

$$\Psi(x_1, x_2, \cdots, x_N, t) = \Psi_E(x_1, x_2, \cdots, x_N) e^{\left(-i\frac{Et}{\hbar}\right)} \tag{A.21}$$

where

$$E = \sum_{i=1,N} E_i \, . \tag{A.22}$$

A.3 HOHENBERG-KOHN THEOREMS DEMONSTRATIONS

A.3.1 *Theorem I*

Suppose that we have two different external potentials $(\hat{V}_{ext}^{(1)}, \hat{V}_{ext}^{(2)})$ that lead to the same ground-state density $n_0(\mathbf{r})$. However since $\hat{V}_{ext}^{(1)} \neq \hat{V}_{ext}^{(2)}$, then $\hat{H}^{(1)} \neq \hat{H}^{(2)} \implies \psi_0^{(1)}(\mathbf{r}) \neq \psi_0^{(2)}(\mathbf{r})$ (they have different ground states). Thus, as $\psi_0^{(2)}(\mathbf{r})$ is not ground state of $\hat{H}_1$ then:

$$E^{(1)} \equiv \langle \psi^{(1)} | \hat{H}^{(1)} | \psi^{(1)} \rangle < \langle \psi^{(2)} | \hat{H}^{(1)} | \psi^{(2)} \rangle \ , \tag{A.23}$$

while in the other hand:

$$\begin{aligned} \langle \Psi^{(2)} | \hat{H}^{(1)} | \Psi^{(2)} \rangle &= \langle \Psi^{(2)} | \hat{H}^{(2)} | \Psi^{(2)} \rangle + \langle \Psi^{(2)} | \hat{H}^{(1)} - \hat{H}^{(2)} | \Psi^{(2)} \rangle \ = \\ &= E^{(2)} + \int \left\{ v_{ext}^{(1)} - v_{ext}^{(2)} \right\} \ n_0(\mathbf{r}) \, d\mathbf{r} \, . \end{aligned} \tag{A.24}$$

Thus, we have that

$$E^{(1)} < E^{(2)} + \int \left\{ v_{ext}^{(1)} - v_{ext}^{(2)} \right\} \ n_0(\mathbf{r}) \, d\mathbf{r} \, , \tag{A.25}$$

but we could have started the other way around and end up with

$$E^{(2)} < E^{(1)} + \int \left\{ v_{ext}^{(2)} - v_{ext}^{(1)} \right\} \ n_0(\mathbf{r}) \, d\mathbf{r} \, . \tag{A.26}$$

Then, by adding both we relations (A.25) and (A.26) we get:

$$E^{(1)} + E^{(2)} < E^{(2)} + E^{(1)} \longleftarrow \text{Contradiction} \tag{A.27}$$

Thus, the initial supposition of the two external potentials leading to the same density $n_0(\mathbf{r})$ is false, and the external potential $(\hat{V}_{ext}, \hat{v}_{ext})$ is determined by the density $n_0(\mathbf{r})$ as stated by the first Hohenberg-Kohn theorem (see 1.2.1).

A.3.2 *Theorem II*

This demonstration is restricted to densities $n_0(\mathbf{r})$ that are V-representable densities (see 1.2.1.1). Since $n_0(\mathbf{r})$ defines v_{ext}, which in turn defines $\hat{H}$, all properties can be determined by $n_0(\mathbf{r})$. Then all properties can be viewed as a functional of $n(\mathbf{r})$, including $E[n]$.

$$E^{(e)}[n] = \underbrace{T_e[n] + V_{e-e}[n]}_{F[n]} + \int v_{ext}(\mathbf{r}) n(\mathbf{r}) \, d\mathbf{r}$$

where $F[n]$ must be universal for all electronic systems in case that T_e and V_{e-e} are functionals that only depend on the density $n(\mathbf{r})$.

Now consider the specific $n_0(\mathbf{r})$ corresponding to that specific v_{ext}, then $E_0^{(e)} \equiv E^{(e)}[n_0]$. However, lets consider another density $n_1(\mathbf{r})$, from theorem I, we know that $\psi^{(1)}$ associated with $n_1(\mathbf{r})$ cannot be the ground state of $\hat{H}$. This, has the direct implication that $E_0^{(e)} \equiv E^{(e)}[n_0] < E^{(e)}[n_1]$ for any $n_1(\mathbf{r})$. Thus, knowing the functional $E^{(e)}[n]$ we can:

$$E^{(e)}[n] \longrightarrow \text{minimize} \longrightarrow \text{Ground state } (n_0(r), E_0^{(e)})$$

Which, is exactly what the second theorem states (1.2.1), a functional for the total energy can be defined in terms of $n(\mathbf{r})$, and such functional is minimized by the the ground state density $n_0(\mathbf{r})$.

A.4 SCHROGINGER'S EQUATION IN A PERIODIC LATTICE

The Schrodinger's equation for a periodic potential reads as

$$\hat{H}(\mathbf{r})\Psi(\mathbf{r},t) = \left[-\frac{\hbar^2}{2m}\frac{\partial^2}{\partial x^2} + V(\mathbf{r})\right]\Psi(\mathbf{r},t) = i\hbar\frac{\partial}{\partial t}\Psi(\mathbf{r},t), \tag{A.28}$$

and holds

$$\hat{H}\Psi_i = E_i\Psi_i \tag{A.29}$$

for the eigenfunctions.

In a solid (or any other condensed matter system) it is also convenient to require to the states to obey Born-von Karman boundary conditions | periodic boundary conditions [225] over a large volume Ω. Then, eigenstates can be rewritten as

$$\psi_i(\mathbf{r}) = \sum_{\mathbf{q}} c_{i,\mathbf{q}} \overbrace{\frac{1}{\sqrt{\Omega}} e^{i\mathbf{q}\cdot\mathbf{r}}}^{\equiv|\mathbf{q}\rangle} \equiv \sum_{\mathbf{q}} c_{i,\mathbf{q}} |\mathbf{q}\rangle, \tag{A.30}$$

by using the fact that any periodic function can be transformed into Fourier components $\exp(i\mathbf{q}\cdot\mathbf{r})/\sqrt{\Omega}$. The set of plane waves $\{|\mathbf{q}\rangle\}$ form an orthonormal basis satisfying

$$\langle\mathbf{q}'|\mathbf{q}\rangle \equiv \frac{1}{\Omega}\int_\Omega e^{i(\mathbf{q}-\mathbf{q}')\cdot\mathbf{r}}\,d\mathbf{r} = \delta_{\mathbf{q},\mathbf{q}'}. \tag{A.31}$$

Inserting (A.30) into the Hamiltonian eigenvector equation (A.29) (changing $E_i \to \varepsilon_i$) and projecting over $\langle\mathbf{q}'|$ leads to:

$$\sum_{\mathbf{q}} c_{i,\mathbf{q}} \langle\mathbf{q}'|\hat{H}|\mathbf{q}\rangle = \varepsilon_i \sum_{\mathbf{q}} c_{i,\mathbf{q}} \langle\mathbf{q}'|\mathbf{q}\rangle = \varepsilon_i c_{i,\mathbf{q}'}. \tag{A.32}$$

The kinetic term in $\hat{H}$ is easy to evaluate:

$$\langle\mathbf{q}'|-\frac{\hbar^2}{2m}\nabla^2|\mathbf{q}\rangle \to \langle\mathbf{q}'|-\frac{1}{2}\nabla^2|\mathbf{q}\rangle = \frac{1}{2}|\mathbf{q}|^2\,\delta_{\mathbf{q},\mathbf{q}'}, \tag{A.33}$$

where we have changed to Hartree atomic units. Now, if the potential is periodic such that $V(\mathbf{r}+\mathbf{T}) = V(\mathbf{r})$ we can write it as a sum of Fourier components proportional to $\{|\mathbf{G}_m\rangle\}$, being $\mathbf{G}_m$ the reciprocal lattice vectors.

$$V(\mathbf{r}) = \sum_m V(\mathbf{G}_m)\, e^{i\mathbf{G}_m\cdot\mathbf{r}}, \tag{A.34}$$

which can be seen directly from imposing the periodicity constraint over $V(\mathbf{r})$. Then, the $V(\mathbf{G}_m)$ components are given by:

$$\begin{aligned} V(\mathbf{G}_m) &\equiv \frac{1}{\Omega}\int_\Omega V(\mathbf{r}) e^{-i\mathbf{G}_m\cdot\mathbf{r}}\, d\mathbf{r} \\ &= \frac{1}{\Omega_{cell}}\int_{\Omega_{cell}} V(\mathbf{r}) e^{-i\mathbf{G}_m\cdot\mathbf{r}}\, d\mathbf{r} \end{aligned} \tag{A.35}$$

since the integrand in the first form has the same periodicity as the lattice. The potential term can be then written as

$$\begin{aligned} \langle \mathbf{q}'|V(\mathbf{r})|\mathbf{q}\rangle &= \sum_m V(\mathbf{G}_m)\,\langle \mathbf{q}'|e^{i\mathbf{G}_m\cdot\mathbf{r}}|\mathbf{q}\rangle \\ &= \sum_m V(\mathbf{G}_m)\,\langle \mathbf{q}'|\mathbf{q}+\mathbf{G}_m\rangle \\ &= \sum_m V(\mathbf{G}_m)\delta_{\mathbf{q}'-\mathbf{q},\mathbf{G}_m}. \end{aligned} \tag{A.36}$$

Thus, the potential terms are only non-zero if $\mathbf{q}$ and $\mathbf{q}'$ differ by some reciprocal lattice vector $\mathbf{G}_m$. It is useful then to define any $\mathbf{q} \equiv \mathbf{k}+\mathbf{G}$, so that $\mathbf{k}$ belongs to the first Brillouin zone. Then the Schrodinger equation (A.32) takes the form:

$$\sum_{\mathbf{q}} c_{i,\mathbf{q}} \left[\frac{1}{2}|\mathbf{q}|^2\,\delta_{\mathbf{q},\mathbf{q}'} + \sum_m V(\mathbf{G}_m)\delta_{\mathbf{q}'-\mathbf{q},\mathbf{G}_m}\right] = \varepsilon_i c_{i,\mathbf{q}'}, \tag{A.37}$$

where if we now change $\mathbf{q} \to \mathbf{k}+\mathbf{G}_n$ and $\sum_{\mathbf{q}} \to \sum_{\mathbf{k},n}$ we get

$$\sum_{\mathbf{k},n} c_{i,n}(\mathbf{k}) \left[\frac{1}{2}|\mathbf{k}+\mathbf{G}_n|^2\,\delta_{n,n'}\delta_{\mathbf{k},\mathbf{k}'} + \sum_m V(\mathbf{G}_m)\delta_{\mathbf{k},\mathbf{k}'}\delta_{n'-n,m}\right] = \varepsilon_i c_{i,n'}(\mathbf{k}'). \tag{A.38}$$

Summing over m and $\mathbf{k}$ as well as switching the $n \leftrightarrow n'$:

$$\sum_{n'} c_{i,n'}(\mathbf{k}) \left[\frac{1}{2}|\mathbf{k}+\mathbf{G}_{n'}|^2\,\delta_{n,n'} + \sum_m V(\mathbf{G}_n-\mathbf{G}_{n'})\right] = \varepsilon_i c_{i,n}(\mathbf{k}), \tag{A.39}$$

which we can now finally rewrite as

$$\begin{cases} \displaystyle\sum_{m'} H_{m,m'}(\mathbf{k}) c_{i,m'}(\mathbf{k}) = \varepsilon_i(\mathbf{k}) c_{i,m}(\mathbf{k}), \\ H_{m,m'}(\mathbf{k}) \equiv \langle \mathbf{k}+\mathbf{G}_m|\hat{H}|\mathbf{k}+\mathbf{G}_{m'}\rangle = \dfrac{1}{2}|\mathbf{k}+\mathbf{G}_m|^2\,\delta_{m,m'} + V(\mathbf{G}_m-\mathbf{G}_{m'}), \end{cases} \tag{A.40}$$

where we have relabeled the eigenvalues of each particular matrix $H(\mathbf{k})$ as $\varepsilon_i(\mathbf{k})$.

A.5 PROPERTIES OF THE SECOND ORDER FORCE CONSTANTS

The second order force constants defining the harmonic Hamiltonian in secion 2.1 satisfy the following relations:

1. $\Phi_{st}^{\alpha\beta} = \Phi_{ts}^{\beta\alpha}$ since
$$\frac{\partial^2 V}{\partial r_{i\alpha}\partial r_{t\beta}} = \frac{\partial^2 V}{\partial r_{t\beta}\partial r_{s\alpha}} \tag{A.41}$$

2. $\sum_t \Phi_{st}^{\alpha\beta} = 0$ since a uniform translation of the lattice $u_{i\alpha} = d_\alpha$ should give zero energy difference from V_0.
$$V - V_0 = \frac{1}{2}\Phi_{st}^{\alpha\beta}u_{s\alpha}u_{t\beta} = \frac{1}{2}\sum_{st\alpha\beta}\Phi_{st}^{\alpha\beta}d_\alpha d_\beta = \frac{1}{2}\sum_{\alpha\beta}d_\alpha d_\beta\sum_{st}\Phi_{st}^{\alpha\beta} =$$
$$= \frac{1}{2}\sum_{\alpha\beta}d_\alpha d_\beta\sum_s\left(\sum_t\Phi_{st}^{\alpha\beta}\right) = 0 \tag{A.42}$$
independently of d, which leads to the so called **acoustic sum rule**.

3. Since every Bravais lattice has inversion symmetry (which maps $\mathbf{T} \to -\mathbf{T}, \vec{u} \to -\vec{u}$): $\Phi_{st}^{\alpha\beta} = \Phi_{ts}^{\alpha\beta}$ witch together with (2) implies $\Phi_{st}^{\alpha\beta} = \Phi_{st}^{\beta\alpha}$.

A.6 CLASSICAL HARMONIC HAMILTONIAN WITH TRANSLATIONAL SYMMETRY

A.6.0.1 *Harmonic lattice dynamics*

In order to solve the classic equations of motion of an harmonic crystal presented in equation (2.10) we assume a solution which is periodic in space and time of the form:
$$u_{i\gamma}(\mathbf{T}) = \frac{\epsilon_{i\gamma}(\mathbf{k})}{\sqrt{M_i}}e^{-i\omega t}e^{i(\mathbf{k}\cdot\mathbf{T})}, \tag{A.43}$$
where now i to the index of the atom within the primitive cell and $\mathbf{T}$ is the cell of the atom. Notice how, in accordance with Bloch's theorem (1.4) solution takes form of a periodic function in $\mathbf{T}$ times a phase factor $e^{i\mathbf{k}\cdot\mathbf{T}}$.

Then, substituting (A.43) into (2.10) we get
$$-M_i\omega^2\frac{\epsilon_{i\gamma}(\mathbf{k})}{\sqrt{M_i}}e^{-i\omega t} = -\sum_{s\alpha}\sum_{\mathbf{T}}\Phi_{is}^{\gamma\alpha}(\mathbf{T})u_{s\alpha}(\mathbf{T}) = -\sum_{s\alpha,\mathbf{T}}\Phi_{is}^{\gamma\alpha}(\mathbf{T})\frac{\epsilon_{s\alpha}(\mathbf{k})}{\sqrt{M_s}}e^{-i\omega t}e^{i(\mathbf{k}\cdot\mathbf{T})} \tag{A.44}$$
$$\Downarrow$$
$$\omega^2\epsilon_{i\gamma}(\mathbf{k}) = \sum_{s\alpha,\mathbf{T}}\frac{\Phi_{is,\mathbf{T}}^{\gamma\alpha}}{\sqrt{M_iM_s}}e^{i\mathbf{k}\cdot\mathbf{T}}\epsilon_{s\alpha}(\mathbf{k}) = \sum_{s\alpha}\underbrace{\left(\sum_{\mathbf{T}}\frac{\Phi_{is}^{\gamma\alpha}(\mathbf{T})}{\sqrt{M_iM_s}}e^{i\mathbf{k}\cdot\mathbf{T}}\right)}_{\text{Dyn matrix}}\epsilon_{s\alpha}(\mathbf{k}) \tag{A.45}$$

Now we can define the Fourier transform of Φ **(the Dynamical matrix)** as:

$$D_{ij}^{\alpha\beta}(\mathbf{k}) = \sum_{\mathbf{T}} \frac{\Phi_{ij}^{\alpha\beta}(\mathbf{T})}{\sqrt{M_i M_j}} e^{i\mathbf{k}\cdot\mathbf{T}}, \tag{A.46}$$

So that we have:

$$\omega(\mathbf{k})^2 \epsilon_{i\gamma}(\mathbf{k}) = \sum_{s\alpha} D_{is}^{\gamma\alpha}(\mathbf{k}) \epsilon_{s\alpha}(\mathbf{k}), \tag{A.47}$$

In general ω will be a function of $\mathbf{k}$ so that $\omega(\mathbf{k})$. Thus, the solutions will be labeled by a mode index μ and a k-vector $\mathbf{k}$, leading to $(\epsilon_{i\alpha\mathbf{k}'}^{\mu}, \omega_{\mathbf{k}}^{\mu})$.

A.6.0.2 *Harmonic total energy*

After solving the problem of the lattice vibrations, we can write any set of displacements $\mathbf{u}_i(\mathbf{T})$ as a sum of solutions to the eigenvalue problem (A.47). In this basis is easy to compute the total kinetic and potential harmonic energies equivalent to the expressions (2.20) and (2.21) in the main text.

$$\begin{cases} u_{i\gamma}(\mathbf{T}) = \sum_{\mu\mathbf{k}} q_{\mu\mathbf{k}} \frac{\epsilon_{i\gamma\mathbf{k}}^{\mu}}{\sqrt{M_i}} e^{-i\omega_{\mu\mathbf{k}}t} e^{i(\mathbf{k}\cdot\mathbf{T})} \\ T^{\text{harm}} = \frac{1}{2} \sum_{\mathbf{T},i\alpha} M_i |\dot{u}_{i\alpha}(\mathbf{T})|^2, \\ U^{\text{harm}} = \frac{1}{2} \sum_{\mathbf{T}_s,\mathbf{T}_t} \Phi_{st}^{\alpha\beta}(\mathbf{T}_s - \mathbf{T}_t) u_{s\alpha}(\mathbf{T}_s) u_{t\beta}(\mathbf{T}_t). \end{cases} \tag{A.48}$$

where each solution of the equations of motion is labeld by $(\mu, \mathbf{k})$. Thus, the kinetik energy is given by

$$\begin{aligned} T^{\text{harm}} &= \frac{1}{2} \sum_{\mathbf{T},i\alpha} M_i \left(\sum_{\mu\mathbf{k}} (-i\omega_{\mu,\mathbf{k}}) q_{\mu\mathbf{k}} \frac{\epsilon_{i\alpha\mathbf{k}}^{\mu}}{\sqrt{M_i}} e^{-i\omega_{\mu\mathbf{k}}t} e^{i(\mathbf{k}\cdot\mathbf{T})} \right) \\ &\times \left(\sum_{\mu'\mathbf{k}'} (i\omega_{\mu'\mathbf{k}'}) q_{\mu'\mathbf{k}'}^{\dagger} \frac{\epsilon_{i\alpha\mathbf{k}'}^{\mu'\dagger}}{\sqrt{M_i}} e^{i\omega_{\mu'\mathbf{k}'}t} e^{-i(\mathbf{k}'\cdot\mathbf{T})} \right) \\ &= \frac{1}{2} \sum_{i\alpha\mu\mu'\mathbf{k}\mathbf{k}'} \omega_{\mu\mathbf{k}} \omega_{\mu'\mathbf{k}'} q_{\mu\mathbf{k}} q_{\mu'\mathbf{k}'}^{\dagger} \epsilon_{i\alpha\mathbf{k}}^{\mu} \epsilon_{i\alpha\mathbf{k}'}^{\mu'\dagger} \exp\left[i(\omega_{\mu',\mathbf{k}'} - \omega_{\mu\mathbf{k}})t\right] \overbrace{\sum_{\mathbf{T}} e^{i(\mathbf{k}-\mathbf{k}')\cdot\mathbf{T}}}^{N_{\text{cell}}\delta_{\mathbf{k}\mathbf{k}'}} \\ &= \frac{N_{\text{cell}}}{2} \sum_{\mu\mu'\mathbf{k}} \omega_{\mu\mathbf{k}} \omega_{\mu'\mathbf{k}} q_{\mu\mathbf{k}} q_{\mu'\mathbf{k}}^{\dagger} \exp\left[i(\omega_{\mu',\mathbf{k}} - \omega_{\mu\mathbf{k}})t\right] \overbrace{\sum_{i\alpha} \epsilon_{i\alpha\mathbf{k}}^{\mu} \epsilon_{i\alpha\mathbf{k}}^{\mu'\dagger}}^{\delta_{\mu\mu'}} \\ &= \frac{N_{\text{cell}}}{2} \sum_{\mu\mathbf{k}} |q_{\mu\mathbf{k}}|^2 \omega_{\mu\mathbf{k}'}^2 \end{aligned} \tag{A.49}$$

while the potential energy is given by

$$
\begin{aligned}
U^{\text{harm}} &= \frac{1}{2}\sum_{\mathbf{T}_s\mathbf{T}_t,s\alpha,t\beta,\mu\mu',\mathbf{k}\mathbf{k}'} \Phi_{st}^{\alpha\beta}(\mathbf{T}_s-\mathbf{T}_t)e^{i\mathbf{k}\cdot\mathbf{T}_s}e^{-i\mathbf{k}'\cdot\mathbf{T}_t} \\
&\times\left(\frac{1}{\sqrt{M_sM_t}}\underbrace{q_{\mu\mathbf{k}}q^{\dagger}_{\mu'\mathbf{k}'}\epsilon^{\mu}_{s\alpha\mathbf{k}}\epsilon^{\dagger\mu'}_{t\beta\mathbf{k}'}e^{-i(\omega_{\mu\mathbf{k}}-\omega_{\mu'\mathbf{k}'})t}}_{A}=\right) \\
&=\{\mathbf{T}\equiv\mathbf{T}_s-\mathbf{T}_t;\mathbf{T}_s\equiv\mathbf{T}+\mathbf{T}_t\} = \frac{1}{2}\sum_{\mathbf{T}\mathbf{T}_t,s\alpha,t\beta,\mu\mu',\mathbf{k}\mathbf{k}'}\Phi_{st}^{\alpha\beta}(\mathbf{T})e^{i\mathbf{k}\cdot\mathbf{T}}e^{-i(\mathbf{k}'-\mathbf{k})\cdot\mathbf{T}_t}\frac{1}{\sqrt{M_sM_t}}A \\
&=\frac{1}{2}\sum_{\mathbf{T}_t,s\alpha,t\beta,\mu\mu',\mathbf{k}\mathbf{k}'}\underbrace{\left(\sum_{\mathbf{T}}\frac{\Phi_{st}^{\alpha\beta}(\mathbf{T})}{\sqrt{M_sM_t}}e^{i\mathbf{k}\cdot\mathbf{T}}\right)}_{D_{st}^{\alpha\beta}(\mathbf{k})}e^{-i(\mathbf{k}'-\mathbf{k})\cdot\mathbf{T}_t}A = \\
&=\frac{1}{2}\sum_{\mathbf{T}_t,s\alpha,t\beta,\mu\mu',\mathbf{k}\mathbf{k}'}D_{st}^{\alpha\beta}(\mathbf{k})e^{-i(\mathbf{k}'-\mathbf{k})\cdot\mathbf{T}_t}\underbrace{q_{\mu\mathbf{k}}q^{\dagger}_{\mu'\mathbf{k}'}\epsilon^{\mu}_{s\alpha\mathbf{k}}\epsilon^{\dagger\mu'}_{t\beta\mathbf{k}'}e^{-i(\omega_{\mu\mathbf{k}}-\omega_{\mu'\mathbf{k}'})t}}_{A} = \\
&=\frac{1}{2}\sum_{t\beta,\mu\mu',\mathbf{k}\mathbf{k}'}\underbrace{\left(\sum_{s\alpha}D_{st}^{\alpha\beta}(\mathbf{k})\epsilon^{\mu}_{s\alpha\mathbf{k}}\right)}_{\omega_{\mathbf{k}}^{\mu 2}\epsilon^{\mu}_{t\beta k}}\underbrace{\left(\sum_{\mathbf{T}_t}e^{-i(\mathbf{k}'-\mathbf{k})\cdot\mathbf{T}_t}\right)}_{N_{cell}\delta_{\mathbf{k}\mathbf{k}'}}q_{\mu\mathbf{k}}q^{\dagger}_{\mu'\mathbf{k}'}\epsilon^{\dagger\mu'}_{t\beta\mathbf{k}'}e^{-i(\omega_{\mu\mathbf{k}}-\omega_{\mu'\mathbf{k}'})t} = \\
&=\frac{1}{2}\sum_{t\beta,\mu\mu',\mathbf{k}}\left(\sum_{\mathbf{k}'}\omega_{\mathbf{k}}^{\mu 2}\epsilon^{\mu}_{t\beta\mathbf{k}}N_{\text{cell}}\delta_{\mathbf{k}\mathbf{k}'}q_{\mu\mathbf{k}}q^{\dagger}_{\mu'\mathbf{k}'}\epsilon^{\dagger\mu'}_{t\beta\mathbf{k}'}e^{-i(\omega_{\mu\mathbf{k}}-\omega_{\mu'\mathbf{k}'})t}\right) = \\
&=\frac{1}{2}\sum_{\mu,\mathbf{k}}\left(\sum_{\mu'}\omega_{\mathbf{k}}^{\mu 2}\underbrace{\sum_{t\beta}\epsilon^{\mu}_{t\beta\mathbf{k}}\,\epsilon^{\dagger\mu'}_{t\beta\mathbf{k}}}_{\delta_{\mu\mu'}}N_{\text{cell}}q_{\mu\mathbf{k}}q^{\dagger}_{\mu'\mathbf{k}}e^{-i(\omega_{\mu\mathbf{k}}-\omega_{\mu'\mathbf{k}})t}\right) \\
&=\frac{1}{2}N_{\text{cell}}\sum_{\mu\mathbf{k}}\left|q_{\mu\mathbf{k}}\right|^2\omega_{\mu\mathbf{k}}^2.
\end{aligned}
\tag{A.50}
$$

Thus, both the kinetik and potential parts contribute equally to the total energy, being the potential energy per cell given by

$$
u^{\text{harm}} = \frac{U^h}{N_{\text{cell}}} = \frac{1}{2}\sum_{\mu\mathbf{k}}|q_{\mu}\mathbf{k}|^2\,\omega_{\mu\mathbf{k}}^2. \tag{A.51}
$$

Notice how for a single supercell (neglecting the translational symmetries), the sum only goes over μ since $N_k = N_{\text{cell}} = 1$, reducing the equation (A.51) to (2.21).

A.6.0.3 *Acoustic modes*

The condition for having acoustic modes (or zero energy fixed translational modes), can be easily seen in this formalism. We impose that all translations

are the same in $u_{i\alpha} = d_\alpha$ (A.43), which implies that $\epsilon_{i\alpha} = \sqrt{M_i} d_\alpha$ as well as $\mathbf{k} = 0$. If we now substitute this in the eigenvalue problem (A.47) we have that

$$\omega^2 \sqrt{M_i} d_\gamma = D_{ij}^{\gamma\alpha}(\mathbf{k}=0)\sqrt{M_j} d_\alpha = \sum_{j\mathbf{T}} \frac{\Phi_{ij}^{\gamma\alpha}(\mathbf{T})}{\sqrt{M_i M_j}} \sqrt{M_j} d_\alpha \tag{A.52}$$

$$\Downarrow$$

$$\omega^2 d_\gamma = \left(\sum_{j\mathbf{T}} \Phi_{ij}^{\gamma\alpha}(\mathbf{T}) \right) d_\alpha \underset{\text{Must be zero freq}}{=} 0 \tag{A.53}$$

Which is the same as the property (2) in Appendix A.5. This is an illustration of Goldstone's theorem, which states that such gapless mode must occur in a translationally invariant Hamiltonian.

A.7 CANONICAL QUANTIZATION OF THE HARMONIC CRYSTAL

We already show that within the Harmonic approximation, which describes a set of coupled harmonic oscillators, the Hamiltonian can be written as

$$\begin{aligned} \hat{H}^{\text{harm}} &= \hat{T}^{\text{harm}} + \hat{U}^{\text{harm}}(\mathbf{R}) \\ &= \sum_{s=1}^{N_I} \sum_{\alpha=1}^{3} \sum_{\mathbf{T}} \frac{\hat{P}_{s\alpha}(\mathbf{T})^2}{2M_s} + \sum_{\mathbf{T},\mathbf{T}',\alpha\beta st} \frac{1}{2} \Phi_{st}^{\alpha\beta}(\mathbf{T}-\mathbf{T}') \hat{u}_{s\alpha}(\mathbf{T}) \hat{u}_{t\beta}(\mathbf{T}') \end{aligned} \tag{A.54}$$

If we then Fourier transform $\hat{u}_{s\alpha}$ and $\hat{P}_{s\alpha}$ as

$$\begin{aligned} \hat{u}_{s\alpha}(\mathbf{k}) &\equiv \frac{1}{\sqrt{N_k}} \sum_{\mathbf{T}} e^{i\mathbf{k}\cdot\mathbf{T}} \hat{u}_{s\alpha}(\mathbf{T}), \\ \hat{P}_{s\alpha}(\mathbf{k}) &\equiv \frac{1}{\sqrt{N_k}} \sum_{\mathbf{T}} e^{i\mathbf{k}\cdot\mathbf{T}} \hat{P}_{s\alpha}(\mathbf{T}), \end{aligned} \tag{A.55}$$

which implies the inverse transforms:

$$\begin{aligned} \hat{u}_{s\alpha}(\mathbf{T}) &\equiv \frac{1}{\sqrt{N_k}} \sum_{\mathbf{k}} e^{-i\mathbf{k}\cdot\mathbf{T}} \hat{u}_{s\alpha}(\mathbf{k}), \\ \hat{P}_{s\alpha}(\mathbf{T}) &\equiv \frac{1}{\sqrt{N_k}} \sum_{\mathbf{k}} e^{-i\mathbf{k}\cdot\mathbf{T}} \hat{P}_{s\alpha}(\mathbf{k}), \end{aligned} \tag{A.56}$$

then, the kinetic energy can be rewritten as

$$\begin{aligned} \hat{T}^{\text{harm}} &= \frac{1}{N_k} \sum_{\mathbf{T}s\alpha} \frac{1}{2M_s} \left(\sum_{\mathbf{k}'} e^{-i\mathbf{k}'\cdot\mathbf{T}} \hat{P}_{s\alpha}(\mathbf{k}') \right) \left(\sum_{\mathbf{k}} e^{-i\mathbf{k}\cdot\mathbf{T}} \hat{P}_{s\alpha}(\mathbf{k}) \right) \\ &= \frac{1}{N_k} \sum_{s\alpha,\mathbf{k}\mathbf{k}'} \frac{1}{2M_s} \hat{P}_{s\alpha}(\mathbf{k}') \hat{P}_{s\alpha}(\mathbf{k}) \overbrace{\sum_{\mathbf{T}} e^{-i(\mathbf{k}+\mathbf{k}')\cdot\mathbf{R}}}^{N_k \delta_{\mathbf{k},-\mathbf{k}'}} = \sum_{s\alpha,\mathbf{k}} \frac{1}{2M_s} \hat{P}_{s\alpha}(-\mathbf{k}) \hat{P}_{s\alpha}(\mathbf{k}). \end{aligned} \tag{A.57}$$

On the other hand, the potential energy

$$\begin{aligned}
\hat{U}^{\text{harm}} &= \sum_{\mathbf{T},\mathbf{T}',\alpha\beta st} \frac{1}{2N}\Phi_{st}^{\alpha\beta}(\mathbf{T}-\mathbf{T}')\left(\sum_{\mathbf{k}} e^{-i\mathbf{k}\cdot\mathbf{T}}\hat{u}_{s\alpha}(\mathbf{k})\right)\left(\sum_{\mathbf{k}'} e^{-i\mathbf{k}'\cdot\mathbf{T}'}\hat{u}_{t\beta}(\mathbf{k}')\right) \\
&= \sum_{\mathbf{T},\mathbf{t},\alpha\beta st,\mathbf{k},\mathbf{k}'} \frac{1}{2N}\Phi_{st}^{\alpha\beta}(\mathbf{t})\hat{u}_{s\alpha}(\mathbf{k})\hat{u}_{t\beta}(\mathbf{k}')e^{-i\mathbf{k}\cdot\mathbf{T}}e^{-i\mathbf{k}'(\mathbf{T}-\mathbf{t})} \\
&= \sum_{\mathbf{t},\alpha\beta st,\mathbf{k},\mathbf{k}'} \frac{1}{2N}\Phi_{st}^{\alpha\beta}(\mathbf{t})\hat{u}_{s\alpha}(\mathbf{k})\hat{u}_{t\beta}(\mathbf{k}')e^{i\mathbf{k}'\mathbf{t}}\overbrace{\sum_{\mathbf{T}} e^{-i(\mathbf{k}+\mathbf{k}')\cdot\mathbf{T}}}^{N\delta_{\mathbf{k},-\mathbf{k}'}} \\
&= \frac{1}{2}\sum_{\alpha\beta st,\mathbf{k}}\left(\overbrace{\sum_{\mathbf{t}}\Phi_{st}^{\alpha\beta}(\mathbf{t})e^{-i\mathbf{k}\mathbf{t}}}^{\equiv\Phi_{st}^{\alpha\beta}(\mathbf{k})}\right)\hat{u}_{s\alpha}(\mathbf{k})\hat{u}_{t\beta}(-\mathbf{k}) \\
&= \frac{1}{2}\sum_{\alpha\beta st,\mathbf{k}}\Phi_{st}^{\alpha\beta}(\mathbf{k})\hat{u}_{s\alpha}(\mathbf{k})\hat{u}_{t\beta}(-\mathbf{k}),
\end{aligned} \tag{A.58}$$

where we relabeled $\mathbf{T}-\mathbf{T}'=\mathbf{t}$, so that $\mathbf{T}'=\mathbf{T}-\mathbf{t}$, and $\Phi(\mathbf{k})$ is the Fourier transform of the force constant matrix (not to be confused with the dynamical matrix). All together, implies that the Hamiltonian (A.54) in reciprocal space can be written in the simpler form

$$\hat{H}^{\text{harm}} = \sum_{s\alpha,\mathbf{k}}\frac{1}{2M_s}\hat{P}_{s\alpha}(-\mathbf{k})\hat{P}_{s\alpha}(\mathbf{k}) + \frac{1}{2}\sum_{\alpha\beta st,\mathbf{k}}\Phi_{st}^{\alpha\beta}(\mathbf{k})\hat{u}_{s\alpha}(\mathbf{k})\hat{u}_{t\beta}(-\mathbf{k}), \tag{A.59}$$

which comes as result of the Bloch theorem. This, can be subsequently diagonalized by selecting the appropriate leather operators

$$\hat{u}_{s\alpha}(\mathbf{k}) = \sum_{\nu}\frac{1}{\sqrt{2M_s\omega_\nu(\mathbf{k})}}\epsilon_{s\alpha}^{\nu}(\mathbf{k})\left(\hat{b}_\nu(\mathbf{k})+\hat{b}_\nu^\dagger(-\mathbf{k})\right), \tag{A.60}$$

$$\hat{P}_{s\alpha}(\mathbf{k}) = -\sum_{\nu}\sqrt{\frac{M_s\omega_\nu(\mathbf{k})}{2}}\epsilon_{s\alpha}^{\nu}(\mathbf{k})\left(\hat{b}_\nu(\mathbf{k})-\hat{b}_\nu^\dagger(-\mathbf{k})\right), \tag{A.61}$$

with the usual commutation relations

$$[\hat{b}_{\nu\mathbf{q}},\hat{b}^\dagger_{\nu'\mathbf{q}'}] = \delta_{\nu\nu'}\delta_{\mathbf{q}\mathbf{q}'},\quad [\hat{b}_{\nu\mathbf{q}},\hat{b}_{\nu'\mathbf{q}'}] = 0,\quad [\hat{b}^\dagger_{\nu\mathbf{q}},\hat{b}^\dagger_{\nu'\mathbf{q}'}] = 0. \tag{A.62}$$

Then by plugging this relations into $\hat{H}^{\text{harm}}$ one gets

$$\hat{H}^{\text{harm}} = \hat{U}_0 + \sum_{\nu\mathbf{k}}\omega_\nu(\mathbf{k})\left(\frac{1}{2}+\hat{b}^\dagger_{\nu\mathbf{k}}\hat{b}_{\nu\mathbf{k}}\right) = \hat{U}_0 + \sum_{\nu\mathbf{k}}\omega_\nu(\mathbf{k})\left(\frac{1}{2}+\hat{n}_{\nu\mathbf{k}}\right), \tag{A.63}$$

given that equation (A.47) holds for the dynamical matrix $D_{st}^{\alpha\beta}(\mathbf{k})$ defined as

$$D_{st}^{\alpha\beta}(\mathbf{k}) \equiv \frac{\Phi_{st}^{\alpha\beta}(\mathbf{k})}{\sqrt{M_sM_t}}. \tag{A.64}$$

B

ADDITIONAL RESULTS

B.1 WILSON LOOPS FOR THE 11 BUCKLED HONEYCOMB PHASES

The eleven possible phases for the BHL in Table 4.2 were realized within the analytical model by giving appropriate values to the 14 independent coupling constants $(a_1, b_1, h_1, e_1, a_2, b_2, e_2, g_2, d_2, h_2, a_3, b_3, e_3, h_3)$ defined in Appendix 4.3.2 . This enables obtaining a numerical result for the phonon spectra at any point without the need for interpolation. The resulting phonon bands were checked for stability (absence of imaginary frequencies) and the existence of gaps separating the isolated subsets over the whole Brillouin zone, not just along the represented path $\Gamma - K - M - \Gamma$. The phonon bands and Wilson loops are given in Figs. B.1-B.11, while the windings of the different subsets have been summarized in TABLE 4.3.

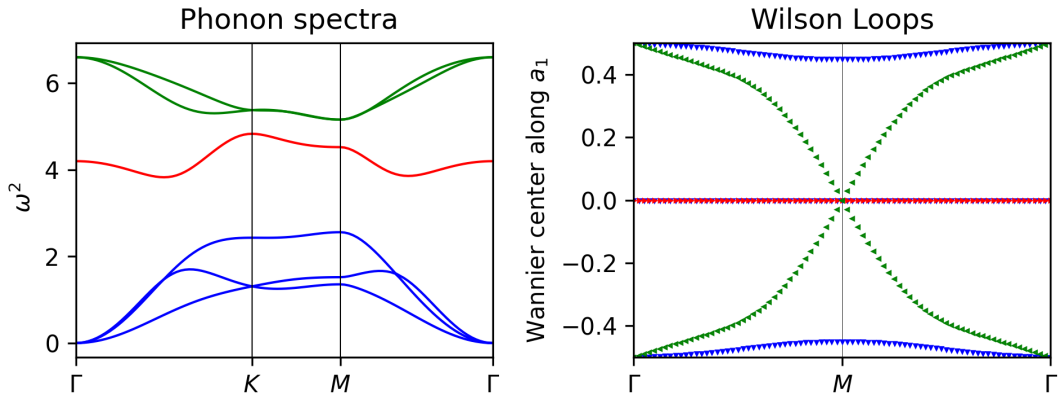

Figure B.1: Phase 1 with Winding 1 in the green subset.
$a_1 = -1;\ e_1 = -0.6;\ b_1 = 0.3;\ h_1 = 0.8;\ a_2 = -0.06;$
$b_2 = 0.02;\ e_2 = -0.06;\ g_2 = 0.06;\ d_2 = 0.04;\ h_2 = 0.04;$
$a_3 = -0.1;\ b_3 = 0.1;\ e_3 = -0.1;\ h_3 = 0.1.$

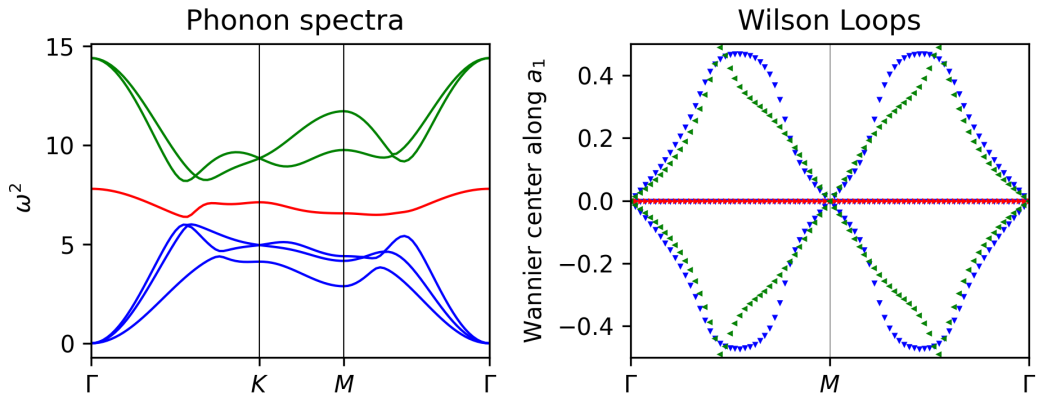

Figure B.2: Phase 2 with Winding 2 in the green subset.
$a_1 = -1;\ e_1 = -0.5;\ b_1 = 0.2;\ h_1 = 0.2;\ a_2 = 0.06.;$
$b_2 = 0.06;\ e_2 = -0.3;\ g_2 = 0.2;\ d_2 = 0.2;\ h_2 = -0.3;$
$a_3 = -1.4;\ b_3 = 0.3;\ e_3 = -0.8;\ h_3 = 0.4.$

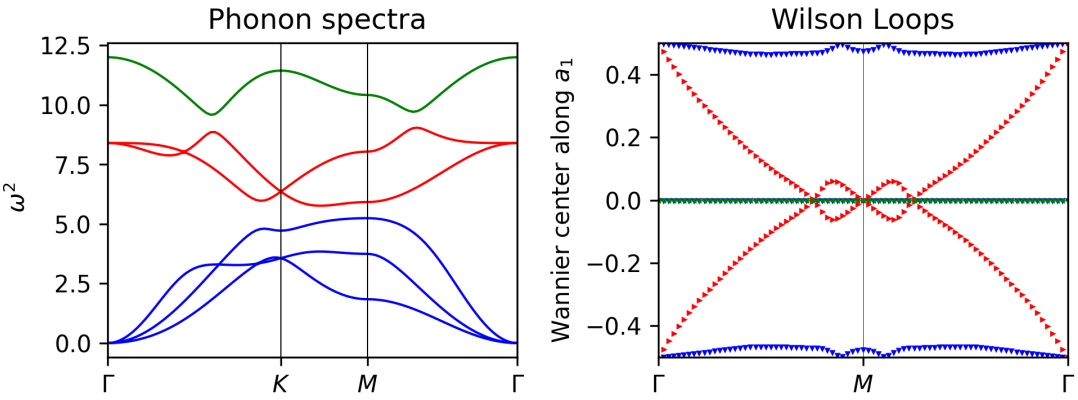

Figure B.3: Phase 3 with Winding 1 in the red subset.
$a_1 = -1;\ e_1 = -2;\ b_1 = 1.12;\ h_1 = 0.4;\ a_2 = -0.2;$
$b_2 = -0.48;\ e_2 = 0;\ g_2 = 0;\ d_2 = -0.4;\ h_2 = -0.12;$
$a_3 = -0.4;\ b_3 = 0;\ e_3 = 0;\ h_3 = 0.04.$

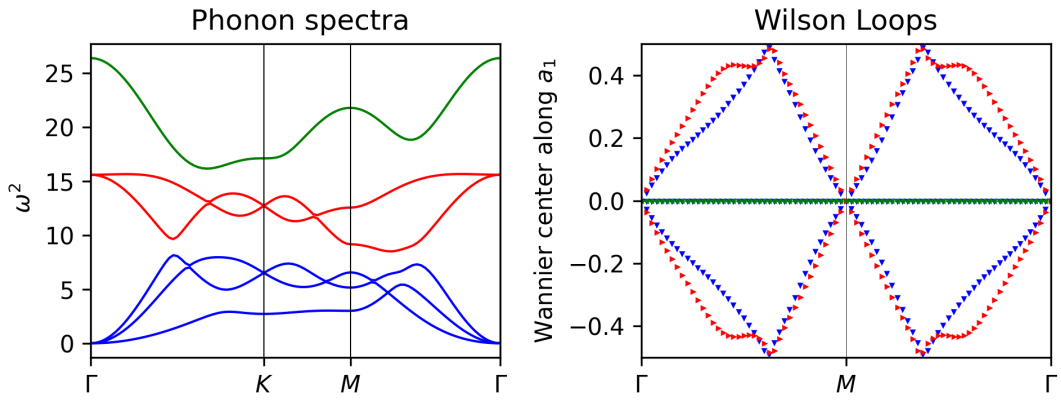

Figure B.4: Phase 4 with Winding 2 in red and blue subsets.
$a_1 = -1$; $e_1 = -1.6$; $b_1 = 0.4$; $h_1 = 1.6$; $a_2 = -0.12$;
$b_2 = 0.2$; $e_2 = 0.2$; $g_2 = -0.4$; $d_2 = -0.2$; $h_2 = -0.6$;
$a_3 = -1.6$; $b_3 = 2$; $e_3 = -2.8$; $h_3 = -0.4$.

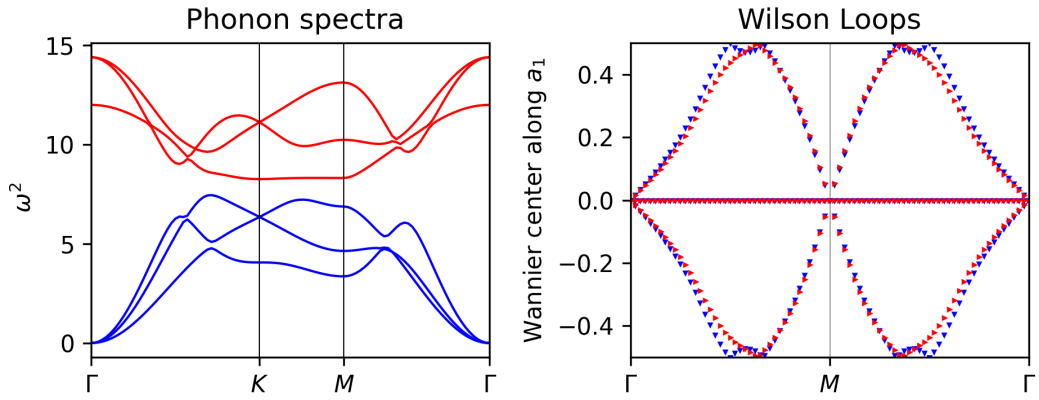

Figure B.5: Phase 5 with Winding 2 in the red subset.
$a_1 = -1$; $e_1 = -1$; $b_1 = 0.2$; $h_1 = 0.6$; $a_2 = 0$;
$b_2 = 0.06$; $e_2 = -0.36$; $g_2 = 0.4$; $d_2 = 0.2$; $h_2 = -0.3$;
$a_3 = -1.4$; $b_3 = 0.5$; $e_3 = -1$; $h_3 = 0.5$.

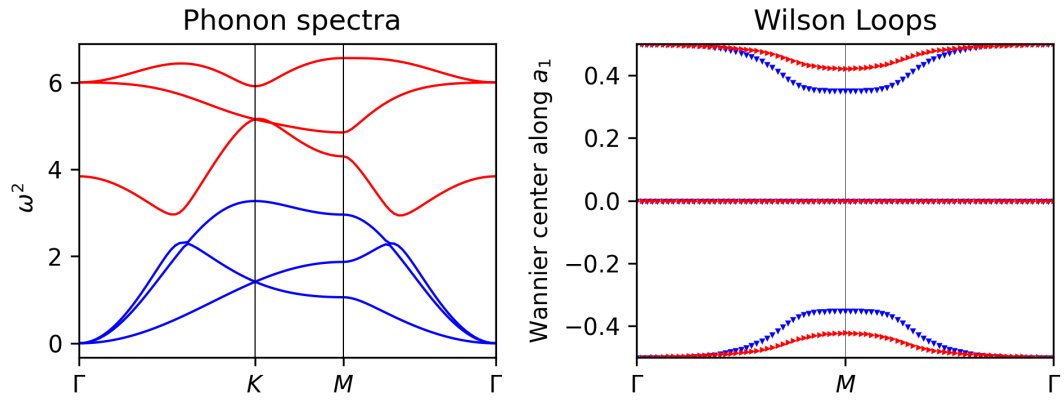

Figure B.6: Phase 6 without any winding.
$a_1 = -1$; $e_1 = -0.6$; $b_1 = 0.4$; $h_1 = 0.3$; $a_2 = -0.2$;
$b_2 = 0.04$; $e_2 = 0.04$; $g_2 = 0.04$; $d_2 = 0.04$; $h_2 = 0.04$;
$a_3 = 0.$; $b_3 = 0.04$; $e_3 = -0.04$; $h_3 = 0.04$.

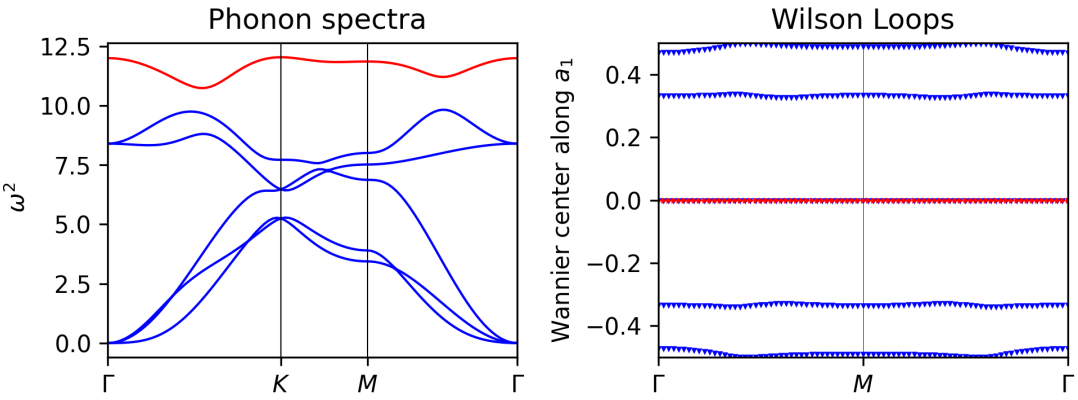

Figure B.7: Phase 7 without any winding.
$a_1 = -1$; $e_1 = -2$; $b_1 = 1.12$; $h_1 = 0.2$; $a_2 = -0.4$;
$b_2 = -0.48$; $e_2 = 0$; $g_2 = -0.4$; $d_2 = -0.4$; $h_2 = -0.12$;
$a_3 = -0.4$; $b_3 = -0.4$; $e_3 = 0$; $h_3 = 0.08$.

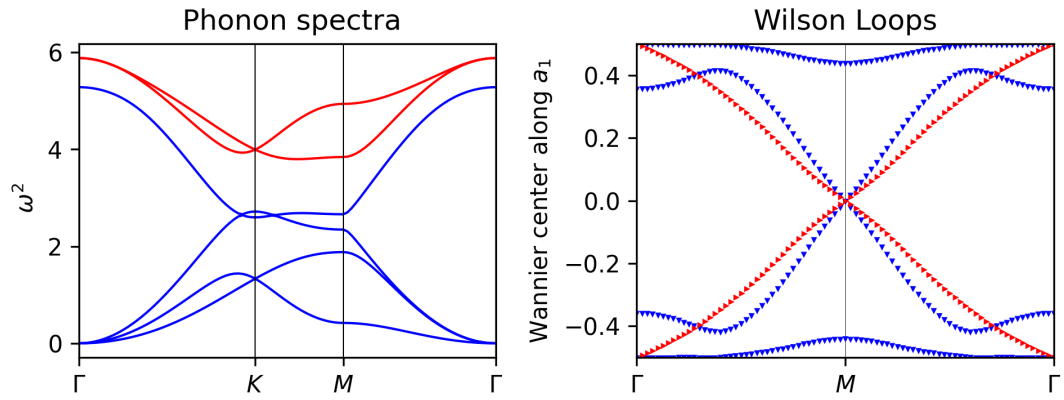

Figure B.8: Phase 8 with Winding 1 in the red subset.
$a_1 = -1$; $e_1 = -0.9$; $b_1 = -0.04$; $h_1 = 0.6$; $a_2 = 0.02$;
$b_2 = 0.02$; $e_2 = 0.02$; $g_2 = 0.02$; $d_2 = 0.02$; $h_2 = 0.02$;
$a_3 = 0.02$; $b_3 = 0.02$; $e_3 = 0.02$; $h_3 = 0.02$.

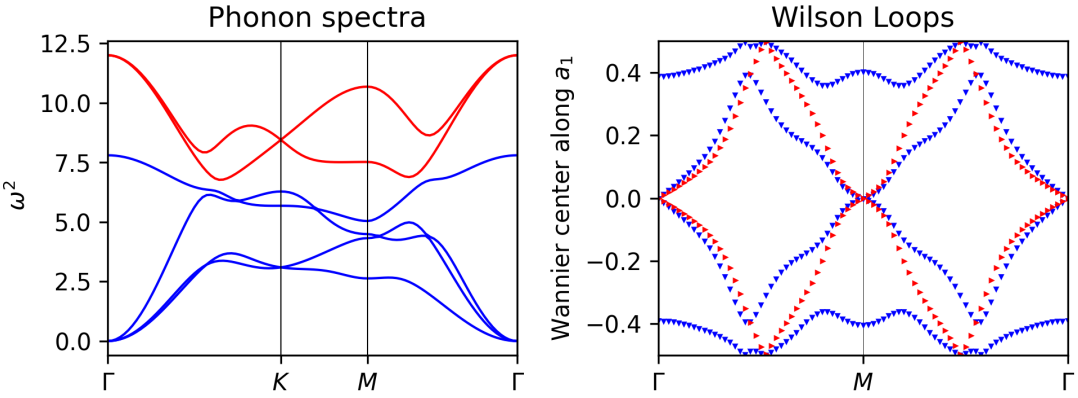

Figure B.9: Phase 9 with Winding 2 in the red subset.
$a_1 = -1$; $e_1 = -0.5$; $b_1 = 0.2$; $h_1 = 0.8$; $a_2 = 0.06$;
$b_2 = 0.1$; $e_2 = -0.3$; $g_2 = 0$; $d_2 = -0.1$; $h_2 = -0.3$;
$a_3 = -1$; $b_3 = -0.3$; $e_3 = -0.8$; $h_3 = 0.4$.

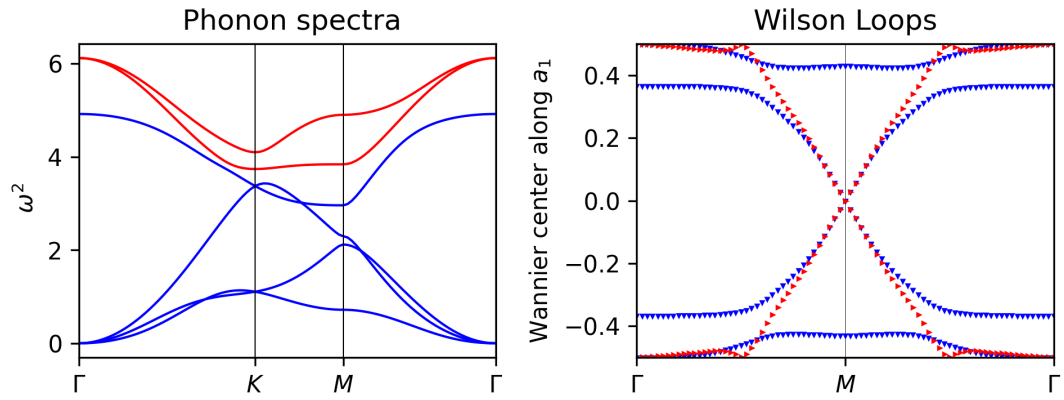

Figure B.10: Phase 10 with Winding 1 in the red subset.
$a_1 = -1$; $e_1 = -0.8$; $b_1 = -0.04$; $h_1 = 0.6$; $a_2 = 0.02$;
$b_2 = 0.02$; $e_2 = -0.02$; $g_2 = -0.02$; $d_2 = -0.2$; $h_2 = 0.02$;
$a_3 = -0.02$; $b_3 = -0.02$; $e_3 = -0.02$; $h_3 = -0.1$.

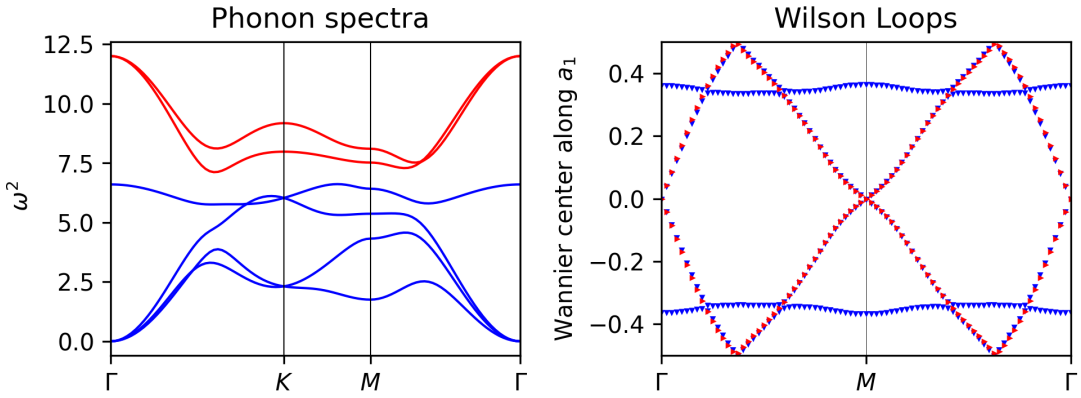

Figure B.11: Phase 11 with Winding 2 in red and blue subsets.
$a_1 = -1$; $e_1 = -0.5$; $b_1 = 0.2$; $h_1 = -0.2$; $a_2 = 0.06$;
$b_2 = 0.1$; $e_2 = -0.3$; $g_2 = 0$; $d_2 = -0.6$; $h_2 = -0.3$;
$a_3 = -1$; $b_3 = 0$; $e_3 = -0.6$; $h_3 = 0.04$.

B.2 RESULTS FOR AgTl, Br_2C_3Si, MoS_2, P_2Sn_2 AND Sn LOW SYMMETRY PHASES

In Chapter 5, we started by studying five possible candidates for two-dimensional materials with a CDW that could lead to a topologically non-trivial metal-insulator phase transition. For all the candidates, we first relaxed the structures according the most unstable modes in the harmonic phonon spectra provided by the database [143] (see Fig. 5.1). Then, we performed a band structure calculation and analyzed the stability by computing the phonon spectra of the low symmetry phase. The possible low-symmetry structures for AgTl, Br_2C_3Si, MoS_2, P_2Sn_2 and Sn are analyzed in figures B.12, B.13, B.14, B.15 and

B.16 respectively. In all cases, each of the phonon and electronic spectra are titled with the **k**-point and irreducible representation of the phonon mode driving the phase transition, as well as the resulting space group.

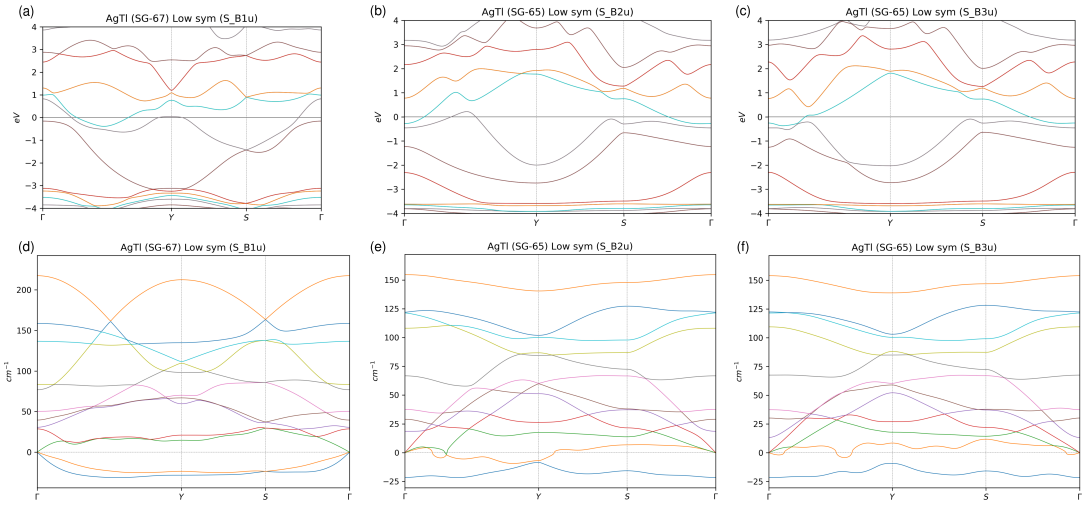

Figure B.12: **Band structures and phonon spectra of** AgTl **low symmetry phases. a,b,c.** Represent the band structures of the three possible low symmetry phases AgTl. **d,e,f.** Show the corresponding phonon spectra, all of them presenting instabilities.

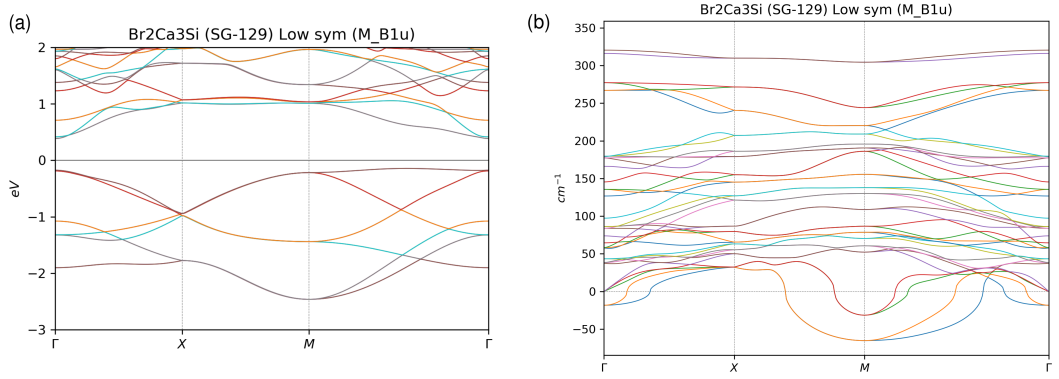

Figure B.13: **Band structures and phonon spectra of** Br_2C_3Si **low symmetry phases. a,b.** Show the electronic and phonon spectra respectively. The phonon spectra is still unstable with an instability at the M point.

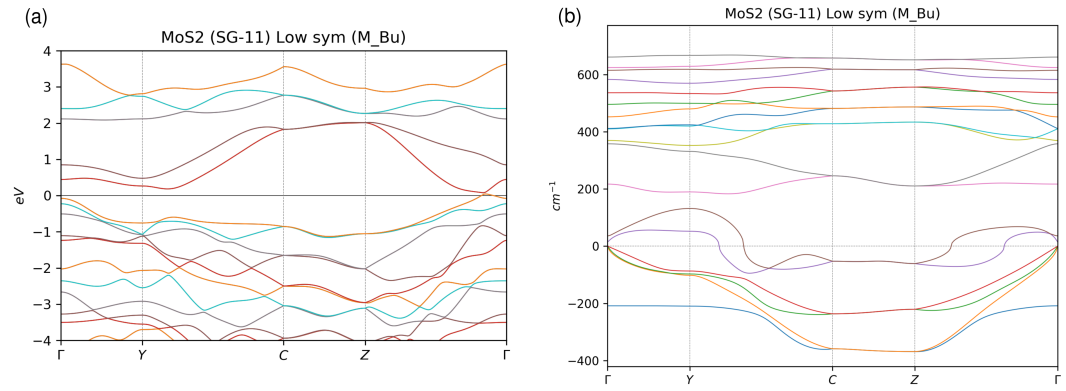

Figure B.14: **Band structures and phonon spectra of MoS_2 low symmetry phases. a,b.** Show the electronic and phonon spectra respectively. The phonon spectra is still highly unstable across the hole Brillouin zone.

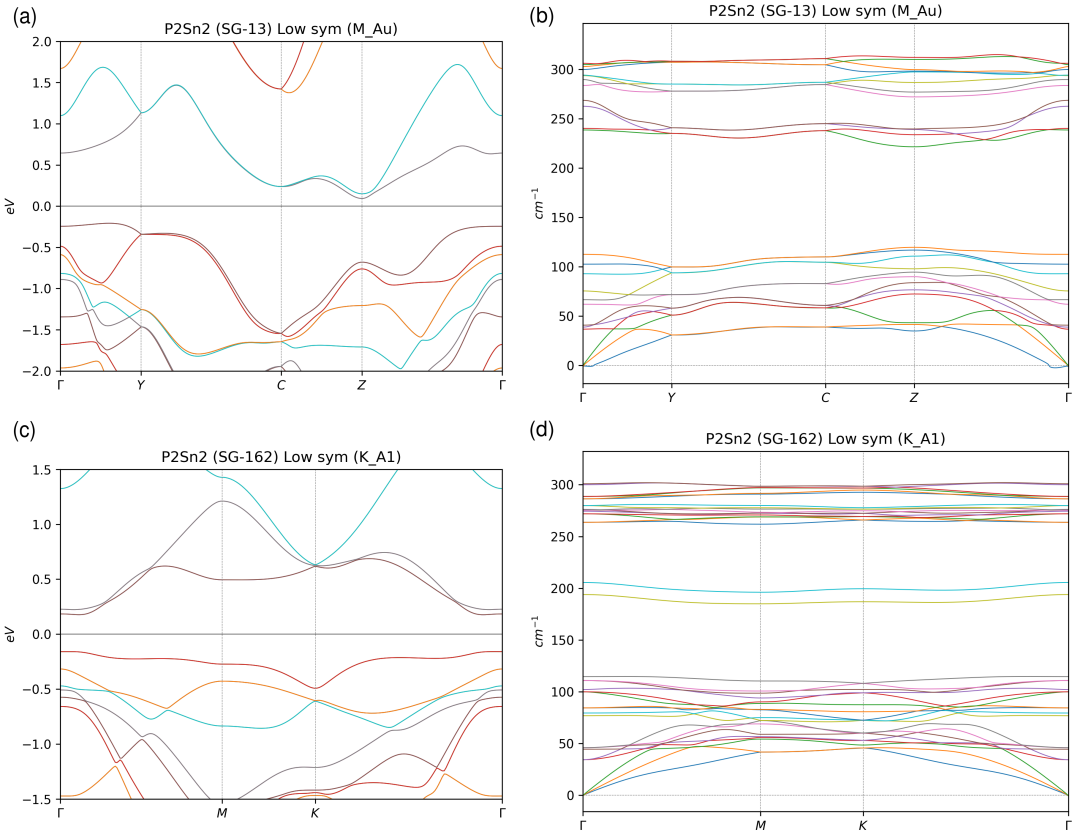

Figure B.15: **Band structures and phonon spectra of P_2Sn_2 low symmetry phases. a,b.** The electronic and phonon spectra of the structure resulting from the condensation of the M mode. **c,d.** The electronic and phonon spectra of the structure resulting from the condensation of the K mode. In both cases, the phonon spectra point to the stability of both low-symmetry phases.

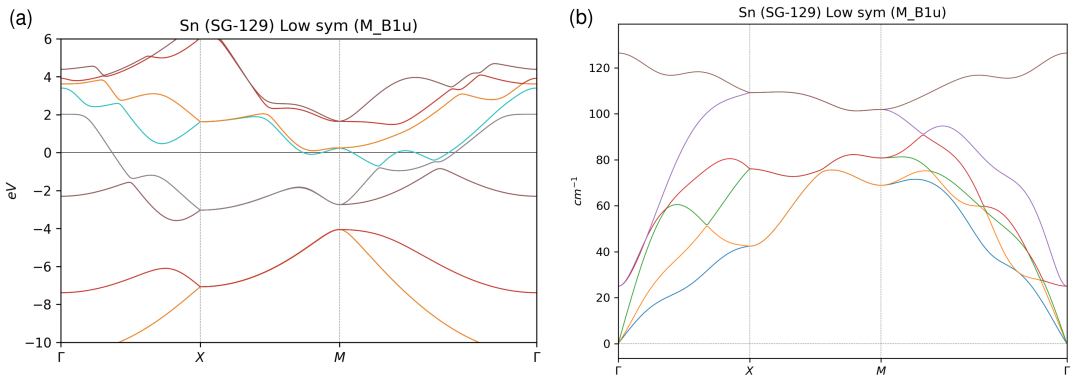

Figure B.16: **Band structures and phonon spectra of** Sn **low symmetry phases. a,b.** Show the electronic and phonon spectra respectively. While the phonon spectra points to the stability of the low-symmetry phase, the electronic spectrum shows that we did not achieve the desired metal-insulator transition.

B.3 CRYSTAL STRUCTURES FOR Sn_4P_3, SnP AND Sn_2P

Table B.1 presents the Sn_4P_3 structure obtained from x-ray measurements, alongside the corresponding theoretical prediction. On the other hand, Table B.2 provides the theoretical predictions for the structural parameters of the individual layers comprising Sn_4P_3, namely SnP and Sn_2P. Additionally, the table also includes the CDW structures SnP-(K/M/Γ) resulting from the SnP monolayer.

Sn_4P_3 SG $R\bar{3}m$ (No. 166)

Lattice parameter (Å)		theory	experiment
$a = b$		4.003	3.971
c		35.798	35.397
atom	Wyckoff pos.	ϵ theory	ϵ experiment
P	3a $(0,0,0)$		
P	6c $(0,0,\pm\epsilon)$	0.42873	0.42915
Sn	6c $(0,0,\pm\epsilon)$	0.13339	0.13406
Sn	6c $(0,0,\pm\epsilon)$	0.28966	0.28943

Table B.1: Experimental x-ray measurements and theoretical prediction of the Sn_4P_3 crystal structure.

SnP Monolayer SG $P\bar{3}m1$ (No. 164)

	$a = b = 3.905$ Å		$c = 13.941$ Å	
atom	Wyckoff pos.	x	y	z
P	2c	0	0	0.18102
Sn	2d	1/3	2/3	0.09356

SnP-K Monolayer SG $P\bar{3}1m$ (No. 162)

	$a = b = 6.779$ Å		$c = 25.157$ Å	
atom	Wyckoff pos.	x	y	z
P	2e	0	0	0.08316
P	4h	1/3	2/3	0.10945
Sn	6k	0.3700138	0	0.05352

SnP-M Monolayer SG $P2/m$ (No. 13)

	$\beta = 0$	$a = 25.157$ Å	$b = 3.914$ Å	$c = 6.779$ Å
atom	Wyckoff pos.	x	y	z
P	4g	0.10091	0.18215	0.28476
Sn	4g	0.05363	0.67507	0.45998

SnP-Γ Monolayer SG $P\bar{3}m1$ (No. 164)

	$a = b = 3.960$ Å		$c = 25.157$ Å	
atom	Wyckoff pos.	x	y	z
P	2d	1/3	2/3	0.10334
Sn	2c	0	0	0.05726

Sn_2P Monolayer SG $P\bar{3}m1$ (No. 164)

	$a = b = 3.684$ Å		$c = 16.000$ Å	
atom	Wyckoff pos.	x	y	z
P	1a	0	0	0
Sn	2d	1/3	2/3	0.10903

Table B.2: Calculated lattice parameters and atomic coordinates of all the studied monolayers. SnP and Sn_2P are the two monolayers that originally form Sn_4P_3. SnP-(K/M/Γ) are the resulting CDW structures after the condensation of the (K/M/Γ) unstable phonons of the SnP monolayer.

BILIOGRAPHY

BIBLIOGRAPHY

[1] P. W. Anderson. "More Is Different." In: *Science* (Aug. 4, 1972). DOI: 10.1126/science.177.4047.393.

[2] L. D. Landau. "On the Theory of Phase Transitions." In: *Zh. Eksp. Teor. Fiz.* 7 (1937). Ed. by D. ter Haar, pp. 19–32. DOI: 10.1016/B978-0-08-010586-4.50034-1.

[3] K. v. Klitzing, G. Dorda, and M. Pepper. "New Method for High-Accuracy Determination of the Fine-Structure Constant Based on Quantized Hall Resistance." In: *Physical Review Letters* 45.6 (Aug. 11, 1980), pp. 494–497. DOI: 10.1103/PhysRevLett.45.494.

[4] D. J. Thouless, M. Kohmoto, M. P. Nightingale, and M. den Nijs. "Quantized Hall Conductance in a Two-Dimensional Periodic Potential." In: *Physical Review Letters* 49.6 (Aug. 9, 1982), pp. 405–408. DOI: 10.1103/PhysRevLett.49.405.

[5] D. C. Tsui, H. L. Stormer, and A. C. Gossard. "Two-Dimensional Magnetotransport in the Extreme Quantum Limit." In: *Physical Review Letters* 48.22 (May 31, 1982), pp. 1559–1562. DOI: 10.1103/PhysRevLett.48.1559.

[6] F. D. M. Haldane. "Model for a Quantum Hall Effect without Landau Levels: Condensed-Matter Realization of the "Parity Anomaly"." In: *Physical Review Letters* 61.18 (Oct. 31, 1988), pp. 2015–2018. ISSN: 0031-9007. DOI: 10.1103/PhysRevLett.61.2015.

[7] C. L. Kane and E. J. Mele. "Z_2 Topological Order and the Quantum Spin Hall Effect." In: *Physical Review Letters* 95.14 (Sept. 28, 2005), p. 146802. DOI: 10.1103/PhysRevLett.95.146802.

[8] Markus König, Steffen Wiedmann, Christoph Brüne, Andreas Roth, Hartmut Buhmann, Laurens W. Molenkamp, Xiao-Liang Qi, and Shou-Cheng Zhang. "Quantum Spin Hall Insulator State in HgTe Quantum Wells." In: *Science* 318.5851 (Nov. 2, 2007), pp. 766–770. DOI: 10.1126/science.1148047.

[9] Liang Fu and C. L. Kane. "Topological Insulators with Inversion Symmetry." In: *Physical Review B* 76.4 (July 2, 2007), p. 045302. DOI: 10.1103/PhysRevB.76.045302.

[10] Alexander Altland and Martin R. Zirnbauer. "Nonstandard Symmetry Classes in Mesoscopic Normal-Superconducting Hybrid Structures." In: *Physical Review B* 55.2 (Jan. 1, 1997), pp. 1142–1161. DOI: 10.1103/PhysRevB.55.1142.

[11] Shinsei Ryu, Andreas P. Schnyder, Akira Furusaki, and Andreas W. W. Ludwig. "Topological Insulators and Superconductors: Tenfold Way and Dimensional Hierarchy." In: *New Journal of Physics* 12.6 (June 2010), p. 065010. ISSN: 1367-2630. DOI: 10.1088/1367-2630/12/6/065010.

[12] Liang Fu. "Topological Crystalline Insulators." In: *Physical Review Letters* 106.10 (Mar. 8, 2011), p. 106802. DOI: 10.1103/PhysRevLett.106.106802.

[13] Barry Bradlyn, L. Elcoro, Jennifer Cano, M. G. Vergniory, Zhijun Wang, C. Felser, M. I. Aroyo, and B. Andrei Bernevig. "Topological Quantum Chemistry." In: *Nature* 547.7663 (July 2017), pp. 298–305. ISSN: 1476-4687. DOI: 10.1038/nature23268.

[14] Jennifer Cano, Barry Bradlyn, Zhijun Wang, L. Elcoro, M. G. Vergniory, C. Felser, M. I. Aroyo, and B. Andrei Bernevig. "Building Blocks of Topological Quantum Chemistry: Elementary Band Representations." In: *Physical Review B* 97.3 (Jan. 16, 2018), p. 035139. DOI: 10.1103/PhysRevB.97.035139.

[15] M. G. Vergniory, L. Elcoro, Zhijun Wang, Jennifer Cano, C. Felser, M. I. Aroyo, B. Andrei Bernevig, and Barry Bradlyn. "Graph Theory Data for Topological Quantum Chemistry." In: *Physical Review E* 96.2 (Aug. 28, 2017), p. 023310. DOI: 10.1103/PhysRevE.96.023310.

[16] Hoi Chun Po, Ashvin Vishwanath, and Haruki Watanabe. "Symmetry-Based Indicators of Band Topology in the 230 Space Groups." In: *Nature Communications* 8.1 (Dec. 2017), p. 50. ISSN: 2041-1723. DOI: 10.1038/s41467-017-00133-2.

[17] Zhida Song, Tiantian Zhang, Zhong Fang, and Chen Fang. "Quantitative Mappings between Symmetry and Topology in Solids." In: *Nature Communications* 9.1 (Dec. 2018), p. 3530. ISSN: 2041-1723. DOI: 10.1038/s41467-018-06010-w.

[18] M. G. Vergniory, L. Elcoro, Claudia Felser, Nicolas Regnault, B. Andrei Bernevig, and Zhijun Wang. "A Complete Catalogue of High-Quality Topological Materials." In: *Nature* 566.7745 (7745 Feb. 2019), pp. 480–485. ISSN: 1476-4687. DOI: 10.1038/s41586-019-0954-4.

[19] Yuanfeng Xu, M. G. Vergniory, Da-Shuai Ma, Juan L. Mañes, Zhi-Da Song, B. Andrei Bernevig, Nicolas Regnault, and Luis Elcoro. "Catalog of Topological Phonon Materials." In: *Science* 384.6696 (May 10, 2024), eadf8458. DOI: 10.1126/science.adf8458.

[20] Juan L. Mañes. "Fragile Phonon Topology on the Honeycomb Lattice with Time-Reversal Symmetry." In: *Physical Review B* 102.2 (July 20, 2020), p. 024307. DOI: 10.1103/PhysRevB.102.024307.

[21] G. Grüner. "The Dynamics of Charge-Density Waves." In: *Reviews of Modern Physics* 60.4 (Oct. 1, 1988), pp. 1129–1181. DOI: 10.1103/RevModPhys.60.1129.

[22] J. Gooth, B. Bradlyn, S. Honnali, C. Schindler, N. Kumar, J. Noky, Y. Qi, C. Shekhar, Y. Sun, Z. Wang, B. A. Bernevig, and C. Felser. "Axionic Charge-Density Wave in the Weyl Semimetal (TaSe4)2I." In: *Nature* 575.7782 (Nov. 14, 2019), pp. 315–319. ISSN: 0028-0836, 1476-4687. DOI: 10.1038/s41586-019-1630-4.

[23] Zhong Wang and Shou-Cheng Zhang. "Chiral Anomaly, Charge Density Waves, and Axion Strings from Weyl Semimetals." In: *Physical Review B* 87.16 (Apr. 12, 2013), p. 161107. ISSN: 1098-0121, 1550-235X. DOI: 10.1103/PhysRevB.87.161107.

[24] Benjamin J. Wieder, Kuan-Sen Lin, and Barry Bradlyn. "Axionic Band Topology in Inversion-Symmetric Weyl-charge-density Waves." In: *Physical Review Research* 2.4 (Oct. 14, 2020), p. 042010. ISSN: 2643-1564. DOI: 10.1103/PhysRevResearch.2.042010.

[25] Chiara Devescovi, Antonio Morales-Pérez, Yoonseok Hwang, Mikel García-Díez, Iñigo Robredo, Juan Luis Mañes, Barry Bradlyn, Aitzol García-Etxarri, and Maia G. Vergniory. *Axion Topology in Photonic Crystal Domain Walls*. May 31, 2023. DOI: 10.48550/arXiv.2305.19805. preprint.

[26] Brenden R. Ortiz, Lídia C. Gomes, Jennifer R. Morey, Michal Winiarski, Mitchell Bordelon, John S. Mangum, Iain W. H. Oswald, Jose A. Rodriguez-Rivera, James R. Neilson, Stephen D. Wilson, Elif Ertekin, Tyrel M. McQueen, and Eric S. Toberer. "New kagome prototype materials: discovery of KV_3Sb_5, RbV_3Sb_5, and CsV_3Sb_5." In: *Physical Review Materials* 3.9 (Sept. 16, 2019), p. 094407. DOI: 10.1103/PhysRevMaterials.3.094407.

[27] Chunyu Guo, Carsten Putzke, Sofia Konyzheva, Xiangwei Huang, Martin Gutierrez-Amigo, Ion Errea, Dong Chen, Maia G. Vergniory, Claudia Felser, Mark H. Fischer, Titus Neupert, and Philip J. W. Moll. "Switchable chiral transport in charge-ordered kagome metal CsV3Sb5." In: *Nature* (Oct. 12, 2022), pp. 1–6. ISSN: 1476-4687. DOI: 10.1038/s41586-022-05127-9.

[28] Chunyu Guo, Maarten R. van Delft, Martin Gutierrez-Amigo, Dong Chen, Carsten Putzke, Glenn Wagner, Mark H. Fischer, Titus Neupert, Ion Errea, Maia G. Vergniory, Steffen Wiedmann, Claudia Felser, and Philip J. W. Moll. "Distinct switching of chiral transport in the kagome metals KV3Sb5 and CsV3Sb5." In: *npj Quantum Materials* 9.1 (1 Feb. 22, 2024), pp. 1–6. ISSN: 2397-4648. DOI: 10.1038/s41535-024-00629-3.

[29] Camron Farhang, Jingyuan Wang, Brenden R. Ortiz, Stephen D. Wilson, and Jing Xia. "Unconventional Specular Optical Rotation in the Charge Ordered State of Kagome Metal CsV3Sb5." In: *Nature Communications* 14.1 (1 Sept. 1, 2023), p. 5326. ISSN: 2041-1723. DOI: 10.1038/s41467-023-41080-5.

[30] Li Yu, Chennan Wang, Yuhang Zhang, Mathias Sander, Shunli Ni, Zouyouwei Lu, Sheng Ma, Zhengguo Wang, Zhen Zhao, Hui Chen, Kun Jiang, Yan Zhang, Haitao Yang, Fang Zhou, Xiaoli Dong, Steven L. Johnson, Michael J. Graf, Jiangping Hu, Hong-Jun Gao, and Zhongxian Zhao. "Evidence of a hidden flux phase in the topological kagome metal CsV_3Sb_5." July 22, 2021.

[31] Xilin Feng, Kun Jiang, Ziqiang Wang, and Jiangping Hu. "Chiral Flux Phase in the Kagome Superconductor AV3Sb5." In: *Science Bulletin* 66.14 (July 30, 2021), pp. 1384–1388. ISSN: 2095-9273. DOI: 10.1016/j.scib.2021.04.043.

[32] C. Mielke, D. Das, J.-X. Yin, H. Liu, R. Gupta, Y.-X. Jiang, M. Medarde, X. Wu, H. C. Lei, J. Chang, Pengcheng Dai, Q. Si, H. Miao, R. Thomale, T. Neupert, Y. Shi, R. Khasanov, M. Z. Hasan, H. Luetkens, and Z. Guguchia. "Time-Reversal Symmetry-Breaking Charge Order in a Kagome Superconductor." In: *Nature* 602.7896 (7896 Feb. 2022), pp. 245–250. ISSN: 1476-4687. DOI: 10.1038/s41586-021-04327-z.

[33] D. Subires, A. Korshunov, A. H. Said, L. Sánchez, Brenden R. Ortiz, Stephen D. Wilson, A. Bosak, and S. Blanco-Canosa. "Order-Disorder Charge Density Wave Instability in the Kagome Metal (Cs,Rb)V3Sb5." In: *Nature Communications* 14.1 (1 Feb. 23, 2023), p. 1015. ISSN: 2041-1723. DOI: 10.1038/s41467-023-36668-w.

[34] E. Schrödinger. "An Undulatory Theory of the Mechanics of Atoms and Molecules." In: *Physical Review* 28.6 (Dec. 1, 1926), pp. 1049–1070. DOI: 10.1103/PhysRev.28.1049.

[35] M. Born and V. Fock. "Beweis des Adiabatensatzes." In: *Zeitschrift für Physik* 51.3 (Mar. 1, 1928), pp. 165–180. ISSN: 0044-3328. DOI: 10.1007/BF01343193.

[36] M. Born and R. Oppenheimer. "Zur Quantentheorie Der Molekeln." In: *Annalen der Physik* 389.20 (1927), pp. 457–484. ISSN: 1521-3889. DOI: 10.1002/andp.19273892002.

[37] D. R. Hartree. "The Wave Mechanics of an Atom with a Non-Coulomb Central Field. Part I. Theory and Methods." In: *Mathematical Proceedings of the Cambridge Philosophical Society* 24.1 (Jan. 1928), pp. 89–110. ISSN: 1469-8064, 0305-0041. DOI: 10.1017/S0305004100011919.

[38] V. Fock. "Näherungsmethode zur Lösung des quantenmechanischen Mehrkörperproblems." In: *Zeitschrift für Physik* 61.1 (Jan. 1, 1930), pp. 126–148. ISSN: 0044-3328. DOI: 10.1007/BF01340294.

[39] J. C. Slater. "The Theory of Complex Spectra." In: *Physical Review* 34.10 (Nov. 15, 1929), pp. 1293–1322. DOI: 10.1103/PhysRev.34.1293.

[40] P. Hohenberg and W. Kohn. "Inhomogeneous Electron Gas." In: *Physical Review* 136 (3B Nov. 9, 1964), B864–B871. DOI: 10.1103/PhysRev.136.B864.

[41] Mel Levy. "Universal Variational Functionals of Electron Densities, First-Order Density Matrices, and Natural Spin-Orbitals and Solution of the v-Representability Problem." In: *Proceedings of the National Academy of Sciences* 76.12 (Dec. 1979), pp. 6062–6065. DOI: 10.1073/pnas.76.12.6062.

[42] Mel Levy. "Electron Densities in Search of Hamiltonians." In: *Physical Review A* 26.3 (Sept. 1, 1982), pp. 1200–1208. DOI: 10.1103/PhysRevA.26.1200.

[43] T. L. Gilbert. "Hohenberg-Kohn Theorem for Nonlocal External Potentials." In: *Physical Review B* 12.6 (Sept. 15, 1975), pp. 2111–2120. DOI: 10.1103/PhysRevB.12.2111.

[44] W. Kohn and L. J. Sham. "Self-Consistent Equations Including Exchange and Correlation Effects." In: *Physical Review* 140 (4A Nov. 15, 1965), A1133–A1138. DOI: 10.1103/PhysRev.140.A1133.

[45] D. M. Ceperley and B. J. Alder. "Ground State of the Electron Gas by a Stochastic Method." In: *Physical Review Letters* 45.7 (Aug. 18, 1980), pp. 566–569. DOI: 10.1103/PhysRevLett.45.566.

[46] J. P. Perdew and Alex Zunger. "Self-Interaction Correction to Density-Functional Approximations for Many-Electron Systems." In: *Physical Review B* 23.10 (May 15, 1981), pp. 5048–5079. DOI: 10.1103/PhysRevB.23.5048.

[47] Frank Herman, John P. Van Dyke, and Irene B. Ortenburger. "Improved Statistical Exchange Approximation for Inhomogeneous Many-Electron Systems." In: *Physical Review Letters* 22.16 (Apr. 21, 1969), pp. 807–811. DOI: 10.1103/PhysRevLett.22.807.

[48] John P. Perdew, Kieron Burke, and Matthias Ernzerhof. "Generalized Gradient Approximation Made Simple." In: *Physical Review Letters* 77.18 (Oct. 28, 1996), pp. 3865–3868. DOI: 10.1103/PhysRevLett.77.3865.

[49] Conyers Herring. "A New Method for Calculating Wave Functions in Crystals." In: *Physical Review* 57.12 (June 15, 1940), pp. 1169–1177. DOI: 10.1103/PhysRev.57.1169.

[50] James C. Phillips and Leonard Kleinman. "New Method for Calculating Wave Functions in Crystals and Molecules." In: *Physical Review* 116.2 (Oct. 15, 1959), pp. 287–294. DOI: 10.1103/PhysRev.116.287.

[51] E. Antončík. "Approximate Formulation of the Orthogonalized Plane-Wave Method." In: *Journal of Physics and Chemistry of Solids* 10.4 (Aug. 1, 1959), pp. 314–320. ISSN: 0022-3697. DOI: 10.1016/0022-3697(59)90007-1.

[52] Morrel H. Cohen and V. Heine. "Cancellation of Kinetic and Potential Energy in Atoms, Molecules, and Solids." In: *Physical Review* 122.6 (June 15, 1961), pp. 1821–1826. DOI: 10.1103/PhysRev.122.1821.

[53] N. W. Ashcroft. "Electron-Ion Pseudopotentials in Metals." In: *Physics Letters* 23.1 (Oct. 3, 1966), pp. 48–50. ISSN: 0031-9163. DOI: 10.1016/0031-9163(66)90251-4.

[54] D. R. Hamann, M. Schlüter, and C. Chiang. "Norm-Conserving Pseudopotentials." In: *Physical Review Letters* 43.20 (Nov. 12, 1979), pp. 1494–1497. DOI: 10.1103/PhysRevLett.43.1494.

[55] Peter E. Blöchl. "Generalized Separable Potentials for Electronic-Structure Calculations." In: *Physical Review B* 41.8 (Mar. 15, 1990), pp. 5414–5416. DOI: 10.1103/PhysRevB.41.5414.

[56] David Vanderbilt. "Soft Self-Consistent Pseudopotentials in a Generalized Eigenvalue Formalism." In: *Physical Review B* 41.11 (Apr. 15, 1990), pp. 7892–7895. DOI: 10.1103/PhysRevB.41.7892.

[57] Gregory H. Wannier. "The Structure of Electronic Excitation Levels in Insulating Crystals." In: *Physical Review* 52.3 (Aug. 1, 1937), pp. 191–197. DOI: 10.1103/PhysRev.52.191.

[58] Nicola Marzari and David Vanderbilt. "Maximally Localized Generalized Wannier Functions for Composite Energy Bands." In: *Physical Review B* 56.20 (Nov. 15, 1997), pp. 12847–12865. DOI: 10.1103/PhysRevB.56.12847.

[59] Henrik Bruus, Karsten Flensberg, Henrik Bruus, and Karsten Flensberg. *Many-Body Quantum Theory in Condensed Matter Physics: An Introduction*. Oxford Graduate Texts. Oxford, New York: Oxford University Press, Sept. 2, 2004. 464 pp. ISBN: 978-0-19-856633-5.

[60] Richard M. Martin. *Electronic Structure: Basic Theory and Practical Methods*. Cambridge: Cambridge University Press, 2004. DOI: 10.1017/CBO9780511805769.

[61] D.J. Hooton. "LI. A New Treatment of Anharmonicity in Lattice Thermodynamics: I." In: *The London, Edinburgh, and Dublin Philosophical Magazine and Journal of Science* 46.375 (Apr. 1, 1955), pp. 422–432. ISSN: 1941-5982. DOI: 10.1080/14786440408520575.

[62] Ion Errea, Matteo Calandra, and Francesco Mauri. "Anharmonic Free Energies and Phonon Dispersions from the Stochastic Self-Consistent Harmonic Approximation: Application to Platinum and Palladium Hydrides." In: *Physical Review B* 89.6 (Feb. 10, 2014), p. 064302. ISSN: 1098-0121, 1550-235X. DOI: 10.1103/PhysRevB.89.064302.

[63] Raffaello Bianco, Ion Errea, Lorenzo Paulatto, Matteo Calandra, and Francesco Mauri. "Second-Order Structural Phase Transitions, Free Energy Curvature, and Temperature-Dependent Anharmonic Phonons in the Self-Consistent Harmonic Approximation: Theory and Stochastic Implementation." In: *Physical Review B* 96.1 (July 18, 2017), p. 014111. ISSN: 2469-9950, 2469-9969. DOI: 10.1103/PhysRevB.96.014111.

[64] Lorenzo Monacelli, Raffaello Bianco, Marco Cherubini, Matteo Calandra, Ion Errea, and Francesco Mauri. "The Stochastic Self-Consistent Harmonic Approximation: Calculating Vibrational Properties of Materials with Full Quantum and Anharmonic Effects." In: *Journal of Physics: Condensed Matter* 33.36 (July 2021), p. 363001. ISSN: 0953-8984. DOI: 10.1088/1361-648X/ac066b.

[65] Lorenzo Monacelli and Francesco Mauri. "Time-Dependent Self-Consistent Harmonic Approximation: Anharmonic Nuclear Quantum Dynamics and Time Correlation Functions." In: *Physical Review B* 103.10 (Mar. 23, 2021), p. 104305. DOI: 10.1103/PhysRevB.103.104305.

[66] Harold T. Stokes and Dorian M. Hatch. *Isotropy Subgroups of the 230 Crystallographic Space Groups*. Singapore ; Teaneck, NY, USA: World Scientific, 1988. 1 p. ISBN: 978-9971-5-0772-5.

[67] C. J. Bradley and Arthur P. Cracknell. *The Mathematical Theory of Symmetry in Solids: Representation Theory for Point Groups and Space Groups*. Oxford Classic Texts in the Physical Sciences. Oxford: Clarendon Press, 2010. 745 pp. ISBN: 978-0-19-958258-7.

[68] M. I. Aroyo, A. Kirov, C. Capillas, J. M. Perez-Mato, and H. Wondratschek. "Bilbao Crystallographic Server. II. Representations of Crystallographic Point Groups and Space Groups." In: *Acta Crystallographica Section A: Foundations of Crystallography* 62.2 (2 Mar. 1, 2006), pp. 115–128. ISSN: 0108-7673. DOI: 10.1107/S0108767305040286.

[69] Mois Ilia Aroyo, Juan Manuel Perez-Mato, Cesar Capillas, Eli Kroumova, Svetoslav Ivantchev, Gotzon Madariaga, Asen Kirov, and Hans Wondratschek. "Bilbao Crystallographic Server: I. Databases and Crystallographic Computing Programs." In: *Zeitschrift für Kristallographie - Crystalline Materials* 221.1 (Jan. 1, 2006), pp. 15–27. ISSN: 2196-7105. DOI: 10.1524/zkri.2006.221.1.15.

[70] M.I. Aroyo, J.M. Perez-Mato, D. Orobengoa, E. Tasci, G. De La Flor, and A. Kirov. "Crystallography Online: Bilbao Crystallographic Server." In: *Bulgarian Chemical Communications* 43.2 (2011), pp. 183–197. ISSN: 0861-9808.

[71] Tosio Kato. "On the Adiabatic Theorem of Quantum Mechanics." In: *Journal of the Physical Society of Japan* 5.6 (Nov. 15, 1950), pp. 435–439. ISSN: 0031-9015. DOI: 10.1143/JPSJ.5.435.

[72] Barry Bradlyn and Mikel Iraola. "Lecture Notes on Berry Phases and Topology." In: *SciPost Physics Lecture Notes* (May 11, 2022), p. 051. ISSN: 2590-1990. DOI: 10.21468/SciPostPhysLectNotes.51.

[73] Jacques Des Cloizeaux. "Analytical Properties of N-Dimensional Energy Bands and Wannier Functions." In: *Physical Review* 135 (3A Aug. 3, 1964), A698–A707. DOI: 10.1103/PhysRev.135.A698.

[74] G. Nenciu. "Existence of the Exponentially Localised Wannier Functions." In: *Communications in Mathematical Physics* 91.1 (Mar. 1, 1983), pp. 81–85. ISSN: 1432-0916. DOI: 10.1007/BF01206052.

[75] Yuanfeng Xu, Luis Elcoro, Zhi-Da Song, Benjamin J. Wieder, M. G. Vergniory, Nicolas Regnault, Yulin Chen, Claudia Felser, and B. Andrei Bernevig. "High-Throughput Calculations of Magnetic Topological Materials." In: *Nature* 586.7831 (Oct. 2020), pp. 702–707. ISSN: 1476-4687. DOI: 10.1038/s41586-020-2837-0.

[76] Maia G. Vergniory, Benjamin J. Wieder, Luis Elcoro, Stuart S. P. Parkin, Claudia Felser, B. Andrei Bernevig, and Nicolas Regnault. "All Topological Bands of All Nonmagnetic Stoichiometric Materials." In: *Science* 376.6595 (May 20, 2022), eabg9094. DOI: 10.1126/science.abg9094.

[77] J. Zak. "Symmetry Specification of Bands in Solids." In: *Physical Review Letters* 45.12 (Sept. 22, 1980), pp. 1025–1028. ISSN: 0031-9007. DOI: 10.1103/PhysRevLett.45.1025.

[78] J. Zak. "Band Representations and Symmetry Types of Bands in Solids." In: *Physical Review B* 23.6 (Mar. 15, 1981), pp. 2824–2835. ISSN: 0163-1829. DOI: 10.1103/PhysRevB.23.2824.

[79] J. Zak. "Band Representations of Space Groups." In: *Physical Review B* 26.6 (Sept. 15, 1982), pp. 3010–3023. DOI: 10.1103/PhysRevB.26.3010.

[80] M. B. Walker and J. Zak. "Site Symmetry and Band Representations for Phonons." In: *Physical Review Letters* 74.19 (May 8, 1995), pp. 3824–3827. ISSN: 0031-9007, 1079-7114. DOI: 10.1103/PhysRevLett.74.3824.

[81] L. Michel, M. B. Walker, and J. Zak. "Continuity of Phonon Spectra for Diamond and Hexagonal Close Packed Structures." In: *Physical Review Letters* 74.24 (June 12, 1995), pp. 4871–4874. DOI: 10.1103/PhysRevLett.74.4871.

[82] María Blanco de Paz, Maia G. Vergniory, Dario Bercioux, Aitzol García-Etxarri, and Barry Bradlyn. "Engineering Fragile Topology in Photonic Crystals: Topological Quantum Chemistry of Light." In: *Physical Review Research* 1.3 (Oct. 14, 2019), p. 032005. DOI: 10.1103/PhysRevResearch.1.032005.

[83] Zhi-Ming Yu, Zeying Zhang, Gui-Bin Liu, Weikang Wu, Xiao-Ping Li, Run-Wu Zhang, Shengyuan A. Yang, and Yugui Yao. "Encyclopedia of Emergent Particles in Three-Dimensional Crystals." In: *Science Bulletin* 67.4 (Feb. 26, 2022), pp. 375–380. ISSN: 2095-9273. DOI: 10.1016/j.scib.2021.10.023.

[84] Tong Zhang, Peng Cheng, Xi Chen, Jin-Feng Jia, Xucun Ma, Ke He, Lili Wang, Haijun Zhang, Xi Dai, Zhong Fang, Xincheng Xie, and Qi-Kun Xue. "Experimental Demonstration of Topological Surface States Protected by Time-Reversal Symmetry." In: *Physical Review Letters* 103.26 (Dec. 23, 2009), p. 266803. DOI: 10.1103/PhysRevLett.103.266803.

[85] B. I. Halperin. "Quantized Hall Conductance, Current-Carrying Edge States, and the Existence of Extended States in a Two-Dimensional Disordered Potential." In: *Physical Review B* 25.4 (Feb. 15, 1982), pp. 2185–2190. DOI: 10.1103/PhysRevB.25.2185.

[86] Zheng-Cheng Gu and Xiao-Gang Wen. "Tensor-Entanglement-Filtering Renormalization Approach and Symmetry-Protected Topological Order." In: *Physical Review B* 80.15 (Oct. 26, 2009), p. 155131. DOI: 10.1103/PhysRevB.80.155131.

[87] Frank Pollmann, Ari M. Turner, Erez Berg, and Masaki Oshikawa. "Entanglement Spectrum of a Topological Phase in One Dimension." In: *Physical Review B* 81.6 (Feb. 26, 2010), p. 064439. DOI: 10.1103/PhysRevB.81.064439.

[88] Xie Chen, Zheng-Cheng Gu, and Xiao-Gang Wen. "Classification of Gapped Symmetric Phases in One-Dimensional Spin Systems." In: *Physical Review B* 83.3 (Jan. 13, 2011), p. 035107. DOI: 10.1103/PhysRevB.83.035107.

[89] Robert-Jan Slager, Andrej Mesaros, Vladimir Juričić, and Jan Zaanen. "The Space Group Classification of Topological Band-Insulators." In: *Nature Physics* 9.2 (Feb. 2013), pp. 98–102. ISSN: 1745-2481. DOI: 10.1038/nphys2513.

[90] Yoichi Ando and Liang Fu. "Topological Crystalline Insulators and Topological Superconductors: From Concepts to Materials." In: *Annual Review of Condensed Matter Physics* 6 (Volume 6, 2015 Mar. 10, 2015), pp. 361–381. ISSN: 1947-5454, 1947-5462. DOI: 10.1146/annurev-conmatphys-031214-014501.

[91] Zhijun Wang, A. Alexandradinata, R. J. Cava, and B. Andrei Bernevig. "Hourglass Fermions." In: *Nature* 532.7598 (Apr. 2016), pp. 189–194. ISSN: 1476-4687. DOI: 10.1038/nature17410.

[92] Wladimir A. Benalcazar, B. Andrei Bernevig, and Taylor L. Hughes. "Quantized Electric Multipole Insulators." In: *Science* 357.6346 (July 7, 2017), pp. 61–66. DOI: 10.1126/science.aah6442.

[93] Wladimir A. Benalcazar, B. Andrei Bernevig, and Taylor L. Hughes. "Electric Multipole Moments, Topological Multipole Moment Pumping, and Chiral Hinge States in Crystalline Insulators." In: *Physical Review B* 96.24 (Dec. 11, 2017), p. 245115. DOI: 10.1103/PhysRevB.96.245115.

[94] Zhida Song, Zhong Fang, and Chen Fang. "$(d-2)$-Dimensional Edge States of Rotation Symmetry Protected Topological States." In: *Physical Review Letters* 119.24 (Dec. 11, 2017), p. 246402. DOI: 10.1103/PhysRevLett.119.246402.

[95] Josias Langbehn, Yang Peng, Luka Trifunovic, Felix von Oppen, and Piet W. Brouwer. "Reflection-Symmetric Second-Order Topological Insulators and Superconductors." In: *Physical Review Letters* 119.24 (Dec. 11, 2017), p. 246401. DOI: 10.1103/PhysRevLett.119.246401.

[96] Benjamin J. Wieder, Barry Bradlyn, Zhijun Wang, Jennifer Cano, Youngkuk Kim, Hyeong-Seok D. Kim, Andrew M. Rappe, C. L. Kane, and B. Andrei Bernevig. "Wallpaper Fermions and the Nonsymmorphic Dirac Insulator." In: *Science* 361.6399 (July 20, 2018), pp. 246–251. DOI: 10.1126/science.aan2802.

[97] Frank Schindler, Ashley M. Cook, Maia G. Vergniory, Zhijun Wang, Stuart S. P. Parkin, B. Andrei Bernevig, and Titus Neupert. "Higher-Order Topological Insulators." In: *Science Advances* 4.6 (June 2018), eaat0346. DOI: 10.1126/sciadv.aat0346.

[98] Eslam Khalaf. "Higher-Order Topological Insulators and Superconductors Protected by Inversion Symmetry." In: *Physical Review B* 97.20 (May 25, 2018), p. 205136. DOI: 10.1103/PhysRevB.97.205136.

[99] Taylor L. Hughes, Emil Prodan, and B. Andrei Bernevig. "Inversion-Symmetric Topological Insulators." In: *Physical Review B* 83.24 (June 28, 2011), p. 245132. DOI: 10.1103/PhysRevB.83.245132.

[100] Ari M. Turner, Yi Zhang, Roger S. K. Mong, and Ashvin Vishwanath. "Quantized Response and Topology of Magnetic Insulators with Inversion Symmetry." In: *Physical Review B* 85.16 (Apr. 12, 2012), p. 165120. DOI: 10.1103/PhysRevB.85.165120.

[101] Chen Fang, Matthew J. Gilbert, and B. Andrei Bernevig. "Bulk Topological Invariants in Noninteracting Point Group Symmetric Insulators." In: *Physical Review B* 86.11 (Sept. 10, 2012), p. 115112. DOI: 10.1103/PhysRevB.86.115112.

[102] Eslam Khalaf, Hoi Chun Po, Ashvin Vishwanath, and Haruki Watanabe. "Symmetry Indicators and Anomalous Surface States of Topological Crystalline Insulators." In: *Physical Review X* 8.3 (Sept. 14, 2018), p. 031070. ISSN: 2160-3308. DOI: 10.1103/PhysRevX.8.031070.

[103] Jorrit Kruthoff, Jan de Boer, Jasper van Wezel, Charles L. Kane, and Robert-Jan Slager. "Topological Classification of Crystalline Insulators through Band Structure Combinatorics." In: *Physical Review X* 7.4 (Dec. 22, 2017), p. 041069. DOI: 10.1103/PhysRevX.7.041069.

[104] Jennifer Cano, Barry Bradlyn, Zhijun Wang, L. Elcoro, M. G. Vergniory, C. Felser, M. I. Aroyo, and B. Andrei Bernevig. "Topology of Disconnected Elementary Band Representations." In: *Physical Review Letters* 120.26 (June 27, 2018), p. 266401. DOI: 10.1103/PhysRevLett.120.266401.

[105] Adrien Bouhon, Annica M. Black-Schaffer, and Robert-Jan Slager. "Wilson Loop Approach to Fragile Topology of Split Elementary Band Representations and Topological Crystalline Insulators with Time-Reversal Symmetry." In: *Physical Review B* 100.19 (Nov. 21, 2019), p. 195135. DOI: 10.1103/PhysRevB.100.195135.

[106] Barry Bradlyn, Zhijun Wang, Jennifer Cano, and B. Andrei Bernevig. "Disconnected Elementary Band Representations, Fragile Topology, and Wilson Loops as Topological Indices: An Example on the Triangular Lattice." In: *Physical Review B* 99.4 (Jan. 25, 2019), p. 045140. DOI: 10.1103/PhysRevB.99.045140.

[107] Hoi Chun Po, Haruki Watanabe, and Ashvin Vishwanath. "Fragile Topology and Wannier Obstructions." In: *Physical Review Letters* 121.12 (Sept. 18, 2018), p. 126402. DOI: 10.1103/PhysRevLett.121.126402.

[108] Roman Süsstrunk and Sebastian D. Huber. "Observation of Phononic Helical Edge States in a Mechanical Topological Insulator." In: *Science* 349.6243 (July 3, 2015), pp. 47–50. DOI: 10.1126/science.aab0239.

[109] Roman Süsstrunk and Sebastian D. Huber. "Classification of Topological Phonons in Linear Mechanical Metamaterials." In: *Proceedings of the National Academy of Sciences* 113.33 (Aug. 16, 2016), E4767–E4775. DOI: 10.1073/pnas.1605462113.

[110] Sebastian D. Huber. "Topological Mechanics." In: *Nature Physics* 12.7 (July 2016), pp. 621–623. ISSN: 1745-2481. DOI: 10.1038/nphys3801.

[111] C. L. Kane and T. C. Lubensky. "Topological Boundary Modes in Isostatic Lattices." In: *Nature Physics* 10.1 (Jan. 2014), pp. 39–45. ISSN: 1745-2481. DOI: 10.1038/nphys2835.

[112] Olaf Stenull, C. L. Kane, and T. C. Lubensky. "Topological Phonons and Weyl Lines in Three Dimensions." In: *Physical Review Letters* 117.6 (Aug. 5, 2016), p. 068001. DOI: 10.1103/PhysRevLett.117.068001.

[113] Jun Mei, Ying Wu, C. T. Chan, and Zhao-Qing Zhang. "First-Principles Study of Dirac and Dirac-like Cones in Phononic and Photonic Crystals." In: *Physical Review B* 86.3 (July 24, 2012), p. 035141. DOI: 10.1103/PhysRevB.86.035141.

[114] Tiantian Zhang, Zhida Song, A. Alexandradinata, Hongming Weng, Chen Fang, Ling Lu, and Zhong Fang. "Double-Weyl Phonons in Transition-Metal Monosilicides." In: *Physical Review Letters* 120.1 (Jan. 5, 2018), p. 016401. DOI: 10.1103/PhysRevLett.120.016401.

[115] Jiangxu Li, Qing Xie, Sami Ullah, Ronghan Li, Hui Ma, Dianzhong Li, Yiyi Li, and Xing-Qiu Chen. "Coexistent Three-Component and Two-Component Weyl Phonons in TiS, ZrSe, and HfTe." In: *Physical Review B* 97.5 (Feb. 12, 2018), p. 054305. DOI: 10.1103/PhysRevB.97.054305.

[116] Martin Esmann, Fabrice Roland Lamberti, Pascale Senellart, Ivan Favero, Olivier Krebs, Loïc Lanco, Carmen Gomez Carbonell, Aristide Lemaître, and Norberto Daniel Lanzillotti-Kimura. "Topological Nanophononic States by Band Inversion." In: *Physical Review B* 97.15 (Apr. 19, 2018), p. 155422. DOI: 10.1103/PhysRevB.97.155422.

[117] Sobhit Singh, QuanSheng Wu, Changming Yue, Aldo H. Romero, and Alexey A. Soluyanov. "Topological Phonons and Thermoelectricity in Triple-Point Metals." In: *Physical Review Materials* 2.11 (Nov. 15, 2018), p. 114204. DOI: 10.1103/PhysRevMaterials.2.114204.

[118] Bo Peng, Yuchen Hu, Shuichi Murakami, Tiantian Zhang, and Bartomeu Monserrat. "Topological Phonons in Oxide Perovskites Controlled by Light." In: *Science Advances* 6.46 (Nov. 13, 2020), eabd1618. ISSN: 2375-2548. DOI: 10.1126/sciadv.abd1618.

[119] Jiangxu Li, Jiaxi Liu, Stanley A. Baronett, Mingfeng Liu, Lei Wang, Ronghan Li, Yun Chen, Dianzhong Li, Qiang Zhu, and Xing-Qiu Chen. "Computation and Data Driven Discovery of Topological Phononic Materials." In: *Nature Communications* 12.1 (Feb. 22, 2021), p. 1204. ISSN: 2041-1723. DOI: 10.1038/s41467-021-21293-2.

[120] Paolo Giannozzi, Stefano Baroni, Nicola Bonini, Matteo Calandra, Roberto Car, Carlo Cavazzoni, Davide Ceresoli, Guido L. Chiarotti, Matteo Cococcioni, Ismaila Dabo, Andrea Dal Corso, Stefano de Gironcoli, Stefano Fabris, Guido Fratesi, Ralph Gebauer, Uwe Gerstmann, Christos Gougoussis, Anton Kokalj, Michele Lazzeri, Layla Martin-Samos, Nicola Marzari, Francesco Mauri, Riccardo Mazzarello, Stefano Paolini, Alfredo Pasquarello, Lorenzo Paulatto, Carlo Sbraccia, Sandro Scandolo, Gabriele Sclauzero, Ari P. Seitsonen, Alexander Smogunov, Paolo Umari, and Renata M. Wentzcovitch. "QUANTUM ESPRESSO: A Modular and Open-Source Software Project for Quantum Simulations of Materials." In: *Journal of Physics: Condensed Matter* 21.39 (Sept. 2009), p. 395502. ISSN: 0953-8984. DOI: 10.1088/0953-8984/21/39/395502.

[121] P. Giannozzi, O. Andreussi, T. Brumme, O. Bunau, M. Buongiorno Nardelli, M. Calandra, R. Car, C. Cavazzoni, D. Ceresoli, M. Cococcioni, N. Colonna, I. Carnimeo, A. Dal Corso, S. de Gironcoli, P. Delugas, R. A. DiStasio, A. Ferretti, A. Floris, G. Fratesi, G. Fugallo, R. Gebauer, U. Gerstmann, F. Giustino, T. Gorni, J. Jia, M. Kawamura, H.-Y. Ko, A. Kokalj, E. Küçükbenli, M. Lazzeri, M. Marsili, N. Marzari, F. Mauri, N. L. Nguyen, H.-V. Nguyen, A. Otero-de-la-Roza, L. Paulatto, S. Poncé, D. Rocca, R. Sabatini, B. Santra, M. Schlipf, A. P. Seitsonen, A. Smogunov, I. Timrov, T. Thonhauser, P. Umari, N. Vast, X. Wu, and S. Baroni. "Advanced Capabilities for Materials Modelling with Quantum ESPRESSO." In: *Journal of Physics: Condensed Matter* 29.46 (Oct. 2017), p. 465901. ISSN: 0953-8984. DOI: 10.1088/1361-648X/aa8f79.

[122] Jennifer Cano, L. Elcoro, M. I. Aroyo, B. Andrei Bernevig, and Barry Bradlyn. "Topology Invisible to Eigenvalues in Obstructed Atomic Insulators." In: *Physical Review B* 105.12 (Mar. 11, 2022), p. 125115. DOI: 10.1103/PhysRevB.105.125115.

[123] W. Kohn. "Construction of Wannier Functions and Applications to Energy Bands." In: *Physical Review B* 7.10 (May 15, 1973), pp. 4388–4398. DOI: 10.1103/PhysRevB.7.4388.

[124] Feliciano Giustino and Alfredo Pasquarello. "Mixed Wannier-Bloch Functions for Electrons and Phonons in Periodic Systems." In: *Physical Review Letters* 96.21 (June 1, 2006), p. 216403. DOI: 10.1103/PhysRevLett.96.216403.

[125] Frank Wilczek and A. Zee. "Appearance of Gauge Structure in Simple Dynamical Systems." In: *Physical Review Letters* 52.24 (June 11, 1984), pp. 2111–2114. DOI: 10.1103/PhysRevLett.52.2111.

[126] Alexey A. Soluyanov and David Vanderbilt. "Computing Topological Invariants without Inversion Symmetry." In: *Physical Review B* 83.23 (June 2, 2011), p. 235401. DOI: 10.1103/PhysRevB.83.235401.

[127] A. Alexandradinata, Zhijun Wang, and B. Andrei Bernevig. "Topological Insulators from Group Cohomology." In: *Physical Review X* 6.2 (Apr. 15, 2016), p. 021008. DOI: 10.1103/PhysRevX.6.021008.

[128] A. A. MARADUDIN and S. H. VOSKO. "Symmetry Properties of the Normal Vibrations of a Crystal." In: *Reviews of Modern Physics* 40.1 (Jan. 1, 1968), pp. 1–37. DOI: 10.1103/RevModPhys.40.1.

[129] *Python Tight Binding (PythTB) Package*.

[130] Maryam Taherinejad, Kevin F. Garrity, and David Vanderbilt. "Wannier Center Sheets in Topological Insulators." In: *Physical Review B* 89.11 (Mar. 3, 2014), p. 115102. DOI: 10.1103/PhysRevB.89.115102.

[131] Stefano Baroni, Stefano de Gironcoli, Andrea Dal Corso, and Paolo Giannozzi. "Phonons and Related Crystal Properties from Density-Functional Perturbation Theory." In: *Reviews of Modern Physics* 73.2 (July 6, 2001), pp. 515–562. DOI: 10.1103/RevModPhys.73.515.

[132] John P. Perdew, Adrienn Ruzsinszky, Gábor I. Csonka, Oleg A. Vydrov, Gustavo E. Scuseria, Lucian A. Constantin, Xiaolan Zhou, and Kieron Burke. "Restoring the Density-Gradient Expansion for Exchange in Solids and Surfaces." In: *Physical Review Letters* 100.13 (Apr. 4, 2008), p. 136406. DOI: 10.1103/PhysRevLett.100.136406.

[133] G. Kresse and J. Furthmüller. "Efficiency of Ab-Initio Total Energy Calculations for Metals and Semiconductors Using a Plane-Wave Basis Set." In: *Computational Materials Science* 6.1 (July 1, 1996), pp. 15–50. ISSN: 0927-0256. DOI: 10.1016/0927-0256(96)00008-0.

[134] G. Kresse and J. Furthmüller. "Efficient Iterative Schemes for Ab Initio Total-Energy Calculations Using a Plane-Wave Basis Set." In: *Physical Review B* 54.16 (Oct. 15, 1996), pp. 11169–11186. DOI: 10.1103/PhysRevB.54.11169.

[135] M. Methfessel and A. T. Paxton. "High-Precision Sampling for Brillouin-zone Integration in Metals." In: *Physical Review B* 40.6 (Aug. 15, 1989), pp. 3616–3621. DOI: 10.1103/PhysRevB.40.3616.

[136] Zhiwei Peng, Xiaolin Chen, Yulong Fan, David J. Srolovitz, and Dangyuan Lei. "Strain Engineering of 2D Semiconductors and Graphene: From Strain Fields to Band-Structure Tuning and Photonic Applications." In: *Light: Science & Applications* 9.1 (Nov. 23, 2020), p. 190. ISSN: 2047-7538. DOI: 10.1038/s41377-020-00421-5.

[137] G. Grüner and A. Zettl. "Charge Density Wave Conduction: A Novel Collective Transport Phenomenon in Solids." In: *Physics Reports* 119.3 (Mar. 1, 1985), pp. 117–232. ISSN: 0370-1573. DOI: 10.1016/0370-1573(85)90073-0.

[138] Z. Z. Wang, M. C. Saint-Lager, P. Monceau, M. Renard, P. Gressier, A. Meerschaut, L. Guemas, and J. Rouxel. "Charge Density Wave Transport in (TaSe4)2I." In: *Solid State Communications* 46.4 (Apr. 1, 1983), pp. 325–328. ISSN: 0038-1098. DOI: 10.1016/0038-1098(83)90662-2.

[139] R. S. Kwok and S. E. Brown. "Thermal conductivity of the charge-density-wave systems $K_{0.3}MoO_3$ and $(TaSe_4)_2I$ near the Peierls transition." In: *Physical Review Letters* 63.8 (Aug. 21, 1989), pp. 895–898. DOI: 10.1103/PhysRevLett.63.895.

[140] Y.-K. Kuo, C. S. Lue, F. H. Hsu, H. H. Li, and H. D. Yang. "Thermal Properties of Lu5IrSi10 near the Charge-Density-Wave Transition." In: *Physical Review B* 64.12 (Sept. 11, 2001), p. 125124. DOI: 10.1103/PhysRevB.64.125124.

[141] Yiping Wang, Ioannis Petrides, Grant McNamara, Md Mofazzel Hosen, Shiming Lei, Yueh-Chun Wu, James L. Hart, Hongyan Lv, Jun Yan, Di Xiao, Judy J. Cha, Prineha Narang, Leslie M. Schoop, and Kenneth S. Burch. "Axial Higgs Mode Detected by Quantum Pathway Interference in RTe3." In: *Nature* 606.7916 (7916 June 2022), pp. 896–901. ISSN: 1476-4687. DOI: 10.1038/s41586-022-04746-6.

[142] Shiming Lei, Samuel M. L. Teicher, Andreas Topp, Kehan Cai, Jingjing Lin, Guangming Cheng, Tyger H. Salters, Fanny Rodolakis, Jessica L. McChesney, Saul Lapidus, Nan Yao, Maxim Krivenkov, Dmitry Marchenko, Andrei Varykhalov, Christian R. Ast, Roberto Car, Jennifer Cano, Maia G. Vergniory, N. Phuan Ong, and Leslie M. Schoop. "Band Engineering of Dirac Semimetals Using Charge Density Waves." In: *Advanced Materials* 33.30 (2021), p. 2101591. ISSN: 1521-4095. DOI: 10.1002/adma.202101591.

[143] Davide Campi, Nicolas Mounet, Marco Gibertini, Giovanni Pizzi, and Nicola Marzari. "Expansion of the Materials Cloud 2D Database." In: *ACS Nano* 17.12 (June 27, 2023), pp. 11268–11278. ISSN: 1936-0851. DOI: 10.1021/acsnano.2c11510.

[144] Venkatesham Tallapally, Richard J Alan Esteves, Lamia Nahar, and Indika U. Arachchige. "Multivariate Synthesis of Tin Phosphide Nanoparticles: Temperature, Time, and Ligand Control of Size, Shape, and Crystal Structure." In: *Chemistry of Materials* 28.15 (Aug. 9, 2016), pp. 5406–5414. ISSN: 0897-4756. DOI: 10.1021/acs.chemmater.6b01749.

[145] Bing Li, Shunli Shang, Jiawei Zhao, Daniil M. Itkis, Xingxing Jiao, Chaofan Zhang, Zi-Kui Liu, and Jiangxuan Song. "Metastable Trigonal SnP: A Promising Anode Material for Potassium-Ion Battery." In: *Carbon* 168 (Oct. 30, 2020), pp. 468–474. ISSN: 0008-6223. DOI: 10.1016/j.carbon.2020.03.048.

[146] F. Weber, S. Rosenkranz, J.-P. Castellan, R. Osborn, G. Karapetrov, R. Hott, R. Heid, K.-P. Bohnen, and A. Alatas. "Electron-Phonon Coupling and the Soft Phonon Mode in $TiSe_2$." In: *Physical Review Letters* 107.26 (Dec. 20, 2011), p. 266401. DOI: 10.1103/PhysRevLett.107.266401.

[147] F. Weber, S. Rosenkranz, J.-P. Castellan, R. Osborn, R. Hott, R. Heid, K.-P. Bohnen, T. Egami, A. H. Said, and D. Reznik. "Extended Phonon Collapse and the Origin of the Charge-Density Wave in 2H−$NbSe_2$." In: *Physical Review Letters* 107.10 (Sept. 1, 2011), p. 107403. DOI: 10.1103/PhysRevLett.107.107403.

[148] Josu Diego, A. H. Said, S. K. Mahatha, Raffaello Bianco, Lorenzo Monacelli, Matteo Calandra, Francesco Mauri, K. Rossnagel, Ion Errea, and S. Blanco-Canosa. "Van Der Waals Driven Anharmonic Melting of the 3D Charge Density Wave in VSe2." In: *Nature Communications* 12.1 (1 Jan. 26, 2021), p. 598. ISSN: 2041-1723. DOI: 10.1038/s41467-020-20829-2.

[149] Jianqiang Sky Zhou, Raffaello Bianco, Lorenzo Monacelli, Ion Errea, Francesco Mauri, and Matteo Calandra. "Theory of the Thickness Dependence of the Charge Density Wave Transition in 1 T-TiTe2." In: *2D Materials* 7.4 (Sept. 2020), p. 045032. ISSN: 2053-1583. DOI: 10.1088/2053-1583/abae7a.

[150] Raffaello Bianco, Lorenzo Monacelli, Matteo Calandra, Francesco Mauri, and Ion Errea. "Weak Dimensionality Dependence and Dominant Role of Ionic Fluctuations in the Charge-Density-Wave Transition of $NbSe_2$." In: *Physical Review Letters* 125.10 (Sept. 1, 2020), p. 106101. DOI: 10.1103/PhysRevLett.125.106101.

[151] Raffaello Bianco, Ion Errea, Lorenzo Monacelli, Matteo Calandra, and Francesco Mauri. "Quantum Enhancement of Charge Density Wave in NbS2 in the Two-Dimensional Limit." In: *Nano Letters* 19.5 (May 8, 2019), pp. 3098–3103. ISSN: 1530-6984. DOI: 10.1021/acs.nanolett.9b00504.

[152] Jianqiang Sky Zhou, Lorenzo Monacelli, Raffaello Bianco, Ion Errea, Francesco Mauri, and Matteo Calandra. "Anharmonicity and Doping Melt the Charge Density Wave in Single-Layer TiSe2." In: *Nano Letters* 20.7 (July 8, 2020), pp. 4809–4815. ISSN: 1530-6984. DOI: 10.1021/acs.nanolett.0c00597.

[153] Adolfo Otero Fumega, Josu Diego, Victor Pardo, Santiago Blanco-Canosa, and Ion Errea. "Anharmonicity Reveals the Tunability of the Charge Density Wave Orders in Monolayer VSe2." In: *Nano Letters* 23.5 (Mar. 8, 2023), pp. 1794–1800. ISSN: 1530-6984. DOI: 10.1021/acs.nanolett.2c04584.

[154] Olle Olofsson. "X-Ray Investigations of the Tin-Phosphorus System." In: *Acta Chemica Scandinavica* 24 (1970), pp. 1153–1162. ISSN: 0904-213X. DOI: 10.3891/acta.chem.scand.24-1153.

[155] A. D. Becke and K. E. Edgecombe. "A Simple Measure of Electron Localization in Atomic and Molecular Systems." In: *The Journal of Chemical Physics* 92.9 (May 1, 1990), pp. 5397–5403. ISSN: 0021-9606. DOI: 10.1063/1.458517.

[156] Andreas Savin, Reinhard Nesper, Steffen Wengert, and Thomas F. Fässler. "ELF: The Electron Localization Function." In: *Angewandte Chemie International Edition in English* 36.17 (1997), pp. 1808–1832. ISSN: 1521-3773. DOI: 10.1002/anie.199718081.

[157] M. Kohout and A. Savin. "Atomic Shell Structure and Electron Numbers." In: *International Journal of Quantum Chemistry* 60.4 (1996), pp. 875–882. ISSN: 1097-461X. DOI: 10.1002/(SICI)1097-461X(1996)60:4<875::AID-QUA10>3.0.CO;2-4.

[158] Nicolas Mounet, Marco Gibertini, Philippe Schwaller, Davide Campi, Andrius Merkys, Antimo Marrazzo, Thibault Sohier, Ivano Eligio Castelli, Andrea Cepellotti, Giovanni Pizzi, and Nicola Marzari. "Two-Dimensional Materials from High-Throughput Computational Exfoliation of Experimentally Known Compounds." In: *Nature Nanotechnology* 13.3 (3 Mar. 2018), pp. 246–252. ISSN: 1748-3395. DOI: 10.1038/s41565-017-0035-5.

[159] Kai Chang, Junwei Liu, Haicheng Lin, Na Wang, Kun Zhao, Anmin Zhang, Feng Jin, Yong Zhong, Xiaopeng Hu, Wenhui Duan, Qingming Zhang, Liang Fu, Qi-Kun Xue, Xi Chen, and Shuai-Hua Ji. "Discovery of Robust In-Plane Ferroelectricity in Atomic-Thick SnTe." In: *Science* 353.6296 (July 15, 2016), pp. 274–278. DOI: 10.1126/science.aad8609.

[160] Takayoshi Sasaki, Mamoru Watanabe, Hideo Hashizume, Hirohisa Yamada, and Hiromoto Nakazawa. "Macromolecule-like Aspects for a Colloidal Suspension of an Exfoliated Titanate. Pairwise Association of Nanosheets and Dynamic Reassembling Process Initiated from It." In: *Journal of the American Chemical Society* 118.35 (Jan. 1, 1996), pp. 8329–8335. ISSN: 0002-7863. DOI: 10.1021/ja960073b.

[161] Fang Yuan, Xiaoyu Song, Guangming Cheng, Nan Yao, Yurij Mozharivskyj, and Leslie M. Schoop. "Magnetic Nanosheets via Chemical Exfoliation of K2 xMnxSn1-xS2." In: *Chemistry of Materials* 34.11 (June 14, 2022), pp. 5084–5093. ISSN: 0897-4756. DOI: 10.1021/acs.chemmater.2c00488.

[162] Fuhua Yang, Jian Hong, Junnan Hao, Shilin Zhang, Gemeng Liang, Jun Long, Yuqing Liu, Nana Liu, Wei Kong Pang, Jun Chen, and Zaiping Guo. "Ultrathin Few-Layer GeP Nanosheets via Lithiation-Assisted Chemical Exfoliation and Their Application in Sodium Storage." In: *Advanced Energy Materials* 10.14 (2020), p. 1903826. ISSN: 1614-6840. DOI: 10.1002/aenm.201903826.

[163] A. Fasolino, J. H. Los, and M. I. Katsnelson. "Intrinsic Ripples in Graphene." In: *Nature Materials* 6.11 (11 Nov. 2007), pp. 858–861. ISSN: 1476-4660. DOI: 10.1038/nmat2011.

[164] Mikel Iraola, Juan L. Mañes, Barry Bradlyn, Titus Neupert, Maia G. Vergniory, and Stepan S. Tsirkin. "IrRep: Symmetry Eigenvalues and Irreducible Representations of Ab Initio Band Structures." Sept. 3, 2020.

[165] Jochen Heyd, Gustavo E. Scuseria, and Matthias Ernzerhof. "Hybrid Functionals Based on a Screened Coulomb Potential." In: *The Journal of Chemical Physics* 118.18 (May 8, 2003), pp. 8207–8215. ISSN: 0021-9606. DOI: 10.1063/1.1564060.

[166] Changgu Lee, Xiaoding Wei, Jeffrey W. Kysar, and James Hone. "Measurement of the Elastic Properties and Intrinsic Strength of Monolayer Graphene." In: *Science* 321.5887 (July 18, 2008), pp. 385–388. DOI: 10.1126/science.1157996.

[167] Simone Bertolazzi, Jacopo Brivio, and Andras Kis. "Stretching and Breaking of Ultrathin MoS2." In: *ACS Nano* 5.12 (Dec. 27, 2011), pp. 9703–9709. ISSN: 1936-0851. DOI: 10.1021/nn203879f.

[168] Lorenzo Monacelli, Ion Errea, Matteo Calandra, and Francesco Mauri. "Pressure and Stress Tensor of Complex Anharmonic Crystals within the Stochastic Self-Consistent Harmonic Approximation." In: *Physical Review B* 98.2 (July 26, 2018), p. 024106. ISSN: 2469-9950, 2469-9969. DOI: 10.1103/PhysRevB.98.024106.

[169] Itiro Syôzi. "Statistics of Kagomé Lattice." In: *Progress of Theoretical Physics* 6.3 (June 1, 1951), pp. 306–308. ISSN: 0033-068X. DOI: 10.1143/ptp/6.3.306.

[170] Dumitru Călugăru, Aaron Chew, Luis Elcoro, Yuanfeng Xu, Nicolas Regnault, Zhi-Da Song, and B. Andrei Bernevig. "General Construction and Topological Classification of Crystalline Flat Bands." In: *Nature Physics* 18.2 (2 Feb. 2022), pp. 185–189. ISSN: 1745-2481. DOI: 10.1038/s41567-021-01445-3.

[171] Mingu Kang, Shiang Fang, Linda Ye, Hoi Chun Po, Jonathan Denlinger, Chris Jozwiak, Aaron Bostwick, Eli Rotenberg, Efthimios Kaxiras, Joseph G. Checkelsky, and Riccardo Comin. "Topological Flat Bands in Frustrated Kagome Lattice CoSn." In: *Nature Communications* 11.1 (1 Aug. 10, 2020), p. 4004. ISSN: 2041-1723. DOI: 10.1038/s41467-020-17465-1.

[172] Mingu Kang, Linda Ye, Shiang Fang, Jhih-Shih You, Abe Levitan, Minyong Han, Jorge I. Facio, Chris Jozwiak, Aaron Bostwick, Eli Rotenberg, Mun K. Chan, Ross D. McDonald, David Graf, Konstantine Kaznatcheev, Elio Vescovo, David C. Bell, Efthimios Kaxiras, Jeroen van den Brink, Manuel Richter, Madhav Prasad Ghimire, Joseph G. Checkelsky, and Riccardo Comin. "Dirac Fermions and Flat Bands in the Ideal Kagome Metal FeSn." In: *Nature Materials* 19.2 (2 Feb. 2020), pp. 163–169. ISSN: 1476-4660. DOI: 10.1038/s41563-019-0531-0.

[173] Thomas Bilitewski. "Disordered Flat Bands on the Kagome Lattice." In: *Physical Review B* 98.23 (2018). DOI: 10.1103/PhysRevB.98.235109.

[174] Nirmal J. Ghimire and Igor I. Mazin. "Topology and Correlations on the Kagome Lattice." In: *Nature Materials* 19.2 (2 Feb. 2020), pp. 137–138. ISSN: 1476-4660. DOI: 10.1038/s41563-019-0589-8.

[175] I. I. Mazin, Harald O. Jeschke, Frank Lechermann, Hunpyo Lee, Mario Fink, Ronny Thomale, and Roser Valentí. "Theoretical Prediction of a Strongly Correlated Dirac Metal." In: *Nature Communications* 5.1 (1 July 1, 2014), p. 4261. ISSN: 2041-1723. DOI: 10.1038/ncomms5261.

[176] He Zhao, Hong Li, Brenden R. Ortiz, Samuel M. L. Teicher, Takamori Park, Mengxing Ye, Ziqiang Wang, Leon Balents, Stephen D. Wilson, and Ilija Zeljkovic. "Cascade of Correlated Electron States in the Kagome Superconductor CsV3Sb5." In: *Nature* 599.7884 (7884 Nov. 2021), pp. 216–221. ISSN: 1476-4687. DOI: 10.1038/s41586-021-03946-w.

[177] Qiangbing Guo, Xiao-Zhuo Qi, Lishu Zhang, Meng Gao, Sanlue Hu, Wenju Zhou, Wenjie Zang, Xiaoxu Zhao, Junyong Wang, Bingmin Yan, Mingquan Xu, Yun-Kun Wu, Goki Eda, Zewen Xiao, Shengyuan A. Yang, Huiyang Gou, Yuan Ping Feng, Guang-Can Guo, Wu Zhou, Xi-Feng Ren, Cheng-Wei Qiu, Stephen J. Pennycook, and Andrew T. S. Wee. "Ultrathin Quantum Light Source with van Der Waals NbOCl2 Crystal." In: *Nature* 613.7942 (7942 Jan. 2023), pp. 53–59. ISSN: 1476-4687. DOI: 10.1038/s41586-022-05393-7.

[178] Subir Sachdev. "Kagome- and Triangular-Lattice Heisenberg Antiferromagnets: Ordering from Quantum Fluctuations and Quantum-Disordered Ground States with Unconfined Bosonic Spinons." In: *Physical Review B* 45.21 (June 1, 1992), pp. 12377–12396. DOI: 10.1103/PhysRevB.45.12377.

[179] Jia-Xin Yin, Biao Lian, and M. Zahid Hasan. "Topological Kagome Magnets and Superconductors." In: *Nature* 612.7941 (7941 Dec. 2022), pp. 647–657. ISSN: 1476-4687. DOI: 10.1038/s41586-022-05516-0.

[180] Brenden R. Ortiz, Samuel M. L. Teicher, Yong Hu, Julia L. Zuo, Paul M. Sarte, Emily C. Schueller, A. M. Milinda Abeykoon, Matthew J. Krogstad, Stephan Rosenkranz, Raymond Osborn, Ram Seshadri, Leon Balents, Junfeng He, and Stephen D. Wilson. "CsV3Sb5: A $\mathbb{Z}_2$ Topological Kagome Metal with a Superconducting Ground State." In: *Physical Review Letters* 125.24 (Dec. 10, 2020), p. 247002. DOI: 10.1103/PhysRevLett.125.247002.

[181] Hengxin Tan, Yizhou Liu, Ziqiang Wang, and Binghai Yan. "Charge Density Waves and Electronic Properties of Superconducting Kagome Metals." In: *Physical Review Letters* 127.4 (July 22, 2021), p. 046401. ISSN: 0031-9007, 1079-7114. DOI: 10.1103/PhysRevLett.127.046401.

[182] Hui Chen, Haitao Yang, Bin Hu, Zhen Zhao, Jie Yuan, Yuqing Xing, Guojian Qian, Zihao Huang, Geng Li, Yuhan Ye, Sheng Ma, Shunli Ni, Hua Zhang, Qiangwei Yin, Chunsheng Gong, Zhijun Tu, Hechang Lei, Hengxin Tan, Sen Zhou, Chengmin Shen, Xiaoli Dong, Binghai Yan, Ziqiang Wang, and Hong-Jun Gao. "Roton Pair Density Wave in a Strong-Coupling Kagome Superconductor." In: *Nature* 599.7884 (7884 Nov. 2021), pp. 222–228. ISSN: 1476-4687. DOI: 10.1038/s41586-021-03983-5.

[183] C. C. Zhao, L. S. Wang, W. Xia, Q. W. Yin, J. M. Ni, Y. Y. Huang, C. P. Tu, Z. C. Tao, Z. J. Tu, C. S. Gong, H. C. Lei, Y. F. Guo, X. F. Yang, and S. Y. Li. "Nodal Superconductivity and Superconducting Domes in the Topological Kagome Metal CsV3Sb5." Mar. 1, 2021.

[184] Xianxin Wu, Tilman Schwemmer, Tobias Müller, Armando Consiglio, Giorgio Sangiovanni, Domenico Di Sante, Yasir Iqbal, Werner Hanke, Andreas P. Schnyder, M. Michael Denner, Mark H. Fischer, Titus Neupert, and Ronny Thomale. "Nature of Unconventional Pairing in the Kagome Superconductors AV_3Sb_5 ($A = \mathrm{K}, \mathrm{Rb}, \mathrm{Cs}$)." In: *Physical Review Letters* 127.17 (Oct. 19, 2021), p. 177001. DOI: 10.1103/PhysRevLett.127.177001.

[185] Jun Ge, Pinyuan Wang, Ying Xing, Qiangwei Yin, Hechang Lei, Ziqiang Wang, and Jian Wang. "Discovery of Charge-4e and Charge-6e Superconductivity in Kagome Superconductor CsV3Sb5." Jan. 25, 2022. DOI: 10.48550/arXiv.2201.10352.

[186] Tian Le, Zhiming Pan, Zhuokai Xu, Jinjin Liu, Jialu Wang, Zhefeng Lou, Zhiwei Wang, Yugui Yao, Congjun Wu, and Xiao Lin. *Evidence for Chiral Superconductivity in Kagome Superconductor CsV3Sb5*. Sept. 1, 2023. DOI: 10.48550/arXiv.2309.00264. preprint.

[187] Noah Ratcliff, Lily Hallett, Brenden R. Ortiz, Stephen D. Wilson, and John W. Harter. "Coherent phonon spectroscopy and interlayer modulation of charge density wave order in the kagome metal CsV_3Sb_5." In: *Physical Review Materials* 5.11 (Nov. 29, 2021), p. L111801. ISSN: 2475-9953. DOI: 10.1103/PhysRevMaterials.5.L111801.

[188] Haoxiang Li, T. T. Zhang, T. Yilmaz, Y. Y. Pai, C. E. Marvinney, A. Said, Q. W. Yin, C. S. Gong, Z. J. Tu, E. Vescovo, C. S. Nelson, R. G. Moore, S. Murakami, H. C. Lei, H. N. Lee, B. J. Lawrie, and H. Miao. "Observation of Unconventional Charge Density Wave without Acoustic Phonon Anomaly in Kagome Superconductors AV_3Sb_5 (A = Rb, Cs)." In: *Physical Review X* 11.3 (Sept. 3, 2021), p. 031050. DOI: 10.1103/PhysRevX.11.031050.

[189] Gan Liu, Xinran Ma, Kuanyu He, Qing Li, Hengxin Tan, Yizhou Liu, Jie Xu, Wenna Tang, Kenji Watanabe, Takashi Taniguchi, Libo Gao, Yaomin Dai, Hai-Hu Wen, Binghai Yan, and Xiaoxiang Xi. "Observation of Anomalous Amplitude Modes in the Kagome Metal CsV3Sb5." In: *Nature Communications* 13.1 (1 June 16, 2022), p. 3461. ISSN: 2041-1723. DOI: 10.1038/s41467-022-31162-1.

[190] Yishuai Xu, Zhuoliang Ni, Yizhou Liu, Brenden R. Ortiz, Qinwen Deng, Stephen D. Wilson, Binghai Yan, Leon Balents, and Liang Wu. "Three-State Nematicity and Magneto-Optical Kerr Effect in the Charge Density Waves in Kagome Superconductors." In: *Nature Physics* 18.12 (12 Dec. 2022), pp. 1470–1475. ISSN: 1745-2481. DOI: 10.1038/s41567-022-01805-7.

[191] Linpeng Nie, Kuanglv Sun, Wanru Ma, Dianwu Song, Lixuan Zheng, Zuowei Liang, Ping Wu, Fanghang Yu, Jian Li, Min Shan, Dan Zhao, Shunjiao Li, Baolei Kang, Zhimian Wu, Yanbing Zhou, Kai Liu, Ziji Xiang, Jianjun Ying, Zhenyu Wang, Tao Wu, and Xianhui Chen. "Charge-Density-Wave-Driven Electronic Nematicity in a Kagome Superconductor." In: *Nature* 604.7904 (7904 Apr. 2022), pp. 59–64. ISSN: 1476-4687. DOI: 10.1038/s41586-022-04493-8.

[192] Mingu Kang, Shiang Fang, Jonggyu Yoo, Brenden R. Ortiz, Yuzki M. Oey, Jonghyeok Choi, Sae Hee Ryu, Jimin Kim, Chris Jozwiak, Aaron Bostwick, Eli Rotenberg, Efthimios Kaxiras, Joseph G. Checkelsky, Stephen D. Wilson, Jae-Hoon Park, and Riccardo Comin. "Charge Order Landscape and Competition with Superconductivity in Kagome Metals." In: *Nature Materials* 22.2 (2 Feb. 2023), pp. 186–193. ISSN: 1476-4660. DOI: 10.1038/s41563-022-01375-2.

[193] Ge He, Leander Peis, Emma Frances Cuddy, Zhen Zhao, Dong Li, Ramona Stumberger, Brian Moritz, Haitao Yang, Hong-Jun Gao, Thomas Peter Devereaux, and Rudi Hackl. *Anharmonic Strong-Coupling Effects at the Origin of the Charge Density Wave in CsV_3Sb_5*. Aug. 14, 2023. preprint.

[194] Q. Stahl, D. Chen, T. Ritschel, C. Shekhar, E. Sadrollahi, M. C. Rahn, O. Ivashko, M. v. Zimmermann, C. Felser, and J. Geck. "Temperature-driven reorganization of electronic order in CsV_3Sb_5." In: *Physical Review B* 105.19 (May 24, 2022), p. 195136. DOI: 10.1103/PhysRevB.105.195136.

[195] Brenden R. Ortiz, Samuel M. L. Teicher, Linus Kautzsch, Paul M. Sarte, Noah Ratcliff, John Harter, Jacob P. C. Ruff, Ram Seshadri, and Stephen D. Wilson. "Fermi surface mapping and the nature of charge density wave order in the kagome superconductor CsV_3Sb_5." In: *Physical Review X* 11.4 (Nov. 11, 2021), p. 041030. ISSN: 2160-3308. DOI: 10.1103/PhysRevX.11.041030.

[196] Christopher Broyles, David Graf, Haitao Yang, Xiaoli Dong, Hongjun Gao, and Sheng Ran. "Effect of the Interlayer Ordering on the Fermi Surface of Kagome Superconductor CsV_3Sb_5 Revealed by Quantum Oscillations." In: *Physical Review Letters* 129.15 (Oct. 3, 2022), p. 157001. DOI: 10.1103/PhysRevLett.129.157001.

[197] Qian Xiao, Yihao Lin, Qizhi Li, Xiquan Zheng, Sonia Francoual, Christian Plueckthun, Wei Xia, Qingzheng Qiu, Shilong Zhang, Yanfeng Guo, Ji Feng, and Yingying Peng. "Coexistence of multiple stacking charge density waves in kagome superconductor CsV_3Sb_5." In: *Physical Review Research* 5.1 (Mar. 9, 2023), p. L012032. DOI: 10.1103/PhysRevResearch.5.L012032.

[198] Rustem Khasanov, Debarchan Das, Ritu Gupta, Charles Mielke, Matthias Elender, Qiangwei Yin, Zhijun Tu, Chunsheng Gong, Hechang Lei, Ethan T. Ritz, Rafael M. Fernandes, Turan Birol, Zurab Guguchia, and Hubertus Luetkens. "Time-reversal symmetry broken by charge order in CsV_3Sb_5." In: *Physical Review Research* 4.2 (June 27, 2022), p. 023244. DOI: 10.1103/PhysRevResearch.4.023244.

[199] Zhaoyang Shan, Pabitra K. Biswas, Sudeep K. Ghosh, T. Tula, Adrian D. Hillier, Devashibhai Adroja, Stephen Cottrell, Guang-Han Cao, Yi Liu, Xiaofeng Xu, Yu Song, Huiqiu Yuan, and Michael Smidman. "Muon spin relaxation study of the layered kagome superconductor CsV_3Sb_5." In: *Physical Review Research* 4.3 (Aug. 23, 2022), p. 033145. DOI: 10.1103/PhysRevResearch.4.033145.

[200] David R. Saykin, Camron Farhang, Erik D. Kountz, Dong Chen, Brenden R. Ortiz, Chandra Shekhar, Claudia Felser, Stephen D. Wilson, Ronny Thomale, Jing Xia, and Aharon Kapitulnik. "High Resolution Polar Kerr Effect Studies of CsV_3Sb_5: Tests for Time-Reversal Symmetry Breaking below the Charge-Order Transition." In: *Physical Review Letters* 131.1 (July 7, 2023), p. 016901. DOI: 10.1103/PhysRevLett.131.016901.

[201] Morten H. Christensen, Turan Birol, Brian M. Andersen, and Rafael M. Fernandes. "Theory of the charge density wave in AV_3Sb_5 kagome metals." In: *Physical Review B* 104.21 (Dec. 27, 2021), p. 214513. DOI: 10.1103/PhysRevB.104.214513.

[202] Yu-Xiao Jiang, Jia-Xin Yin, M. Michael Denner, Nana Shumiya, Brenden R. Ortiz, Gang Xu, Zurab Guguchia, Junyi He, Md Shafayat Hossain, Xiaoxiong Liu, Jacob Ruff, Linus Kautzsch, Songtian S. Zhang, Guoqing Chang, Ilya Belopolski, Qi Zhang, Tyler A. Cochran, Daniel

Multer, Maksim Litskevich, Zi-Jia Cheng, Xian P. Yang, Ziqiang Wang, Ronny Thomale, Titus Neupert, Stephen D. Wilson, and M. Zahid Hasan. "Unconventional chiral charge order in kagome superconductor KV3Sb5." In: *Nature Materials* 20.10 (10 June 10, 2021), pp. 1353–1357. ISSN: 1476-4660. DOI: 10.1038/s41563-021-01034-y.

[203] M. Michael Denner, Ronny Thomale, and Titus Neupert. "Analysis of Charge Order in the Kagome Metal AV_3Sb_5 (A =K,Rb,Cs)." In: *Physical Review Letters* 127.21 (Nov. 19, 2021), p. 217601. ISSN: 0031-9007, 1079-7114. DOI: 10.1103/PhysRevLett.127.217601.

[204] Yu-Ping Lin and Rahul M. Nandkishore. "Complex charge density waves at Van Hove singularity on hexagonal lattices: Haldane-model phase diagram and potential realization in the kagome metals AV_3Sb_5 (A=K, Rb, Cs)." In: *Physical Review B* 104.4 (July 14, 2021), p. 045122. DOI: 10.1103/PhysRevB.104.045122.

[205] Jin-Tao Jin, Kun Jiang, Hong Yao, and Yi Zhou. "Interplay between Pair Density Wave and a Nested Fermi Surface." In: *Physical Review Letters* 129.16 (Oct. 10, 2022), p. 167001. DOI: 10.1103/PhysRevLett.129.167001.

[206] Junze Deng, Ruihan Zhang, Yue Xie, Xianxin Wu, and Zhijun Wang. "Two elementary band representation model, Fermi surface nesting, and surface topological superconductivity in AV_3Sb_5 (A = K, Rb, Cs)." In: *Physical Review B* 108.11 (Sept. 12, 2023), p. 115123. DOI: 10.1103/PhysRevB.108.115123.

[207] Yaofeng Xie, Yongkai Li, Philippe Bourges, Alexandre Ivanov, Zijin Ye, Jia-Xin Yin, M. Zahid Hasan, Aiyun Luo, Yugui Yao, Zhiwei Wang, Gang Xu, and Pengcheng Dai. "Electron-phonon coupling in the charge density wave state of CsV_3Sb_5." In: *Physical Review B* 105.14 (Apr. 5, 2022), p. L140501. DOI: 10.1103/PhysRevB.105.L140501.

[208] Zhiwei Wang, Yu-Xiao Jiang, Jia-Xin Yin, Yongkai Li, Guan-Yong Wang, Hai-Li Huang, Sen Shao, Jinjin Liu, Peng Zhu, Nana Shumiya, Md Shafayat Hossain, Hongxiong Liu, Youguo Shi, Junxi Duan, Xiang Li, Guoqing Chang, Pengcheng Dai, Zijin Ye, Gang Xu, Yanchao Wang, Hao Zheng, Jinfeng Jia, M. Zahid Hasan, and Yugui Yao. "Electronic nature of chiral charge order in the kagome superconductor CsV_3Sb_5." In: *Physical Review B* 104.7 (Aug. 25, 2021), p. 075148. DOI: 10.1103/PhysRevB.104.075148.

[209] Titus Neupert, M. Michael Denner, Jia-Xin Yin, Ronny Thomale, and M. Zahid Hasan. "Charge Order and Superconductivity in Kagome Materials." In: *Nature Physics* 18.2 (2 Feb. 2022), pp. 137–143. ISSN: 1745-2481. DOI: 10.1038/s41567-021-01404-y.

[210] Chongze Wang, Shuyuan Liu, Hyunsoo Jeon, Yu Jia, and Jun-Hyung Cho. "Charge density wave and superconductivity in the kagome metal CsV_3Sb_5 around a pressure-induced quantum critical point." In: *Physical Review Materials* 6.9 (Sept. 20, 2022), p. 094801. DOI: 10.1103/PhysRevMaterials.6.094801.

[211] Mehdi Frachet, Liran Wang, Wei Xia, Yanfeng Guo, Mingquan He, Nour Maraytta, Rolf Heid, Amir-Abbas Haghighirad, Michael Merz, Christoph Meingast, and Frederic Hardy. *Colossal c-axis response and lack of rotational symmetry breaking within the kagome plane of the CsV_3Sb_5 superconductor*. Oct. 9, 2023. DOI: 10.48550/arXiv.2310.06102. preprint.

[212] Francesco Ferrari, Federico Becca, and Roser Valentí. "Charge Density Waves in Kagome-Lattice Extended Hubbard Models at the van Hove Filling." In: *Physical Review B* 106.8 (Aug. 8, 2022), p. L081107. DOI: 10.1103/PhysRevB.106.L081107.

[213] Alaska Subedi. "Hexagonal-to-base-centered-orthorhombic 4Q charge density wave order in kagome metals KV_3Sb_5, RbV_3Sb_5, and CsV_3Sb_5." In: *Physical Review Materials* 6.1 (Jan. 14, 2022), p. 015001. DOI: 10.1103/PhysRevMaterials.6.015001.

[214] Martin Gutierrez-Amigo, Fang Yuan, Davide Campi, Leslie M. Schoop, Maia G. Vergniory, and Ion Errea. "Purely anharmonic charge density wave in the two-dimensional Dirac semimetal SnP." In: *Physical Review B* 109.17 (May 14, 2024), p. 174112. DOI: 10.1103/PhysRevB.109.174112.

[215] Ion Errea, Francesco Belli, Lorenzo Monacelli, Antonio Sanna, Takashi Koretsune, Terumasa Tadano, Raffaello Bianco, Matteo Calandra, Ryotaro Arita, Francesco Mauri, and José A. Flores-Livas. "Quantum Crystal Structure in the 250-Kelvin Superconducting Lanthanum Hydride." In: *Nature* 578.7793 (7793 Feb. 2020), pp. 66–69. ISSN: 1476-4687. DOI: 10.1038/s41586-020-1955-z.

[216] G. Kresse and D. Joubert. "From Ultrasoft Pseudopotentials to the Projector Augmented-Wave Method." In: *Physical Review B* 59.3 (Jan. 15, 1999), pp. 1758–1775. DOI: 10.1103/PhysRevB.59.1758.

[217] Andrea Corso. "Pseudopotentials Periodic Table: From H to Pu." In: *Computational Materials Science* 95 (Dec. 1, 2014), pp. 337–350. DOI: 10.1016/j.commatsci.2014.07.043.

[218] Arash A. Mostofi, Jonathan R. Yates, Giovanni Pizzi, Young-Su Lee, Ivo Souza, David Vanderbilt, and Nicola Marzari. "An Updated Version of Wannier90: A Tool for Obtaining Maximally-Localised Wannier Functions." In: *Computer Physics Communications* 185.8 (Aug. 1, 2014), pp. 2309–2310. ISSN: 0010-4655. DOI: 10.1016/j.cpc.2014.05.003.

[219] QuanSheng Wu, ShengNan Zhang, Hai-Feng Song, Matthias Troyer, and Alexey A. Soluyanov. "WannierTools: An Open-Source Software Package for Novel Topological Materials." In: *Computer Physics Communications* 224 (Mar. 1, 2018), pp. 405–416. ISSN: 0010-4655. DOI: 10.1016/j.cpc.2017.09.033.

[220] Xiangwei Huang, Chunyu Guo, Carsten Putzke, Martin Gutierrez-Amigo, Yan Sun, Maia G. Vergniory, Ion Errea, Dong Chen, Claudia Felser, and Philip J. W. Moll. "Three-dimensional Fermi surfaces from charge order in layered CsV_3Sb_5." In: *Physical Review B* 106.6 (Aug. 23, 2022), p. 064510. DOI: 10.1103/PhysRevB.106.064510.

[221] A. Korshunov, H. Hu, D. Subires, Y. Jiang, D. Călugăru, X. Feng, A. Rajapitamahuni, C. Yi, S. Roychowdhury, M. G. Vergniory, J. Strempfer, C. Shekhar, E. Vescovo, D. Chernyshov, A. H. Said, A. Bosak, C. Felser, B. Andrei Bernevig, and S. Blanco-Canosa. "Softening of a Flat Phonon Mode in the Kagome ScV6Sn6." In: *Nature Communications* 14.1 (1 Oct. 20, 2023), p. 6646. ISSN: 2041-1723. DOI: 10.1038/s41467-023-42186-6.

[222] Hong Li, Siyu Cheng, Brenden R. Ortiz, Hengxin Tan, Dominik Werhahn, Keyu Zeng, Dirk Johrendt, Binghai Yan, Ziqiang Wang, Stephen D. Wilson, and Ilija Zeljkovic. "Electronic Nematicity without Charge Density Waves in Titanium-Based Kagome Metal." In: *Nature Physics* 19.11 (11 Nov. 2023), pp. 1591–1598. ISSN: 1745-2481. DOI: 10.1038/s41567-023-02176-3.

[223] Xiaokun Teng, Ji Seop Oh, Hengxin Tan, Lebing Chen, Jianwei Huang, Bin Gao, Jia-Xin Yin, Jiun-Haw Chu, Makoto Hashimoto, Donghui Lu, Chris Jozwiak, Aaron Bostwick, Eli Rotenberg, Garrett E. Granroth, Binghai Yan, Robert J. Birgeneau, Pengcheng Dai, and Ming Yi. "Magnetism and Charge Density Wave Order in Kagome FeGe." In: *Nature Physics* 19.6 (6 June 2023), pp. 814–822. ISSN: 1745-2481. DOI: 10.1038/s41567-023-01985-w.

[224] Haoyu Dong, Peihan Sun, Le Lei, Yanyan Geng, Jianfeng Guo, Yan Li, Li Huang, Rui Xu, Fei Pang, Wei Ji, Weichang Zhou, Zheng Liu, Zhong-Yi Lu, Hong-Jun Gao, Kai Liu, and Zhihai Cheng. *Emergent Electronic Kagome Lattice in Correlated Charge-Density-Wave State of 1T-TaS_2*. Jan. 14, 2023. DOI: 10.48550/arXiv.2301.05885. preprint.

[225] Neil Ashcroft and N. Mermin. *Solid State Physics*. New York, Jan. 2, 1976. 848 pp. ISBN: 978-0-03-083993-1.